Matter under extreme conditions: modelling giant planets

Dissertation

zur

Erlangung des akademischen Grades

doctor rerum naturalium (Dr. rer. nat.)

der Mathematisch-Naturwissenschaftlichen Fakultät

der Universität Rostock

vorgelegt von:

Nadine Nettelmann

geb. am 2. Juli 1975 in Hannover

aus Rostock

urn:nbn:de:gbv:28-diss2011-0159-8

1. Betreuer:	Prof. Dr. Ronald Redmer, Universität Rostock, Institut für Physik
2. Betreuer:	Prof. Dr. Ralph Neuhäuser, Universität Jena, Astrophysikalisches Institut und Universitätssternwarte
Abgabe:	7. September 2009
Verteidigung:	Freitag, den 13. November 2009

Abstract

Jupiter and Saturn have been observed for several thousand years, Uranus and Neptune for more than 100 years, and hydrogen, helium, and water under high pressure have been investigated for many decades. Still, these objects of human interest hold many riddles, and this thesis is devoted to study their relationships, and to outline paths to walk on in the years to come.

We calculate the core mass, metallicity and cooling curves of these planets and evaluate the results with respect to the hydrogen equation of state, the phase diagram of water, and immiscibility of helium in hydrogen. We conclude a likely occurrence of He sedimentation, core erosion, and inhibited convection in these planets and propose alternative structure models as improved representations of these planets.

Contents

1 Introduction **1**

2 Equations of state **3**
2.1 Hydrogen EOS . . . 4
2.2 Helium EOS . . . 9
2.3 Metals . . . 10
2.4 Linear mixing . . . 12

3 Calculating structure models **14**
3.1 Observables and constraints . . . 14
3.1.1 Luminosity . . . 14
3.1.2 Surface temperature . . . 19
3.1.3 Mass and Radius . . . 20
3.1.4 Helium abundance . . . 21
3.1.5 Heavy element abundance . . . 22
3.1.6 Rotational frequency and Gravitational moments . . . 23
3.1.7 The standard three-layer structure type of a giant planet . . . 24
3.2 Basic Equations . . . 25
3.3 The potential of a rigidly rotating planet . . . 27
3.3.1 Multipole expansion of $V(\vec{r})$ . . . 27
3.3.2 Multipole expansion of $Q(\vec{r})$ . . . 30
3.4 Theory of Figures . . . 31
3.4.1 Level surfaces . . . 32
3.4.2 $\mathbf{s_0}$ . . . 32
3.4.3 The potential: $U(l)$ . . . 37
3.4.4 The force: $-dU/dl$ . . . 43
3.5 Accuracy, Bugs, and Procedure . . . 43

4 Three-layer structure models of the Outer Planets **46**
4.1 JUPITER . . . 51
4.1.1 Jupiter models with SCvH EOS and LM-REOS . . . 51
4.1.2 Jupiter models with Sesame EOS . . . 56
4.1.3 Jupiter models with various EOS: core mass and metallicity . . . 57
4.1.4 Towards Militzer model . . . 59
4.1.5 Towards more acceptable Jupiter models with FT-DFT-MD . . . 61
4.2 SATURN . . . 63
4.2.1 Core mass . . . 63
4.2.2 Helium abundance and metalicities predicted by LM-REOS . . . 65
4.3 URANUS and NEPTUNE . . . 67

4.3.1 Similar or dissimilar planets Uranus and Neptune . . . 70
4.3.2 Phases of water in Uranus and Neptune . . . 70
4.4 Standard Three-Layer Pie Charts . . . 73

5 Planetary Evolution 75
5.1 The cooling equation . . . 76
5.2 Homogeneous evolution . . . 79
5.2.1 Introduction . . . 79
5.2.2 Performance . . . 81
5.2.3 Results for Jupiter, Saturn, Uranus, and Neptune . . . 81
5.3 Inhomogeneous evolution . . . 85
5.3.1 H/He phase separation: the phase diagram . . . 86
5.3.2 H/He phase separation in Saturn: first results (work in progress) . . . 89
5.3.3 H/He phase separation in other planets than Saturn . . . 90
5.3.4 Inhibited convection in Uranus and Neptune . . . 91

6 From the far past to the near future 93
6.1 Giant Planet Formation . . . 93
6.2 Core erosion . . . 95
6.3 Layer boundaries . . . 97
6.4 Extrasolar Planets . . . 99

7 Summary 101

Bibliography 103

A Long Tables 109
A.1 Table A.1: EOS applied to Jupiter . . . 109
A.2 Table A.2: Observed parameters . . . 110
A.3 Table A.3: Gravitational moments . . . 111
A.4 Table A.4: Interior models with and without the 2 bugs . . . 113
A.5 Table A.5: Selected interior models . . . 114

B Supplementary Figures 115

C Calculating the entropy 119

D Derivations and Proofs 122
D.1 Derivation of equations 3.18 and 3.19 . . . 122
D.2 Derivation of equation 3.46 . . . 123
D.3 Legendre polynomials: useful properties . . . 127
D.3.1 Calculating products $P_m * P_n$ . . . 127
D.3.2 Proofs and comments . . . 127
D.4 Proof of equation 5.10 . . . 128

E The 2 Bugs 130

F Theory of Figures: coefficients 132

Chapter 1

Introduction

Matter under extreme conditions

Extreme conditions considered in this thesis are thermodynamic states beyond the conditions found in our natural environment on planet's Earth surface, conditions too hostile for life to exist. Extreme conditions we are interested in here cause molecules to dissociate, and atoms to get stripped off weakly bound electrons; but still we can distinguish between various elements such as hydrogen, helium, and oxygen, the most abundant elements in the universe and presumably also in giant planets. Individual molecules and ions under extreme conditions are restricted in their freedom to move, strong Coulomb forces screened by released electrons enforce a coupled motion, and the fermion nature of the electrons rises the pressure. In laboratory experiments, megabar pressures are required to prevent matter under such extreme conditions from exploding. Fortunately, giant planets are massive enough to hold high-pressure matter imprisoned through gravity; contrary to stars, they are cold enough to not let thermal energy, but the interaction potential determine the motion of particles; and they are dense but not too compact to be dominated by degeneracy. Giant planets are natural laboratories to study *warm dense matter*.

Motivation

For many decades, scientists have been working hard on creating warm dense matter (temperatures of $\sim 10^3 - 10^5\,\mathrm{K}$, electron densities of $\sim 10^{20} - 10^{26}\,\mathrm{g/cm^3}$) in laboratories. Further experiments are in preparation to finally understand the simplest elements H and He and the important molecule H_2O. What drives people to explore these materials under extreme conditions? Certainly, the desire for strategic and political power has pushed the development of nuclear weapons, and fusion of deuterium is one of the most intensive energy sources available on Earth. Nowadays, the growing need of alternative energy sources for civil application has spurred research on initial confinement fusion of deuterium and tritium, for which the understanding of the equation of state of H and H_2O is crucial. Scientists investigating properties of warm dense hydrogen, helium, and water often motivate their work also by importance for planetary science. How can planetary scientists motivate their work?

Interest in planets dates back to more than 3000 years ago. The ancient Babylonians carefully observed the apparent motion of planets across the sky in order to foresee their destiny: the five closest planets, observable with the naked eye, were considered gods influencing human affairs. Since then, observations of the Sun, planets, and moons in the solar system have shaped our imagination of the structure of the universe [Kan91]. Brahe's (1546-1601) accurate observations of the apparent motion of planets for instance revealed a non-circular, non-constant velocity motion

contradicting the geometric idealizations of planets and the universe as postulated since the time of Platon (4th cent. BC). After Newton had found the law of gravity, knowledge of the Galilean satellites orbiting Jupiter, and the planets orbiting the Sun, inspired Kant (1724-1804) to look for evidence of the Sun orbiting an even larger mass concentration. The galactic dimension of the Milky Way was found. To date, research on planets in general and on planet formation, planetary structure and evolution in particular, is certainly motivated by the prospect to detect and later on to colonize Earth-like planets around neighboured stars, an inevitable task for future inhabitants of the Earth.

Modelling Giant Planets

An important step from the mythological kind of considering planets towards our present scientific understanding of planets was achieved in the 6th cent. BC by greek philosophers, who thought of planets and the Moon as physical objects composed of elements originating from Earth, i.e. of fire and rocks [Kan91]. The mass of heavy elements including rocks inside Jupiter is among the main topics addressed in this work.

Our current understanding of giant planets as prevalently made of hydrogen and possibly a dense rocky core is relatively young, see Wildt (1947) for a nice review of the beginnings of modern planetary science. With improved equations of state taking into account non-ideality effects, a transition from molecular to metallic hydrogen in Jupiter was already discussed by DeMarcus (1958). Hubbard (1969) concluded an adiabatically stratified, convective interior of Jupiter in order to explain the observed excess luminosity. *Voyager 2* measurements finally completed the sets of assumptions and constraints that constitute the state-of-the-art picture of Jupiter and the other giant planets in the solar system.

Outline

In § 2, I describe equations of state for H, He, and H_2O with special emphasis on the chemical picture based SCvH EOS and ab initio data based LM-REOS. Before we apply them in § 4 to interior structure models of giant planets and in § 5 to their evolution, we learn in § 3 in detail about the parameters constraining interior models (§ 3.1), the basic equations sufficient for non-rotating planets (§ 3.2), their expansion to rotating planets (§ 3.3), the standard method of calculating the shape and observational signatures of rigidly rotating planets (§ 3.4), and in § 3.5 and appendix E we compare the output of computer codes with analytical test cases. In § 3, we also become familiar with the gravitational moments and their sensitivity to pressure levels of interest.

In § 4 we take advantage of this magnificent property to probe the pressure-density relation of giant planets and evaluate high-pressure equations of state. Besides, we obtain results for the core mass and metallicity of Jupiter (§ 4.1), Saturn (§ 4.2), and Uranus and Neptune (§ 4.3). The point of interest is the response of the range of acceptable solutions to the equation of state used. In § 5, we include the luminosity into the set of parameters to be reproduced by our models and present cooling curves for the outer planets. We discuss the results with respect to H/He phase separation and inhibited convection in § 5.3. We propose in § 6 new paths of constructing interior models with respect to the number of layers that are consistent with core erosion, He sedimentation, and formation scenarios. After a summary of this work in § 7, the reader is invited to find tables, supplementary figures, derivations, coefficients, and a method of calculating the entropy in the appendix. References and acknowledgements close this dissertation.

Chapter 2

Equations of state

Interior models of Jupiter, Saturn, Uranus, and Neptune require equation of state (EOS) data for H, He, and metals from $70-170\,\mathrm{K}$ at 1 bar up to about $7000\,\mathrm{K}$ at $7\,\mathrm{Mbar}$ (Neptune) or up to about $25,000\,\mathrm{K}$ at $45\,\mathrm{Mbar}$ (Jupiter). No state-of-the-art thermodynamic model is capable of providing accurate EOS data for all relevant materials in this wide temperature-pressure range. Various EOS data sets have been constructed for this purpose by combining various methods known to give good results in limiting cases.

In the following, I give an overview about equations of state of hydrogen, helium, and metals that have been applied to Jupiter, with particular emphasis on SCvH EOS and LM-REOS. They are not only representatives of the competing chemical and physical pictures; SCvH EOS is widely used in astrophysics for giant planets, brown dwarfs, and low-mass stars, and LM-REOS shows the currently best agreement with available laboratory experimental data in high-pressure physics.

The chemical picture. The chemical picture assumes a certain number of species (e.g. H_2 and H) that remain distinct under all conditions. Advanced chemical picture EOS such as SCvH include chemical equilibrium (e.g. $\mu_{H_2} = 2\mu_H$) and ionization equilibrium (e.g. $\mu_H = \mu_p + \mu_e$) between different species. Other chemical picture EOS alternatively are constructed by interpolation between regimes where certain species certainly dominate the composition. Examples are LM EOS and Sesame EOS.

Many-body effects are accounted for by using effective pair potentials obtained by fitting experimental data. However, these are reliable only for those species which have been investigated experimentally and only in the regime probed. In case of hydrogen, the H_2-H_2 potential is well-known up to 10 GPa, and various H-H potentials have been suggested. When the interparticle distances become smaller with increasing density or pressure, the potentials proposed for atomic H may happen to be less repulsive than for H_2-H_2. This is certainly an upper limit for a useful application of chemical picture EOS and they must be combined with other methods more appropriate at high densities, for instance with Padé formulas or simulations. Consequently, the chemical picture is especially appropriate for not too dense systems with a small number of species, since all interaction potentials must be reasonable.

A common property of chemical picture EOS is the assumption, that the partition function of the system can be factorized and hence the free energy F be written in terms of a linear superposition. Different chemical picture EOS differ in the expressions contributing to F. References of detailed chemical picture descriptions can be found in [Juranek04, SauGui04] and are not repeated here.

The physical picture. In the physical picture, basic particles are ions and electrons interacting via Coulomb forces. Thermodynamic quantities are usually obtained by means of computer simulations, where a thermodynamic equilibrium configuration is obtained after sufficiently frequent collisions. Compared to interactions in the chemical picture, ab initio simulations directly include many-body collisions between all kinds of ions or neutrals. Methodically different descriptions of the electronic system and the ionic system are required in order to take care of the quantum nature of the electrons. Real quantum molecular dynamics simulations including also the quantum nature of the ions are being developed but not used in this work. Many difficulties of the physical picture approach are related to the description of the electronic system. Density functional theory (DFT) offers a state-of the-art method to obtain the electronic equilibrium configuration for a given ion distribution. Among the largest uncertainties related to DFT is the proper choice of the interaction potential at very short distances, where a pure Coulomb potential would naturally produce highly oscillating electron wave functions. In this sense, the ab initio idea is limited. Its great advantage for the region of partial ionization lies in its conceptual independence on the distinction between bound states and free electrons. Hence, in priciple, all ionization states realized in nature should also occur in the simulation. For long, the main drawback has been a tremendous amount of computing time for convergence of the simulated system into an equilibrium state. Fortunately, the past years have seen a vast progress in available CPU time, and most giant planet interior models presented in this work are finally based on ab inito EOS data.

2.1 Hydrogen EOS

At temperatures above 1000 K, with increasing pressure hydrogen becomes a partially ionized fluid, with the result that for $P > 1$ Mbar it becomes a fully dissociated, metallic, atomic fluid. The transition from a non-metallic to a metallic fluid (NM-M transition) is clearly seen in conductivity and reflectivity measurements. However, the way this transition occurs is still a matter of intense debate and is not discussed in detail in this work. Unsolved questions are, for instance: Does, with increasing pressure, molecular H first become pressure dissociated and then the atoms pressure ionized? Is the transition from neutral, molecular hydrogen to conducting, atomic hydrogen of first order? Or in other words: is there a plasma phase transition (PPT)? Below 1000 K (or 300 K), does metallic hydrogen solidify and form a solid metal?

We consider various H-EOS both in the chemical and in the physical picture that give various answers to these questions and that give (or are claimed to give) acceptable planetary models.

• LM EOS

The linear mixing model of Ross (1998) assumes the total Helmholtz free energy F of a system of H_2 molecules and metallic H as linear superposition of the free energies $F_{\rm mol}$ and $F_{\rm met}$ of the single components, respectively. The original EOS was constructed to reproduce the gas gun data by adjusting the effective molecular pair potential, and to fit their low reshock temperatures by addition of a fitting term $F_{\rm fit}$ in the total free energy. This term causes a region where $\nabla_{ad} < 0$ along the Jupiter isentrope.

Saumon and Guillot (2004) avoided this behaviour by taking into account electron screening in the metallic component **(LM-SOCP)** or by admixing of D_4 chains as a further species **(LM-H4)**. Along the principal Hugoniot, LM-SOCP has a small compressibility almost in agreement with the Z-pinch data, but predicts higher temperatures than obtained with Nova Laser data, which are well reproduced by LM-H4.

• **Sesame**

The Sesame data table [SESAME table (1992)] provides equations of state for many elements and materials, including H, He, and H_2O. The H-EOS *Sesame 5251* is the deuterium EOS 5263 scaled in density as developed by Kerley in 1972. It is based on the chemical picture and built upon the assumption of three phases: a molecular solid phase, an atomic solid phase, and a fluid phase which takes into account chemical equilibrium between molecules and atoms and ionization equilibrium between atoms, protons and electrons. A completely revised version [Kerley03] includes, among many other improvements, fits to more recent shock compression data resulting into a larger compressibility at ~ 0.5 Mbar, and a smaller one at ~ 10 Mbar. We call this improved version **H-Sesame-K03**. It has a first-order phase transition between solid and fluid hydrogen with a critical point at ≈ 3500 K and 3.2 Mbar and a continuous NM-M transition. This revised version also gives very good agreement with sound velocity data up to 20 GPa. Saumon and Guillot (2004) patched the original version 5251 at pressures between 100 bar and 0.4 Mbar with another EOS in order to reproduce the gas gun data and label this version **H-Sesame-p**.

• **H-SCVH**

For a detailed description of these EOS see [SauChaHor95] and references therein. SCvH-ppt and SCvH-i are data tables for mass density $\rho(P,T)$, number concentration of molecules $X_{H_2}(P,T)$ and atoms $X_H(P,T)$, specific entropy $s(P,T)$, internal energy $u(P,T)$, and partial derivatives. SCvH-i covers the range of pressures and temperatures relevant for giant planets, brown dwarfs, low-mass stars, and white dwarf atmospheres. Hence, it is widely used in astrophysics. SCvH-ppt equals SCvH-i everywhere apart from a region $10^3 < T < 2\,10^4$ K, $0.1 < P < 100$ Mbar where molecular hydrogen transits to metallic H^+. In this region, a thermodynamic instability $(\partial P/\partial V) > 0$ is found and encountered by constructing a first-order phase transition (SCvH-ppt), or alternatively by interpolating across the regime of partial ionization (SCvH-i). Isotherms of both versions in this important regime are compared in Fig. 2.1 in $P-\rho$ space. In this figure, five isotherms are indicated by the color code: solid lines are for SCvH-ppt EOS and dashed lines for SCvH-i EOS. Within the region enclosed by the black lines, molecular phase and metallic phase coexist. Pairs of points of the same color visualize the low-density point of the molecular phase and the high-density point of the metallic phase, respectively. For the $\log T = 4.18$ ($T = 15,135$K) isotherm, both points coincide: the blue point is the critical point. The coexistence region predicted by SCvH-ppt EOS extends in temperature from $10^{3.54} \approx 3500$ K to $10^{4.18}$ K and in pressure from 63 GPa at the critical point to 229 GPa. Regarding planetary models, it is important to recognize that the interpolated isotherms are more compressible in the dense molecular region but less compressible at supercritical pressures than the isotherms they interpolate. The higher the temperature, the more the interpolated isotherms tend to extrapolate the molecular region thereby enhancing the pressure up to 0.5 Mbar, which gives a better agreement with Z-Pinch Hugoniot data, see Fig. 2.2.

SCvH-ppt and SCvH-i EOS are based on the chemical picture assuming species H_2, H, H^+, and e^-. Neutral particles are treated by a Helmholtz free energy (F) minimization method, where F is minimized with respect to the degree of dissociation. The grand partition function $\mathcal{Z}$ is factorized into three terms regarding ideal contributions $\mathcal{Z}_{kin}$, internal energy contributions $\mathcal{Z}_{int}$ occupying energy levels according to an occupation probability function which takes into account the *excluded volume concept*, and $\mathcal{Z}_{conf}$. $\mathcal{Z}_{int}$ is coupled to $\mathcal{Z}_{conf}$, which accounts for interparticle interactions using effective pair potentials, from which equivalent hard sphere diameters are derived that determine the excluded volume. Charged particles at high densities are described by a screened one component plasma model (SOCP) and at very high densities by the OCP model. Interactions between neutral and charged particles are considered by a polarization potential. Saumon et al. (1995) conclude the unstable transition region from the molecular to the ionized atomic system as an unavoidable outcome of the chemical picture, when methods developed for different regimes

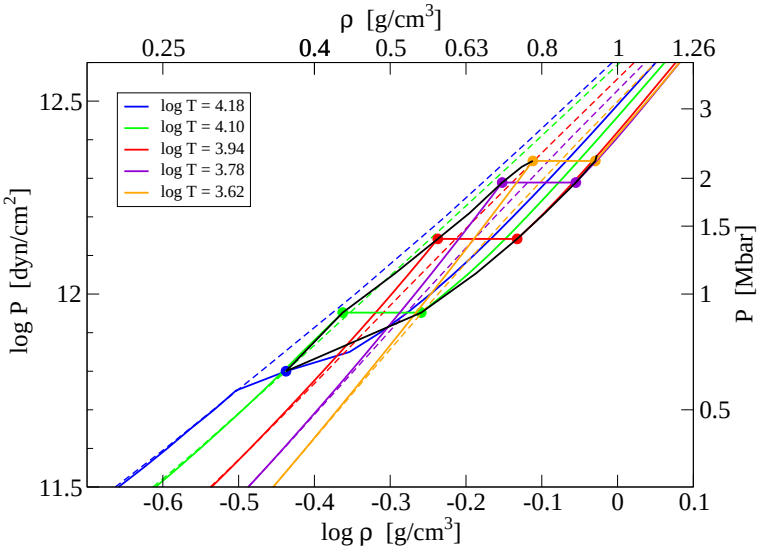

Figure 2.1: Isotherms of SCvH-ppt (*solid*) and SCvH-i (*dashed*) at five temperatures coded by color including the critical isotherm at $\log T = 4.18$. Circles highlight the instability region of SCvH-ppt. This figure shows that by construction, SCvH-i is significantly stiffer for pressures around 1 to 100 Mbar.

(H, H_2 on the one hand, H^+, e^{-1} on the other hand) are applied to the regime of partial ionization. There, both methods become invalid because of an improper treatment of bound states. The credibility of such a phase transition is questionable.

• **FVT**

For references see [Juranek04], [RedmerEtAl06b] and [HolNettRed07]. Several chemical picture EOS for H and He based on Fluid Variational Theory (FVT) have been developed in Rostock and applied in this work. A general starting point is the partition of the Helmholtz free energy into

$$F = F_0 + F_\pm + F_{pol} \quad \text{with} \quad F_0 = F_0^{id} + F_0^{int} \quad , \quad F_\pm = F_\pm^{id} + F_\pm^{int} \quad . \tag{2.1}$$

F_0 is the free energy of the neutral system, in particular $\{H, H_2\}$ for hydrogen. $F_\pm$ is the free energy of the fully ionized system $\{H^+, e^-\}$. F_{pol} accounts for the interaction between neutrals on the one hand and charged particles on the other hand by means of a polarization potential. F_0 and $F_\pm$ can be split into an ideal part (*id*) and an interaction part (*int*). In order to obtain F_0^{int}, FVT is applied and for $F_\pm^{int}$ Padé formulas are used. With FVT, F_0^{int} is found by minimizing the right hand side of the Bogolyubov inequality $F \leq F_0 + (\phi - \phi_0)_0$ with respect to the diameter of hard spheres and the degree of dissociation, where index 0 denotes the hard sphere reference system, ϕ the potential, and $()_0$ is a weight function for the interparticle distances of the hard spheres. This is the point where the effective potential ϕ enters the procedure. We chose exponential-6 potentials for $H_2 - H_2$, $H - H_2$, and $H - H$ with coefficients suggested by Ree (1988) or by Fried et al. (2002). In order to obtain $F_\pm^{int}$, Juranek (2004) implemented Padé formulas by Stolzmann and Blöcker, and Holst et al. (2007) those by Potekhin and Chabrier.

FVT EOS. At temperatures below 1000 K and pressures between 1 bar and 0.5 Mbar, hydrogen forms molecules and atoms, which means ionization is neglegible and $F_\pm$ can be omitted. We label this H-EOS *FVT EOS*. Its prediction for the shock velocity and the sound velocity at $P < 50$ GPa

shows good agreement with Z-Pinch and gas gun data as well as with the LM model by Ross. More accurate sound velocity measurements would be helpful. For instance, the theoretical models are within the exerimental error bars of gas gun measurements by Holmes (2001, *unpublished*), but predict c_s to be rising with pressure, while the data points are not [Juranek04, JuranekEtAl05].

FVT$^+_{id}$ EOS. When Padé formulas are applied in the regime of partial ionizaion, $P(T, \rho)$ is well-known to become unrealistically small. This complicates the construction of selfconsistent EOS in this regime. A first step to include ionization is to consider only the ideal quantum gas contribution $F^{id}_{\pm}$. We label the corresponding EOS FVT$^+_{id}$. Already at this step, an important influence on the onset of pressure ionization is seen dependent on the volume that the wave functions of point-like particles are allowed to occupy. We applied the reduced-volume-concept [HolNettRed07] and corrected the hard-sphere-diameter resulting from the free energy minimization procedure in order to avoid survival of molecules and atoms at pressures > 10 Mbar and to be consistent with the maximal packing fraction. FVT$^+_{id}$ was successfully applied to Jupiter in [RedmerEtAl06a], but predicted a maximal compressibility ≈ 6 along the Hugoniot not in agreement with Z-pinch experimental data. For $P \leq 0.6$ Mbar, the agreement with gas gun data and with explosives shock compression data is very good, in particular when using the less compressible effective H-H potential by Fried et al. (2002), see [RedmerEtAl06b].

FVT$^+$ EOS. Padé formulas were finally included by Holst and the resulting EOS was named FVT$^+$. The instability region was encountered by a Maxwell construction. Various versions were generated by Holst, some found to have an increasing, some a decreasing coexistence line in $P-T$ space. A common feature was a critical point around 17000 K and in $P-\rho$ space a very broad transition region, greatly enhancing the maximal compression along the Hugoniot. I transformed the FVT$^+$ data into the clever SCvH EOS format for application to Jupiter. Because of its large compressibility, we obtained a metal-free envelope inconsistent with observational constraints. These results marked the end of our trials to construct a chemical picture hydrogen EOS in the warm dense matter regime typical for Jupiter's interior.

• **H-REOS**

The hydrogen Rostock equation of state (H-REOS) was constructed for application to Jupiter. It combines FVT EOS, FVT$^+$ EOS, and ab initio EOS data. More than 97% of Jupiter's mass lies in the high-pressure regime where H-REOS relies on the ab initio data. Hence these data dominate the behaviour of Jupiter interior structure models. The underlying method of generating these data has been described in detail elsewhere [KietzmannEtAl07, HolRedDes08, NettelmannEtAl08, FrenchEtAl09]. That's why I only outline some main characteristics here.

FT-DFT-MD simulations. The ab initio data for H used in this work have been calculated by Holst using the code VASP (Vienna ab initio simulation package). The ions (here: protons) are treated by classical Monte Carlo simulations (MD), and the electrons by density functional theory (DFT) including finite temperature effects (FT-DFT). The electronic wave functions are represented by plane waves and calculated using projector augmented wave (PAW) pseudopotentials. Those equal the Coulomb potential at sufficiently large interparticle distances and are constructed at small interparticle distances in such a way as to avoid strong oscillations of the wave functions that would be difficult to handle numerically. Interactions between ions and electrons and the electrons themselves are accounted for by the exchange correlations functional, the central input into DFT. It is calculated within generalized gradient approximation. In DFT, the internal energy is minimized with respect to the electronic ground state density distribution. Finite temperature effects are included by Fermi occupations of Kohn-Sham orbitals. Once the electron distribution is

known, the forces onto the ions can be calculated using the Hellman-Feynman theorem. Then the ions are moved in one time step according to the forces they feel. One time step is typically chosen to be 0.5 fs, while several ps are required until convergence of pressure and internal energy. There are further quantities on which the quality of quantum MD simulations (regarding the e^- system) crucially depends, for instance the plane wave energy cut-off (H: 1200 eV chosen). Convergence was also checked with respect to the number of particles in a box with periodic boundary condition. It has to be mentioned that with increasing computer power, more particles can be considered, and the convergence check always depends on the unknown systematic error of the many-particle reference system. H-EOS data from FT-DFT-MD used in this work were obtained with 64-182 particles per box. My collegues French, Holst, and Kietzmann estimated the overall uncertainty of EOS data based on FT-DFT-MD below 5%.

H-REOS includes FT-DFT-MD data for $0.2 \leq \rho \leq 9$ g/cm^3 at $1000 \leq T \leq 50,000$ K. Below 0.1 g/cm^3 and $T \geq 1000$ K, FVT$^+$ data are used and below 0.1 g/cm^3 and $T < 1000$ K, FVT data. Solid states are not seen at these low temperatures, and we avoided larger densities at $T < 1000$ K. For each isotherm, the data were interpolated around 0.1-0.2 g/cm^3. With FVT$^+$ and FT-DFT-MD we observed different regimes of dissociation as indicated by the decrease in internal energy before it strongly rises at high densities due to electron degeneracy. So there remains some degree of freedom of connecting data sets obtained by different methods. With respect to pressure, FVT$^+$ and FT-DFT-MD data agree very well around 0.2 g/cm^3. This is just before the phase transition in the FVT$^+$ data occurs, and H-REOS shows no indication of a PPT. There is room for improvement in the future, for instance regarding the smoothness of first and second order derivatives.

• DFT-MD EOS

Applying density functional molecular dynamics (FVT-MD) to simultaneous simulation of H and He nuclei (100 H and 9 He nuclei in periodic boundary conditions), Militzer et al. (2008) were the first to provide an EOS including H/He mixing effects for a broad range of densities and temperatures relevant for Jupiter's interior. They used the CP-MD code with Troullier-Martins norm-conserving pseudopotentials and the VASP code with projector augmented wave pseudopotentials to generate EOS data at $\rho \geq 0.2$ g/cm^3 and $T \geq 500$ K. At smaller densities they used classical Monte Carlo simulations. Holst and Lorenzen compared single data points and found no significant differences. Therefore we expect DFT-MD EOS being similar to H-REOS.

Comparing H-EOS: Hugoniot curves and isentropes

In Fig. 2.2 we compare theoretical Hugoniot curves and in Fig. 2.3 Jupiter isentropes obtained with SCvH-ppt (*green*), SCvH-i (*orange*), and FT-DFT-MD (*black solid*). The Hugoniot curves and experimental data points are scaled in density by the experimental initial state density $\rho_0 \approx 0.17$ g/cm^3 for deuterium and $\rho_0 \approx 0.085$ g/cm^3 for hydrogen in order to compare with a broad set of experimental data. The thick grey line in Fig. 2.2 is a guide to the eye for the average compression ratio of experimental data. Below 50 GPa, the EOS shown are in good agreement with the highly accurate gas gun data and the Z-pinch data. Best agreement is obtained with FVT EOS. Around 25 GPa, the theoretical curves begin to spread, before all of them approach the limit $\rho/\rho_0 = 4$ at pressures far beyond 10 Mbar. Between 0.5 and 1 Mbar, best agreement with Z-pinch and explosives shock compession data is obtained with FT-DFT-MD EOS, which has a relatively small maximal compressibility of only 4.5 at relatively small pressures of 40 GPa compared to SCvH EOS and FVT EOS.

Significant differences between SCvH EOS and H-REOS are evident also in the Jupiter isentropes. Surprisingly, the relative pressure difference with respect to the SCvH-i based isentrope

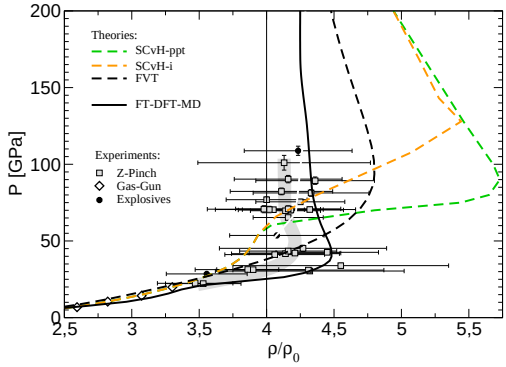

Figure 2.2: Hugoniot curves of chemical picture EOS (SCvH-i, SCvH-ppt, FVT), physical picture EOS (FT-DFT-MD) in comparison with data points from shock compression experiments with D and H. This figure was partially prepared by Holst (pers. comm.)

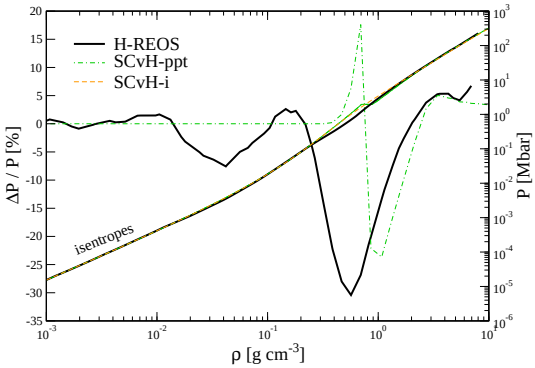

Figure 2.3: Jupiter isentropes calculated with SCvH-i (*orange*), SCvH-ppt (*green*), and FT-DFT-MD (*black*) in $P-\rho$ space (*diagonal lines*) and their relative difference in pressures evaluated at same ρ with respect to SCvH-i isentropes.

reveals a larger compressibility of H-REOS persisting up to 2 g/cm^3 at 10 Mbar with a maximum difference of 30% at 1 Mbar. This feature is already in the offing in Fig. 2.2 before the steep increase in pressure due to rising temperature. The behaviour of the SCvH-ppt Jupiter isentrope compared to the SCvH-i isentrope is completely consistent with the behaviour of their isotherms in Fig.2.1.

Densities probed by Hugoniot curves are below 0.5g/cm^3. Densities along the Jupiter isentrope, defined by constant specific entropy fixed at $T(1\text{ bar})= 170$ K, are with up to 4g/cm^3 much higher at comparable temperatures of order 10^4 K. In order to probe the Jupiter isentrope, isentropic compression experiments are urgently needed. First data points have already been obtained [Fortov, pers. comm. 2008], and future laboratory experiments (e.g. in the framework of LAPLACE at GSI) will help to probe the hydrogen EOS at Jupiter interior conditions.

We have introduced and compared in this chapter various H EOS. There are large differences in compressibility up to 30% in the $\geq$ 0.4 Mbar pressure regime between chemical models (FVT, SCvH) and ab initio EOS (FT-DFT-MD). From experience, by variation of the atomic interaction potential, the excluded volume, the polarization potential, or the method of cutting the atomic partition function, we found no way to end up with a chemical picture EOS similar to FT-DFT-MD in the regime of partial ionization. We can take this as a challenge to improve our understanding of warm dense hydrogen by aiming to construct models that agree with, e.g. FT-DFT-MD EOS, using the 'degrees of freedom' mentioned above.

2.2 Helium EOS

Helium equations of state that are used in combination with the equations of state of hydrogen described above are listed in Tab. A.1. The He EOS **He-SCvH** is introduced in [SauChaHor95]. Fluid Variational Theory is applied to minimize the free energy of neutral He atoms. Interactions

between He atoms are taken into account by soft-sphere potentials proportional to $1/r^{12}$, whereas interactions between charged particles (He^+ and He^{++}) are treated by a Debye-Hückel potential appropriate for weak ion coupling. The transition between the neutral He and He^+ as well as between neutral He and He^{++} is interpolated. He^+ ions are found only in a narrow temperature interval and not in case of pressure ionization. **He-Sesame-K04** is another chemical picture based He EOS described in [Kerley04b]; **He-DFT-MD** is described in [VorTamMilBon06]; **He-REOS** was published in [NettelmannEtAl08] and the underlying FT-DFT-MD data were discussed in [KietzmannEtAl07]. Relative differences in pressure and internal energy along relevant isotherms of these He EOS are within 30%. With an average H/He particle number ratio below 1/10, the impact of the He EOS on giant planet interior models lies less in the $P-\rho$ relation but more in the mixing ability with hydrogen and the possibility of He sedimentation (§ 5.3). Next we have a look at He-REOS, since it was extensively applied to giant planet interior models in this work.

• **He-REOS**

The helium EOS named 'He-REOS' is a combination of FT-DFT-MD data for densities between 0.16 and 10 g/cm^3 and temperatures between 4,000 and 58,000 K calculated by Kietzmann, and of Sesame 5761 data [SESAME table (1992)]. In the ideal gas limit at low densities, $P(\rho,T) \sim \rho^\alpha$, where exponent α is independent on T. Hence I could easily extrapolate the Sesame data towards smaller densities below 10^{-3}g/cm^3 in order to cover a sufficiently large grid in $P-T$ space. Similarly, I extrapolated $P(T)$ at constant densities in order to obtain isotherms below 116 K. Sesame data are then included into He-REOS for densities between 10^{-3} and $0.01-0.04$g/cm^3 depending on temperature, and for $\rho > 16.7$g/cm^3. Between the data sets, I interpolated $\log P(\log\rho)$ and $\log u(\log\rho)$ linearly, and within the coarse grid of FT-DFT-MD data points I applied cubic spline interpolation. This construction of He-REOS is visualized in Fig. 2.4 and aimes to avoid the occurrence of two minima, or of one minimum and one maximum in the internal energy (*right panel*). Before the NM-M transition at ≈ 1.3 g/cm^3 [KietzmannEtAl07], P and u exhibit their largest deviations, compare *thin solid lines* and *circles* in Fig. 2.4.

2.3 Metals

Imagine a two-component system with molecular weight $\mu_1 = 2$ g/mol of component 1 and $\mu_2 = 20$g/mol of component 2, and mass fractions $X_1 = 0.90, X_2 = 0.10$ (case A) or $X_1 = 0.10, X_2 = 0.90$ (case B). Hence, $\alpha_A := (X_1/X_2)(\mu_2/\mu_1) = 90$ (case A) and $\alpha_B = 10/9$ (case B). The particle number ratio $n_2 = N_2/N$ of the heavy element component 2 would be $n_2 = 1/(1+\alpha) = 1\%$ in case A and $n_2 = 47\%$ in case B. Case A roughly corresponds to Jupiter and case B to the interior of water-rich planets where component 1 is H-He and component 2 is water with some admixture of rocks. Thus even in water-rich planets, the EOS and other properties (e.g. conductivity) of hydrogen and helium still play an important role.

Everything that is not H or He we call *metals* or, alternatively, *heavy elements*. Metals can be single ions, small molecules such as CO_2, or large molecules of several hundred atoms such as observed in cold, dense molecular clouds in star-forming regions. Metals in protostellar clouds are either dissolved in the gas component or forming dust. A convenient assumption is that dust is formed by those particles, whose condensation temperature is above the temperature of the gas in the cloud. For silicates, this can be fulfilled quite close to the parent star, while for H_2O, the condensation to ice-particles occurs at several AU away from the protostar. At thermodynamic normal conditions on Earth, silicate-rich molecules form rocks, and H_2O is in the ice-I phase. At thermodynamic conditions inside the Earth mantle, the abundant elements Si, Mg, Fe typically form molecules such as Mg_2SiO_4 (forsterite), $MgSiO_3$ (perovskite), MgO (magnesiowustite), Fe_2SiO_4 (fayalite) [ValenciaEtAl09], altogether termed *rocks*. At sufficiently

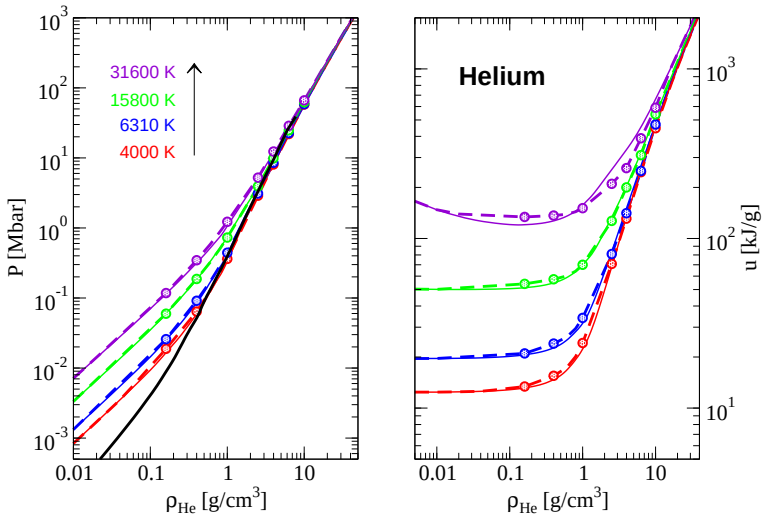

Figure 2.4: Isotherms for helium for $T = 4000$, 15800, and 31600K and three different EOS tables: Sesame 5761 (*thin solid*), FT-DFT-MD (*circles*), and He-REOS (*thick dashed*). The *left panel* shows pressure and the *right panel* shows inernal energy vs. density. The *thick solid* line shows the pressure-density relation of the helium fraction along a typical Jupiter isentrope. This figure visualizes the construction of He-REOS.

low temperatures and low pressures, the abundant elements C,N,O,S are preferably found as H_2O, CH_4, NH_3, and H_2S, briefly called *ices*. All metals are subdivided into *rocks* or *ices*, regardless of the phase they would adopt according to temperature, pressure, and composition of the surrounding material in the protostellar cloud or in giant planets.

EOS of *rocks* and *ice*. A few experiments have been performed to obtain the pressure-density relations of *rocks* and of *ices* in planetary interiors. Hubbard and Marley (1989) offer fit-formulas $P(\rho)$ for "rocks" (38% SiO_2, 25%MgO, 25% FeS, and 12% FeO) and "ices" (56.6% H_2O, 32.5% CH_4, 11% NH_3) appropriate for, as they say, $\sim 10,000$K and pressures in the central region of giant planets. These formulas are often used as EOS for metals in the envelopes and in the core of giant planets. For interior models of the Earth, satellites, and Super-Earths usually more sophisticated EOS are used [ValSassConn07]). Cores of ice and rocks are labeled 'IR cores'.

This work. I apply the fit-formula for rocks [HubbMar89] to the core region of my giant planet interior models with 'rocky' cores. For water-core models I use H_2O-REOS, and metals in the envelopes are either represented by H_2O-REOS or by He4-REOS. These will be introduced next.

• H_2O-REOS and He4-REOS

The water equation of state H_2O-REOS is a combination of four data sets. FT-DFT-MD data [FrenchEtAl09] are considered for $1000 \leq T \leq 10,000$ K between 2 and 7 g/cm^3, as well as for $10,000 \leq T \leq 24,000$ K between 5 and 15 or 20 g/cm^3. For the phases ice-I (the only water ice phase naturally occuring on Earth) and liquid water we apply accurate data tables named 'FW' and 'WP' in Fig. 2.5 (*left panel*), respectively. All other regions are filled up with Sesame water EOS 7150 [SESAME table (1992)] and, as for He-REOS, the data sets are joined via interpolation. In particular, for $T = 1000 - 10000$ K, I carefully used cspline interpolations around $\rho = 1.5 - 2.5$ g/cm^3, and simple logarithmic interpolation between 7 and 20 g/cm^3, where FT-DFT-MD data and Sesame 7150 show large deviations. For higher temperatures, interpolated regions are

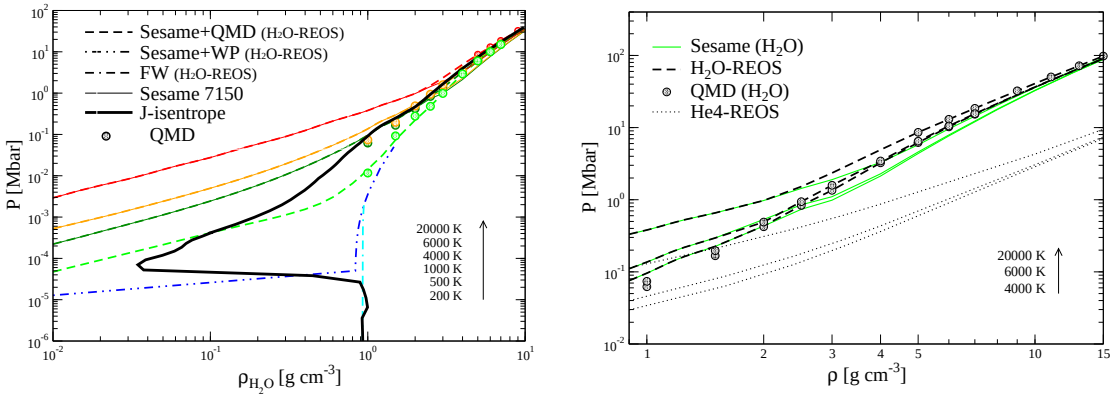

Figure 2.5:

Left panel: Water isotherms for six color-coded temperatures according to different H_2O EOS tables: H_2O-REOS (*dashed*), Sesame 7150 (*solid*), FT-DFT-MD data (*circles*), and ice-I [FeiWag06] at 200 K (*dashed-dot-dashed*), and water at 500 K (*dot-dashed-dot*) combining Sesame 7150 with WP [WagPru02]. The *thick black solid* line shows the $P-\rho$ relation of the water mass fraction along a typical Jupiter isentrope where water represents envelope metals. These isotherms are incorporated into H_2O-REOS.
Right panel: Z-component isotherms for three temperatures. H_2O-REOS: (*dashed*), He4-REOS (*dotted*), and illustration of the construction of H_2O-REOS from Sesame-H_2O EOS 7150 (*green solid*), and FT-DFT-MD data (*circles*).

between 2 and 5 g/cm^3 and between 15 and 20 or 20 and 25 g/cm^3. Exemplary isotherms are shown in Fig. 2.5 in both panels, where the *left panel* illustrates the construction of H_2O-REOS, and the *right* panel additionally shows isotherms of He4-REOS. The latter EOS is just He-REOS, where the density is scaled by a factor of 4 in order to represent the mean molecular weight of oxygen. Until now, we did not completely clarify the enormously larger compressibility of He4-REOS with pressures of only 1/10 of that of H_2O at relevant Jupiter deep interior conditions. Enhanced ideal contributions by free electrons and correspondingly more pronounced Coulomb interactions might play a role. Both equations of state are applied to Jupiter in this work [NettelmannEtAl08] in order to study the influence of the uncertainty in the EOS of metals on resulting interior models. Along a typical Jupiter isentrope, the phases of water can be read from the *thick black* line.

Today's laboratory experiments using shock wave compression and diamond anvil cells have achieved pressures in H, He, and H_2O up to several Mbar off the Jupiter isentrope. The future seems bright: Laser driven shocks at the National Ignition Facility at LLNL (USA) and Z-machine data at Sandia (USA) up to several 10 Mbar for various materials are in preparation, as well as shock compression experiments for relevant planetary materials along the Jupiter isentrope (Russia). In addition, the number of particles per box to be handled in computer simulations increases as computer power grows, and the accuracy of ab initio EOS data for H, He, H_2O, and their mixtures may soon reach the threshold of only 1% uncertainty, greatly reducing the uncertainty of planetary models.

2.4 Linear mixing

In lack of equations of state for mixtures it is still common usage –since the pioneering work of DeMarcus (1958)– to generate an equation of state of a mixture of N components with mass

fractions X_i by linear mixing and the additive volume assumption [Peebles64]. It states

$$V(P,T) = V_1(P,T) + \ldots + V_N(P,T) \qquad \text{and} \qquad M = M_1 + \ldots + M_N \quad ,$$

where $V_i(T,P)$ is the volume occupied by the mass M_i of an isolated component i at given pressure P and temperature T, and V is the final volume (M the final mass) of the mixture at (P,T) such that $\rho(P,T) = V/M$. Consequently,

$$\frac{1}{\rho(P,T)} = \sum_{i=1}^{N} \frac{X_i}{\rho_i(P,T)} \qquad , \quad U(P,T) = \sum_{i=1}^{N} X_i\, U_i(P,T) \quad ,$$

for the mass density of the mixture and the extensive thermodynamic quantity internal energy $U(P,T)$, respectively. For the entropy it is recommended [SauChaHor95], because of dissociation and ionization changing the particle numbers, to add the ideal entropy of mixing. Non-ideality effects between different components are thus not taken into account.

When representing metals by H_2O-REOS and $T < 1000$ K, I first generate an H-He isentrope without water. Then I add the desired water mass fraction according to $\rho_{H_2O}(P,T)$ along the isentrope. Above $T \geq 1000$ K, the mixture is first generated by linear mixing. After that the isentrope is calculated as described in § C in the Appendix.

Various equations of state that are applied to giant planets and discussed in this work are listed in Tab. A.1. Special emphasis is given to LM-REOS, the Linear-Mixing Rostock Equation of State, a linear mixture of H-REOS, He-REOS, and H_2O-REOS or, alternatively, He4-REOS. Work is in progress to develop REOS that will include non-linear mixing effects between H and He.

Conclusions

In § 2 we introduced and compared various equations of state of H, He, H_2O, and rocks appropriate for giant planet interior conditions.

Among the H-EOS considered, SCvH-ppt, FVT^+ and H-REOS are the ones that least make use of interpolation in the regime of partial ionization and the NM-M transition. SCvH-ppt and FVT^+ consequently apply the chemical picture considering the species molecules, atoms, protons, and electrons. H-REOS includes ab initio data for a coupled non-conducting molecular system up to a fully ionized system. The occurrence of a PPT in SCvH-ppt has afterwards been judged an artefact by its authors: hence, we can consider H-REOS the currenctly best hydrogen EOS both with respect to the methodical approach and the agreement with experimental data. Also for He and H_2O new equations of state have been developed that make use of ab initio data in the warm dense matter region which are in excellent agreement with available experimental data. It was the effort of my collegues Juranek, Holst, French, and Kietzmann to calculate EOS data for H, He, and H_2O, and my effort to generate large-scale data tables. The current version LM-REOS does not exhibit a PPT of any component, and the NM-M transition occurs below 1 Mbar for relevant mixtures. Further work is required to enforce large-scale thermodynamic consistency and smooth derivatives, as well as to include non-linear mixing effects. The first EOS already including them is DFT-MD EOS. LM-REOS challenges SCvH EOS.

Chapter 3

Calculating structure models

3.1 Observables and constraints

An acceptable interior model should satisfy all of the available constraints. Some of them have been obtained with great accuracy from observations and impose strong constraints, some of them depend on theories that change with time or on interpretation of observational data and are thus less accurately known. Others are not considered relevant for interior models or by far exceed the current status of giant planet modelling and are thus neglected. Table A.2 in § A.2 (Appendix) lists all astrophysical data considered in the modelling procedure.

3.1.1 Luminosity

All planets receive energy from their parent star. Part of this energy is immediately reflected by the atmosphere. This part has the same spectrum as that of the incoming radiation. For the Sun with an effective temperature of 5800 K, the energy spectrum has its maximum in the visible range at wavelengths of $400 - 800$ nm. The other part of the incoming energy is absorbed, converted into heat, and re-emitted at wavelengths that correspond to the effective temperature of the planet. This part is typically in the infrared regime at $5 - 200\mu$m. From the observational side, reflected and emitted energy are thus well-separated and the intrinsic luminosity L_{int} can be determined, i.e. the difference in emitted and absorbed energy per time in the infrared. Jupiter, Saturn, and Neptune radiate about twice the energy into space than they absorb from the Sun: they have a large intrinsic luminosity. Uranus on the other hand radiates less than 10% more than it receives: its intrinsic luminosity is very low.

L_{int} is an extremely important quantity. It gives us clues as on (i) the present energy content of a planet, (ii) the way it evolved to its present state, and (iii) the way the energy is transported from the interior to the surface where it is radiated away from. In § 5 we will come back to points (i) and (ii). Here we focus on point (iii). Instead of L_{int}, we consider the equivalent quantity

$$F_{int} = \frac{L_{int}}{4\pi R^2} \quad , \tag{3.1}$$

the energy flux per unit area. For Jupiter, Saturn, and Neptune the relatively large observed flux implies a steep temperature gradient. This initiates convection. Convection again tends to homogenize the interior. From the size of F_{int}, a temperature profile very close to that of an adiabat is derived. Since the work of Hubbard (1968, 1969), all three properties –convective instability, homogeneity, and adiabatic temperature profile– have become fundamental assumptions of giant planet interior models. In this section we derive and explain these properties in detail, mainly

following the work of [KippWei94], § 5.1, 5.2, 6.1, and 7.1. At the end of this section, we extend the theory toward the assumption of inhomogeneity.

Heat can be transferred along a temperature gradient by conduction, radiation, or by convection. Which of these processes dominates depends on the thermal and electrical conductivity. They can be summarized into a single parameter: the opacity. We give formal analogue expressions for the heat flux F_c transported by conduction and for the heat flux F_{rad} transported by radiation in terms of an opacity. Then we give criteria for the onset of convection and apply mixing length theory to derive an expression for the heat flux F_{conv} due to convection. The general equation of heat conduction reads

$$\mathbf{F} = -k\nabla T \,. \tag{3.2}$$

With the heat transport coefficient k_c for conduction and a formally introduced coefficient k_{rad} for radiation, the heat flux from both conduction and radiation can be written in the form

$$\mathbf{F} = \mathbf{F}_c + \mathbf{F}_{rad} = -(k_c + k_{rad})\nabla T \,, \tag{3.3}$$

where

$$k_{rad} = \frac{4ac}{3}\frac{T^3}{\kappa_{rad}\rho} \quad , \quad k_c = \frac{4ac}{3}\frac{T^3}{\kappa_c\rho} \,, \tag{3.4}$$

and a is the *radiation-density constant*, c the *vacuum velocity of light*, $4ac = \sigma$ the Stefan-Boltzmann constant, κ_{rad} the *mean absorption coefficient* in [area/mass], also called *opacity*, and ρ mass density. A simple derivation of k_{rad} in (3.4) is given in [KippWei94], k_c is simply put in formal analogy with k_{rad} by introducing an opacity of conduction κ_c. Replacing the energy flux by the interior luminosity $l(r) = 4\pi r^2 * F$ and the temperature gradient ∇T by dT/dr for a spherically symmetric planet with radius coordinate r, and combining the opacities by

$$1/\kappa := 1/\kappa_{rad} + 1/\kappa_c \quad , \tag{3.5}$$

equation (3.2) transforms to

$$\frac{dT}{dr} = -\frac{3}{16\pi ac}\frac{\kappa\rho\, l}{r^2 T^3} \,. \tag{3.6}$$

With the equation of hydrostatic equilibrium

$$\frac{dP}{dr} = -\frac{Gm\rho}{r^2} \,,$$

which will be introduced later in § 3.2, and the usual dimensionless abbreviation

$$\nabla_{rad} := \left(\frac{d\ln T}{d\ln P}\right)_{rad} = \frac{P}{T}\left(\frac{dT}{dP}\right)_{rad} = \frac{P}{T}\left(\frac{(dT/dr)}{(dP/dr)}\right)_{rad} \quad , \tag{3.7}$$

we arrive at the standard expression often given in literature

$$\nabla_{rad} = \frac{3}{16\pi acG}\frac{\kappa\, l\, P}{mT^4} \quad . \qquad (\textit{temperature profile for radiative energy transport}) \tag{3.8}$$

By definition, ∇_{rad} will denote the temperature profile if the whole energy flux is transported by radiation. If not, ∇_{rad} will deviate from the temperature profile realized. The equality sign in (3.8) can be interpreted in two ways. First, if the energy is transported by radiation and conduction, then ∇_{rad} describes the real temperature gradient, and the right hand side tells us the amount of energy l transported this way for known κ, P, and T. On the other hand, if we know the energy flux, then (3.8) tells us the temperature gradient necessary to transport the whole flux by radiation (conduction included). For given P and T, all difficulties in calculating ∇_{rad} are hidden behind the single parameter κ, the opacity.

Convection in Giant Planets

In convective regions, the temperature gradient realized is larger than the adiabatic gradient

$$\nabla_{ad} := \left(\frac{d\ln T}{d\ln P}\right)_s \quad , \qquad (\textit{adiabatic temperature gradient}) \tag{3.9}$$

where index s denotes the specific entropy. ∇_{ad} describes the $T-P$ profile along curves of constant entropy in the EOS table. In case of a homogeneous medium, if the calculated radiative gradient ∇_{rad} in (3.8) surpasses the calculated adiabatic gradient, the *Schwarzschild criterion* for convective stability

$$\nabla_{rad} < \nabla_{ad} \qquad \textit{(Schwarzschild criterion)} \tag{3.10}$$

becomes violated. In the convectively unstable medium, a new temperature gradient

$$\nabla_T := \frac{d\ln T}{d\ln P} \qquad \textit{(realized temperature gradient)} \tag{3.11}$$

establishes with the property

$$\nabla_{ad} < \nabla_T < \nabla_{rad}\,. \tag{3.12}$$

This inequality tells us that the realized gradient in a convective medium is not large enough to transport all the energy by radiation. And it cannot become that large, because the interior is already convective.

Whether (3.10) holds or not depends on the opacity, see (3.8). Guillot et al. (1994) calculated the so-called *Rosseland mean* opacities in the interior of Jupiter and Saturn and compared it with the critical opacity κ_{crit} above which the medium is too opaque to satisfy the Schwarzschild criterion. They found convection ensured at small pressures through strong absorption by water, methane, and collision-induced absorption of hydrogen molecules and at high pressures through frequent collisions of ions and atoms. Depending on the presence of the strong absorbers sodium and potassium [GuiSteHubbSau03], a small region around 2000 K may exist where the Schwarzschild criterion holds. Since these elements have been detected in brown dwarf atmospheres – their presence in the outer planets is still unclear – Jupiter and Saturn are assumed to posses fully convective envelopes unless there is a mechanism that inhibits convection. For Uranus and Neptune no such datailed calculations of ∇_{rad} have been performed, but due to their large abundance of water and methane, the assumptions of efficient absorption seems reasonable, too. Hence, the interior of the outer planets –unlike solar-like stars– is characterized by

$$\nabla_{ad} \ll \nabla_{rad} \quad . \tag{3.13}$$

Still borrowing the main ideas from [KippWei94], we next derive the heat flux transported in a convective medium by means of

Mixing length theory

It is a great merit of mixing-length theory that relatively simple expressions for the heat flux and the temperature gradient in a convectively unstable medium can be obtained at all. From here on we denote by F_{rad} the heat flux due to both radiation and conduction via κ. For the total energy flux we thus have

$$F = F_{conv} + F_{rad} \quad . \tag{3.14}$$

Starting point of mixing length theory are the somewhat ill-looking equations

$$F_{conv} + F_{rad} = \frac{4acG}{3}\frac{mT^4}{\kappa r^2 P}\nabla_{rad} \tag{3.15}$$

and

$$F_{rad} = \frac{4acG}{3}\frac{mT^4}{\kappa r^2 P}\nabla_T \quad . \tag{3.16}$$

Equation (3.15) is obtained by replacing the luminosity l in (3.8) by the total heat flux $4\pi r^2 F$ and interpreting ∇_{rad} as the ought-to-be gradient if F was to be transported solely by radiation (including conduction). But since $\nabla_T < \nabla_{rad}$ (3.12) in a convective medium, only a fraction proportional to ∇_T can be transported by radiation (including conduction), which is stated in (3.16).

While in a stable medium, energy is transferred between particles that are in local thermodynamical equilibrium with their surroundings, in a convective medium, energy can be transported by the displacement of mass elements into a region of different thermodynamic state. We assume that a radially displaced element of initial mass density ρ, specific heat capacity c_P, moving with velocity v_e, always remains in pressure balance $DP = 0$ with its surrounding, but has an excess temperature $DT = T_e - T$, where T_e is the element's local temperature. We furthermore assume that an element, once displaced, expands or contracts adiabatically. If it resolves in its new surrounding, it has transported locally the energy flux

$$F_{conv,e} = \rho\, v_e\, c_P\, DT\ . \tag{3.17}$$

Mixing length theory is based on the simplifying assumption that this equality also holds for the average convective energy flux between two spheres or spherical mass shells of different temperatures if DT is properly replaced by the temperature gradient. Expressions for DT and v_e in (3.17) are provided by mixing length theory. They read

$$DT = \frac{T}{H_P}(\nabla_T - \nabla_{ad})\frac{l_m}{2} \qquad \text{and} \tag{3.18}$$

$$v_e^2 \;\approx\; \frac{1}{2} f_{buo}\frac{l_m}{2} = \frac{g\delta}{2H_P}(\nabla_T - \nabla_{ad})\left(\frac{l_m}{2}\right)^2 \quad . \tag{3.19}$$

Derivations of these expressions are given in § D.1 in the Appendix.

Inserting (3.18) and the square root of (3.19) into (3.17), we finally have an expression for the heat flux transported by convection:

$$F_{conv} = \rho c_P T\sqrt{g\delta}\frac{l_m^2}{4\sqrt{2}}\, H_P^{-3/2}(\nabla_T - \nabla_{ad})^{3/2} \quad . \tag{3.20}$$

Equivalent fomulas are given in [Hubbard68] and [GuiSteHubbSau03]. This result for F_{conv} is of great importance for our understanding of planetary interiors and hence the construction of planetary models. It allows to estimate ∇_T and convection velocities v_e in the interior. Salpeter (1973) for instance derives a circulation time for Jupiter of 3 years.

Adiabatic interior

Since the observational quantity $F = F_{conv} + F_{rad}$ is an upper boundary for the convective flux, one can calculate an upper boundary for the superadiabatic temperature gradient required to transport the observed heat flux. For typical values for the parameters in (3.20) in different regimes of Jupiter's interior Guillot et al. (2003) calculated the superadiabaticity needed to reproduce the observed values of F and the convection velocities. They found $(\nabla_T - \nabla_{ad}) \simeq 10^{-5} - 10^{-10}$ implying an essentially adiabatically stratified interior, and $v_e \approx 10$ cm/s. Furthermore, because of $F \sim \nabla_{rad}$ and $F_{rad} \sim \nabla_T$ (equations 3.15 and 3.16), the convective flux can be expressed by the total flux as

$$F_{conv} = F - F_{rad} = F(1 - F_{rad}/F) \simeq F(1 - \nabla_T/\nabla_{rad}) \quad .$$

With $\nabla_T \approx \nabla_{ad}$ and (3.13), one simply has $F_{conv} \approx F$. There is essentially no heat transfer other than by convection. The interior of Jupiter-like giant planets is thus characterized by

$$\nabla_{ad} \simeq \nabla_T \ll \nabla_{rad} \qquad \textit{(convective, isentropic interior)} \quad . \tag{3.21}$$

Homogeneity and Inhomogeneity in Giant Planets

In general, convection in a multi-component system leads to homogeneity, i.e. absence of compositional gradients. However, a few exceptions are possible. Sedimentation of immiscible components can cause an inhomogeneous transition region at the high-density end of the immiscibility region. A compositional gradient due to erosion of core material can inhibit convection and cause the formation of a boundary layer with transport of heat and particles across by diffusion [ChaBar07]. A compositional gradient can furthermore arise from a first order phase transition [SalSte75], or be a remnant of the formation process [Stevenson, pers. comm. 2008].

In presence of a compositional gradient, the Schwarzschild criterion (3.10) is no longer sufficient to describe the onset of convection and has to be replaced by the Ledoux criterion, which we derive here in detail. Again we assume that a displaced mass element with excess temperature DT and excess density $D\rho$ over its surrounding expands or contracts adiabatically. This assumption is justified since we already know that heat conduction does not play an essential role. Due to small particle diffusion velocities compared to convective velocities, it will preserve its initial composition which might differ from that of the surrounding in case of an inhomogeneous interior.

If $DT > 0$, then $D\rho < 0$ at pressure equilibrium. As long as $D\rho < 0$, the radial buoyancy force per unit mass $f_{bou} = -gD\rho/\rho$ will drive the mass element upwards. With

$$D\rho = \frac{dD\rho_e}{dr}\Delta r = \left[\left(\frac{d\rho_e}{dr}\right)_{ad} - \frac{d\rho}{dr}\right]\Delta r \quad ,$$

where ρ_e is the element's local density, and $(d\rho_e/dr)_{ad}$ the element's local adiabatic density profile, the condition for termination of upward motion therefore is

$$\left(\frac{d\rho_e}{dr}\right)_{ad} - \frac{d\rho}{dr} > 0 \qquad \textit{(general condition for stability)} \quad . \tag{3.22}$$

In order to see the dependence of this condition on the gradients of temperature and composition, we replace $d\rho$ in (3.22) for both the adiabatically rising (or falling) element and the surrounding by means of the equation of state using

$$\frac{d\rho}{\rho} = \alpha\frac{dP}{P} - \delta\frac{dT}{T} + \phi\frac{d\mu}{\mu} \quad ,$$

where the partial derivatives α, δ and ϕ are defined as usual in literature as

$$\alpha := \left(\frac{\partial \ln\rho}{\partial \ln P}\right)_{T,\mu} \quad \delta := -\left(\frac{\partial \ln\rho}{\partial \ln T}\right)_{P,\mu} \quad \phi := \left(\frac{\partial \ln\rho}{\partial \ln\mu}\right)_{T,P} \quad . \tag{3.23}$$

Note that μ here denotes the mean molecular weight and *not* the chemical potential. The general condition for stability (3.22) becomes

$$\left(\left(\frac{\alpha}{P}\frac{dP}{dr}\right)_{ad} - \left(\frac{\delta}{T}\frac{dT}{dr}\right)_{ad} + \left(\frac{\phi}{\mu}\frac{d\mu}{dr}\right)_{ad}\right) - \left(\left(\frac{\alpha}{P}\frac{dP}{dr}\right) - \left(\frac{\delta}{T}\frac{dT}{dr}\right) + \left(\frac{\phi}{\mu}\frac{d\mu}{dr}\right)\right) > 0 \quad .$$

Because of $DP = 0$, the first and the fourth term cancel each other. Because of $(d\mu/dr)_{ad} = 0$ (the mass element is maintaining its initial composion) the third term vanishes as well. Dividing this inequality by $-(1/P)\,dP/dr > 0$ we have

$$\delta\frac{P}{T}\left(\frac{dT}{dP}\right)_{ad} - \delta\frac{P}{T}\left(\frac{dT}{dP}\right) + \phi\frac{P}{\mu}\left(\frac{d\mu}{dP}\right) > 0 \quad .$$

Using definitions (3.9), (3.11) as well as

$$\nabla_\mu := \left(\frac{d\ln\mu}{d\ln P}\right)_s \quad , \tag{3.24}$$

the condition for stability finally becomes

$$\nabla_{rad} < \nabla_{ad} + \frac{\phi}{\delta}\nabla_\mu \qquad (Ledoux - criterion) \quad . \tag{3.25}$$

By this criterion, a small but infinitely sharp density discontinuity is able to inhibit convection; for a finite density gradient, it depends on the temperature gradient whether convection is inhibited or not.

Summary and comments at § 3.1.1

Summarizing this section, the observed high luminosity of Jupiter, Saturn, and Neptune indicates a convective, isentropic and homogeneous interior on large scales. Due to its low intrinsic luminosity, this conclusion cannot be applied to Uranus. However, by observation, the T-profile in Uranus' troposphere at a few bar is adiabatic –as it is the case for the other outer planets.

Some experts [MilitzerEtAl08] believe in perfect homogeneity (apart from a dense, central core) of Jupiter's envelope due to convection. Others, e.g. Stevenson (pers. comm. 2008), more believe in moderate inhomogeneity of Jupiter's envelope in agreement with the Ledoux criterion.

In my personal point of view, the simplicity of the standard theory presented above might deceive us about other possibilities. Let us imagine two isolated planets, one of them fully convective, the other one divided into two convectively separated layers with low energy transport across the layer boundary. Both planets loose internal energy and cool down with time. But the region involved into effective energy transport to the surface including subsequent energy loss is *larger* in case of the fully convective planet; it will appear more luminous (flux $F^{(1)}(t)$) and cool faster when averaged over all mass shells, while heat in the other planet remains stored in the inner layer just slowly escaping across the layer boundary. This planet will appear less luminous ($F^{(2)}(t)$) during the first period of cooling. After some long period of time the ratio of their luminosities will invert, when the fully convective planet has cooled so much that it cannot maintain anymore an adiabatic profile. An observer in the first period who observed $F^{(1)}$ and $F^{(2)}$, calculated $\nabla^{(1)}_{ad}$ and $\nabla^{(2)}_{ad}$ and found $\nabla_{rad} > \nabla_{ad}$ for both planets, will think of both planets being convective. Applying (3.20) and because of $F^{(2)} < F^{(1)}$, he will think of the inhomogenous planet as the more perfectly adiabatic one. The further out the layer boundary, the more perfectly adiabatic it will seem to be. Once a point is reached when the outer layer of the inhomogeneous planet has cooled so much (due to too small energy supplies from the deep interior) that the temperature drop at the layer boundary becomes large enough to initiate convection around the layer boundary. When some heat has escaped from the deep interior, a new density gradient may stabilize. Such a scenario may happen in Uranus.

Nevertheless, the assumption of an adiabatically stratified, homogeneous interior certainly is a reasonable good first approximation. Detailed interior structure models and careful evolution calculations are required to validate or contradict this assumption.

3.1.2 Surface temperature

The surface of a giant planet is conveniently defined as the 1-bar pressure level. Since levels of constant pressure and equipotential levels coincide with each other, the surface's shape is expressed by a geoid whose normal vectors at any point are perpendicular to the equipotential surface that corresponds to the 1-bar pressure level. The surface temperature T_1 defines the entropy of the

isentropic interior between the surface and, if any, the first layer boundary. Since the entropy and with it the temperatures of any deeper layer depend on the boundary conditions, the surface temperature even influences central temperatures and is thus an important input parameter for planetary models.

Atmospheric temperatures of Solar giant planets have been derived from radio occultation data acquired with spacecraft. For example, the analysis of radio signals received from *Voyager 2* during its occultation by Neptune in August 1989 has provided temperatures at pressure levels ranging from 10^{-3} to 6 bar. A detailed method description is given in [Lindal92]. First, the vertical profile of the refractivity was determined from the tracking of signals after traversing Neptune's atmosphere during ingress and egrees of occultation. For this, the composition of the atmosphere has to be known or guessed in advance. In case of Neptune for instance, although the *ices* CH_4, NH_3, H_2O and H_2S are supposed to contribute a large fraction of the planetary mass, they were neglected in the atmosphere above the tropopause, CH_4 assumed to have constant humidity between the tropopause and the pressure level of 2 bar where it condensates, and to have constant CH_4/H number ratio at higher pressures. Once the path taken by a photon ray emitted from the spacecraft and received at the tracking station is determined, the measured spectral intensity can be used to derive the vertical absorption profile. Depending on the composition assumed, the particle density profile $n(r)$ can be obtained from the refractivity profile, and the pressure profile $P(r)$ from $n(r)$ by integrating the equation of hydrostatic equilibrium. From these and an equation of state, finally the temperature profile $T(r)$ is derived. With radio occultation data from *Voyager 2*, the pressure-temperature relation could be observed between ≈ 0.4 and 6300 mbar (Neptune), 0.5 and 2300 mbar (Uranus), 0.6 and 1300 mbar (Saturn), and from 1 to 1000 mbar (Jupiter). These observations confirmed adiabaticity at the 1-bar pressure level and below.

3.1.3 Mass and Radius

The mass determined from the planet's orbital period by means of the Keplerian laws is the mass M_p of the planet plus the masses of its orbiting moons. Hence, accurate planetary mass determinations require knowledge of the existence of moons and their masses. Many satellites were detected by spacecraft flybys. To obtain masses and other graviational properties, e.g. radius and gravitational moments, the path taken by the spacecraft is compared with its theoretically predicted one, where the gravitational properties of the planet and its satellites appear as unknowns that are solved for in the Newtonian path description [AndSchu07]. The paths taken by the *Pioneer* and *Voyager* spacecraft were tracked from tracking stations in Goldstone, Madrid and Canberra by means of 64-m radio signals received and sent by the spacecraft. See [CamSyn85] for a summary of corrections applied to the tracking data during Jovian system encounters and [CamAnd89] during Saturnian system encounters.

In the analysis of the planetary system's orbital period and the spacecraft's path through that system, the fundamental quantity is the product of mass and gravitational constant G. The relative uncertainty of the product GM_p could be reduced below the uncertainty of G itself for all four Solar giant planets, see Tab. A.2. For most of the models of Saturn and all models of Uranus presented in this work, the more recent value of G [CODATA 2006] is used whereas for some models of Jupiter and Neptune an older one from CODATA 1998.

The geoid that best fits the tracking data is defined by the planetary equatorial radius R_{eq} together with the planetary mass, the gravitational moments and the angular velocity. Thus by inverting the tracking data, these quantities can be obtained. Anderson & Schubert (2007) also used the dependence of the pressure profile on the geoid and chose a geoid that minimizes the energy needed to drive the winds at Saturns' 100 mbar level to obtain new gravitational data for Saturn, see Tab. A.2. In this thesis, total planetary mass is labeled M_p, M, or for certain planets sometimes M_{Jup} for instance for Jupiter; if the radius is referred to as R_p or R_{Jup}, the distinction

between equatorial and mean radius at this point then is not of importance.

Let surface temperature, mean radius $\bar{R}_p$ and some uniform composition derived from atmospheric observations be given. In general, it is not possible to match the planetary mass without assuming an enrichment with heavy elements deeper inside. One could, for instance, introduce one layer boundary with an enhanced deep envelope composition, or confine all additional heavy elements to a central core and vary the size of the core in order to reproduce $M_p(\bar{R}_p)$. Hence, the simplest planetary structure type that is able to reproduce the observational quantities T_1, M_p and $\bar{R}$ and the tropospheric mass abundance Z_1 of heavy elements requires two layers: a convective, isentropic, homogeneous outer envelope and a core enriched or totally composed of heavy elements.

3.1.4 Helium abundance

Mean abundance. The primordial He abundance predicted by Big Bang Nucleosynthesis is 25% per mass. For the protosolar cloud where the sun and the giant planets formed of, Bahcall & Pinsonneault (1995) calculated a value of 27.0 to 27.8%, depending mainly on the inclusion of He and heavy element diffusion into solar evolution models. Unless otherwise stated, in all of the models presented here a value of 0.2750(1) for the mean He abundance in mass $\bar{Y}$ with respect to the H/He subsystem is assured, i.e.

$$\bar{Y} := \frac{M_{\rm He}}{M_{\rm He} + M_{\rm H}} = 0.275 \quad ,$$

where $M_{\rm X}$ is the mass of the particle species X contained in the planet. This value is consistent with *Voyager* infrared and radio occultation data obtained in 1986 for Uranus and in 1989 for Neptune [GautierEtAl95].

Atmospheric He abundance. In the Eighties, measurements of He abundances in the atmospheres of Jupiter and Saturn revealed a depletion of He compared to the protosolar value of 0.27 to 0.278. In particular, combining *Voyager* infrared spectrometer (IRIS) measurements and Voyager radio occultation (RSS) temperature profiles, a modest depletion $\mathrm{He/H_2} = 0.110 \pm 0.032$ was found in Jupiter, and a strong depletion $\mathrm{He/H_2} = 0.034 \pm 0.024$ in Saturn. These particle ratios correspond to mass mixing ratios $Y_{atm}^{(\mathrm{J})} = 0.18 \pm 0.04$ for Jupiter and $Y_{atm}^{(\mathrm{S})} = 0.06 \pm 0.05$ for Saturn, see [ConGau00] for an overview. In the Nineties however, the He abundance detector (HAD) aboard the Galileo probe measured *in situ* Jupiter's atmospheric $\mathrm{He/H_2}$ to be 0.157 ± 0.003 [ZahHunLeh98] corresponding to $Y_{atm} = 0.238 \pm 0.006$. This unique measurement is generally considered the most precise abundance measurement ever obtained in a giant planet atmosphere[1]. Since He is not expected to be affected by meteorological processes, the value found is assumed to be representative for the whole outer convective region of Jupiter. Because of the discrepancy with former results, the previous Voyager data for Jupiter and Saturn were re-examined by Conrath & Gautier (2000). They found the Voyager data for Jupiter could be made consistent with the Galileo data if the temperature profile obtained by Voyager RSS measurements were shifted 2 K towards colder temperatures. Since the possibility of a systematic error of the RSS data still remains unclear, Conrath & Gautier (2000) developed an inversion algorithm to infer the He/H ratio and the temperature profile from the Saturnian IRIS spectra alone. Their results suggest a significantly larger He abundance of $Y = 0.18 - 0.25$ of Saturn's atmosphere. Unfortunately, their method cannot be checked by application to Jupiter due to disturbing NH_3 cloud formation in the spectral range of interest in Jupiter's slightly warmer atmosphere.

Motivated by his Saturn interior models, Kerley (2004a) instead suggested to accept the ratio of He abundances for the two planets as derived originally from Voyager IRIS and RSS data. With

[1] Construction of instrument HAD and subsequent data analysis were performed in the group of Prof. von Zahn, Institut für Atmosphärenphysik, Kühlungsborn.

$Y_{\rm atm}^{\rm (J)} = 0.238$, $m_{\rm He} = 4$g/mol and $({\rm H/He})_{\rm S} = (0.034 \pm 0.24)/(0.11 \pm 0.04)\ ({\rm H/He})_{\rm J}$, this would give

$$Y_{\rm atm}^{\rm (S)} = \frac{m_{\rm He}\,({\rm He/H})_{\rm S}}{m_{\rm He}\,({\rm He/H})_{\rm J}} \times \frac{1 + m_{\rm He}\,({\rm He/H})_{\rm J}}{1 + m_{\rm He}\,({\rm He/H})_{\rm S}}\, Y_{\rm atm}^{\rm (J)} = (0.421^{+0.390}_{-0.310}) * 0.238 = 0.100^{+0.095}_{-0.08} \quad .$$

Concluding, Jupiter's $Y_{\rm atm}$ is well known, whereas Saturn's $Y_{\rm atm}$ appears highly uncertain. For Jupiter models presented here we take $Y_{\rm atm} = 0.238$, for Uranus and Neptune models we take $Y_{\rm atm} = \overline{Y} = 0.275$, and for Saturn we calculate and discuss models with $Y_{\rm atm} = 0.18$ and with $Y_{\rm atm} = 0.10$.

Atmospheric and mean He abundance are highly important constraints for giant planet models: due to convection, the atmospheric abundance is believed to equal that of the planetary interior. The observed depletion of He, however, tells us that He is not distributed homogeneously over the whole interior. There might (i) exist a convection barrier below which the missing He has accumulated, or (ii) an inhomogeneous region with modest molecular weight gradient in accordance with the Ledoux criterion and increasing He abundance towards the center. Physical reasons for such scenarios are discussed in § 5.3.

The simplest structure type describing either case is a separation of the whole envelope into two layers called outer (layer No. 1) and inner (layer No. 2) envelope, both of them characterized by an adiabatic temperature profile and homogeneity, but differing in their He abundances Y_1 and Y_2, respectively. By considering the He abundance Y_n of layer No. n as this layer's mean He abundance, we roughly also encompass the case of inhomogeneity in presence of convection. For all structure models we set $Y_1 = Y_{atm}$ and chose Y_2 as to satify $\bar{Y}$.

3.1.5 Heavy element abundance

We adopt the convention of astrophysical literature and term all elements heavier than H and He *heavy elements* or *metals*.

For convective regions it is reasonable to assume a homogeneous distribution of all elements. This assumption may not hold for those elements which are affected by condensation and sedimentation, where homogeneity becomes a question of the velocity of convection compared to cloud formation, droplet formation and sedimentation velocities. Heavy element abundances of giant planets are accessible to observation in the outermost part of the outer convective envelope. In a first step, measured abundances can be compared to solar abundances $Z_\odot$; in a second step, we may try to explain the certainly non-solar distribution by chemical reactions including cloud formation and sedimentation processes; and in a third step a prediction can be derived for a representative total heavy element abundance of the outer envelope.

Throughout this work, I use $Z_\odot = 1.92\%$ in agreement with Guillot (1999), who refers to Anders & Grevesse (1989). More recently, Lodders (2003) has proposed a smaller value $Z_\odot = 0.015$. For an evaluation of this discrepancy, the reader is refered to the literature.

Some important observational findings for the outer planets I like to list here. Determinations of the C,N,O abundances in Uranus and Neptune rely on earthbound as well as *Voyager 2* spectra in the microwave to radiowavelengths regime, in which absoption lines of CH_4, CO, HCN, NH_3, and H_2O are located. Apart from CO (and N_2), these species are suspected to condense in the tropospheres. Fortunately, cloud formation of CH_4 occurs above the deepest studied pressure of a few bars, and C/H is derived $30 - 60$ times solar [GautierEtAl95]. Such a large value is possibly a result of CH_4 outgassing from deeper ice shells [HubbPodSte95]. NH_3 seems about solar or slightly supersolar in Uranus, but depleted in Neptune, CO and HCN was detected in Neptune, but not in Uranus. Suggested explanations for these measurements are under debate and involve non-equilibrium chemistry in Neptune and inhibited convection in Uranus [GautierEtAl95]. H_2O was not detected in both planets, probably because of cloud formation below 10 bar and further reaction of H_2O traces with CH_4 to form CO. With presumably the same representative enrichment

factor of C, N, and O, Uranus and Neptune appear to have at least $25 \times Z_\odot \approx 50\%$ ices in their interior.

Abundance measurements in Jupiter and Saturn are reviewed in [GuiGauHubb97, Guillot99, Kerley04a, Guillot05] and [MouAliBen06]. Summarizing these references, derived enrichment factors in Saturn are 4-6 for C, 2-4 for N, and unknown for O and S; enrichment factors in Jupiter are 3 for CH_4, 2-4 for C, 2.2-3.4 for N, about 2 for noble gases, and O is depleted. Oxygen is expected to be mainly in form of H_2O in the upper layers of Saturn and Jupiter and to condense to form clouds at deeper layers than accessible to observation. Measurements therefore give only lower limits. However, according to arguments from formation theory (§ 6.1) and the cosmic O abundance, O is expected to be at least as abundant as C in Jupiter and Saturn [Kerley04a]. Hence we adopt here the general assumption of $Z_{atm} \approx 4 - 6\ Z_\odot$ for Saturn and $Z_{atm} \approx 2 - 4\ Z_\odot$ for Jupiter. Clearly, in case the assumption /H∼C/H will prove wrong by future measurements, Z_{atm} will reduce.

Concluding, an accurate and representative heavy element abundance for the outer convective envelope of giant planets puts an important constraint on interior models. Abundance determinations down to 100 bar, below the water condensation level, are highly desired.

3.1.6 Rotational frequency and Gravitational moments

On images, the steamlined cloud patterns and oblated shapes of Jupiter and Saturn immeadiately catch the eye, indicating rapid rotation. Rotation and tidal effects due to surrounding satellites cause distortions in the gravity field that constitute a considerable source of information about internal mass distributions including deep seated clouds and the size of the core. Deviations from spherical symmetry in the gravity field are expressed by gravitational moments. They are weight-functions for the spherical harmonics in the Legendre expansion of the external gravity field. See § 3.4 for mathematical details. The strongest moments are J_2 and J_4, meaning that centrifugal forces dominate over tidal forces.

Combined data from *Pioneer 10, 11* and *Voyager 1, 2* missions have allowed high-accuracy determination of the elliptical deformation J_2 for the outer planets. Recent data from the *Cassini* mission helped to significantly reduce the error bar of Saturn's J_4 value [AndSchu07]. Yet the observational uncertainty in J_4 allows for a variety of interior models of all Solar giant planets. Experimental values for gravitational moments of Jupiter, Saturn and Neptune were obtained through spacecraft flybys. In case of Uranus, J_2 and J_4 were not determined by spacecraft data but by analyzing the precession of the Uranian rings [Lindal92].

Values of Jupiter's J_2 and J_4 marked by a star ($\star$) in Tab. A.2 and of Saturn's J_2 and J_4 without a star have been used in the literature since 1991. Couriously, they are generally referred to [CamSyn85], but deviate from those given in that reference, see Tab. A.2. Gudkova & Zharkov (1999) state that they obtained the commonly used values by adding corrections for the effect of differential rotation as calculated. The corrections taken from corresponding references in [GudZha99], however, do not account for the deviations. Lindal (1992) mentioned the normalization of the gravitational moments to another equatorial radius than given in [CamSyn85], which might shift the problem of discrepancy from the gravitational moments to the radius. Hence, the origin of the values for Jupiter used in literature later than 1991 remains unclear.

While the period of rotation ω enters the equations solved in the modelling procedure explicitly, the gravitational moments J_2 and J_4 do not and impose two further constraints that have to be accounted for in an iterative procedure. Unless otherwise stated in this work, we follow the method of Guillot (1999) and invoke two variable parameters in order the adjust them: the metallicities Z_1 and Z_2 in the envelopes.

Further constraints

Available accurate further constraints are magnetic field data for all four outer planets. During my PhD time, modelling of magnetic dynamos in spherical geometry has extraordinarily improved, and first dynamo models for Jupiter and Saturn (Glatzmeier, pers. comm. 2008) and for Uranus and Neptune [StaBlo06] have been presented. Comparing interior models obtained by the constraints mentioned above with interior models predicted by conditions for magnetic field generation will certainly help to improve our understanding of the planets.

Apart from a few exceptions, e.g. Kerley (2004a), available seismic data for Jupiter are usually not considered. Future work at this point is necessary.

3.1.7 The standard three-layer structure type of a giant planet

In direct consequence of the aforementioned observables we define the standard three-layer structure type appropriate for negligibly irradiated giant planets. It has two homogeneous, adiabatic envelopes composed of H, He, and metals, and an isothermal core of rocks and/or ices. Models of this structure type are uniquely defined by the observables mentioned above, apart from the position of the layer boundary between the envelopes. The He mass abundances Y_n, where index $n = 1, 2$ enumerates the layers from top to bottom, the mass abundances of metals Z_1 and Z_2, the core mass M_{core}, and the outer envelope adiabat or, equivalently, the specific entropy s are constrained by the observables Y_{atm}, $\bar{Y}$, J_2, J_4, $R(M)$, and $T(1\text{ bar})$. The observables M and ω enter the equations to be solved explicitly and thus do not require a special choice of any parameter. The inner envelope adiabat is defined by the condition of continuity $T_1(P_{1-2}) = T_2(P_{1-2})$, where P_{1-2} is the transition pressure between the envelopes. P_{1-2} is a free parameter and of large influence on interior model solutions. Historically, P_{1-2} was introduced in order to separate regions of different phases, such as molecular and metallic H in case of an underlying H-EOS with PPT [ChaSauHubbLun92], or to separate regions of different solubility such as the temperature- and pressure-dependent solubility of He in H [SteSal77] as predicted by various theories. This is the standard 3-layer structure type of a giant planet. In the case of extrasolar giant planets (EGP)s, J_2 and J_4 are unknown todate, and hence Z_1 and Z_2 are also free parameters within the boundaries imposed by the constraint $M_{core} \geq 0$. Having the discontinuities in Y, Z, and s in our mind, we call the envelopes quasi-adiabatic, quasi-homogeneous.

Acceptable models. We call interior models of the outer planets Jupiter, Saturn, Uranus, and Neptune *acceptable* if they match R, T_1, Y_1, $\bar{Y}$, J_2, J_4, (J_6), and $Z_1 \geq Z_\odot$ within the uncertainties given in Tab. A.2. We keep in mind that the condition $Z_1 \geq Z_\odot$ depends on theoretical arguments from formation theory and chemistry, and can be as well $Z_1 \gg Z_\odot$, if O/H is large.

We conclude this subsection by appreciating the great set of accurate constraints made available to planetary modelers and by emphasizing the great need for future deep entry probe measurements of chemical abundances.

3.2 Basic Equations

We introduce the variables and equations required to calculate interior models of giant planets.

Notations. We denote by P pressure, T temperature, ρ mass density, v volume, s specific entropy of a mixture of arbitrary components, μ its molecular weight; r, ϕ, θ are the polar coordinates with respect to the center of the planetary mass, $m(r)$ the mass enclosed within an equipotential surface of radius $r(\varphi, \theta)$ which equals a sphere of radius r for spherical planets. We call the total potential U, the gravitational potential V, Q is a centrifugal potential of a planet rotating with angular velocity ω, and G is the gravitational constant.

Conservation of momentum is described by the hydrostatic equation of equilibrium and conservation of energy by the luminosity balance equation. The first one will be explained in case of a non-rotating spherical planet in the following paragraph, the latter one is not relevant for stationary structure models and will be explained in connection with planetary evolution in § 5.1.

Conservation of momentum. For every mass element m_i occupying a volume v_i, conservation of momentum implies cancellation of all forces acting on it. One of these forces is the gravitational attraction

$$\vec{F}_{grav} = -\frac{Gm(r)m_i}{r^2}\,\vec{\mathrm{e}}_r \tag{3.26}$$

by all other mass elements. Other forces result from the gravity fields of the Sun and of surrounding moons raising tidal distortions. For all planets in the solar system, such *external* fields are small and are neglected in this work. Without gravity, if all mass elements were in thermodynamic equilibrium, they would not feel any force. Thus in the presence of gravity, thermodynamic equilibrium is not possible and a pressure gradient builds up rising a force $\vec{F}_{mat} = -\vec{F}_{grav}$. Let us consider a mass element m_i with cylindrical shape oriented parallel to $\vec{e}_r$ at some point $\vec{r}$, with height dr and top or bottom area A. Then the force onto the bottom of the cylinder due to the surrounding material (not neccessarily gas) at $r\,\vec{e}_r$ is $\vec{F}_{bottom} = AP(r)\vec{e}_r$, and the force onto the top of the cylinder due to the surrounding material at $(r + dr)\,\vec{e}_r$ is $\vec{F}_{top} = -AP(r + dr)\vec{e}_r$. For the total force onto the cylinder and the pressure gradient we then have, with volume $v = A\,dr$ and $\rho = m_i/v$,

$$\vec{F}_{mat} = \vec{F}_{top} + \vec{F}_{bottom} = -A(P(r + dr) - P(r))\,\vec{\mathrm{e}}_r = -v\frac{dP}{dr}\,\vec{\mathrm{e}}_r = -\frac{m_i}{\rho}\frac{dP}{dr}\,\vec{\mathrm{e}}_r \quad . \tag{3.27}$$

Conservation of momentum for a mass element m_i is realized if

$$0 = \vec{F}_{mat} + \vec{F}_{grav} \quad . \tag{3.28}$$

Inserting (3.26) and (3.27) into (3.28), we finally have

$$0 = m_i\left(-\frac{1}{\rho(r)}\frac{dP}{dr} - \frac{Gm(r)}{r^2}\right)\vec{\mathrm{e}}_r \quad . \tag{3.29}$$

If this holds for every m_i, the planet is called to be in *hydrostatic equilibrium*. For a spherical, non-rotating planet the equation of hydrostatic equilibrium thus reads

$$\frac{1}{\rho}\frac{dP}{dr} = -\frac{Gm(r)}{r^2} \quad . \tag{3.30}$$

In form of (3.30), the equation of hydrostatic equilibrium is often used to calculate mass-radius relations. On the left hand side, there appears a pressure gradient as response of the material to

some forces. On the right hand side, there appear the forces per mass element m_i. Beside gravity, there might be other forces felt by m_i such as centrifugal acceleration in case of rotation. In the specific case of rigidly rotating spherical planets, the hydrostatic equation of equilibrium reads

$$\frac{1}{\rho}\frac{dP}{dr} = -\frac{Gm(r)}{r^2} + \frac{2}{3}\omega^2 r \quad . \tag{3.31}$$

This form is often used for structure models of evolving planets with known present-time angular velocity ω. The centrifugal force per mass element

$$F_{fug}/m_i = \frac{2}{3}\omega^2 r$$

will be derived in § 3.3. We first turn to the second basic equation:

The mass equation. The hydrostatic equation of equilibrium cannot be solved without knowledge of $m(r)$. That is easily obtained by summing up all mass shells dm up to the radius r:

$$m(r) = \int_0^r dm(r) \quad , \tag{3.32}$$

where $dm(r)$ is the product of the mass density $\rho(r)$ with the volume $4\pi r^2 dr$ of that mass shell. The differential equation for the mass coordinate thus reads

$$\frac{dm}{dr} = 4\pi r^2 \rho(r) \quad . \tag{3.33}$$

Boundary conditions. For given boundary conditions at the surface $P_1 = 1$ bar

$$r(P_1) = R_p \qquad (BC1) \tag{3.34}$$

$$m(R_p) = M_p \qquad (BC2) \tag{3.35}$$

and a given $P - \rho$ relation, equations 3.33 and 3.30 (or 3.31) can now be integrated inward. The $P - \rho$ relation demanded by the hydrostatic equation of equilibrium is the one and only point, where the equation of state enters the modelling procedure. In the simplest case, the EOS is of polytropic form

$$P(\rho) = K\rho^\gamma \tag{3.36}$$

with given polytropic exponent γ and constant K. In any other case, both the surface temperature T_1 and the temperature gradient ∇_T have to be supplied in order to obtain $\rho(T, P)$,

$$\nabla_T \,\&\, T_1 \implies T(P) \implies \rho(T(P), P) \quad , \tag{3.37}$$

and unique solutions $P(r)$ and $m(r)$. As written in § 3.1.1 and 3.1.2, for solar giant planets T_1 is measured and $\nabla_T \approx \nabla_{ad}$. At the center $r = 0$, there is the boundary condition

$$m(r = 0) = 0 \qquad (BC3) \quad . \tag{3.38}$$

Our system of two first-order differential equations for $P(r)$ and $m(r)$ is thus overdetermined, and we need one additional degree of freedom in order to also satisfy *BC3*. As written in § 3.1.3, we could allow for a core and satisfy *BC3* by a particular choice of the core mass M_{core}; or we could choose a particular envelope metallicity Z. Since we always must have $M_{core} \geq 0$ and $Z \geq 0$, there might be no interior solutions for arbitrary values of M_p, R_p, and T_1. If, on the other hand, R_p is free, we can choose any values $0 \leq M_{core} \leq M_p$ and $0 \leq Z \leq 1$ and satisfy *BC3* by a particular choice of R_p. This applies to the calculation of $MR-$relations and of profiles of evolving planets as displayed in Tab. 3.1.

Proceeding from spherical, rotating planets toward oblate, rotating planets, we next switch from a description by forces to a description by potentials.

Table 3.1: Similarity of parameters of interior profiles for different applications.

	$MR-$relations	evolution
given parameter	M_p, M_{core}, Z, T_1	M_p, M_{core}, Z, T_1
running parameter	M_p	T_1
resulting parameter	R_p	R_p

This table is to show that calculating MR relations and planetary evolution makes use of essentially the same procedure for generating interior profiles. Just the running variable differs.

3.3 The potential of a rigidly rotating planet

The forces relevant for rigidly rotating, oblate planets are gravitational (F_{grav}) and centrifugal forces (F_{fug}). F_{grav} is conservative, and the equivalence of heavy and inert mass motivates to introduce a potential for F_{fug}, too. We define the gravitational potential V and a centrifugal potential Q by

$$\frac{1}{m_i}\vec{F}_{grav} =: -\text{grad}\, V(\vec{r}) \tag{3.39}$$

$$\frac{1}{m_i}\vec{F}_{fug} =: -\text{grad}\, Q(\vec{r}) \tag{3.40}$$

With

$$U(\vec{r}) := V(\vec{r}) + Q(\vec{r}) \quad , \tag{3.41}$$

the momentum equation takes the short form

$$\frac{1}{\rho}\nabla P(\vec{r}) = -\nabla U(\vec{r}) \tag{3.42}$$

appropriate for oblate, rotating planets. Notations and main equations presented in this subsection follow [ZhaTru78], § 24 – 26, and are in some equations indicated by brackets [ ].

3.3.1 Multipole expansion of $V(\vec{r})$

The general expression for the gravity field raised by a mass distribution $\rho(\vec{r}\,')$ in volume V measured at location $\vec{r}$ is obtained as solution of the Poisson equation

$$\Delta V(\vec{r}) = 4\pi G\rho(\vec{r}) \tag{3.43}$$

and reads, equivalently to the general solution of the Poisson equation for the Coulomb potential in electrodynamics (ED),

$$V(\vec{r}) = -G\int_V d^3r' \frac{\rho(\vec{r}\,')}{|\vec{r}-\vec{r}\,'|} \quad . \tag{3.44}$$

In spherical coordinates (r, ϑ, φ), this expression can be rewritten as a series of decreasing and increasing powers of r, corresponding to a separation into an external ($r > r'$) and an internal ($r < r'$) gravity field. For this, the factor $1/|\vec{r}-\vec{r}\,'|$ in (3.44) is expanded into series of Legendre polynomials $P_l(\cos\psi)$, where ψ is the angle between $\vec{r}$ and $\vec{r}\,'$. Calculating $\vec{r}\cdot\vec{r}\,'/rr'$, we find

$$\cos\psi = \sin\vartheta\sin\vartheta'\,\cos(\varphi-\varphi') + \cos\vartheta\cos\vartheta' \quad . \tag{3.45}$$

The expansion [ZT78 – eq. 25.4]

$$\frac{1}{|\vec{r}-\vec{r}\,'|} = \frac{1}{r} \times \begin{cases} \sum_{n=0}^{\infty} \left(\frac{r'}{r}\right)^n P_n(\cos\psi) & : \quad (r > r') \\ \sum_{n=0}^{\infty} \left(\frac{r'}{r}\right)^{-(n+1)} P_n(\cos\psi) & : \quad (r < r') \end{cases} \tag{3.46}$$

is a multipole expansion with pole moments of order $2n$. A derivation is given in the appendix, § D.2. Inserting this expansion into (3.44), external and internal gravity field take the form

$$V(\vec{r}) = -\frac{G}{r} \sum_{n=0}^{\infty} \int_{\mathsf{V}(r)} d^3r'\, \rho(\vec{r}') \left(\frac{r'}{r}\right)^k P_n(\cos\psi) \quad , \quad \begin{cases} k = n & : \text{ external field} \\ k = -(n+1) & : \text{ internal field} \end{cases} \tag{3.47}$$

where the notation $\mathsf{V}(r)$ is to remind the separation into an external volume with radial boundaries $0 \le r' \le r$ and an internal volume with radial boundaries $r \le r' \le r_{max}$, and r_{max} just has to be large enough in order to cover to whole mass distribution. Next we express $V(\vec{r})$ in terms of $r, r', \vartheta, \vartheta', \varphi$, and φ' using (3.45) and $P_n(\cos\psi)$ without proof as given in [ZT78 – eq. 25.10],

$$P_n(\cos\psi) = P_n(\cos\theta)P_n(\cos\theta') + 2\sum_{m=1}^{n} \frac{(n-m)!}{(n+m)!} \cos m(\varphi-\varphi')\, P_n^m(\cos\theta)\, P_n^m(\cos\theta') \quad , \tag{3.48}$$

where P_n^m are the associated Legendre Polynomials. Inserting (3.49) into (3.48) gives

$$\begin{aligned} V(\vec{r}) = -\frac{G}{r} \sum_{n=0}^{\infty} \Bigg(& P_n(\cos\vartheta) \int_{\mathsf{V}(r)} d^3r'\, \rho(\vec{r}\,')P_n(\cos\vartheta') \left(\frac{r'}{r}\right)^k \\ & + 2\sum_{m=1}^{n} P_n^m(\cos\vartheta)\frac{(n-m)!}{(n+m)!} \cos m\varphi \int_{\mathsf{V}(r)} d^3r'\, \rho(\vec{r}\,')P_n^m(\cos\vartheta') \cos m(\varphi') \left(\frac{r'}{r}\right)^k \\ & + 2\sum_{m=1}^{n} P_n^m(\cos\theta)\frac{(n-m)!}{(n+m)!} \sin m\varphi \int_{\mathsf{V}(r)} d^3r'\, \rho(\vec{r}\,')P_n^m(\cos\vartheta') \sin m(\varphi') \left(\frac{r'}{r}\right)^k \Bigg) \end{aligned} \tag{3.49}$$

with $k = n$: external , $k = -(n+1)$: internal field.

Expression (3.50) is general and applies to all planets including the Earth. It simplifies significantly for certain symmetry conditions appropriate for rotating, isolated giant planets.

Symmetries

In rotating giant planets, if the axis of rotation $\vec{e}_\omega$ is constant with time, the density distributes equally with respect to the axis of rotation. If we chose the coordinate system $(\vec{e}_r, \vec{e}_\vartheta, \vec{e}_\varphi)$ in such a way that $\vec{e}_\omega \cdot \vec{e}_\varphi = 0$ for all φ, this property translates into independence of $\rho(\vec{r})$ on φ. Consequently, both gravitational and centrifugal potential should not depend on φ. Deviations of this symmetry of rotation may arise under tidal forces by satellites or the parent star. However, signatures from tidal forces in the gravity field of the solar giant planets are up to now (April 2009) below the detection thresholds. This motivates to neglect deviations from azimuthal symmetry in this work. For the expected signatures of Jupiter's gravity field disturbance arised by its satellite Io, the interested reader is refered to the work of [Kramm08]. If ρ does not depend on φ, we have

$$\int_0^{2\pi} d\varphi'\, \rho \cos m(\varphi-\varphi') = \int_0^{2\pi} d\varphi'\, \rho \sin m(\varphi-\varphi') = 0 \quad \textit{(azimuthal symmetry)} \quad . \tag{3.50}$$

and the last two terms in (3.50) vanish.

Secondly, switching round the axis of rotation from $\vec{e}_\omega$ to $-\vec{e}_\omega$ should also not effect $\rho(\vec{r})$. This property translates into the condition of $\rho(r,\vartheta)$ being an even function of ϑ. Consequently, odd terms of ϑ in (3.50) must vanish, and we only need to consider terms of order $2n$. Both symmetry properties are supported by Jupiter's cloud pattern. The gravitational potential simplifies considerably and can be written as

$$V(r,\vartheta) = -\frac{G}{r}\sum_{n=0}^{\infty}\left(r^{-2n}D_{2n}(r) + r^{2n+1}D'_{2n}(r)\right)P_{2n}(\cos\vartheta) \tag{3.52}$$

with

$$D_n(r) = 2\pi\int_0^\pi\int_{r'<r} r'^2\,\sin\vartheta' dr' d\vartheta'\,\rho(r',\theta')(r')^n P_n(\cos\vartheta') \tag{3.53}$$

$$D'_n(r) = 2\pi\int_0^\pi\int_{r'>r} r'^2\sin\vartheta' dr' d\vartheta'\,\rho(r',\vartheta')(r')^{-(n+1)}P_n(\cos\vartheta') \tag{3.54}$$

The external field $V^{(e)}$

Accessible to observation is the external part $V^{(e)}$ of a planet's gravity field. $V^{(e)}$ can be derived from the motion of satellites as done in case of Uranus, or from the course taken by a spacecraft in the planets' (and its satellites') gravity field, see § 3.1.6. By custom, $V^{(e)}$ is expressed in terms of multipole moments, the so-called *gravitational moments* J_n, the equatorial radius R_{eq}, and the planetary mass M as

$$V^{(e)} = -\frac{GM}{r}\left(1 - \sum_{n=1}^{\infty}\left(\frac{R_{eq}}{r}\right)^{2n} J_{2n}P_{2n}(\cos\vartheta)\right) \tag{3.55}$$

with

$$J_n = -\frac{1}{MR_{eq}^n}\int_V d^3r'\rho(\vec{r}')(r')^n P_n(\cos\vartheta') \quad , \quad n>0 \tag{3.56}$$

measuring the deviation of the gravity field from spherical symmetry.

Spherical symmetry

For the gravitational potential V_0 of a rigidly rotating sphere of radius R the symmetry considerations above apply. In addition, V_0 does not depend on ϑ. Because of $P_0 = 1, P_n(\cos\vartheta) \sim (\cos\vartheta)^n +$ terms of higher order in n, terms containing $P_{n,\,n>0}$ in (3.52) must vanish, and $V_0(r)$ is given by the zeroth order of the multipole expansion (3.52),

$$\begin{aligned} V_0(r) &= -\frac{G}{r}\left(D_0 + rD'_0\right) \\ &= -\frac{4\pi G}{r}\left(\int_0^r r'^2 dr'\,\rho(r') + r\int_r^R r'^2 dr'\,\frac{\rho(r')}{r'}\right) \\ &= -\frac{Gm(r)}{r} - 4\pi G\int_r^R r' dr'\,\rho(r') \quad . \end{aligned} \tag{3.57}$$

With dm/dr from (3.33) we recover the force

$$\begin{aligned} -\frac{1}{m_i} F_{grav,\,0} &= \frac{dV_0}{dr} \\ &= \frac{Gm(r)}{r^2} - \frac{G}{r}\,\frac{dm}{dr} + 4\pi G \frac{d}{dr}\left[\int_R^r dr'\, r'\rho(r')\right] \\ &= \frac{Gm(r)}{r^2} - \frac{G}{r}\,4\pi r^2\rho(r) + 4\pi G\, r\rho(r) \\ &= \frac{Gm(r)}{r^2} \end{aligned} \tag{3.58}$$

in its well-known form. In this form, F_{grav} is only valid for the condition of spherical symmetry.

3.3.2 Multipole expansion of $Q(\vec{r})$

The centrifugal force on a mass element m_i, $\vec{F}_{fug} = m_i\,\vec{\omega}\times(\vec{\omega}\times\vec{r})$, acts perpendicular to the axis of rotation $\vec{\omega}$. In order to obtain an expression for Q as defined in (3.40), we first consider the problem in cylinder coordinates (ρ,φ,z). With $\vec{\omega} = \omega\,\vec{e}_z$, $\vec{r} = \rho\,\vec{e}_\rho$ we have $\vec{F}_{fug} = m_i\,\omega^2\rho\,\vec{e}_\rho$. With

$$grad = \frac{\partial}{\partial\rho}\,\vec{e}_\rho + \frac{1}{\rho}\frac{\partial}{\partial\varphi}\,\vec{e}_\varphi + \frac{\partial}{\partial z}\,\vec{e}_z$$

we can satisfy equation (3.40) by $Q = -(1/2)\,\omega^2\rho^2$. Transforming these expressions to spherical coordinates, we have $\rho = r\sin\vartheta$, $F_{fug} := \left|\vec{F}_{fug}\right| = m_i\,\omega^2 r\sin\vartheta$, and $Q = -(1/2)\,\omega^2 r^2\sin^2\vartheta$. With $\sin^2+\cos^2 = 1$ and the Legendre polynomials given in (D.32, D.34) we finally find the multipole expansion

$$Q(r,\vartheta) = -\frac{1}{3}\,\omega^2 r^2\,(P_0 - P_2(\cos\vartheta)) \quad . \tag{3.59}$$

Spherical symmetry

Since Q depends on ϑ independently on the density distribution, there are no analogons to (3.57) and (3.58). In order to calculate interior profiles of rotating, spherically symmetric planets as needed, e.g. for evolution sequences of Jupiter and Saturn, we can build an average centrifugal force $\overline{F}_{fug}(r) = m_i\,\omega^2 r\overline{\sin\vartheta}$ using

$$\overline{\sin\vartheta} = \frac{\int_0^\pi d\vartheta\,\sin\vartheta}{\int_0^\pi d\vartheta} = \frac{2}{\pi} \quad .$$

The result $\overline{F}_{fug}(r)/m_i = \frac{2}{\pi}\,\omega^2 r$ differs only slightly from the zero-order term

$$\frac{1}{m_i}\,F_{fug,\,0} = -grad\;Q_0(r,\vartheta) = \frac{2}{3}\,\omega^2 r \quad , \tag{3.60}$$

which is the derivative of the zero-order term

$$Q_0(r,\vartheta) = -\frac{1}{3}\,\omega^2 r^2 \tag{3.61}$$

of the expansion (3.59). This justifies the usual application of (3.61) in evolution calculations.

At this point we are able to calculate interior profiles of rotating spherical planets. The forces are given by (3.58) and (3.60) as gradients of the zero-order terms of the multipole expansions (3.52−3.54) and (3.59) of the corresponding potentials. In this picture, rotating spherical planets appear as zero-order approximation.

Real planets, however, are not spherical. Fluid rotating planets are oblate, and the mass density obeys azimuthal and north-south symmetry [ZhaTru78] as considered in § 3.3.1. When solving the hydrostatic equation of motion for real planets, the second-order (quadrupole) term of the centrifugal potential (3.59) necessarily causes the density to deviate from spherical symmetry. By (3.52−3.54), a non-spherical density distribution rises higher-order terms in the gravitational potential, again influencing the solution of the hydrostatic equation of motion. The resulting density distribution $\rho(r, \vartheta)$ also determines the shape of the planet. Instead of expanding $\rho(r, \vartheta)$ into a series of Legendre polynomials, it is more practical to consider the density along surfaces of constant potential, and then to write down these equipotential surfaces in terms of multipoles. Hence we have to solve simultaneously for the potential, the density distribution $\rho(r_l(\vartheta))$, and the equipotential surfaces $r_l(\vartheta)$ of the planet, l indexing the surface, in a selfconsistent manner. Selfconsistent means that the density distribution derived from a given gravitational and centrifugal potential is the same as the source of this gravitational potential.

Our procedure solving that task is devided into two parts. In the first part, we calculate for a given one-dimensional density distribution the planetary potential and shape using the *Theory of Figures* developed by Zharkov & Trubitsyn in the 70ies. In the second part, we apply this potential to the hydrostatic equation of motion, and obtain the (new) density distribution. We then iteratively repeat these two steps in order to ensure self-consistency. This procedure constitutes the heart of numerically modelling rotating giant planet interiors.

3.4 Theory of Figures

The *Theory of Figures* is the most general theory for calculating the observable external gravitational potential (3.55) and the shape of a planet. Our motivation in particular is to obtain J_2, J_4 and J_6 for comparison with observed values, and the total potential as input to the equation of motion (3.42). The *Theory of Figures* relies on three conditions.

1. The planet is in hydrostatic equilibrium. This condition is not true, for instance, for solid planets.

2. The density distribution $\rho(r, \vartheta_0)$ along some path (r, ϑ_0) of constant angle ϑ_0 to the axis of rotation is given. This condition is relatively easy to meet by a good guess and iterative approximation to the real density distribution.

3. Gravity surpasses centrifugal acceleration. This criterion is quantified by the ratio q of these forces at the equator, or, alternatively, by the ratio m defined as

$$q := \frac{\omega^2 R_{eq}^3}{GM} \quad , \quad m := \frac{\omega^2 \, l_1^3}{GM} \quad , \tag{3.62}$$

   where l_1 is the mean radius at the 1-bar pressure level to be defined in § 3.4.1.

3.4.1 Level surfaces

Surfaces of constant potential, pressure, and density coincide in hydrostatic equilibrium. In the theory of figures they are called *level surfaces* $l(r,\vartheta)$. If we take (l,ϑ) as independent variables instead of (r,ϑ), then by definition, for $l = const.$ neither the total potential U, nor the pressure, nor the density depend on ϑ. The *gradient* of U therefore is perpendicular to surfaces of constant l and reduces to $\vec{e}_l\, d/dl$. Equation (3.42) then becomes one-dimensional and of the same form as in the spherical case,

$$\frac{1}{\rho(l)}\,\frac{dP(l)}{dl} = -\frac{dU(l)}{dl} \quad . \tag{3.63}$$

Next we need an expression for the equipotential surfaces $r_l(\vartheta)$. For rotating planets, deviations from spherical symmetry are expected to be small. Lyapunov thus suggested [ZhaTru78] the ansatz

$$r_l(\vartheta) = l\left(1 + \sum_{n=0}^{\infty} s_{2n}(l)\, P_{2n}(\cos\vartheta)\right) \tag{3.64}$$

and demonstrated in 1903 that this ansatz solves (3.42). In the Theory of Figures, the expansion coefficients $s_n(l)$ are called *figure functions*. Taken at the surface l_1, their size relates to the smallness parameter m from (3.62) like

$$s_{2n} \sim m^n \quad . \tag{3.65}$$

By Lyapunov's ansatz (3.64), there is still some degree of freedom to relate the level parameter l to the size of the planet. One could choose the equatorial radius $l := a = r(\vartheta = \pi/2)$, or the polar radius as $l := b = r(\vartheta = 0)$. However, Zharkov & Trubitsyn (1978) recommend to choose the mean radius $l := \bar{l}$ of a level surface defined by equality of volumes enclosed:

$$\frac{4\pi}{3}\,\bar{l}^3 := \int_0^{2\pi} d\varphi \int_0^{\pi} d\vartheta \int_0^{r(\bar{l},\vartheta)} dr\ r^2 \sin\vartheta \quad . \tag{3.66}$$

At the surface we have $\bar{l} = l_1$. In the following we omit the accent and simply write l.

3.4.2 s_0

Definition (3.66) implies one constraint on the figure functions $s_{2n}, n = 0, 1, \ldots$. In order to derive this constraint, we introduce the abbreviations

$$\left(1 + \sum_{n=0}^{\infty} s_{2n}(l)\, P_{2n}(\cos\vartheta)\right) \quad =: \quad (1 + \Sigma(l,\vartheta)) \quad =: \quad (1+\Sigma) \tag{3.67}$$

$$\text{and} \qquad \cos\vartheta \quad =: \quad t \quad , \tag{3.68}$$

and insert (3.64) into (3.66) using $dr = (dr/dl)\, dl = (1+\Sigma)\, dl$, and $\sin\vartheta\, d\vartheta = -dt$. We then have

$$\begin{aligned}
\frac{4\pi}{3}\,\bar{l}^3 &= 2\pi \int_{-1}^{1} dt \int_0^{\bar{l}} dl\ l^2 (1 + \Sigma(l,t))^3 \\
2\pi \int_0^{\bar{l}} dl\, l^2 \Big[2\Big] &= 2\pi \int_0^{\bar{l}} dl\ l^2 \Big[\int_{-1}^{1} dt\ (1 + \Sigma(l,t))^3\Big] \\
\Rightarrow \qquad 2 &= \int_{-1}^{1} dt\ (1 + \Sigma(l,t))^3 \quad .
\end{aligned} \tag{3.69}$$

To propagate further, we need some

Basic properties of the Legendre Polynomials.

1. Being defined as solutions to the usual Legendre differential equation, they can be expressed as [ZT78 – eq. 25.5]

$$P_n(t) = \frac{1}{2^n n!}\,\frac{d^n}{dt^n}(t^2-1)^n \tag{3.70}$$

The usual recursion relation[2] found in literature relates P_n with P_{n-1} and P_{n+1}. More useful for proofs by the method of induction is the simple recursion relation

$$\begin{aligned} P_{n+1} &= \frac{1}{2\cdot 2^n}\,\frac{1}{(n+1)\,n!}\,\frac{d}{dt}\,\frac{d^n}{dt^n}\left[(t^2-1)^n(t^2-1)\right] \\ &= \frac{1}{2(n+1)}\,\frac{d}{dt}\left[P_n\cdot(t^2-1)\right] \end{aligned} \tag{3.71}$$

2. From (3.71) we see that P_n is a power series in t^j. The highest power occurring is t^n as proved in § D.3.2. Since the set $\{P_n(t)|n=0,1,2,\ldots,\infty\}$ and the set of power functions $\{t^n|n=0,1,2,\ldots,\infty\}$ are complete and orthogonal sets of basic functions in $\mathbb{R}$, they can be transformed into each other as

$$(a)\quad P_n(t)=\sum_{j=0}^{n} a_j\,t^j \qquad , \qquad (b)\quad t_n=\sum_{j=0}^{n} b_j\,P_j(t) \quad , \tag{3.72}$$

with rational coefficients a_j and b_j to be determined by (3.70).

3. Because of properties (3.72a,b) also products of Legendre polynomials can be expanded into a power series as well as into a series of Legendre polynomials:

$$(a)\quad P_n(t)*P_m(t)=\sum_{j=0}^{n+m} c_j\,t^j \qquad , \qquad (b)\quad P_n(t)*P_m(t)=\sum_{j=0}^{n+m} d_j\,P_j(t) \quad . \tag{3.73}$$

4. Furthermore,

$$(a)\quad \int_{-1}^{1} dt\,P_n(t)=0 \qquad (n\neq 0) \qquad \text{and} \qquad (b)\quad \int_{-1}^{1} dt\,P_n(t)P_m(t)=0 \qquad (n\neq m) \quad , \tag{3.74}$$

For poofs of (a) and the orthogonality relation (b) the reader is referred to § D.3.2.

Calculating the rational coeffients $a_j, b_j, c_j, d_j, n = 0, 1, 2,$ etc. in the transformations (3.72 a,b, 3.73 a,b) is straightforward but time-consuming. For this I wrote a C++ program. It is contained in my program package LegendreDevelop. We also have to define the order of approximation A.

Order of approximation

Due to the north-south symmetry, only even Legendre polynomials of index $2n$ can occur in the multipole expansions of the gravitational potential $V(r,\vartheta)$ and the equipotential surfaces $r_l(\vartheta)$. Since $s_{2n} \sim m^n$ and $m \ll 1$, it is convenient to call the order of approximation the order of the highest index n considered in the expansions (3.52) and (3.64). Hence, J_2 is the first-order coefficient, J_4 the second-order coefficient etc.. In case of Jupiter, the current observational error bars of J_2 and J_4 are of the size of J_6. We therefore have to develop the Theory of Figures at least

[2] usual recursion relation: $(n+1)P_{n+1} = (2n+1)\,t\,P_n - n\,P_{n-1}$

up to third order, in order to have sufficiently accurate theoretical J_2 and J_4 values to compare with the observed ones. The error bar of Jupiter's J_6 is almost 100% and thus we do not need to consider higher order terms in the expansion. This might change with the *Juno*-mission, to be launched in a few years.

Nevertheless, the behaviour of Jupiter interior models in dependence on the order of approximation itself is an important topic. It serves i) as a check for the numerical modelling procedure and ii) while currently being just an exercise, in light of the *Juno*-mission it is an inevitable basis of next generation Jupiter models. Thus we here develop the theory of figures up to fifth order. We remind the reader:

Theory of Figures in n-th order	$\Longleftrightarrow$	terms of index $m = 0, 2, 4, \ldots, 2n$ are considered.

When we calculate products of Σ as for instance in (3.69), we only have to consider those terms where the sum of indices is less or equal than 2 times the order of approximation. I give an example at this place, since this simple rule accelerates enormously the calculations, when using a computer (like I did) or a pencil. We calculate $(s_2 + s_4 + s_6 + s_8)^3$ in fifth order:

$$\begin{aligned}(s_2 + s_4 + s_6 + s_8)^3 \quad &= \quad (s_2^3 + 3s_2^2 s_4 + 3s_2^3 s_6 + 3s_2^2 s_8) + (s_4^3 + 3s_4^2 s_2 + 3s_4^2 s_6 + 3s_4^2 s_8) \\ &\quad + (s_6^3 + 3s_6^2 s_2 + 3s_6^2 s_4 + 3s_6^2 s_8) + (s_8^3 + 3s_8^2 s_2 + 3s_8^2 s_4 + 3s_8^2 s_6) \\ &\quad + 6s_2 s_4 s_6 + 6s_2 s_4 s_8 + 6s_2 s_6 s_8 + 6s_4 s_6 s_8 \\ &\overset{\text{(5th order)}}{=} \quad s_2^3 + 3s_2^2 s_4 + 3s_4^2 s_2 \quad . \qquad \textit{(Exercise)}\end{aligned}$$

For puzzled readers one more exercise: the order of $s_2 s_4^2 s_8$ is $(2 + 2 * 4 + 8)/2 = 9$.

We proceed with calculating s_0 in fifth order and begin with equation (3.69).

$$\begin{aligned} 2 \quad &= \quad \int_{-1}^{1} dt\, (1+\Sigma)^3 = \int_{-1}^{1} dt\, (1 + 3\Sigma + 3\Sigma^2 + \Sigma^3) \\ \Leftrightarrow \quad 0 \quad &= \quad \int_{-1}^{1} dt\, 3\Sigma + \int_{-1}^{1} dt\, 3\Sigma^2 + \int_{-1}^{1} dt\, \Sigma^3 \quad . \end{aligned} \tag{3.75}$$

Due to (3.74), from the first integral in (3.75) only the P_0 term survives: $\int_{-1}^{1} dt\, 3\Sigma = 6s_0$. For the second integral we use the orthogonality relation (D.39) and the *exercise* from above and find

$$\int_{-1}^{1} dt\, 3\Sigma^2 \;=\; \int_{-1}^{1} dt\, 3\left[s_0^2 P_0^2 + s_2^2 P_2^2 + s_4^2 P_4^2 \;+ \mathcal{O}(\text{6-th order})\right] \;=\; 3\left(2s_0^2 + \frac{2}{5}s_2^2 + \frac{2}{9}s_4^2\right) \quad . \tag{3.76}$$

For the third integral in (3.75), we remember that $(a + b + \ldots + z)^3 = a^3 + b^3 + \ldots z^3 + 3a^2 b + \ldots + 3a^2 z + 3z^2 a + \ldots + 3z^2 y + 6abc + \ldots + 6xyz$ and (3.74), and find

$$\begin{aligned}\int_{-1}^{1} dt\, \Sigma^3 \quad &= \quad \int_{-1}^{1} dt \Big[s_0^3 + s_2^3 P_2^3 + \mathcal{O}(m^6) \\ &\qquad + \quad 3s_2^2 s_0 P_2^2 + 3s_2^2 s_4 P_2^2 P_4 + 3s_2^2 s_6 P_2^2 P_6 + 3s_4^2 s_0 P_4^2 + 3s_4^2 s_2 P_2 P_4^2 + \mathcal{O}(m^6) \\ &\qquad + \quad 6s_0 s_2 s_4 P_2 P_4 + \ldots (\text{no contribution}) \Big] \\ &= \quad 2s_0^3 + 3\,\frac{2}{5} s_0 s_2^2 + 3\frac{2}{9} s_0 s_4^2 + \int_{-1}^{1} dt\, \left[s_2^3 P_2^3 + 3s_2^2 s_4 P_2^2 P_4 + 3s_2^2 s_6 P_2^2 P_6 + 3s_4^2 s_2 P_2 P_4^2 \right] \quad .\end{aligned}$$

Next we have to expand the products P_2^3, $P_2^2P_4$, $P_2^2P_6$, and $P_2P_4^2$ as in (3.73b). An example how this can be done is given in § D.3.1. For the first three products this example is sufficient to determine relevant terms contributing to the integral:

$$P_2^3 = (P_2 * P_2)P_2 \to \tfrac{2}{7}P_2^2 \quad , \quad P_2^2P_4 = (P_2 * P_2)P_4 \to \tfrac{18}{35}P_4^2 \quad , \quad P_2^2P_6 = (P_2 * P_2)P_6 \to 0 \quad .$$

For the fourth product, $P_2P_4^2$, we have to know the P_2-term of the expansion of $P_4 * P_4$. The result from LegendreDevelop is $P_2(P_4 * P_4) \to 100/693P_2^2$. Using again the orthogonality relation (D.39), we have

$$\begin{aligned}\int_{-1}^{1} dt\,\Sigma^3 &= 2s_0^3 + \frac{6}{5}s_0s_2^2 + \frac{2}{3}s_0s_4^2 + \int_{-1}^{1} dt\,\left[\frac{2}{7}s_2^3P_2^2 + 3\frac{18}{35}s_2^2s_4P_4^2 + 3\frac{100}{693}s_2s_4^2P_2^2\right] \\ &= 2s_0^3 + \frac{6}{5}s_0s_2^2 + \frac{2}{3}s_0s_4^2 + \frac{4}{35}s_2^3 + \frac{12}{35}s_2^2s_4 + \frac{120}{693}s_2s_4^2 \quad . \end{aligned} \tag{3.77}$$

Summing up all three terms in (3.75), we get

$$\begin{aligned} 0 &= 6s_0 + 6s_0^2 + \frac{6}{5}s_2^2 + \frac{2}{3}s_4^2 + 2s_0^3 + \frac{6}{5}s_0s_2^2 + \frac{2}{3}s_0s_4^2 + \frac{4}{35}s_2^3 + \frac{12}{35}s_2^2s_4 + \frac{120}{693}s_2s_4^2 \\ \Leftrightarrow -s_0 &= s_0^2 + \frac{1}{3}s_0^3 + \frac{1}{5}s_0s_2^2 + \frac{1}{9}s_0s_4^2 + \frac{1}{5}s_2^2 + \frac{2}{105}s_2^3 + \frac{1}{9}s_4^2 + \frac{2}{35}s_2^2s_4 + \frac{20}{693}s_2s_4^2 \quad . \end{aligned} \tag{3.78}$$

Still we don't know the order of s_0. The lowest order term known on the right hand side (*rhs*) of (3.78) is $\frac{1}{5}s_2^2$. Candidates for compensating terms are s_0, s_0^2, and $\frac{1}{3}s_0^3$. *If* $s_2^2 \sim s_0^2 + \mathcal{O}(m^3)$, we would have $s_0 \sim s_2$ and thus no counterpart for s_0 in (3.78). *If* $s_2^2 \sim s_0^3 + \mathcal{O}(m^3)$, we would have $s_0 \sim s_2^{2/3}$ and also no counterpart. *If* otherwise $s_2^2 \sim s_0 + \mathcal{O}(m^3)$, we would have $s_0^2 \sim s_2^4$, i.e. of 4th order with available counterparts in (3.78), and $s_0^3 \sim s_2^6$, i.e. of 6th order and to be neglected. With $s_0 \sim s_2^2$ we can compare the second order terms and the third order terms in (3.78) and find

$$\begin{aligned} -s_0 &= \frac{1}{5}s_2^2 \qquad \textit{(2nd order)} \\ \text{and} \qquad -s_0 &= \frac{1}{5}s_2^2 + \frac{2}{105}s_2^3 \qquad \textit{(3rd order)} \end{aligned} \tag{3.79}$$

$$\Rightarrow \qquad s_0^2 = \frac{1}{25}s_2^4 + \frac{4}{525}s_2^5 + \mathcal{O}(m^6) \tag{3.80}$$

Neglecting the 6th order term s_0^3 and inserting (3.79)[3] and (3.80) into the *rhs* of (3.78) we finally find s_0 in fifth order:

$$-s_0 = \frac{1}{5}s_2^2 + \frac{2}{105}s_2^3 + \frac{1}{9}s_4^2 + \frac{2}{35}s_2^2s_4 + \frac{20}{693}s_2s_4^2 + \frac{2}{525}s_2^5 \quad . \qquad \textit{(5th order)} \tag{3.81}$$

At this point, we have derived and presented the principal ideas for modelling rotating giant planets. We know that we are going to solve the one-dimensional equation of motion (3.63) perpendicular to equipotential surfaces (3.64). Obviously, we are still in need of equations for practically *calculating* the figure functions $s_2(l), s_4(l)$ etc. and the potential $U(l)$ in third order or more. We have seen (3.52) that the gravity field contains many different powers of the radial coordinate r, and that in order to be able to calculate anything, e.g. (3.66), we have to linearize $r(l, \vartheta)$ with respect to Legendre polynomials. The example above has shown us that this is best performed by a computer program optimized with respect to the order of approximation and to properties of

[3] In [ZT78 – eq. 28.12] there is a misprint; they use also (3.79) for further calculations.

Legendre polynomials.

Before we proceed with § 3.4.3, I think it is time to sustain the reader's motivation by a visualization of Legendre polynomials and the figure of Jupiter. Fig. 3.1 shows, from the upper left panel to the lower right panel, (a): $P_2(t)$ where $t = \cos\vartheta$, (b): $P_4(t)$, (c): $P_6(t)$, (d): $1 + 10 \times s_2(l_1)\,P_2(t)$ illustrating Jupiter's quadrupolar shape deformation at the surface $l = l_1$, (e): $1 + 10^2 \times s_4(l_1)\,P_4(t)$ illustrating Jupiter's octupolar shape deformation, (f): $1 + 10^3 \times s_6(l_1)\,P_6(t)$ illustrating Jupiter's 16-polar shape deformation, (g): $1 + s_2(l_1)\,P_2(t)$, (h): $1 + s_4(l_1)\,P_4(t)$, and (i): $1 + \sum_{n=1,2,3}[s_{2n}(l_1)\,P_{2n}(t)]$. In some panels, the equator is indicated by a dotted line. In all of these panels, ϑ runs from 0 to 2π, and the values of s_2, s_4, s_6 are taken from a calculated model of Jupiter.

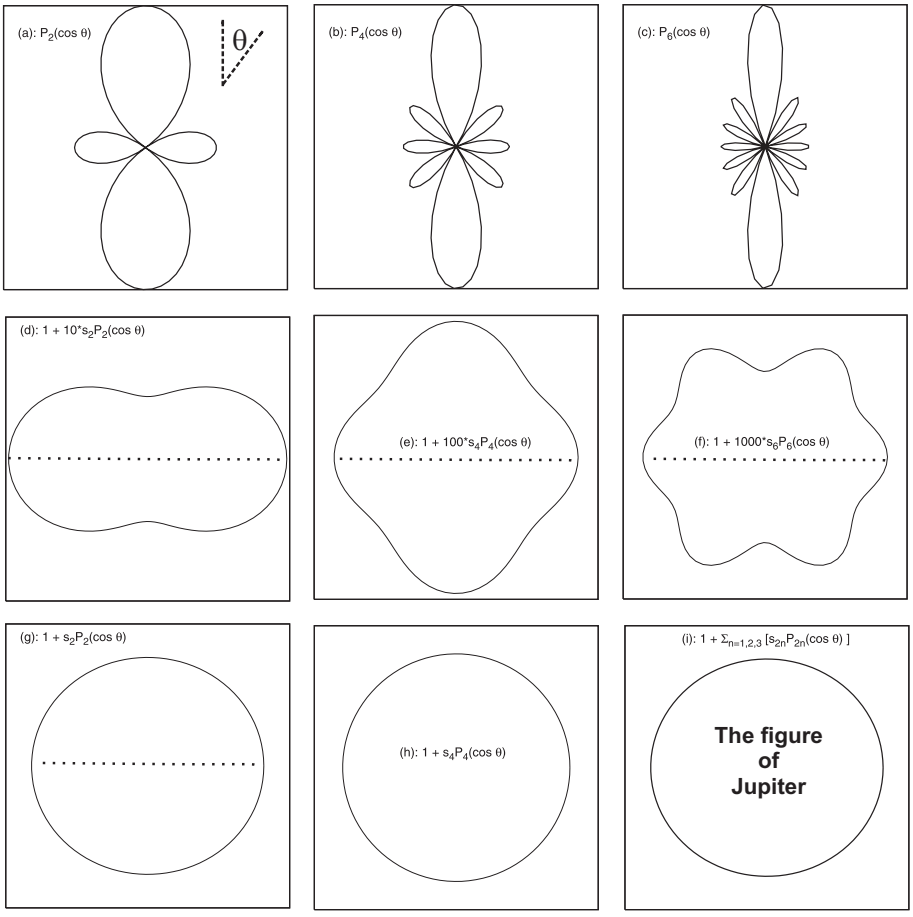

Figure 3.1: From the upper left to the lower right: (a), $P_2(\cos\theta)$, (b): $P_4(\cos\theta)$, (c): $P_6(\cos\theta)$, (d)-(f): 10 times the quadrupolar (s_2), 100 times the octupolar (s_4), and 1000 times the 16-polar (s_6) shape deformation of Jupiter, (g)-(h): Jupiter's quadrupolar and octupolar shape moment, (i) Jupiter's shape.

3.4.3 The potential: $U(l)$

We aim to find appropriate equations to calculate equipotential surfaces $U(l)$ and the figure functions $s_{2n}(l), n = 1, 2\ldots$ in third order or more. Formally, we can write [ZhaTru78]

$$U(l,\vartheta) = \frac{4\pi}{3} G\bar{\rho} l^2 \sum_{n=0}^{\infty} A_{2n}(l)\, P_{2n}(\cos\vartheta) \tag{3.82}$$

where $\bar{\rho} = M/(4/3)\pi l_1^3$ is the mean density and all complicated dependence on the level parameter l is hidden in the functions $A_{2n}(l)$ to be determined. Because of $U = V + Q$, we can also split the A_{2n} into

$$A_{2n}(l) = A_{2n}^{(V)}(l) + \frac{m}{3} A_{2n}^{(Q)}(l) \tag{3.83}$$

and determine the contributions arising from the gravitational potential ($A_{2n}^{(V)}$) and those from the centrifugal potential ($A_{2n}^{(Q)}$) separatly. By definition of l, if l is fixed, $U(l,\vartheta)$ must not depend on ϑ (otherwise it would not be an equipotential surface). Hence, all terms in (3.82) depending on ϑ must vanish. We thus have

$$U(l) = \frac{4\pi}{3} G\bar{\rho} l^2\, A_0(l) \qquad , \qquad A_{2n}(l) \equiv 0\ (n > 0) \quad . \tag{3.84}$$

The conditions $A_2(l) \equiv 0$, $A_4(l) \equiv 0, \ldots$, will be used to determine the figure functions $s_2(l), s_4(l), \ldots$. Comparing (3.52) and (3.82), obviously the A_{2n} contain diverse powers of $r(\vartheta)$ and diverse integrals $D_{2n}(r)$ and $D'_{2n}(r)$ over the interior density distribution. Note that these density integrals are defined in (3.53, 3.54) in terms of the radial coordinate r, and the integration is performed in spherical coordinates where the information about the shape of the planet is solely contained in $\rho(r', \vartheta')$. However, we can change the order of summing up the mass elements $\rho(r', \vartheta')\, r^2 dr\, \sin\vartheta d\vartheta$ by replacing r with our new radial coordinate l. Doing this, we implicitly change the integral boundaries in space from spheres to equipotial spheroids preserving the volume enclosed, see (3.66), thereby $\rho(l)$ becoming a purely radial function. With the transformation formulas

$$\left.\begin{array}{lllll}
r^2 dr & = r^2(l,\vartheta)\frac{dr}{dl}\, dl & = \frac{1}{3}\frac{d}{dl} r^3\, dl & & \\
d^3r\, r^n & = 2\pi r^{2+n} dr\, \sin\vartheta\, d\vartheta & = \frac{2\pi}{n+3}\, \frac{d}{dl} r^{n+3}\, d\cos\theta & & \\
d^3r\, r^{-(n+1)} & = 2\pi r^{2-(n+1)} dr\, \sin\vartheta\, d\vartheta & = \frac{2\pi}{2-n}\, \frac{d}{dl} r^{2-n}\, d\cos\vartheta & (n \neq 2) & \\
d^3r\, r^{-(n+1)} & = 2\pi r^{-1} dr \sin\vartheta\, d\vartheta & = \frac{d\ln r}{dl}\, d\cos\vartheta & (n = 2) & \\
t & = \cos\vartheta \quad , & & &
\end{array}\right\} \tag{3.85}$$

the density integrals D_n, D'_n take the form [ZhaTru78]

$$D_n(l) = \frac{2\pi}{n+3} \int_0^l dl'\, \rho(l') \int_{-1}^{1} dt'\, P_n(t') \frac{d\, r^{n+3}}{dl} \tag{3.86}$$

$$D'_n(l) = \frac{2\pi}{2-n} \int_l^{l_1} dl'\, \rho(l') \int_{-1}^{1} dt'\, P_n(t') \frac{d\, r^{(2-n)}}{dl'} \quad (n \neq 2) \tag{3.87}$$

$$D'_2(l) = 2\pi \int_l^{l_1} dl'\, \rho(l') \int_{-1}^{1} dt'\, P_2(t') \frac{d\, \ln r}{dl'} \quad . \tag{3.88}$$

Using the dimensionless coordinate $\beta := l/l_1$, the density integrals $D_{2n}(r)$ and $D'_{2n}(r)$ can be brought into the dimensionless form $S_n(\beta)$ and $S'_n(\beta)$ defined as [ZT78 – 28.6]

$$S_n(\beta) = \frac{3}{4\pi\bar{\rho}\, l^{n+3}}\, D_n(l) \qquad , \quad S'_n(\beta) = \frac{3}{4\pi\bar{\rho}\, l^{2-n}} D'_n(l) \quad . \tag{3.89}$$

In particular at $l = l_1$, $S_{2n}(1) = (1/M)D_{2n}(l_1)$. Moreover, the dimensionless density integrals can be written as [ZT1978 – 28.10]

$$S_n(\beta) = \frac{1}{\beta^{n+3}} \int_0^\beta dz\, \frac{\rho(z)}{\bar{\rho}}\, \frac{d[z^{n+3} f_n]}{dz} \tag{3.90}$$

$$S'_n(\beta) = \frac{1}{\beta^{(2-n)}} \int_\beta^1 dz\, \frac{\rho(z)}{\bar{\rho}}\, \frac{d[z^{2-n} f'_n]}{dz} \tag{3.91}$$

$$S_0(\beta) = \frac{m(\beta)}{M\beta^3} \tag{3.92}$$

which we are going to show next.

Proof of (3.90– 3.92). The proof of (3.91) for $n \neq 2$ is equivalent to the proof of (3.90), if the index $n+3$ occuring in S_n and D_n is properly exchanged by $n-2$. It is thus sufficient to proof (3.91) only for $n = 2$. We insert (3.86) and (3.88) into relations (3.89) and obtain

$$\begin{aligned} S_n(\beta) &= \frac{3}{2}\frac{1}{n+3}\frac{1}{l^{n+3}} \int_0^l dl'\, \frac{\rho(l')}{\bar{\rho}} \int_{-1}^1 dt\, P_n(t') \frac{d}{dl'} \left[r^{n+3}(l', t') \right] \\ S'_2(\beta) &= \frac{3}{2} \int_l^{l_1} dl'\, \frac{\rho(l')}{\bar{\rho}} \int_{-1}^1 dt\, P_n(t') \frac{d}{dl'} \big[\ln\, r \big] \quad . \end{aligned}$$

Remembering $\beta = l/l_1$, we also replace l' in the integrals above by $z := l'/l_1$ which leaves $dl'\, \frac{d}{dl'} = dz\, \frac{d}{dz}$ invariant and $r(l', t')$ becomes $r(z, t') = l_1 z(1 + \Sigma(z, t'))$. We thus have

$$S_n(\beta) = \frac{3}{2}\frac{1}{n+3}\frac{1}{\beta^{n+3}} \int_0^\beta dz\, \frac{\rho(z)}{\bar{\rho}} \int_{-1}^1 dt\, P_n(t') \frac{d}{dz} \left[z^{n+3} \left(1 + \Sigma(z, t')\right)^{n+3} \right] , \tag{3.93}$$

$$S'_2(\beta) = \frac{3}{2} \int_\beta^1 dz\, \frac{\rho(z)}{\bar{\rho}} \int_{-1}^1 dt\, P_n(t') \frac{d}{dz} \Big[\ln\, z l_1 \left(1 + \Sigma(z, t)\right) \Big] \quad . \tag{3.94}$$

The derivative d/dz we pull out of the integral over $\cos\vartheta'$ and collect all remaining factors not appearing in (3.90) and (3.91) respectively and call them f_n and f'_n. We thus have recovered

$$(3.90) \qquad \text{with} \qquad f_n = \frac{3}{2(n+3)} \int_{-1}^1 dt\, P_n(t) * (1 + \Sigma)^{n+3} \tag{3.95}$$

$$(3.91),\ n \neq 2, \qquad \text{with} \qquad f'_n = \frac{3}{2(n-2)} \int_{-1}^1 dt\, P_n(t) * (1 + \Sigma)^{n-2} \tag{3.96}$$

$$(3.91),\ n = 2, \qquad \text{with} \qquad f'_2 = \frac{3}{2} \int_{-1}^1 dt\, P_n(t) * \ln(1 + \Sigma) \tag{3.97}$$

In order to obtain f'_2 we have used $\frac{d}{dz}[\ln\, z l_1 (1+\Sigma)\,] = 1/z + \frac{d}{dz}[\ln\,(1+\Sigma)\,]$. The integral $\int_{-1}^1 dt$ in (3.94) is thus split into two parts with integrands P_2/z and $P_2 \frac{d}{dz}\,[\ln(1+\Sigma)\,]$, respectively. From

(3.74a) we know that the first part vanishes. In § 3.4.2 we have learned and practised how to calculate products Σ^m; we can also calculate products $(1+\Sigma)^m$ and $\ln(1+\Sigma)$ using

$$(a): \quad (1+\Sigma)^m = \sum_{k=0}^{m} \binom{m}{k} \Sigma^k \qquad , \qquad (b): \ln(1+\Sigma) = \Sigma - \frac{\Sigma^2}{2} + \frac{\Sigma^3}{3} \mp \dots \quad . \tag{3.98}$$

Equation (3.98a) is applied to calculate the functions $f_{2n}(z)$ and $f'_{2n,n\neq 2}(z)$, and equation (3.98b) for $f'_2(z)$. The results are given in Tab. F.2 in the Appendix.

Assuming $r = r_l(\vartheta)$, then $D_{2n}(l) = D_{2n}(r_l(\vartheta))$. $D_0(r)$ in (3.53) evidently is just the mass $m(r)$ within the sphere of radius r, and thus $D_0(l)$ is the mass $m(l)$ within or up to level $l = \beta l_1$. Thus we have

$$S_0(\beta) = \frac{3\, D_0(l)}{4\pi l^3\, \bar{\rho}} = \frac{3\, m(l)\, 4\pi l_1^3}{4\pi l^3\, 3M} = \frac{m(\beta)}{M\beta^3}$$

as stated in (3.92).

We have learned to re-interpret $D_{2n}(r)$ and $D'_{2n}(r)$ as $D_{2n}(l)$ and $D'_{2n}(l)$, and transformed further to $S_{2n}(\beta)$ and $S'_{2n}(\beta)$. Comparing (3.52) with (3.82), we are almost ready to write the $A_{2n}(l)$ in terms of the external integrals $S_{2k}(\beta)$, the internal integrals $S'_{2k}(\beta)$ and the figure functions $s_{2k}(l)$. Inserting (3.89) into (3.52) we get for the gravitational potential

$$V = -G\sum_{k=0}^{\infty} \Big(r^{-2k-1} D_{2k}(r) + r^{2k} D'_{2k}(r) \Big) P_{2k}(t) \tag{3.99}$$

$$= -\frac{4\pi}{3}\, G\bar{\rho}\, l^2 \sum_{k=0}^{\infty} \Big((r/l)^{-2k-1}\, P_{2k} \Big) S_{2k}(\beta) + \Big((r/l)^{2k}\, P_{2k} \Big) S'_{2k}(\beta) \quad , \tag{3.100}$$

Equation (3.99) may mislead to conclude the $A_{2n}^{(V)}$ were just the expression in parentheses. Before we can read the coefficients $A_{2n}^{(V)}$, we first have to expand the terms in front of S_{2n}, S'_{2n}. Because of $r/l = 1+\Sigma$, all factors of type $(1+\Sigma)^m P_{2k}$ occurring in (3.100) can be written as

$$(1+\Sigma)^m P_{2k} = \sum_{n=0}^{\infty} B_{2n}^{(2k,m)} P_{2n} \quad , \quad B_{2n}^{(2k,m)} = B_{2n}^{(2k,m)}(l) = B_{2n}^{(2k,m)}(s_2(l), s_4(l), s_6(l), \dots) \quad , \tag{3.101}$$

where $B_{2n}^{(2k,m)}$ are functions of the figure functions depending on l, indexed by $(2k,m)$ to keep trace of different products (3.101). In this notation, we can rewrite V as

$$V(l,t) = -\frac{4\pi}{3}\, G\bar{\rho}\, l^2 \sum_{n=0}^{\infty} \left\{ \sum_{k=0}^{\infty} B_{2n}^{(2k,-2k-1)}(l)\ S_{2k}(l) + B_{2n}^{(2k,2k)}(l)\ S'_{2k}(l) \right\} P_{2n}(t) \quad , \tag{3.102}$$

and simply read $A_{2n}^{(V)}$ as the expression in curled brackets. The coefficients $B_{2n}^{2k,-2k-1}$ are listed in Tab. F.4 and the coefficients $B_{2n}^{2k,2k}$ in Tab. F.5 up to fifth order in the expansion.

After all these considerations we are well-prepared to easily find an equivalent expression for $Q(l,t)$. With m defined in (3.62) and $r = r(l,t)$ we can rewrite the centrifugal potential (3.59) in the form

$$Q(l,t) = -\frac{4\pi}{3} G\bar{\rho}\, l^2 \left(\frac{m}{3}(1+\Sigma)^2 (1 - P_2) \right) \tag{3.103}$$

$$= -\frac{4\pi}{3} G\bar{\rho}\, l^2\, \frac{m}{3} \sum_{n=0}^{5} A_{2n}^{(Q)}(l) P_{2n}(t) \quad . \tag{3.104}$$

Obviously we just need to sum up the expansion of $(1+\Sigma)^2$ and $-(1+\Sigma)^2 * P_2$. The resulting coefficients

$$A_{2n}^{(Q)} = \sum_{k=0}^{\infty} C_k^{(2n)} \quad , \quad C_k^{(2n)} = C_k^{(2n)}(l) = C_k^{(2n)}(s_2(l), s_4(l), s_6(l), \ldots)$$

are given in Tab. F.1 up to fifth order. Like $B_{2n}^{(2k,m)}$, also $C_k^{(m)}$ are functions of the figure functions.

On equipotential surfaces, $U = const$ per definition, and thus $A_{2n} = A_{2n}^{(V)} + (m/3)A_{2n}^{(Q)} \equiv 0$ for $n > 0$ in order to get rid of any dependence on t. The final expansion of the total potential is

$$U(l) = \frac{4\pi}{3} G\bar{\rho}\, l^2 \left(A_0^{(V)}(l) + \frac{m}{3} A_0^{(Q)}(l) \right) \tag{3.105}$$

$$\text{with} \quad A_0^{(V)}(l) = \sum_{k=0}^{\infty} B_0^{(2k,-2k-1)}(l)\ S_{2k}(l) + B_0^{(2k,2k)}(l)\ S'_{2k}(l) \quad , \tag{3.106}$$

$$A_0^{(Q)}(l) = \sum_{k=0}^{\infty} C_k^{(0)}(l) \quad . \tag{3.107}$$

All coefficients $B_0^{(2k,m)}$, $C_k^{(0)}$, and the density integrals S_{2k}, S'_{2k} depend on the figure functions. For $n \geq 0$, the coefficients A_{2n} are given in Tab. F.3 in third order. Higher order terms can easily be read from tables F.4, F.5, and F.1 using (3.105) and (3.83). For reasons mentioned below, most planetary models presented in this work have been calculated using the Theory of Figures in third order. $A_0(l)$ in third order is

$$A_0 = \left[1 + \frac{2}{5}s_2^2 - \frac{4}{105}s_2^3\right] S_0(l) + S'_0 \left[-\frac{3}{5}s_2 + \frac{12}{35}s_2^2\right] S_2(l) + \left[\frac{2}{5}s_2 + \frac{2}{35}s_2^2\right] S'_2 + \frac{m}{3}\left[1 - \frac{2}{5}s_2 - \frac{9}{35}s_2^2\right] \tag{3.108}$$

Calculating the gravitational moments

Comparing (3.52), (3.55), and using (3.89), the moments J_{2n} are related to the density integrals D_{2n} and S_{2n} by

$$J_{2n} = -\frac{1}{MR_{eq}^{2n}} D_{2n}(l = l_1) \tag{3.109}$$

$$= -\left(\frac{l_1}{R_{eq}}\right)^{2n} S_{2n}(1) \quad . \tag{3.110}$$

Equation (3.110) is implemented within the program package NordOst. We can also define radius-dependent moment functions $J_{2n}(l) = -\frac{1}{MR_{eq}^{2n}} D_{2n}(l)$. The relation between $J_{2n}(l)$ and $S_{2n}(\beta)$ consequently becomes

$$J_{2n}(l) = -\frac{1}{MR_{eq}^{2n}} \frac{4\pi}{3} \bar{\rho}\, l^{2n+3}\, S_{2n}(\beta)$$

$$= -\left(\frac{l_1}{R_{eq}}\right)^{2n} \beta^{2n+3}\, S_{2n}(\beta) \quad . \tag{3.111}$$

Calculating the figure functions

A recipe for calculating the figure functions is given in [ZhaTru78], § 37. Basically, we know $A_{2n} \equiv 0$ for all $n > 0$, and a short glance at Tab. F.3 reveals a structure like $0 = A_{2n} = (-s_{2n} + h1_{2n}^{(n)})S_0 + h2_{2n}^{(n)}$ where $h1$ and $h2$ are functions of order $\geq n$ depending on diverse powers of $(s_2, s_4, s_6, \ldots)$ and on the integrals S_{2n} and S'_{2n}. Thus we can write

$$s_{2n}(l) = h1_{2n}^{(n)}(s_2, s_4, s_6, \ldots) + \frac{1}{S_0} h2_{2n}^{(n)}(s_2, s_4, s_6, \ldots) =: H_{2n}(s_2, s_4, s_6, \ldots) \tag{3.112}$$

In particular, the lowest order term of order 1 in H_2 is the $m-$term. So as initial condition for an iterative procedure we have $s_2^{(1)}(l) = -m/3$ for all l. Next we can insert $s_2^{(1)}$ into H_4 and obtain a first guess $s_4^{(1)}(l)$, and so on for all higher indices:

$$s_2^{(1)} = H_2^{(1)}(0, 0, 0, \ldots) \quad , \quad s_4^{(1)} = H_4^{(1)}(s_2^{(1)}, 0, 0, \ldots) \quad , \quad s_6^{(1)} = H_6^{(1)}(s_2^{(1)}, s_4^{(1)}, 0, \ldots) \quad \ldots$$

From here on the iteration scheme is straightforward and can be expressed at iteration m for any figure function s_{2n} as

$$s_{2n}^{(m+1)} = H_{2n}^{(m+1)}(s_2^{(m)}, s_4^{(m)}, s_6^{(m)}, \ldots) \quad . \tag{3.113}$$

Typically 15 iterations are required for convergence of s_2 below 0.1%, s_4 below 0.1% and s_6 below 1% uncertainty. An example is shown in Fig. 3.2 for a standard three-layer structure model of Saturn.

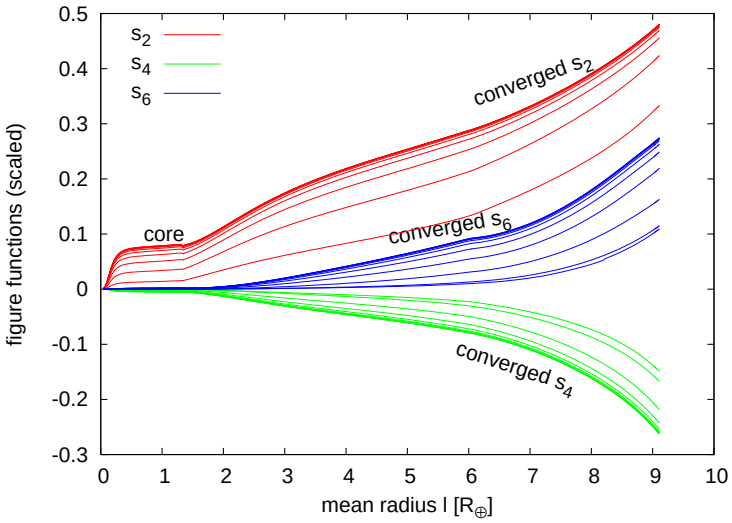

Figure 3.2: Iteratively determined figure functions $s_2(l)$, $s_4(l)$, $s_6(l)$, scaled by a factor of $1/m^n$, where $2n$ is the index of the respective figure function, for a typical model of Saturn. Shown are intermediate results of several iterations in order to illustrate the convergent behaviour. The underlying Saturn interior model has three layers (outer H/He envelope with $Z_1 = 9\%$, inner H/He envelope with $Z_2 = 28\%$ starting at 0.8 Mbar and $l = 6R_\oplus$, and a $\sim 6M_\oplus$ rock core).

As soon as converged figure functions have been obtained, they can be inserted into (3.108) to yield numerical values for the total potential $U(l)$. Before we have a closer look at the resulting forces in Fig. 3.4, we first check sign and order of the figure functions s_{2n} and the integrals S_{2n}, S'_{2n}. This check is presented in the appendix (§ B), since it is not an essential part of the method description. From Fig. B.2 displaying $S_{2n}(l)$ and $J_{2n}(l)$, I conclude that NordOst produces a reasonable behaviour.

Gravitational moments: the contribution function

In can be shown, e.g. in Fig. B.2, that the planetary deep interior contributes much less to the values $J_{2n}^{(\mathrm{obs})}$ observed at the surface than the outer shells. We can define a normalized contribution function $c_{J_{2n}}(l)$ that measures the contribution of a mass shell at level l to the final value. A reasonable choice is

$$c_{J_{2n}}(l) = \frac{\frac{d}{dl'}\big|_l J_{2n}(l')}{\int_0^R dl' \, \frac{d}{dl'} J_{2n}(l')} \quad . \tag{3.114}$$

These contribution functions are shown in Fig. 3.3 in case of the polytropic ($n = 1$) Jupiter model by Zharkov & Trubitsyn (1978).

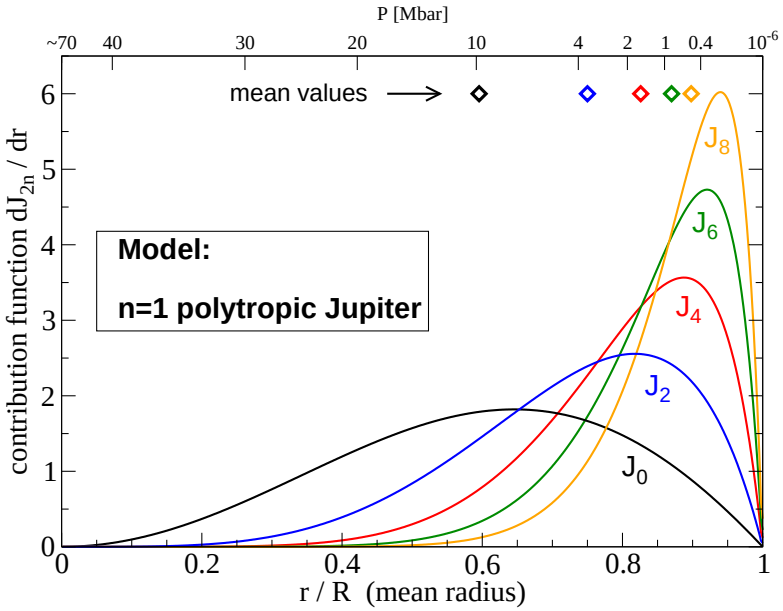

Figure 3.3: Normalized functions $c_{J_{2n}}$ representing the contribution of a level radius to the gravitational moments J_{2n}. Diamonds indicate the radius where half of the final integral value is achieved. The underlying interior model is a polytropic density model of Jupiter also referred to in Tab. A.3. This figure follows the example of [Guillot05], figure 4 therein, and demonstrates the shift of the sensitivity of the gravitational moments with incresasing index toward higher layers. The curve labeled J_0 is simply $(1/M)(dm/dl)$. Pressure values at the alternate x-axis refer to the radius coordinate and are taken from a typical Jupiter model calculated using SCvH-i EOS.

From this figure we learn that Jupiter's moments have a maximal sensitivity with respect to a certain level radius (or mass shell) in the outer 25% of its mean radius. This corresponds to the 1 to 4 Mbar pressure regime. Both the maximal sensitivity and the mean contribution shift with increasing index toward higher levels. Qualitatively, these properties also hold for the other planets. It is due to this shift that we can adjust different moments by the metallicity in different layers. While the sensitivity of J_2 to the central region, e.g. the core mass, is small but non-zero, higher moments only feel the mass distribution in the outer $\sim 50\%$ of Jupiter and are most sensitive around 80-95% of Jupiter's radius. However, this is just the region where the NM-M transition

of hydrogen occurs. It is this coincidence that does offer us the great opportunity to probe H equations of state in the partial ionized plasma regime around the NM-M at $\sim 0.5 - 5$ Mbar. Hence, modelling Jupiter offers an alternative to high-pressure shock-waves experiments.

3.4.4 The force: $-dU/dl$

The force dU/dl could be calculated by numerically differentiating $U(l)$. In order to reduce numerical noise from differentiating higher order terms, I use the analytic zero-order derivative $dV^{(0)}/dl = -GMm(l)/l^2$ and the analytic first-order derivative $dQ^{(1)}/dl = 2/3\omega^2 l$, and add the numerical derivatives of the second- and higher order terms arising from the theory of figures. Those contribute only by $0.1 - 1\%$ to the final forces, as can be seen in Fig. 3.4. The left hand panel shows second and third order contributions to the centrifugal force dQ/dl, the gravitational force dV/dl, and their sum dU/dl; the right hand panel shows the analytic derivatives of zero- and first order. The underlying interior profile from which these forces have been calculated is the three-layer Jupiter model J11a [NettelmannEtAl08]. The core-mantle boundary as well as the inter-envelope boundary are indicated by arrows. At these points, instabilities in the numerical derivatives may occur. The reason for numerical noise in the core region is unclear yet. Due to its relative smallness compared to the zero-order force, it does not affect the final solution. In the outer 50% of Jupiter, the centrifugal force reduces gravitational attraction by $\sim 5\%$. The meaning of the red curve will be explained in § 3.5.

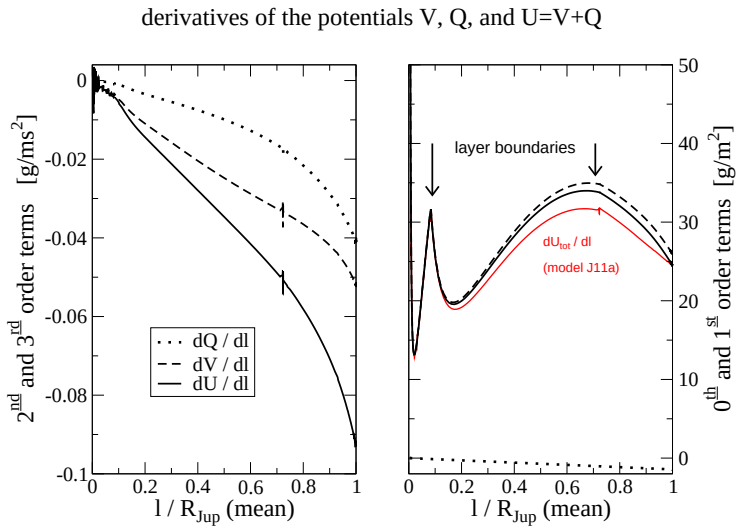

Figure 3.4: Derivatives of the zero- and first order terms (*right panel*) and of the second- and third order terms (*left panel*) of the potentials Q (*dotted*), V (*dashed*), and U (*solid*).

3.5 Accuracy, Bugs, and Procedure

Accuracy

In order to give reliable results for the interior structure models and to study the influence of different EOS data sets, the numerical treatment has to ensure a definite precision. The accuracy

of acceptable interior models should be of the order of or smaller than the relative error of the most accurate observed quantity to be adjusted during the procedure. For M_J, R_{eq}, and J_2 the observational error is below 0.01% and for $\bar{Y}$, $Y_{\rm mol}$, T_1, and J_4 larger than 1%. The uncertainty associated with the FT-DFT-MD data themselves induces an error of the order of 1-5% to the isentropes. Hence we may consider a numerical accuracy of 0.1% as sufficient to study the effect of the uncertainty of the less accurately known observables and for conclusive interior models regarding the EOS applied.

We have tested the accuracy of integrating the differential equations (3.30) and (3.33) for a non-rotating polytrope of index 1. Our numerical results for the profiles $m(r)$ and $P(r)$ obtained via a fourth-order Runge-Kutta method with adaptive stepsize control in regions with steep gradients differ by less than 0.001% from the analytical solution in the outer 80% of the planet. In the inner 20% of the planet including the core region, a shooting splitting method is applied to localize the outer boundary of the core. We then search for a solution starting from the center to meet the envelope solution there with a deviation of less than 0.1%. Since a polytropic model does not have a core, this method cannot be applied there and the difference rises to 50% for the mass and 0.1% for the pressure near the center. This result is shown in Fig. B.1 in the appendix.

To estimate the error resulting from the calculation of the integrals and its enhancement during the iteration procedure, I compared fully converged planetary models. The resulting mass fractions $Z_{\rm mol}$ and $Z_{\rm met}$ and the size of the core differ by less than 2% if the number of intervals dl' in the integrations is doubled. Since density discontinuities at layer boundaries are extended over a small but finite intervall, they do not cause numerical difficulties. Extending this intervall from 0.001 R_J to 0.01 R_J affects the resulting core mass by about 0.1 $M_\oplus$ and the heavy element abundance by about 2%.

I conclude that a convergence of our numerical procedure within 0.1% can be ensured, but the resulting values for the model parameters are uncertain within ± 0.1 $M_\oplus$ or 2%.

Bugs

The numerical inaccuracy mentioned above may result from (in)appropriate choices of numerical methods and/or from bugs in the code. Bugs not causing evident, strange behaviour may persist unrecognized in the code. In order to reveal such kind of bugs it is important to check the solutions against as many as possible analytical solutions and compare with other people's results.

In May 2009, I finally found two bugs, from here on referred to as 'the 2 bugs', that were nothing but a wrong minus sign (bug '-') and a wrong dot (bug '.'). The latter one affected the potential and lead to the *red curve* instead of the *black solid curve* in Fig. 3.4, a relatively large effect; the other bug relates to a shift in the gravitational moments. Hence, I repeated a careful study of the numerical values for the J_{2n} which is given in § E. Many Jupiter and Saturn interior models I recalculated in June 2009. The 2 bugs affected the solutions for Jupiter and Saturn. Fortunately, qualitative conclusions published in papers, talks, and posters remain essentially valid. Unfortunately, some important properties were shielded. Old and new solutions are compared in § 4.1 and in § E. Conclusions presented in this thesis refer to the new solutions.

Procedure: Fitting J_2 and J_4

My code is written in C++ and much less optimized for speed or accuracy than with respect to fast, error-avoiding programming, reusability, easy choice setting and possible functional extension by making use of objective programming and compiler-delivered type controls. Details of code construction or procedures are not presented in this work apart from one particularly important feature: the procedure of fitting J_2 and J_4 as illustrated in Fig. 3.5.

J_2 and J_4 are fitted iteratively by repetitive adjustment of Z_1 and Z_2. Since large increments in Z_1, Z_2, or transiting from a first-guess zero-order solution with small core mass to a third-order

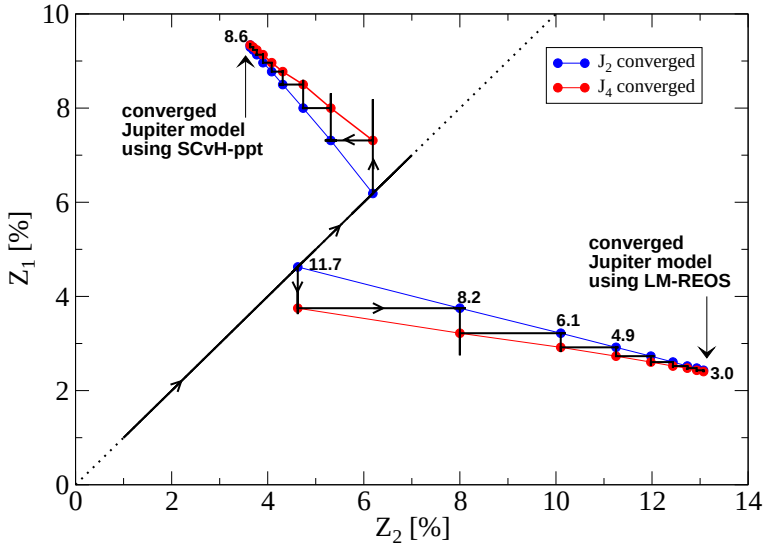

Figure 3.5: Illustration of convergent behaviour of envelope metalicities Z_1 and Z_2 chosen to reproduce J_2 and J_4. Shown are two examples of Jupiter models obtained using SCvH-ppt EOS, typically yielding $Z_1 > Z_2$, and LM-REOS, typically yielding $Z_1 \ll Z_2$. Blue (red) lines connect solutions, where J_2 (J_4) is converged, marked by blue (red) circles; black lines connect all intermediate solutions; the dotted is a guide to the eye for $Z_1 = Z_2$. Numbers close to selected intermediate solutions give the core mass in $M_\oplus$.

solution can cause oscillations of the figure functions before convergence, often leading to pretended no-core solutions, my procedure allows only for small changes in Z_1 and Z_2. The closer the observed J_2 and J_4 values have been approached and in general the smaller M_{core} has become, the smaller the increments in Z_1 and Z_2 allowed for. This procdure requires many iterations. Great advantages to be put against time-requirements are finding of small-core solutions and revelance of dependencies $M_{core}(Z_1, Z_2)$, $J_2(Z_1, Z_2)$, and $J_4(Z_1, Z_2)$. The procedure starts with $Z := Z_1 = Z_2 = 1\%$, then slowly incrementing Z until $J_2 > J_2^{obs}$. $Z(J_2 = J_2^{obs})$ is then found by a bisection method. At this point (the first *blue circle* in Fig. 3.5), J_4 is not met in general. Z_1 is then used to adjust J_4, and the first *red circle* is found, following the arrows in Fig. 3.5, where J_4 at this point is converged but J_2 not anymore. From here on, repeatedly J_2 and J_4 are fitted as illustrated by blue and red circles respectively by proceeding along lines of constant Z_1 and Z_2 values (*black lines*). Numbers at blue circles give core mass in Earth masses $M_\oplus$. When blue and red lines cross each other, a convergent model is found. Depending on the choice of other parameter values, this can happen for $M_{core} > 0$ as shown here for a LM-REOS based and a SCvH-ppt EOS based solution, or not happen due to $M_{core} \to 0$.

In the Rostock statistical and planetary physics group headed by R. Redmer there is now a code available for calculating quasi-adiabatic multi-layer models of giant planet interiors automatically aiming to match available constraints. This code uses given EOS data for various materials and is called NordOst.

We will apply this code in § 4 – 6 to the outer planets. Empirically, modelling giant planets begins to attract people's attention when given constraints cannot be matched. We then have to think about a failure of the EOS, the planetary structure type assumed, or the constraint itself. Several such 'problems' will be addressed in the following chapters.

Chapter 4

Three-layer structure models of the Outer Planets

Jupiter ($M = 317.8\ M_\oplus$) is by far the most massive planet in the solar system. Jupiter's mean density of $1.3\,\mathrm{g/cm^3}$ resembles that of water at normal conditions with some admixture of rocks. However, thermodynamic conditions in Jupiter are very different from those known on Earth and we cannot simply expect to derive a giant planet's composition by analogies to our everyday experience. Thermodynamic conditions in the deep interior of Jupiter and other giant planets are beyond the present scope of laboratory experiments despite great efforts over decades. Hence up to now we must rely on theoretical predictions about thermodynamic properties of matter inside Jupiter and the other outer planets [1] in the solar system: Saturn, Uranus, and Neptune. The same holds for extrasolar giant planets.

Saturn ($M = 95.2\ M_\oplus$) is a planet of extraordinary low mean density (only $0.7\,\mathrm{g/cm^3}$); judged by this quantity, it resembles cometary material such as low pressure ice phases of H_2O and CH_4. Once more, this is a coincidence not necessarily reflecting a planet's real composition.

Uranus ($M = 14.5\ M_\oplus$) and Neptune ($M = 17.1\ M_\oplus$) exist in the cold outer regions of our planetary system. Uranus orbits the Sun in 19.1 AU and receives only 3/1000 times the irradiation that the Earth receives from the Sun; Neptune travels around the Sun in a distance of 30 AU on a very circular orbit and receives 1/1000 times the irradiation of Earth. Beyond Neptuns's orbit, in the *Kuiper belt* between 30 and 500 AU, many more bodies are known with masses up to the mass of Pluto. They are cores of comets with sometimes rather eccentric orbits. Around 80 to 100 AU, the present distance of *Voyager I* and *II*, the solar wind meets the interstellar gas. This is not the end of the solar system if we understand it as all matter which is gravitationally bound to the Sun: in a distance of $40,-100,000$ AU there is a circular agglomeration of several billion comets, the Oort cloud. The existence of giant planets in those far regions of the solar system is not excluded but unprobable. An illustration of the extension and objects in the solar system is shown in Fig. 4.1 [NASA/Caltech]. There the orbit of comet Sedna (*lower right panel*) is nicely put in relation to the extension of the Oort cloud (*lower left panel*), to the orbits of the outer planets (*upper right panel*), and the orbit of Jupiter to the inner solar system (*upper left panel*).

Uranus is just slightly less dense than Jupiter. Since Uranus certainly formed beyond the so-called snowline (the orbit around the proto-sun beyond which temperatures were low enough for oxygen to condense to ice), Uranus is expected to contain a significant fraction of H_2O. With $1.68\,\mathrm{g/cm^3}$, Neptune has the largest mean density of the outer planets and is equally expected to be ice-rich. Hence, Uranus and Neptune are sometimes termed *ice giants*. One of the intentions of

[1] The classification of Jupiter, Saturn, Uranus, and Neptune as *outer planets* was introduced by Humboldt in the 18th century.

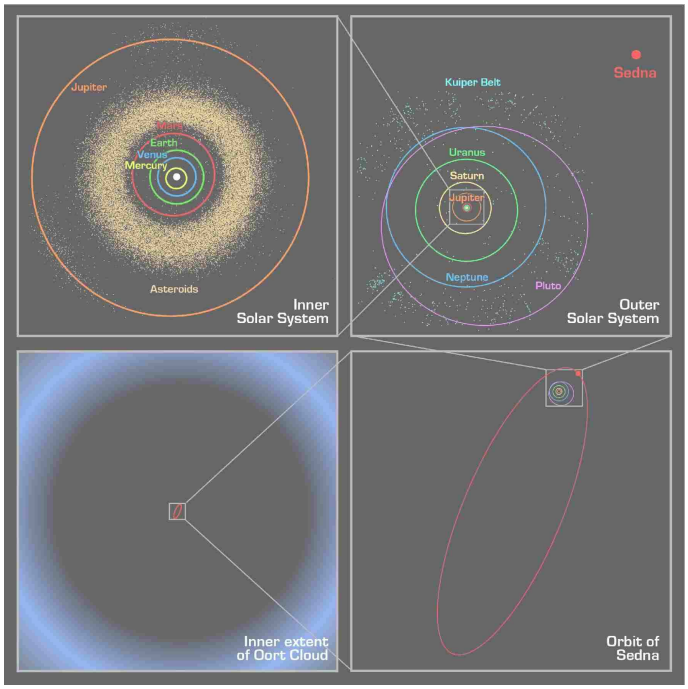

Figure 4.1: Illustration of the solar system, taken from NASA homepage.

§ 4.3 is to show that *ice* is an unprobable constituent of Uranus and Neptune.

We start getting familiar with the outer planets by looking upon their interior profiles.

Interior profiles. In Figures 4.2 and 4.3 two models are presented for each planet, indicated by *dashed* and *solid* lines. All of them are three-layer models with rocky cores. Transition pressure and metallicity of course differ between these models. The position of layer boundaries can most clearly be seen from the density profiles (*lower left panels*). Detailed properties of these models are not of interest at this point. They have been chosen to cover roughly the variety of models that are allowed by the constraints as described in § 3.1. These profiles tell us important general information:

- Pressures in Jupiter are larger than in Saturn by factor of 4 to 10. About 90% of Jupiter's extension is in a high-pressure state beyond the 1 Mbar level, and about 60% has $P > 10$ Mbar with central pressures between 40 and 70 Mbar depending on the size of the core. In Saturn, pressure rises more moderate, and about 60% of its extension is in a high-pressure range between 1 and 10 Mbar.

- The 2000 K level in Tiperju and Tusnar is left behind very far out. Temperatures then rise almost linearly to $\sim 10,000$ K in Saturn and $\sim 20,000$ K in Jupiter.

- The layer boundary between outer and inner envelope occurs deeper inside Saturn, at $\sim 60\%$ of its radius. In Jupiter, locations between 70 and 90% of its radius are possible.

- Uranus and Neptune appear more similar to each other, but especially for Neptune, the spread of possible solutions for a certain EOS is larger than for Jupiter or Saturn.

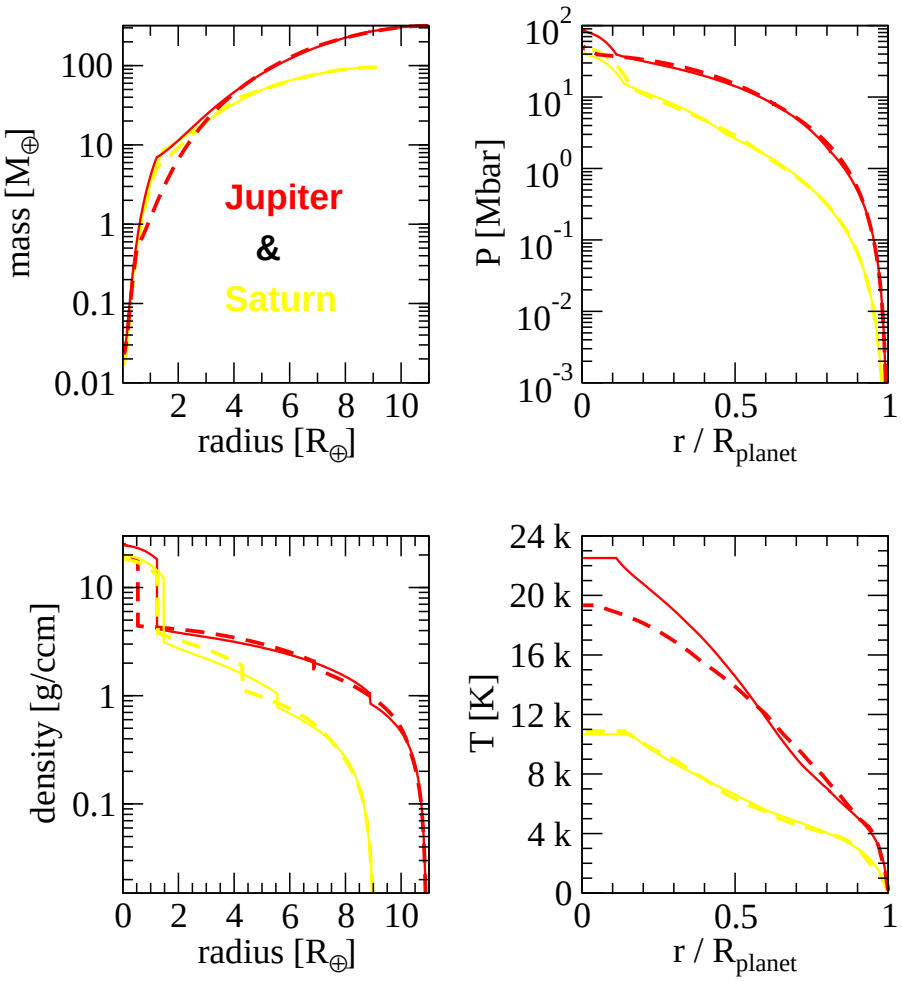

Figure 4.2: Interior profiles of mass, pressure, density, and temperature of Jupiter (red) in comparison with Saturn (yellow). For each planet, two profiles are shown representing the variety of solutions within the 3-layer approach. In detail model J1 (*dashed*) has $P_{1-2} = 8$ Mbar and is based on LM-REOS, model J2 (*solid*) has $P_{1-2} = 1.74$ Mbar and is based on SCvH-ppt EOS, model S1 (*dashed*) has $P_{1-2} = 3$ Mbar and is based on LM-REOS, model S2 (*solid*) has $P_{1-2} = 1.4$ Mbar and is based on SCvH-i EOS. For more properties of these models see Tab. A.5. Layer boundaries are best seen in the density profiles. The line style chosen here for these models has no particular meaning.

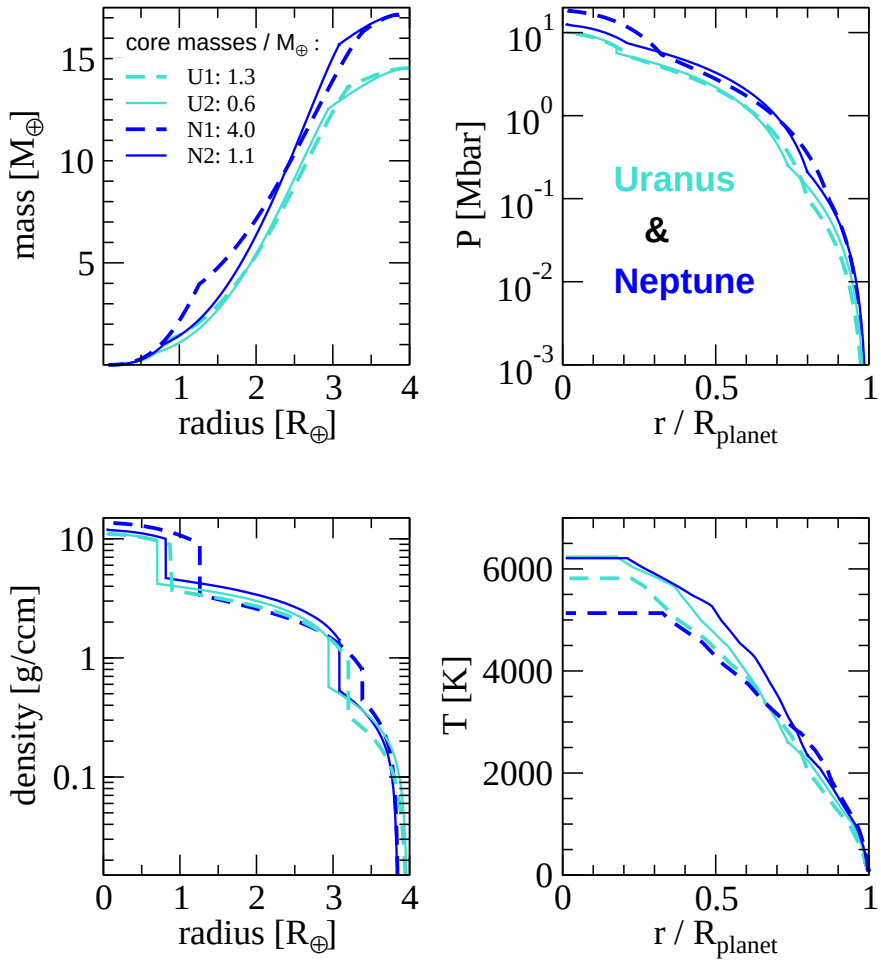

Figure 4.3: Interior profiles of mass, pressure, density, and temperature of Uranus (turquoise) and Neptune (blue) calculated using LM-REOS. For each planet, two profiles are shown representing the variety of solutions within the 3-layer approach with water for envelope metals and rocky cores. Model U1 (*dashed*) has $P_{1-2} = 0.1$ Mbar, $Z_1 = 0.10$, and $Z_2 = 0.88$, model U2 (*solid*) has $P_{1-2} = 0.25$ Mbar, $Z_1 = 0.3$ and $Z_2 = 0.93$, model N1 (*dashed*) has $P_{1-2} = 0.1$ Mbar, $Z_1 = 0.40$, and $Z_2 = 0.79$, model N2 (*solid*) has $P_{1-2} = 0.21$ Mbar, $Z_1 = 0.30$ and $Z_2 = 0.93$. Core masses of these models are given in the upper left panel. The temperature profiles are quite inaccurate due to interpolation on a coarse T-grid of H_2O-REOS.

- Central temperatures are found between 5000 and 6500 K in both Uranus and Neptune. Due to its larger mass, deep envelope pressures are somewhat larger in Neptune. At the core-mantel boundary, pressures are 4.5 to 6 Mbar in Uranus and 5 to 8 Mbar in Neptune.
- For Sanuur and Pentune, the layer boundary is located between 70 and 85% of their extension at a transition pressure of 0.1 to 0.3 Mbar.

Structure parameters. Important interior structure parameters of giant planets are the core mass M_{core}, the envelope mass of metals $M_{Z,\,env}$ or the total mass of metals $M_Z = M_{core} + M_{Z,\,env}$, and the envelope metallicities. These structure parameters are results of computational models. Envelope metallicities can be given in terms of solar units $Z_\odot$ or simply in terms of mass fraction Z with X+Y'+Z=1 for each envelope and

$$X = M_{\rm H}/M\,, \qquad Y' = M_{\rm He}/M = (1-Z)Y\,, \quad Y = M_{\rm He}/(M_{\rm He}+M_{\rm H})$$

$$Z = M_Z/M\,, \qquad \text{and} \qquad M = M_{\rm H} + M_{\rm He} + M_Z\,.$$

In accordance with Guillot (1999) and Guillot et al. (2004), I use $Z_\odot = 1.92\%$ throughout this work. More recently, a lower value $Z_\odot = 1.49\%$ was proposed by Lodders (2003). Abundance determinations of single important species (C,N,O) change with time [ForHubb03] and we have to keep in mind the possibility of a correction towards a smaller solar metallicity.

Before we turn to examine the outer planets in detail, we estimate some of their general properties through simple considerations. Structure parameters predominantly respond to the density profile which in turn is determined by the pressure density relation along the quasi-isentrope. By satisfying the constraints described in § 3.1, we select certain *acceptable* density profiles. The less material of a particular density profile is contributed by the H/He component, the more material has to come from the Z-component. Stiff H/He-EOS will be accompanied by a high total metallicity. How these metals are distributed between outer envelope, inner envelope and core depends on the compressibility of the H/He subsystem along the quasi-isentrope. Because J_2 and J_4 are most sensitive around ≈ 1 Mbar, this is the region which has the largest influence on the distribution of metals. An overall high (small) envelope metallicity is usually accompanied by a small (large) core mass in order to conserve the total planetary mass.

We apply the three-layer structure type assumption to interior models of Jupiter, Saturn, Uranus & Neptune in detail in § 4.1-4.3.

4.1 JUPITER

Peebles (1964) was the first to use a digital computer in order to calculate systematically series of Jupiter models with predictions for the He content and the core mass. Observations of Jupiter's high intrinsic luminosity led Hubbard (1968) conclude a convective interior on large scales with central temperatures above 10,000 K, and consequently the need for accurate H-He equations of state in the warm dense matter regime became evident. Using SCvH EOS, Guillot (1999) introduced what we label in this work the *standard three-layer structure* and presented the full set of interior structure solutions that are consistent with most recent observational constraints.

In this chapter we found on preceding work and study the response of Jupiter's core mass and heavy element abundance on observational error bars and the equation of state assumed. We conclude by evaluating Jupiter models obtained with LM-REOS and DFT-MD (§ 4.1.4, 4.1.5). In order to help the reader to understand results and conclusions presented here, I explain in § 4.1.1 in detail the behaviour of planet interior solutions.

4.1.1 Jupiter models with SCvH EOS and LM-REOS

Results for Jupiter's structure parameters M_{core} and M_Z are shown in Fig. 4.4a (*upper panel*) and the envelope metallicities Z_1 and Z_2 are shown in in Fig. 4.4b (*lower panel*). This figure contains a lot of information and the reader is advised to rely on the following description when staring at the diagrams.

Closed areas give the whole range of solutions found for a given EOS. Equations of state considered here are SCvH-ppt (*green*), SCvH-i (*orange*), and LM-REOS with H_2O-REOS representing metals (*black*) or with He4 for metals (*grey*). The areas obtained for SCvH EOS have been taken from Guillot et al. (2004) and are the same as in [Guillot99]. Tristan Guillot (TG) varied the observables within their 1σ error, varied the ice/rock ratio in the core, and also considered rotation on cylinders by fitting slightly shifted gravitational moments as predicted by Zharkov & Trubitsyn's theory of differential rotation on cylinders, adjusted to observed cloud motions in Jupiter's atmosphere [ZhaTru78].

For verification of my code, I also used SCvH EOS. Models calculated in 2007 are indicated by filled circles. The agreement with TG's sets of solutions appeared sufficient at that time, particularly since TG, as formerly suggested by Chabrier et al. [ChaSauHubbLun92], uses a linear mixture of only H and He and derives the content of metals from the excess fraction of He required to match J_2 and J_4. However, in 2007 I could not obtain solutions with $Z_1 < Z_2$ using SCvH-ppt EOS or with $Z_2 > Z_1$ using SCvH-i EOS, while TG evidently could do. In the latter case, after removing the 2 bugs reported in § 3.5, I finally found such kind of solutions, too (*orange open circles*). Recalculations of models with SCvH-ppt EOS remain to be done. At a first glance, the agreement with respect to M_Z does not really seem better than before. As we have seen in § 2.3, He4 is a relatively compressible EOS for metals, and as we will see below, the response of interior solutions to a compressible Z-EOS is a small metallicity.

Areas in black and grey are the same as published in [NettelmannEtAl08]. Improved solutions by June 2009, i.e. without the 2 bugs, are indicated by open circles. Comparing old and new results with LM-REOS: when using H_2O for metals (LM-REOS-H_2O), M_Z shifts from $\approx 40 M_\oplus$ by $\approx 10 M_\oplus$ to smaller values, and if using He4 for metals, M_Z shifts from $\approx 30 M_\oplus$ by $\approx 8 M_\oplus$ to smaller values. These strong shifts in M_Z are mainly due to shifts in Z_2 by 4−6 percentage points, corresponding to $\sim 0.04 - 0.06 * 200\, M_\oplus = 8 - 12\, M_\oplus$ less mass of envelope metals. These shifts in M_Z are significant when comparing LM-REOS based models with SCvH-i EOS based models.

In [NettelmannEtAl08], the different solutions obtained with different EOS were explained by the different behaviour of the H adiabats as shown in Fig. 2.3. Characteristics found for LM-REOS solutions compared to SCvH-i were a slightly larger core mass for the same transition pressure

because of a smaller compressibility around 10 Mbar, and by 5 to 6 percentage points smaller outer envelope metallicities because of $\sim 30\%$ larger densities around 1 Mbar. This large compressibility of LM-REOS lead to unacceptable large $|J_4|$ values if Z_1 was not kept small enough, i.e. below $\sim 3\%$, and if the low-Z region did not extend relatively deep into the interior, at least up to 4 Mbar. Both these requirements tend to decrease J_2. In order to still match J_2, Z_2 had to be chosen with $7-9.5\,Z_\odot$ quite large for LM-REOS-H_2O (*black box*). Finally, by the huge uncertainty in the EOS of metals, M_Z was considered comparable with that of SCvH-i EOS based models (the *grey* and the *black* box embrace the *orange* box).

Jupiter models based on LM-REOS as published in [NettelmannEtAl08] have $Z_1 \approx 1\,Z_\odot$, and $P_{1-2} \approx 4$ Mbar. While P_{1-2} in these models is a free parameter that will be discussed in § 5 and § 6, Z_1 must be in accordance with measurements, see § 3.1.5. For any acceptable model, we thus require $Z_1 \geq 1 \times Z_\odot$ and prefer models with $Z_1 = 2 - 4 \times Z_\odot$. Because of the large compressibility of H-REOS compared to SCvH-i around 1 Mbar along the Jupiter isentrope, *not* along the Hugoniot (Figs. 2.2,2.3), outer envelope metallicities above $2\,Z_\odot$ could not be obtained. This mismatch we did (and still do) take as a serious hint for the importance of H-He mixing effects. Vorberger et al. (2006) also performed large-scale ab initio EOS calculations via DFT-MD simulation methods for H-He mixtures and found a volume enhancement (density reduction) by about 5% at constant pressure at (P,T) conditions where our H-REOS exhibits the smallest volume (highest compressibility) relative to SCvH-i. For small mass fractions of metals $Z_1 < 2\,Z_\odot \simeq 3.8\%$, a compensation of a 2% density reduction on average of the H-He subsystem in the whole outer envelope would require the mass fraction of metals to rise by that amount giving Z_1 values up to $3\,Z_\odot$ which is just the average of observed particle species.

After the removal of bugs we now have Z_1 as before and both M_{core} and M_Z smaller than in case of SCvH-i. Before we evaluate the new solutions (the grey and black open circles) we investigate the behaviour of the (old) solutions under variations of the parameters indicated by the arrows in Fig. 4.4.

As our reference models we take the solutions obtained for $T_1 = 170$ K, $J_4/10^{-4} = -5.84$[2], $P_{1-2} = 4$ Mbar, and $\bar{Y} = 0.275$. The reference models are indicated by the two black (He4: grey) filled circles in Fig. 4.4. In the molecular outer envelope where the isentrope is more sensitive with respect to temperature than in the degenerate deep envelope, a cooler interior initiated by a smaller T_1 of 165 K enhances the partial density of the H-He mixture and reduces the need for metals by $1\,M_\oplus$, see Fig. 4.4a. Because of $J_4 \sim \int_0^R d^2r\,\rho(r)r^4$ by Eqs. (3.109,3.53), $|J_4|$ increases strongly with Z_1. The other way round: a larger $|J_4|$ to be matched requires a larger Z_1. With Z_1, also J_2 increases and thus the need for metals in the inner envelope in order to match J_2 lessens: Z_2 decreases (Fig. 4.4b). Finally, a smaller envelope metallicity leaves more mass to built up a core. Due to this propagation of effects, M_{core} rises with $|J_4|$, which is clearly seen in Fig. 4.4a. Solutions with $|J_4|/10^{-4}$ below 5.84 using LM-REOS are not considered, since they result in $Z_1 \ll 1 Z_\odot$ or $M_{core} = 0$. Surprisingly, by far not as much attention has been paid in literature to the influence of the transition pressure as it deserves judged by its strong impact on the structure models. For $P_{1-2} < 3$ Mbar, no solution exists with $Z_1 > Z_\odot$. The highest outer envelope enrichment factor of $2\,Z_\odot$ was found for $P_{1-2} = 7$ Mbar, before the core mass became zero. For the new solutions, the behaviour of Z_1 and M_{core} with P_{1-2} and J_4 will be presented in Fig. 4.9 below. Other uncertainties (M, R, ω) are too small to affect the solutions significantly.

We now evaluate the new solutions. When comparing old (with the 2 bugs) and new (without) solutions using SCvH-i EOS we had seen (Tab. A.4) that Z_1 becomes smaller by ~ 2 and Z_2 by ~ 3.5 percentage points. For our reference solutions in Fig. 4.4 we thus expect $Z_1 \simeq 0$. In fact, the

[2]This was the mean observational value [GuiSteHubbSau03] before analysis of Galileo gravity data by Jacobson [Jacobson03] who obtained $J_4/10^{-4} = -5.87$

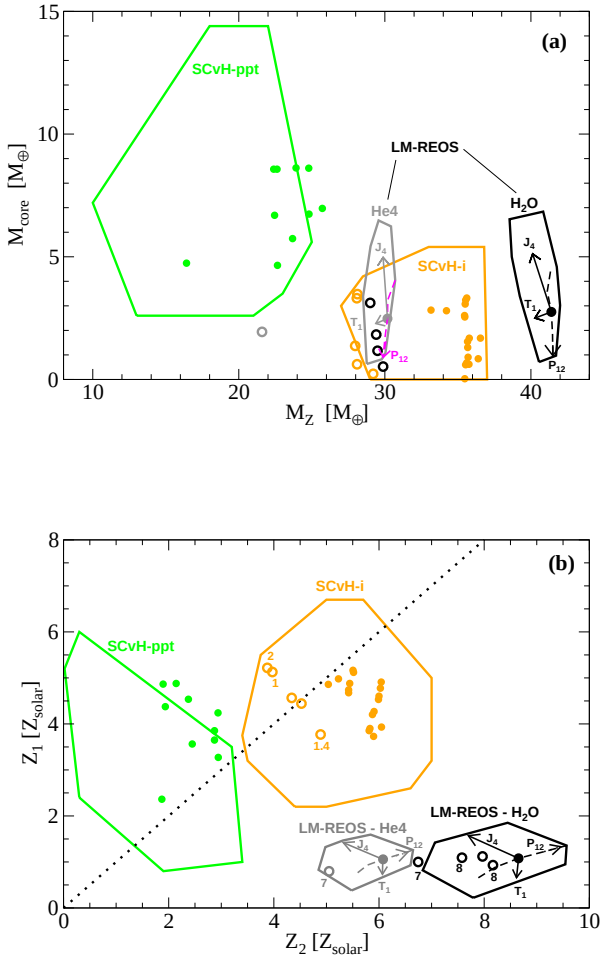

Figure 4.4: Mass of heavy elements and core mass (a), and metallicities (b) in solar units $Z_\odot = 0.0192$ in the outer envlope (Z_1) and in the inner envelope (Z_2) of Jupiter for three different EOS: SCvH-ppt (*green*), SCvH-i (*orange*), and LM-REOS including H_2O-REOS for metals (*black*) or He4 (*grey*). Filled circles are my calculations from 2007, open circles from 2009. The dotted line is a guide to the eye for $Z_1 = Z_2$. Arrows indicate the shifts of a reference solution J11a ($T_1 = 170\,\mathrm{K}$, $P_{1-2} = 4\,\mathrm{Mbar}$, $J_4/10^{-4} = -5.84$), see [NettelmannEtAl08], if T_1 is decreased to 165 K, $|J_4|$ increased by 1σ, or P_{1-2} enhanced from 3 to 5 Mbar. Numbers close to open circles in panel (b) are transition pressures in Mbar.

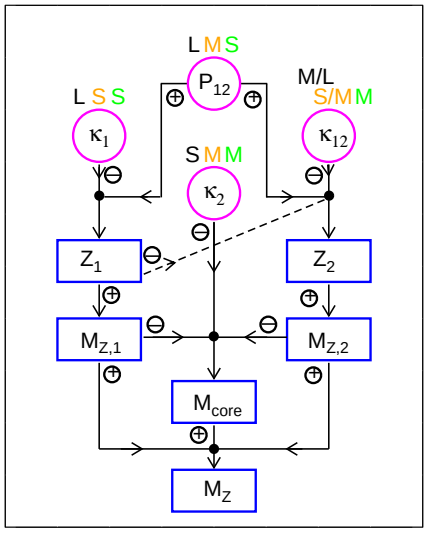

Figure 4.5: Scheme of dependencies of the parameters M_Z, M_{core}, the envelope masses of metals $M_{Z,1}$, $M_{Z,2}$, and envelope metallicities Z_1, Z_2, on the mean envelope compressibilities κ_1, κ_2 and the compressibility κ_{12} around the transition pressure P_{1-2}. Arrows indicate the direction of influence and $\oplus$ and $\ominus$ signs the tendency to increase (decrease) the dependent parameter. Capital L (large), M (medium), and S (small) roughly quantify the compressibility of H-REOS (*black*), SCvH-i (*orange*), and SCvH-ppt (*green*).

numerical routine stops at $Z_1 = 0.001\%$ with $J_4/10^{-4} = -5.85$, not being able to reach the desired value of -5.84. There are two ways to obtain solutions with larger Z_1 values as we have learned from the considerations above: enhancing P_{1-2} and/or requiring larger $|J_4|$ values to be matched, thereby approaching the upper limit of the observational error bar. For $J_4/10^{-4} = -5.84$, I still find $Z_1 < Z_\odot$ at the maximal P_{1-2} before $M_{core} = 0$. Hence, we must consider models with $J_4/10^{-4} < -5.84$. For the new observational mean value $J_4/10^{-4} = -5.87$, P_{1-2} must be as high as 8 Mbar in order to get $Z_1 \geq Z_\odot$. This solution already has M_{core} as low as $0.6\,M_\oplus$ implying that for this J_4 value, $P_{1-2} \approx 8$ gives the only one acceptable Jupiter model. For the upper 1σ limit $|J_4|/10^{-4} = -5.89$, acceptable solutions are found between $P_{1-2} = 7$ (with $M_{core} = 3\,M_\oplus$) and 9 Mbar ($M_{core} = 0$). These acceptable solutions are indicated by open circles in Fig.4.4; numbers in the lower panel are transition pressures in Mbar.

Apparently, the effect of the intermediate compressible region along the Jupiter isentrope (Fig. 2.3) dominates the behaviour of the solutions much more than previously thought. It leads to $P_{1-2} \geq 8$ Mbar, $J_4/10^{-4} \leq -5.87$, and $M_{core} \leq 3\,M_\oplus$ [3]. If by any improvement of the H-EOS or H-He EOS the compressibility rises by a few percent, then these three conditions will not relax, as we will see in 4.1.5.

A reason why M_Z for LM-REOS based models is smaller than for SCvH-i based model, I cannot see: especially since H_2O-REOS is a relatively stiff EOS for metals. Future work should include investigating the isentropes of H-He-metals mixtures of equal abundances, not just the H-isentropes.

So far we have restricted our comparisons of Jupiter models to those based on LM-REOS and SCvH-i EOS. Even though the adiabatic $P - \rho$ relations predicted by SCvH-i allow for a much larger set of acceptable Jupiter models and consequently might approximate the real behaviour

[3] This core mass limit holds for rocky cores. For pure water cores using H_2O-REOS, the core mass increases by $\sim 50\%$.

better than the other EOS, one should not forget about its origin as an interpolation, how ever well it may work. The underlying H-EOS built upon principles of chemical and ionization equilibrium is SCvH-ppt.

We thus must explain SCvH-i and LM-REOS based Jupiter models in comparison with SCvH-ppt based models. Deviations of LM-REOS- and SCvH-ppt isentropes from the SCvH-i reference isentrope (Fig. 2.3) are largest between 0.5 and 2 Mbar: the SCvH-ppt isentrope becomes much stiffer, and the LM-REOS isentrope much more compressible. In this regime Jupiter's J_4 is very sensitive to the density profile and hence SCvH-ppt based Jupiter models tend to large Z_1 values, LM-REOS based models to low Z_1 values. Surprisingly, with SCvH-i, as high Z_1 values as for SCvH-ppt EOS can happen. This occurs, for example, if the transition pressure of SCvH-i based models is chosen larger than the location of the PPT as obtained with SCvH-ppt EOS (always ~ 1.7 Mbar along Jupiter isentropes), then its extraordinary stiff $P-\rho$ relation at super-critical pressures, see Fig. 2.1, also contributes to the outer envelope leading to roughly as high Z_1 values as obtained for SCvH-ppt EOS in Fig. 4.4b.

In fact, as we have seen in case of important examples above, resulting values of M_{core}, M_Z, Z_1, and Z_2 are maps of the compressibility of hydrogen along the quasi-isentrope. To very good approximation, the slope of $d\log P/d\log\rho$ along the isentrope is constant within the molecular region and within the metallic region, see Fig. 2.3. We can thus usefully characterize the compressibility κ along the Jupiter isentrope or pure hydrogen by κ_1, κ_2, and κ_{12}, where κ_1 is some characteristic value at pressures in the outer envelope, κ_2 in the inner envelope, and κ_{12} in the transition region around P_{1-2}. The scheme of dependencies of M_{core}, M_Z, Z_1, Z_2 on the compressibility is illustrated in Fig. 4.5. $M_{Z,1}$, and $M_{Z,2}$ denote the mass of metals in the two envelopes. This scheme is based on my experience and works at least for the equations of state that I applied to Jupiter: FVT-PA, FVT$^+$, Sesame, SCvH-i, SCvH-ppt, and LM-REOS. In this figure, arrows point toward dependent parameters, and signs $\oplus$ ($\ominus$) mean the dependent parameter increases (decreases) with the parameter the arrow starts from. The intensity of a parameter's response can be different between different EOSs.

With the help of Fig. 4.5, we see, for instance, that the influence of the transition pressure on the core mass is ambiguous, it depends on the EOS used. As described above and shown in Fig. 4.4a, in case of LM-REOS we see a clear diminishing of M_{core} with increased P_{1-2}. Figure 4.5 explains this behaviour by an enhanced Z_2, increasing $M_{Z,2}$, decreasing M_{core}. In case of SCvH-i EOS on the other hand, the influence of P_{1-2} on Z_1 is much stronger and the decrement in Z_2 by Z_1 surpasses its direct enhancement by P_{1-2} so that in the end, the decrement in M_{core} by Z_1 is balanced by a decrease in Z_2: with SCvH-i EOS, M_{core} does not significantly change with P_{1-2}. This might be the reason why the influence of P_{1-2} on M_{core} is not studied in literature, since everybody uses SCvH-i EOS. The range in M_{core} obtained with SCvH-i and SCvH-ppt EOS is mainly due to the uncertainty in J_4 [GuiGauHubb97].

Using LM-REOS, a heavy element discontinuity is necessary in order to match both J_2 and J_4. The placement of the layer boundary at high pressures ≥ 7 Mbar is necessary in order to get $Z_1 \geq 1 \times Z_\odot$. Physical reasons for such a layer boundary will be discussed in § 6.3. With SCvH-ppt and SCvH-i EOS, a heavy element discontinuity is not required. However, phase separation into a molecular and a metallic phase due to a PPT of the H component as predicted by SCvH-ppt may initiate a redistribution of minor constituents in order to ensure chemical equilibrium, justifying the more general three-layer structure assumption. The placement of the layer boundary in this case is exactly at the phase transition pressure, i.e. at ~ 1.7 Mbar with SCvH-ppt. Regardless of such a PPT-induced layer boundary, for the same physical reasons that we have to find in case of the layer boundary predicted by LM-REOS based Jupiter models, we could as well assume a layer boundary at higher pressures > 5 Mbar when using SCvH-ppt EOS and calculate four-layer models. In that case, $Z_3 > Z_2$ would not be seen by J_2, but reduce the core mass. Concluding,

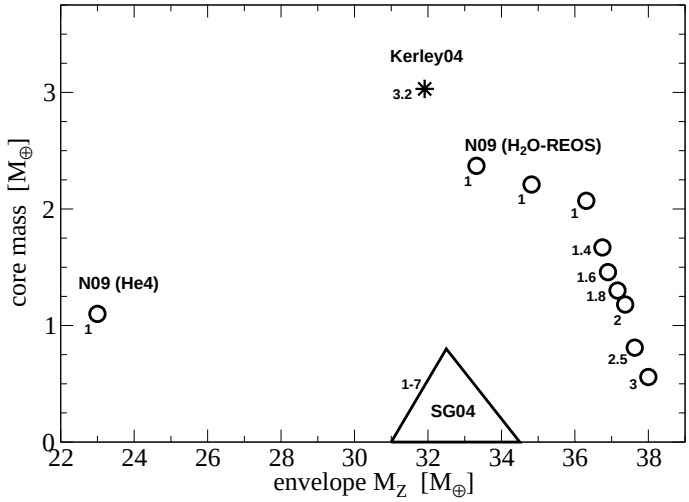

Figure 4.6: Jupiter interior models calculated with Sesame EOS by three different authors and slightly different versions of Sesame EOS. In particular: Kerley (2004) (*star*) using Sesame-K03, Saumon & Guillot (2004) using Sesame-p, and NN (*circles*) using Sesame 5251 for H from the Sesame Database (1992). Numbers are the transition pressure in Mbar for the discontinuity in He (Kerley: also in metals).

no-core solutions are possible due to the uncertainty in J_4 and/or the existence and position of layer boundaries. Hence, Jupiter models are consistent with both core accretion formation and disk instability formation, see § 6.1.

4.1.2 Jupiter models with Sesame EOS

Using Sesame EOS for H and He, solutions are very difficult to obtain. The stiffness of the hydrogen (density scaled deuterium) Sesame EOS at low pressures $\approx$ 10 GPa requires a high envelope metallicity in both envelopes resulting into a small core mass, and its softness at $\approx$ 10 Mbar tends to decrease the core mass even more. Very small increments in metallicity are required for the iteration procedure in order to not confuse an invalid 'no core' solution with an existing solution.

Saumon and Guillot (2004) did not find solutions at all, unless they softened the D-EOS Sesame 5362 at small pressures thereby improving agreement with deuterium Hugoniot data [NellisEtAl83]. Even with this version SESAME-p, they only found a very small set of solutions, all of them with core masses below $1M_\oplus$. Kerley (2003) calculated an impoved D-EOS that gives better agreement with the low pressure Hugoniot data than the original version from 1972. Together with an improved version for He [Kerley04b], he finds a Jupiter core mass as large as $3M_\oplus$. I tried to reproduce the results in [SauGui04] using the original versions Sesame 5251 (H) and Sesame 5761 (He). In the same manner as in [SauGui04], I assumed $Z_1 = Z_2$ and $P_{1-2} \geq 1\,\mathrm{Mbar}$ (He discontinuity). Resulting envelope metallicities are about $20 - 24M_\oplus$ when using He4 for metals, whereas using H_2O-REOS for metals, I obtain $M_{Z,env} \geq 33\,M_\oplus$. Both Kerley (2004a) and Saumon & Guillot (2004) use a mixture of ices and rocks and thus obtain envelope metallicities somewhere between the extreme cases of He4 and pure water, see Fig. 4.6. In this figure, my calculations are denoted by circles, and numbers give the transition pressure in Mbar. Models with $P_{1-2} > 3\,\mathrm{Mbar}$ and thus $M_{core} < 0.5M_\oplus$ I did not yet calculate. But from these considerations alone it is already clear that the Sesame models in [SauGui04] can in principle be reproduced even without modifying the Sesame EOS if an appropriate EOS for metals and a high enough transition pressure is used.

Note that –as for LM-REOS Jupiter models– the shrinking of M_{core} with P_{1-2} can already be read from Fig. 4.5, and only the $\ominus$-sign along the dashed line in Fig. 4.5 can invert this relation.

Compared to LM-REOS, the core mass will approach zero at significantly smaller transition pressures of $\sim$ 3 Mbar. Interestingly, the J_4 values are within the error bars when assuming $Z_1 = Z_2$. Concluding, SESAME EOS 5251 (H) and 5761 (He) predict a homogeneous heavy element distribution with enrichment factor of $5-6$ times solar and small core masses below $3M_\oplus$.

4.1.3 Jupiter models with various EOS: core mass and metallicity

The status of Jupiter models by the year 2003 is documented in [SauGui04]. In the following years, new equations of state have seen the light of day (Sesame-K04, LM-REOS, DFT-MD) and corresponding Jupiter models by Kerley, NN, or Militzer et al. (2008) have enriched the variety of solutions for Jupiter's M_{core}, M_Z, Z_1, and Z_2. Figure 4.7a,b shows the full set of Jupiter models based on diverse EOS of H, He, and metals, that give or are claimed to give acceptable Jupiter models. In this figure I did not include solutions with SCvH-ppt, since Saumon himself did not mention these solutions anymore in publication [SauGui04]. An overview about the EOS used and the authors responsible for the Jupiter model calculations is given in Tab. A.1 in § A.1 in the Appendix. Column 5 describes the structure type assumed. The only two-layer model is that based on DFT-MD by Militzer et al. (2008), all others being three-layer models with a discontinuity in metals ($Z_1 \neq Z_2$) or without ($Z_1 = Z_2$).

Similar to Fig. 4.4a,b, figure 4.7a,b shows the resulting mass of the core and the mass $M_{Z,\,env}$ of metals, but here only in the envelope(s), and the mass fraction of heavy elements between the two envelopes, but here not scaled by the solar abundance. Note that all these solutions have $\bar{Y} = 0.275 \pm 0.01$ except DFT-MD models, which have $\bar{Y} = 0.238$. To better compare these solutions, enhancing $\bar{Y}$ by 3 percentage points to 0.27 in case of DFT-MD solutions requires replacing $\sim 9M_\oplus$ of metals by He. In this case, DFT-MD models have metal-free envelopes. To avoid this problem, Militzer et al. (2008) suggest a He layer above the core due to He sedimentation yielding rocky core masses of 5–9 $M_\oplus$ instead of 14–18 $M_\oplus$ in better agreement with the other solutions.

The other extreme of high envelope metallicity up to $37M_\oplus$ is found using LM-SOCP (and Sesame EOS with water for metals) as was shown in the previous figure. Heavier elements, i.e. magnesium-silicates, would give lower M_Z values, as we have seen in Fig. 4.4a.

If these EOS really reflect our current knowledge, we must conclude that the interior of Jupiter is badly constrained with a possible core mass ranging from 0 to 18 $M_\oplus$ and an envelope metallicity from 0 to 37 $M_\oplus$. Taking these large uncertainties seriously, a prediction about Jupiter's formation process and subsequent evolution is highly unreliable.

However, if we ignore for a while the Jupiter model by DFT-MD EOS, Jupiter's core mass becomes well constrained down to 0–5 $M_\oplus$ with this uncertainty not due to the EOS used, but due to J_4 and P_{1-2}. Jupiter's mean envelope metallicity still remains uncertain by $\sim 25\ M_\oplus$ with a lower boundary of 11 $M_\oplus$ corresponding to $11/(318-2) = 3.5\% \cong 2\times$ solar mean heavy element enrichment in the envelope.

For tentative evaluation of this huge set of Jupiter models, we compare Z_1 in Fig. 4.7b with the atmospheric heavy element mass fraction of 2–4× solar derived from observations as discussed in § 3.1.5. By the theoretical arguments of O being the third abundant element in Jupiter (and in giant planets in general), if the real O/H ratio in Jupiter is less than 2× solar, the lower boundary of the dotted region in Fig. 4.7b would decrease, otherwise if it is larger than 4× solar, the upper boundary would rise. Assuming O/H is 2–4× solar, not all EOS in Fig. 4.7b yield Jupiter models that are consistent with this assumption. Please remember that these EOS are in good overall agreement with experimental Hugoniot data. As we have seen in Fig. 4.5, there are several

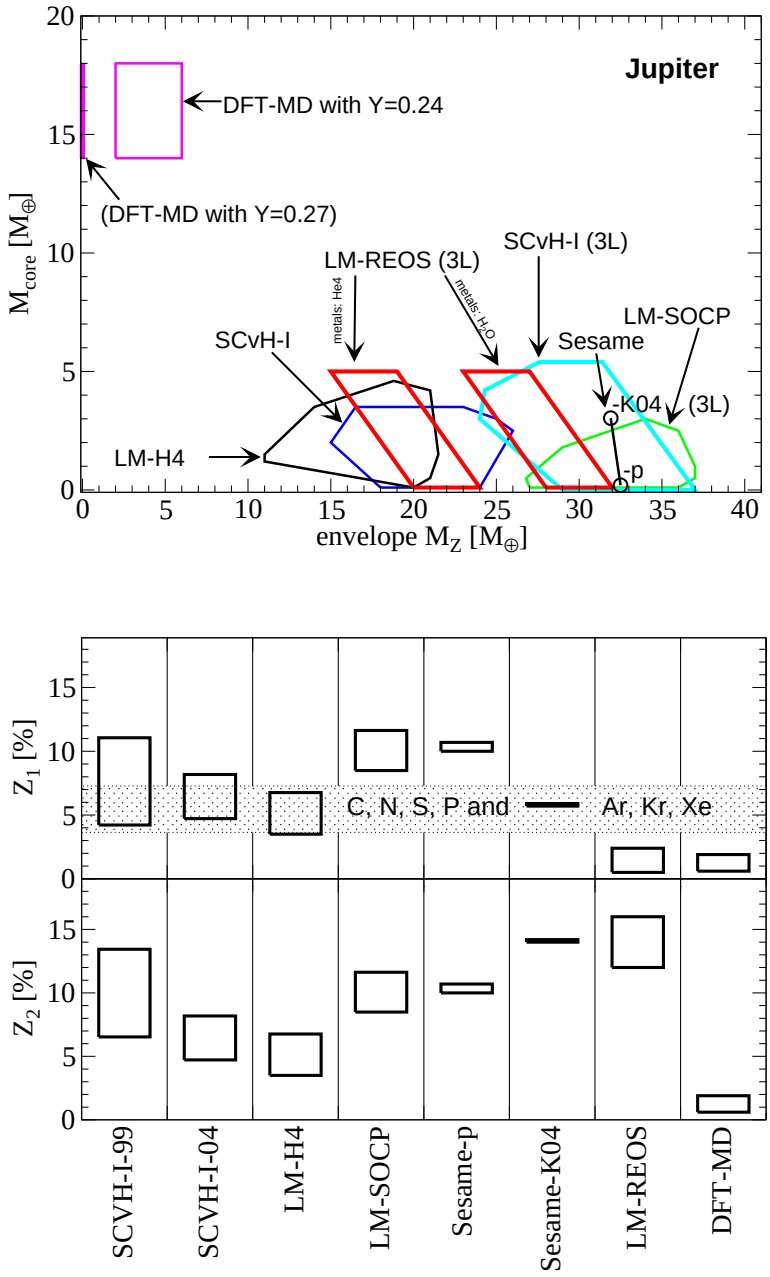

Figure 4.7: Core mass and envelope metallicity in Earth masses *(upper panel)*, and outer (Z_1) and inner (Z_2) envelope metallicity *(lower panel)* for the EOS and authors listed in Tab. A.1. Model series labeled (3L) are standard three-layer models, other series have $Z_1 = Z_2$ by definition. Boxes for LM-REOS do not give the full set of solutions but are estimates based on a few models without the 2 bugs. The dotted region gives measured abundances of single species believed to be representative for the outer envelope heavy element mass fraction.

quantities that affect the resulting heavy element abundance. LM-SCOP and Sesame-p models have no discontinuity in metals (only in He) and thus the influence of P_{1-2} is strongly reduced: allowance for a discontinuity in heavy elements could help to decrease resulting Z_1 values. On the other side, LM-REOS models and DFT-MD models stand out by yielding too low Z_1 values. Judged by the Hugoniot, this behaviour is unexpected since both EOS give relatively stiff Hugoniot curves with a low maximal compression. Experimental data off the Hugoniot are urgently needed. Even more unexpected is the large difference in Jupiter models calculated by myself using LM-REOS and by Hubbard using DFT-MD (Militzer model).

4.1.4 Towards Militzer model

The difference between the Militzer et al. (2008) Jupiter model and my Jupiter models using LM-REOS is unlike differences to models based on other EOS. Since the underlying EOS data for the overwhelming mass fraction of $\sim 95\%$ in both model series are based on similar methods (DFT-MD and FT-DFT-MD, see § 2), one would expect also similar interior models. Their strong disagreement would not have attracted much attention, if not for more than two decades progress in understanding Jupiter was hoped to come from ab initio EOS data (Stevenson, pers. comm. (2008)). Finally, those data have been calculated independently by two groups. But their application to Jupiter by about the same two groups results into a much larger spread of solutions than was considered to be already bracketed by SCvH-ppt and SCvH-i EOS [Guillot99]. This situation is unsatisfying and the reason for the discrepancies in the Jupiter models has to be found. It does attract attention [Stevenson *(pers. comm.)*, Fortney *(pers. comm.)* 2008] and must be clarified in order to gain public confidence and once to relieve SCvH EOS of its priority status regarding giant planet interior models.

Militzer et al. (2008) argue that these differences are due to different structure type assumptions: their two-layer model (IR core + 1 adiabatic envelope) challenges the standard three-layer model (IR core + 2 adiabatic envelopes). In the following I will show that this cannot be the source of disagreement and will suggest other possibilities. Table 4.1 lists the properties of two typical Jupiter models to be compared. The 'J-N09' labeled model is one of my models by June 2009; the 'J-MH08' labeled model is taken from the manuscript version of the Militzer et al. (2008) paper[4]

Table 4.1: Parameters of Jupiter models to be compared

Model	P_{1-2} [Mbar]	J_2 [10^{-2}]	J_4 [10^{-4}]	Y_1 [1]	$\bar{Y}$ [1]	Z_1 [%]	Z_2 [%]	M_{core} [$M_\oplus$]
obs.	–	1.4696(2)	5.87(2)	0.238	0.275 ± 0.01	(1.92/1.49)	–	–
J-N09	7.0	1.4697	5.87	0.238	0.275	1.60	14.11	1.9
J-MH08	–	1.4718	6.20	0.238	0.238	0.67	0.67	16.7

Legend: obs.: observational constraints; J-N09: one of my Jupiter models using LM-REOS; J-MH08: Militzer and Hubbard model (*arXiv-version*).

My procedure to adjust J_2 and J_4 by the choice of Z_1 and Z_2 is described in § 3.5. In Fig. 4.8 we see the application of the procedure to model J-N09 and to another one labeled 'non-convergent due to $Z_1 \ll 1$'. The procedure starts with $Z_1 = Z_2 = 1\%$ and proceeds as indicated by the black arrows in Fig. 4.8. Model J-N09 is obtained by first increasing $Z_1 = Z_2$ until J_2 becomes

[4]It is this model that Militzer proposed at conferences (e.g. in spring 2007 [T. Guillot, *personal communication* (2007)] and at SCCS 2008, Italy) and still on his homepage. The models published in the ApJ letter suddenly do not deviate anymore so strongly from the observational constraints J_2, J_4, and $Z^{(atm)}$.

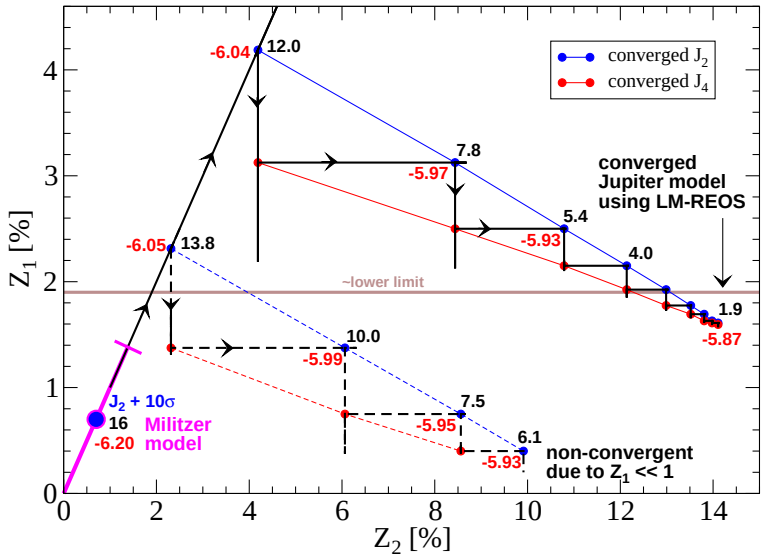

Figure 4.8: Militzer-Hubbard Jupiter model J-MH08 (*blue circle with magenta error bars*) in comparison with my model J-N09 labeled 'converged Jupiter model using LM-REOS' and an intermediate Jupiter model based on an artificial H-EOS labeled 'non-convergent'.
Shown are the model parameters Z_1 and Z_2 (axis), $M_{core}/M_\oplus$ (*black numbers*), and $J_4/10^{-4}$ (*red numbers*) of the final models and of intermediate models occuring during the course of my convergent procedure. The 'lower limit' labeled line is placed at $Z_1 = 1 \times Z_\odot$ with $Z_\odot = 1.92\%$. This figure is (i) to illustrate that the assumption of two envelope layers (we) instead of one (MH08) is the not the main reason for difference between the Militzer-Hubbard Jupiter model and our models, and (ii) to illustrate how Militzer-Hubbard-like models (*black dashed line*) can be approached by modifying the underlying H-EOS.

larger than $J_2^{(obs)}$. This happens at about $Z_1 = Z_2 > 4.2\%$. Then J_2 is adjusted by a simple bisection method, still keeping $Z_1 = Z_2$. This first indermediate model has $M_{core} = 12.0\ M_\oplus$ and $J_4/10^4 = -6.04$. The procedure proceeds by alternatingly fitting J_2 (blue points) and J_4 (red points). At blue points the core mass (black numbers) and $J_4/10^{-4}$ (red numbers) are given. Solutions where J_2 is matched are connected by a blue line, solutions where J_4 is matched are connected by a red line. The intersection point of both lines is the finally converged Jupiter model J-N09. Obviously, as soon as we leave the path $Z_1 = Z_2$ as indicated by the arrows, Z_1 decreases, Z_2 increases and M_{core} decreases. For model J-N09, Z_1 decreases so much that it drops below the line $Z_1 \equiv 1.92\%$ labeled '∼lower limit'. This is necessary in order to bring $J_4/10^{-4}$ down to -5.87.

To illustrate the influence of the compressibility of the H-EOS, I have artificially lowered the pressure of the H-EOS by 2% in the regime $\rho = 0.2 - 4.0\,\mathrm{g/cm^3}$ and $T = 2000 - 8000\,\mathrm{K}$. This acts to rise the compressibility along the adiabat. With $P_{1-2} = 7$ Mbar, the enhanced compressibility region is located in the outer envelope. Using this modified H-EOS, the procedure follows the dashed path in Fig. 4.8. The right-hand turn from the line $Z_1 = Z_2$ already occurs at envelope metallicities of only 2.4%, where M_{core} and J_4 are somewhat larger than for the unmodified H-EOS. In order to reach $J_4/10^{-4} = -5.87$, Z_1 must be lowered as before. However, Z_1 soon becomes very small, and the procedure breaks at $Z_1 = 0.001$, an unreasonable low value. Hence a convergence to both J_2 and J_4 is not possible for this EOS. The reader is invited to explain this behaviour with help of Fig. 4.5. Clearly, if we would enhance the compressibility further in this regime, the right-hand turn would occur at an even lower envelope metallicity.

Intermediate models along the line $Z_1 = Z_2$ can be compared to the 2-layer models, which additionally have $Y_1 = Y_2 = Y^{(obs)} < 0.275$, the desired mean He abundance. Such 2-layer models

thus have lower $Y := Y_2$ values and hence need larger $Z := Z_1 = Z_2$ values in order to match J_2. Furthermore, we see that the core mass decreases with envelope metallicity along the line $Z_1 = Z_2$.

The Militzer & Hubbard Jupiter model J-MH08 is such a 2-layer model. From the considerations above, it is solely explained by an H-EOS of large compressibility in the $\rho - T$ regime as mentioned above. Still at the extremely low turn-off point of $Z = 0.067$, their calcuated J_2 is too high by 10σ (in their ApJ letter, this deviation has reduced to 1σ). They claim that a 2-layer model (core + 1 envelope) is a natural consequence of the absence of a phase transition along the adiabat, and consequently they do not turn right. From Fig. 4.8 it is clear that they cannot turn right even if they wanted to: Z_1 would immediately vanish. So they do not have this degree of freedom that we have to match both J_2 and J_4. Their large core mass of $16M_\oplus$ has to compensate the low-mass envelope in order to meet $M_{\rm Jup}$.

The question I propose is: why have Hubbard and Militzer such a large compressibility along the adiabat at pressures below 7 or less Mbar that they cannot turn-right from the line $Z_1 = Z_2$ and match J_4? Instead they need to find a re-interpretation of the measured gravitational moments by invoking deep-seated differential rotation –much deeper than has been shown by Liu, Goldreich & Stevenson (2007) to be consistent with observed zonal wind velocities. Interestingly, even in their ApJ letter, by managing to re-interpret J_2 and J_4 to be consistent with their Jupiter model, they miss J_6 by 2σ, which was acceptable without their differential rotation hypothesis. Hubbard (1974) himself had investigated the information content of J_4 and J_6 and had found that they essentially contain the same information. The violation of this conclusion by Jupiter model J-MH08 in my opinion points to (i) a bug in *their* code for calculating the gravitational moments or (ii) a strange behaviour of the EOS in the region where J_4 and J_6 have different sensitivity, see Fig. 3.3, or (iii) a strange behaviour of the adiabat resulting from their method of constructing a thermodynamically consistent free energy from their EOS data. Since Militzer and Hubbard do not describe their method to push their EOS data towards thermodynamic consistency, point (iii) remains speculative. Our method of calculating the entropy is simple if judged by the equations to be solved. However, our in this way numerically derived entropy is vulnerable to noisy EOS data, noisy derivatives of the EOS and non-independence on the path along which the integration is performed. Invalid adiabats of both groups calculated from otherwise excellent EOS data is –in my opinion– the most probable explanation for the large disagreement of Jupiter models. Exchanging adiabats and EOS data and calculating Jupiter models with various codes would of course help to rule out bugs.

4.1.5 Towards more acceptable Jupiter models with FT-DFT-MD

Using LM-REOS, we found too small outer envelope metallicities to be consistent with a 2- to 4-fould enhancement over solar value. Hence, in order to achieve acceptable models we aim to get as large an outer envelope metallicity Z_1 as possible. Above we have have seen that Z_1 increases with P_{1-2}, $|J_4|$, and with the stiffness along the adiabat.

Here we examine the response to an artificial shift in pressure of the H-REOS in a certain density-temperature regime, thereby imitating a variable stiffness. EOS data from simulations have statistical uncertainties due to a finite simulation time and systematic uncertainties due to, e.g., finite size effects. All known uncertainties have been carefully checked by my colleagues who performed the simulations and narrowed the uncertainty in pressure to at most 5%. Furthermore, inconsistency of the EOS data due to merging of different grids and due to intensive interpolations between the grid points adds an uncertainty to the pressure-density relations along the isentrope which is much more difficult to quantify, see Appendix. Thus we shift the pressure between $0.2 \leq \rho \leq 4\,{\rm g/cm^3}$ and $2000 \leq T \leq 8000\,{\rm K}$ by up to 4%, calculate the adiabats and Jupiter models as before and observe Z_1 in Fig. 4.9.

Without shifting the pressure ($\Delta P/P = 0$), only a small range of solutions is found (in Fig. 4.9:

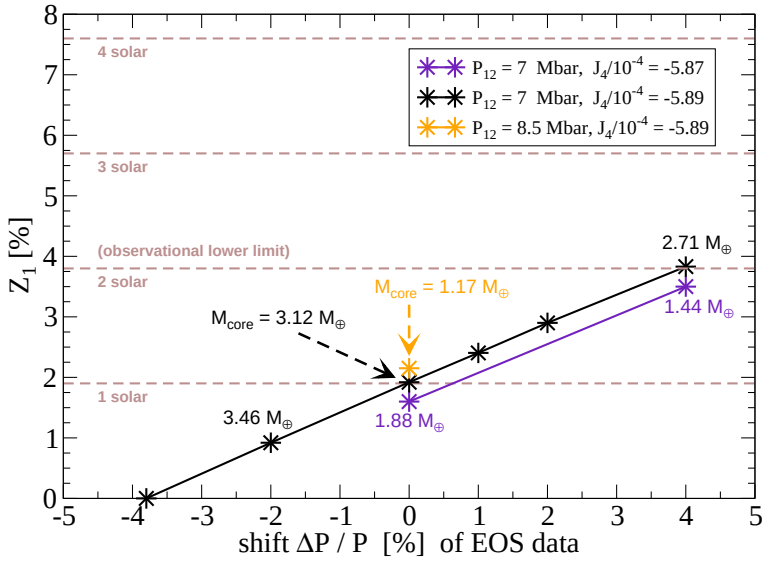

Figure 4.9: Response of Jupiter's outer envelope metallicity Z_1 on a pressure shift $\Delta P/P$ between $0.2 \leq \rho \leq 4\mathrm{g/cm}^3$ and $2000 \leq T \leq 8000\,\mathrm{K}$ in H-REOS. P_{1-2} and J_4 are varied as given in the legend. Numbers close to selected solutions, all of them calculated in June 2009 using LM-REOS, are core mass in $M_\oplus$. *Brown dashed* lines are multiples of solar metallicity $Z_\odot = 1.9\%$.

two solutions), and only with $|J_4|/10^{-4} = -5.89$ at the upper limit of the observational error bar. Increasing P_{1-2} much beyond 8 Mbar is not possible, since the core mass decreases and finally becomes zero. For instance, no solution exists with $P_{1-2} = 10\,\mathrm{Mbar}$ independent on the other parameters. The largest Z_1 obtained without pressure shift (and without the 2 bugs) is 2.3% for $P_{1-2} = 8.5\,\mathrm{Mbar}$. Hence, the only way to achieve higher envelope metallicities is by artificially enhancing the pressure.

The lower observational limit of 2×solar is reached with a pressure shift of 4% in the specified regime. For this solution, we still have to make use of the error bar of J_4 (*black*). Solutions with the recently revised J_4 value of -5.87×10^{-4} (preferred *violet* solutions) still demand metalities below the desired observational lower limit. Evidently, a small shift of a few % in pressure has a huge effect on the quality of the solutions. Enhancing the pressure at given (ρ, T) is equivalent to lowering the density at given P, T. Larger pressures or smaller densities along the Jupiter adiabat can be obtained in two ways. First, the temperature gradient may be superadiabatic instead of adiabatic as was concluded by equation 3.20 derived from mixing-length theory and the observed heat flux; second, the real mass density of the H-He subsystem along the Jupiter adiabat may be smaller than calculated by linear mixing. First results in this direction were presented by Vorberger et al. (2006) within DFT-MD simulations. They find that the volume at constant pressure is enhanced up to 5% at temperatures of several 1000 K and pressures around 1 Mbar where H-REOS exhibits the largest compressibility, i.e. smallest volume compared to SCvH-i, see Fig. 2.3. Taking into account the small fraction of metals, a compensation of a 2% density reduction on average of the H-He subsystem in the outer envelope would require a $0.02 * (1 - Z_1) \simeq 2\%$ density increment in metals, in good agreement with the behaviour seen in Fig. 4.9. Similar non-linear mixing effects were recently observed by Lorenzen (Diploma Thesis and pers. comm.).
We conclude that LM-REOS is not the final answer to the high-pressure behaviour of hydrogen, helium and water. Non-linear mixing effects should be included and the H-EOS be investigated in favour of a smaller compressibility around 1 Mbar. Solutions with $Z_1 \geq 1\%$ are accompanied by

$M_{core} \approx 0 - 3\,M_\oplus$. Jupiter's maximum rock core mass obtained with LM-REOS is $3\,M_\oplus$.

Conclusions

We conclude the Jupiter section with the following comments.

- We have seen how difficult it is to obtain acceptable solutions at all with available EOS. Current EOS working for Jupiter are SCvH-ppt, SCvH-i, LM-SOCP, LM-He4, Sesame, and LM-REOS. Among them, SCvH-ppt and LM-REOS are the ones that make least use of interpolation between different regimes. The authors of SCvH-ppt are careful and unsure about trusting the PPT occurring in their EOS and prefer the interpolated version. Thus LM-REOS is currently the one that remains.
- LM-REOS based solutions are consistent with available constraints apart from the mass fraction of metals in the outer region of Jupiter. We interpret this as an overestimation of the compressibility of H-REOS along the adiabat by $\geq 4\%$.
- A possible reason for an overestimation of the compressibility is the application of linear mixing at pressures where mixing effects might not be negleglible. Another possible reason is superadiabaticity induced by the layer boundary. Allowing for one more layer would further decrease Z_1. Thus we conclude that LM-REOS confirms the standard three-layer model.
- Jupiter's core mass obtained between 1970 and 1999 was observed [ForNett09] to shrink when the EOS data improved. This trend is confirmed with LM-REOS: the maximum core mass has further decreased to $3\,M_\oplus$. We are still learning about the behaviour of H and H-He mixtures at high pressures, in particular the phase diagram. Understanding Jupiter and understanding H and H-He mixtures appears a strongly coupled system with extreme conditions for modelers.
- Progress may come from combining interior structure models and H-He material properties with evolution calculations, with magnetic field models, and by measurements of higher-order gravitational moments, envelope metallicities, and seismically detected layer boundaries.

4.2 SATURN

Of the great benefits for planetary science from the *Cassini* mission to Saturn, the highly accurate determination of J_4 [AndSchu07] can be considered the most important improvement of observational constraints regarding interior models. With only 0.04% uncertainty, Saturn's J_4 error bar has become even smaller than that of Jupiter (0.3%). Saturn's 1-bar temperature error bar is twice that of Jupiter's T_1 with values between 135 [Lindal85] and 145 K [Guillot99]. For all models presented here, we use $T_1 = 135 - 140\,\mathrm{K}$. In § 4.1.1 we investigated the influence of the uncertainty in Jupiter's J_4, T_1, and P_{1-2} on resulting values of Jupiter's M_{core}, M_Z, Z_1, and Z_2. For Jupiter, we had seen a minor effect of T_1 and a major influence of J_4 and P_{1-2}: their choice even decided about the acceptability of the models. For standard three-layer models of Saturn, we will focus on the transition pressure P_{1-2} between outer and inner envelope and investigate its influence on Saturn's M_{core}, Z_1, and Z_2. Most models presented here are calculated using LM-REOS.

4.2.1 Core mass

In Figure 4.10 we investigate the influence of the transition pressure on the core mass of Saturn. The transition pressure has been varied between 50 GPa (models from 2008) or 100 GPa (models from 2009) and the maximum value before the core mass becomes zero. The interior models are

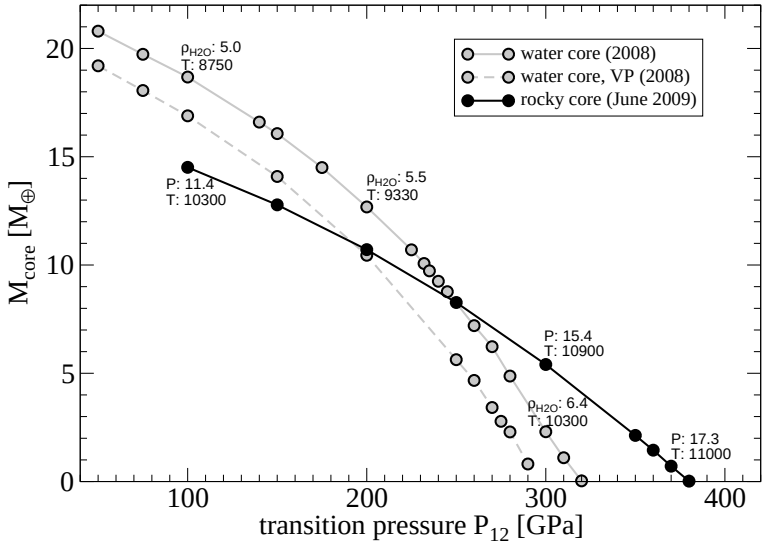

Figure 4.10: Core mass of Saturn interior models as a function of transition pressure. All models are for LM-REOS with water representing envelope metals. *Black solid curve:* models with rocky cores recently recalculated (without the 2 bugs), using recent observational data from the *Cassini* mission; *Grey curves:* models by 2008 (with the 2 bugs) with water cores, *grey solid*: using *Cassini* data, *grey dashed*: using *Voyager/Pioneer* (VP) data. Numbers along the black curve are pressure in Mbar and temperature in K at the core-mantle boundary; numbers along the grey solid curve are density of water core material in g/cm^3 and temperature in K at the core-mantle boundary.

calculated using LM-REOS with water for envelope metals. Models from 2008 have water cores and $T_1 = 135$ K, models from 2009 (after removel of the 2 bugs, see § 3.5), have rocky cores and $T_1 = 140$ K. Under these conditions, the core mass is uncertain within a range of 0 to 20 $M_\oplus$ even for a single EOS applied (LM-REOS). This uncertainty and the upper limit are much larger than for Jupiter, Uranus, or Neptune. The large uncertainty in M_{core} mostly arises from the freedom to place the layer boundary. The upper bound for P_{1-2} is, as figure 4.10 shows, at 3 to 4 Mbar. Hence in order to narrow Saturn's core mass, additional constraints for one (or more) layer boundaries are crucial. Comparing the *solid grey curve* and the *dashed grey curve* we see that improved observational data from Cassini mission regarding the mean values of J_2, J_4, and ω act to shift the core mass of interior models by $2\,M_\oplus$ to higher values. More important in this respect, but not shown here, is the smaller error bar of Cassini data compared to Voyager/Pioneer data, so that the solid curves can be considered robust against this uncertainty.

A larger uncertainty of about 50% arises from the composition of the core material. As already stated in the Jupiter section, assuming cores of water (*grey curves*) yields larger core masses than cores of rocks (*black curve*) for the same transition pressure. The crossing of the black curve (rocky cores) with the grey curves (water cores) is only due to the 2 bugs in the 2008 models. Recalculation of water core Saturn models remains to be done. Due to their larger extension, water cores extend into cooler regions of the deep interior with temperatures of $9, -10,000$ K. For rocky cores, I find a maximal core temperature of $11,000$ K. Since the solutions do weakly respond to the temperature profile in the core, real central temperatures can be larger. The change in pressure and density at the core-mantle boundary also is solely an effect of the extension of the core into the deep envelope.

Any other differences between former calculation from (2008) and recent calculations (2009) is due to the 2 bugs.

Comparison with former results. We briefly compare these results with literature values. Hubbard & Marley (1989) find core masses between 9 and $20M_\oplus$ depending on core material and the envelope $P-\rho$ relation assumed. Guillot (1999), assuming the standard three-layer structure type and using SCvH EOS, finds $M_{core} = 0-22M_\oplus$; Gudkova & Zharkov, assuming a five-layer structure type with a dense He layer surrounding the ice-rock (IR) core and using SCvH-i EOS, find $M_{core} = 3-5.5M_\oplus$ and $M_{core} + M_{\rm He} < 17M_\oplus$; Saumon & Guillot (2004), assuming a three-layer structure without envelope discontinuity in metals and applying various EOS, find $M_{core} = 9-26\,M_\oplus$. Kerley (2004), assuming a standard three-layer structure with $P_{1-2} = 2.27$ Mbar and using Sesame-K04 EOS, finds $M_{core} = 3\,M_\oplus$. We conclude that a central agglomeration of dense material (rocks, ice, He) of the order of $0-25\,M_\oplus$ is a common feature of Saturn models. Within this range, small core masses are only obtained if at least one envelope density discontinuity of metals is allowed for ([Guillot99, GudZha99], this work). Large core masses are obtained for low transition pressures ([GudZha99], this work). Saturn's interior structure is probably much more complicated than suggested by these models calculations. We will address this topic in § 5.

4.2.2 Helium abundance and metalicities predicted by LM-REOS

In Figure 4.11 we investigate the influence of the transition pressure and the atmospheric He abundance Y_1 on the envelope metalicities Z_1 and Z_2. *Dashed* curves are for $Y_1 = 18\%$ corresponding to the lower boundary of the atmospheric He abundance inferred from re-analysis of Voyager infrared spectral data ($21.5 \pm 3.5\%$), and *solid* curves are for $Y_1 = 10\%$. This value is within the error bar of the original value ($6 \pm 5\%$) derived from both Voyager infrared and radio occultation data. It corresponds to the value if the ratio of He/H concentrations of Saturn's and Jupiter's atmosphere originally derived from the Voyager data was correct but taking the more accurate Galileo value for Jupiter, see § 3.1.4.

As explained in § 4.1.1 and illustrated in Fig. 4.5, Z_1 and Z_2 rise with P_{1-2}. In case of a relatively large outer envelope He abundance of 18% however, Z_1 does not rise enough and fails to reach the *lower limit* of 1.9% in Fig. 4.11; it also fails to reach the more recently proposed solar abundance of 1.5% [Lodders03]. With $Y_1 = 10\%$ instead, we obtain ~ 3 fold enhancement in the outer envelope in good agreement with observed particle abundances for C and N.

The first and simplest explanation for this behaviour is a real outer envelope abundance around 10%, but certainly not as large as 18%. If such a large abundance really would proof true, it could still be possible that a larger depletion in He occurs in deeper shells of the outer envelope due to H/He phase separation with ongoing He rain towards deeper shells. This case would allow us to find solutions with Z_1 values between those of the dashed black curve and the solid black curve. The occurrence of H/He phase separation in Saturn will be discussed in § 5.3. Furthermore, as for Jupiter interior models using LM-REOS, we cannot ignore the possibility of a failure of the underlying adiabat. Among the projects planned for the near future, improving the calculation of the entropy and creating smooth, thermodynamically consistent EOS on large scales will be given high priority.

Compared to our Jupiter interior models with LM-REOS all of which had $Z_1 \ll Z_2$, we here also find solutions with $Z_1 = Z_2$, and even with $Z_1 > Z_2$, when setting $Y_1 < 0.18$ and P_{1-2} small enough. In particular for our preferred series with $Y_1 = 0.10$, the heavy element discontinuity inverts at about $P_{1-2} = 180$ GPa, with important implications for the formation process and subsequent evolution. For instance, $Z_1 > Z_2$ indicates late planetesimal capture. Clearly, the determination of P_{1-2} and Y_1 by other methods is of great importance.

Despite the large sensitivity of M_{core} and Z_2 (*red curves* in Fig. 4.11) to P_{1-2}, the total metallicity using LM-REOS with water for envelope metals and rocky cores varies only within

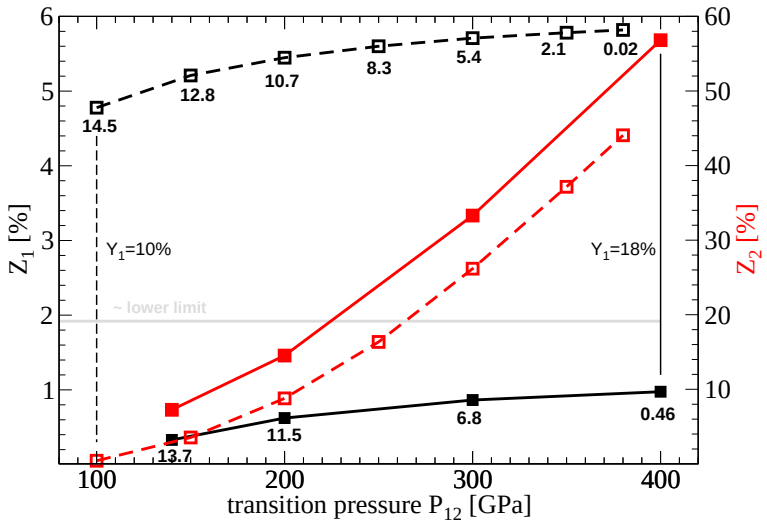

Figure 4.11: Outer envlope metallicity Z_1 (*black*) and inner envelope metallicity Z_2 (*red*) as a function of transition pressure. *Solid lines* are for models with outer envelope He mass fraction $Y_1 = 0.18$ and *dashed lines* for $Y_1 = 0.10$. Squares are calculated models by June (2009) using LM-REOS with water for metals and a rocky core; numbers give the core mass in $M_\oplus$.

16% and 19% ($15M_\oplus$ and $18M_\oplus$). Using other EOS and *Voyager/Pioneer* gravity data[Guillot99, GudZha99, SauGui04, Kerley04a], the range of total metallicities increases to 15%-30% and is, beyond all interior model and EOS uncertainties, larger than for Jupiter ($4 - 11\%$).

Sensitivity of the gravitational moments While the uncertainties regarding Saturn's core mass and envelope metalicities are larger than in case of Jupiter, they are much less sensitive on the H-EOS used [Guillot99, SauGui04]. Instead, they are more sensitive to uncertainties in the pre-*Cassini* J_4 value (former calculations), to the structure type assumption $Z_1 = Z_2$ or not, to P_{1-2} ([SauGui04], this work) and to Y_1 [Guillot99], and to the composition of metals [this work]. In order to understand why Saturn models respond less to the H-EOS than Jupiter models do I calculated the contribution function dJ_n/dr as in Fig. 3.3, but for a typical Saturn model based on LM-REOS, with a core of $8.5\,M_\oplus$. We see the result in Fig. 4.12. Astonishingly, despite very different model assumptions (Jupiter model: $n = 1$ polytrope, Saturn model: centrally condensed 3-layer model), the sensitivity of the gravitational moments changes weakly with radius level. Mapped onto pressure level, however as shown by the *alternate x-axis* in Fig. 4.12, the maximum and the mean sensitivity occurs at lower pressures in Saturn of at most 0.5 Mbar. Below this pressure level, the H-EOS is well-probed by gas-gun shock-compression data and consequently competing theories better agree with each other.

Conclusions

We have seen a great influence of transition pressure and outer envelope He abundance on the interior structure of Saturn. While Y_1 even decides about the acceptability of models, P_{1-2} strongly influences the core mass, the behaviour $Z_1 >$ or $< Z_2$, and Z_2. We found acceptable solutions for $1 < P_{1-2} < 4$ Mbar with rocky core masses between 14 and 0 $M_\oplus$. The uncertainty in the H-EOS and the adiabat is unsatisfying, but affects Saturn models much less than Jupiter models. This is because of the sensitivity of Saturn's gravitational moments at pressure levels where the H-EOS is relatively well-known. Even if remaining H-EOS related uncertainties can be reduced in the future,

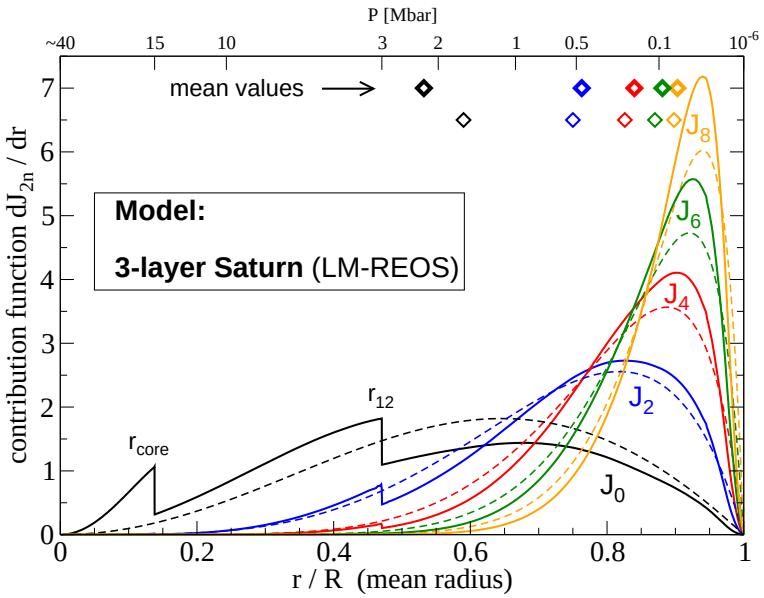

Figure 4.12: Same as Fig. 3.3 but for Saturn and an underlying density profile based on the a standard three-layer model using LM-REOS. The radial position of the core and of the layer boundary are clearly seen. *Dashed lines* and *thin lower row diamonds* are for Jupiter and are the same as in Fig. 3.3.

the uncertainty in Y_1 and P_{1-2} prevents reasonable conclusions about Saturn in comparison with Jupiter, apart from the property of larger average metallicity in Saturn. Constraints on Y_1 and P_{1-2} are urgently required. The measured depletion in He indicates active H/He phase separation and sedimentation in Saturn and the presence of a layer boundary. Hence we can expect advances in our understanding of Saturn to come from evolution calculations on the basis of an appropriate H/He phase diagram. This will be further discussed in § 5.3.

4.3 URANUS and NEPTUNE

In view of the large $M - R$ plane giant planets are found to span, Uranus and Neptune are quite similar planets. They are only about 25% larger than (theoretical) pure icy planets in the mass range $10 - 20 M_\oplus$. Water, together with methane, is thus expected to constitute a large fraction of their mass. Due to the ambiguity of the EOS of water and a mixture of lighter elements, say H-He, and heavier elements, say rocks, their true composition is still unknown. This problem is well known and of course also applies to other Neptune-sized planets [AdaSeaElk08, NettKraRedNeu09] and even to Super-Earths [ValSassConn07]. Hence, further constraints on the composition are crucial. It is thought, for instance, that the protosolar ice-to-rock (I/R) ratio is realized in these planets or at least gives an upper bound [HubbPodSte95] to the ice content. Endmember cases, such as a solar or sub-solar I/R ratio together with some H/He either uniformly mixed (first case) or confined to three shells of rocks, ices, and H/He respectively (second case), can already be excluded by the gravity field data. The first case model would have a too large moment of inertia and the latter model would be too centrally condensed. Apart from those extreme solutions, a vast range of models is still possible by the gravity field data due to the relatively large error bar of J_4. Podolak, Podolak, and Marley (2000) encounter this problem by generating random density distributions that fit the observational constraints. They further suggest to select those where the density profile is consistent with EOS data for a reasonable mixture of H-He, ice, and rocks. In lack of accurate

EOS data for ices and high-pressure rocks, this task remains to be done.

Compared to uncritical H-He EOS data in the outer part of the planets, the density distributions by Podolak, Podolak & Marley (2000) point to a strong enrichment of heavier elements in the outer region. Since the heavy element abundance is not expected to decrease with depth, an even stronger enrichment in the deep interior seems unavoidable. Other previous work,e.g., [HubbPodSte95, PodRey81] support this conclusion, as did chemical composition measurements. In both planets, the atmospheric CH_4/H ratio is as high as $\sim 25\times$ solar. On the other hand, O was not detected and N/H is strongly underabundant. However, the measured abundances are not considered representative for a significant mass fraction of Uranus and Neptune: O/H and N/H are strongly affected by cloud formation at deeper levels, and the more volatile CH_4 molecules are supposed to have been outgassed from a deeper seated huge ice shell. If the measured CH_4 abundance was representative also for other ices as well as for a large, convective region, it would imply a mass fraction of metals of 45%. Concluding, the outer envelope composition of Uranus and Neptune is unknown, but model calculations and measurements point to a strong enrichment with ices.

As for Jupiter and Saturn, all –to my knowledge– interior models of Uranus and Neptune assume adiabatic, homogeneous envelopes. This is certainly a reasonable first starting point of interior models, in particular since suggested formation scenarios for Uranus and Neptune [LissauerEtAl95] predict a hot start driving large scale convection. However, the radiation transport efficiency of a mixture of ices, rocks, and H-He is poorly known, and thus superadiabaticity cannot be excluded. An adiabatic temperature profile at high altitudes [Lindal92] was derived from *Voyager* occultation data. Interestingly, even for a moderate (i.e. adiabatic) rise in temperature, H_2O leaves the ice I phase after only 0.03%, and the liquid water phase after 0.2% of Neptune's total mass. H_2O then becomes an ionic fluid [Stevenson82], never crossing the boundary to an ice phase again [FrenchEtAl09]. If H_2O does not prefer an ice phase, the less we expect more volatile molecules CH_4 and NH_3 to do. The possibility of a thin, conducting layer in Uranus and Neptune is predicted [StaBlo06] in order to explain their magnetic fields. Those are so strong that they indicate an active dynamo process in the interior. Of course, in case of a strong superadiabaticity as suggested by Hubbard, Podolak, and Stevenson (1995), the occurrence of high-pressure ice phases becomes even less probable. Nevertheless, Uranus and Neptune are called *ice giants*, regardless of the thermodynamic phase the constituents adopt.

In this work, interior models of Uranus and Neptune rely on exactly the same structure assumptions as the models for Jupiter and Saturn from the previous section: three layers (rocky core + two homogeneous, adiabatic envelopes) composed of H, He, and metals. Models presented here are based on LM-REOS using water for metals. I do not present earlier models based on Sesame EOS, since resulting interior models turned out similar in core mass and metallicity despite large deviations in the water EOSs [FrenchEtAl09]. Figure 4.13 shows the set of solutions found with respect to the envelope metallicities Z_1 and Z_2 and the transition pressure P_{1-2}. For a given transition pressure, the solutions move in $Z_1 - Z_2$ space along almost straight lines, and changing P_{1-2} causes a parallel shift of the line. Decreasing Z_1 requires a higher inner envelope metallicity in order to match J_2. Simultaneously, the mass of the core shrinks, with $M_{core} = 0$ defining the largest possible Z_2 value for a given layer boundary. Obviously, pure water envelopes are not allowed.

Replacing a remaining H-He mass fraction of 5% (10%, 12%) by the molecular weight of CH_4 and conserving the mean molecular weight results into a H_2O/CH_4 mass ratio of 0.6 (0.2, 0), but those models with an inner envelope of pure 'icy' composition of 100% CH_4-H_2O have not been calculated here. H_2O/CH_4 mass ratios below 0.5 are unprobable anyway, since the cosmological O/C particle ratio is about 2. On the other hand, replacing some H_2O by rocks will result into a higher H/He fraction, and in the more realistic case of a solar ice/rock ratio of ~ 2.7, H-He free

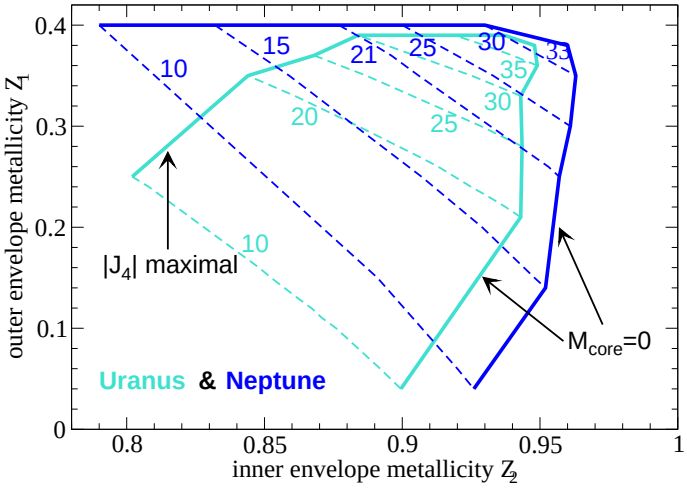

Figure 4.13: Mass fraction of metals in the outer envelope (Z_1) and in the inner envelope (Z_2) of three-layer models of Uranus (*turquoise*) and Neptune (*blue*). The thick *solid lines* indicate the range within solutions have been found. *Numbers* at dashed lines give the transition pressure P_{1-2} in GPa, and *dashed lines* show the behaviour of solutions if P_{1-2} is kept constant and J_4 is varies within the 1σ-error. Increasing Z_1 increases $|J_4|$. No Uranus solutions are found above the upper thick line. Neptune's J_4-error bar is large, so we stopped arbitrarily at $Z_1 = 40\%$. Decreasing Z_1 results into higher Z_2 values and smaller core masses. Below the lower thick lines, no solutions exists. These models are based on LM-REOS using water for metals.

deep envelopes can be excluded. Hence, we conclude the presence of a significant amount of H-He in the deep interior of Uranus and Neptune. These results are in good agreement with those by Hubbard & Marley (1989).

Most Uranus and Neptune models presented here have a significant heavy element (water) enrichment also in the outer envelope. An upper limit of Uranus' Z_1 is given by the requirement to meet J_4; for Neptune, the large error bar of J_4 allows for even higher outer envelope metallicities than 40%. All models have a pronounced heavy element discontinuity. No Uranus (Neptune) models are found with $P_{1-2} > 38$ (33) GPa because of $M_{core} \to 0$. I did not calculate models with $P_{1-2} < 10$ GPa, since this discontinuity in metals is most likely caused by the transition from molecular water to ionic dissociated water, which occurs around 20 GPa [Stevenson82, FrenchEtAl09].

While the calculated envelope metallicities Z_1 and Z_2 qualitatively indicate a strong heavy element enrichement, the real water content unfortunately remains undetermined by the gravity data due to the ambiguity of the EOS of water and a mixture EOS of H-He plus rocks. We can estimate it using three assumptions:

1. the protosolar I/R ratio of about 2.5 to 3 is realized in these planets. It gives an upper boundary for the real I/R content since volatiles can be lost easier;

2. the Z-material component of models obtained using the water EOS for metals reflects the true Z-material component for a mixture of ices and rocks (silicates + iron). This is an overestimation because any replacement of water by rocks would reduce Z in order to conserve the mass density, and correspondingly the H-He fraction would rise. We assume $Z_1 = 20\%$ and $Z_2 = 85\%$.

3. the mass fraction of ice contains 50% water and 50% methane. This probably underestimates the water content in light of a cosmological O/C ratio ≈ 2.

With these assumptions, we obtain $Z_1^{\mathrm{H_2O}} \approx (1/2)\times(3/4)\times 0.2 = 0.075$ and $Z_2^{\mathrm{H_2O}} \approx (1/2)\times(3/4)\times 0.85 = 0.32$. Properties of high-pressure water (EOS, phase diagram, conductivity) probably play an important role for interior models of Neptune-like planets.

4.3.1 Similar or dissimilar planets Uranus and Neptune

At a first glance on figures 4.3 and 4.13, Uranus and Neptune seem to be very similar planets with respect to their core mass, temperature profile and total heavy element enrichments. Such similarities were also found in [HubbPodSte95]. However, with respect to their internal heat flux, Uranus and Neptune are very different planets, and this difference has been argued [HubbPodSte95] to possibly arise from a combination of a warmer interior of Uranus compared to that of Neptune, and a larger mass fraction beneath the layer boundary around 20 GPa in Uranus, altogether building up a larger internal heat reservoir in Uranus. This topic will be further addressed in § 5.3.4; here we will see, in which way different temperature profiles can be obtained within the standard assumption of quasi-adiabatic, homogeneous envelope layers (and if this way is consistent with a larger heat reservoir in Uranus).

A closer look on figures 4.3 and 4.13 shows that the range of possible solutions for each planet is quite large. It is however not clear in advance whether the temperature rises more in the metal-poor case or in the metal-rich case. Therefore, I calculated Neptune isentropes for different mass fractions of water, with the result that the temperature rises more in the metal-poor case, and a maximal difference of 1000 K occurs around 0.2 Mbar. This result is visualized in Fig. B.3 in the appendix.

Thus, in order to get larger internal temperatures in Uranus, we would need a small Z_1 value and a large extension of the small-Z region, i.e. large transition pressures. From Fig. 4.13 we know, the smallest Z_1 values allowed increase with P_{1-2}, and so does Z_2 (which we also wish to keep small). Thus there is an optimal combination of these parameters, namely $Z_1 = 0.23$, $Z_2 = 0.93$, $P_{1-2} \approx 20$ GPa yielding an Uranus model (U3) with $T_{core} = 6300$ K and $M_{core} = 0.4\ M_\oplus$. A corresponding optimization for Neptune gives $Z_1 = 0.40$, $Z_2 = 0.83$, $P_{1-2} \approx 15$ GPa with $T_{core} = 5500$K and $M_{core} = 3.3 M_\oplus$ (N3). Significantly warmer interior models for Uranus or colder interior models for Neptune are not possible with the standard 3-layer approach. Exchanging the water EOS by a more realistic mixture of ices and rocks will slighty shift both models in the same direction, probably not enhancing their difference in T_{core} of ~ 1000 K.

The relatively warm Uranus model U3 has $m_{12}(P_{1-2})/M_{\mathrm{U}} = 0.89$, the relatively cold Neptune model N3 has $m_{12}(P_{1-2})/M_{\mathrm{N}} = 0.93$ slightly counteracting the hypothesis of a larger heat reservoir in Uranus. Which of these models really does contain the larger amount of heat also depends on the heat capacity c_v of the deep envelope material of the planets and cannot be decided at this point. We conclude instead, that we cannot decide about the warmer or more metal-rich planet and whether they have the same transition pressure/a similar transition region or not. In the frame of adiabatic envelopes, their largest possible difference in central temperature is 1000 K, and in core mass it is $4\ M_\oplus$.

We remember that we have been looking for a warmer interior solution for Uranus, because a larger heat reservoir is one of the few possibilities proposed to explain their different observed heat flux. If differences of models like U3 and N3 will turn out insufficient to explain the heat flux, this would point to an inappropriate underlaying assumption about the structure type, for instance the assumption of adiabatic interiors. This will be discussed in § 5.3.4.

4.3.2 Phases of water in Uranus and Neptune

Poor knowledge of the EOS of ices is one of the main drawbacks of our limited insight into Neptune-mass giant planets [BarChaBar08]. In this sense, the calculation of accurate water EOS data and

the water phase diagram is an important first step forward. Those calculations have recently been performed [MattDes06, FrenchEtAl09].

As mentioned at the beginning of § 4.3, according to the range of pressures and possible temperatures along interior profiles of Uranus and Neptune, water can potentially adopt several different thermodynamic phases. If these phases can indeed be realized in the presence of H-He, other ices and rocks is unclear. Ab initio simulations with several hundreds or thousends of particles per box potentially could help to decide about the phases realized, including demixing of components, in such a multi-component system. Computer power within the next years may improve enough to encouter these questions. Until now, the behaviour of water in a multicomponent system of H, He, CH_4, NH_3, and rocks is highly uncertain. Nevertheless, as starting point we can concentrate on the phases of (isolated) water. In the most favorable cases of (i) differentiation of species into separate layers (e.g. rocks forming a central core, CH_4 forming a diamond layer and metallic hydrogen miscible with water), or (ii) just a contamination of water phases and not an inhibition by minor constituents, this starting point is reasonable.

Figure 4.14 (*right panel*) shows the water phase diagram for pressures above 1 GPa obtained with FT-DFT-MD. The fill color of circles indicates the phase. The character of a phase transition is hard to determine by simulations with finite number of particles in a box. Signs are found suggesting first-order transitions towards ice phases and towards the superionic phase[5], other transitions being continuous. At pressures > 30 GPa, different experimental and theoretical investigations predict different phase boundaries between molecular water and ice VII, ice VII and ice X, ice VII and superionic water, and ice X and superionic water.

The violet line shows $\rho_{H_2O}(T, P)$ along a typical Neptune isentrope in (T, P) space, where the water mass fraction of the underlying Neptune model is chosen to give an acceptable interior model among the ones presented in Fig. 4.13. Uranus isentropes are very similar, they just end at smaller densities. Of great interest for us is the large extension of the superionic phase with respect to temperature and density. In order to not overlap with this phase, a typical Neptune (or Uranus) isentrope must be colder or warmer by several 1000 K. Such a shift of the Neptune-isentrope in temperature is beyond the range of uncertainty found in § 4.3.1, and beyond the uncertainties of phase boundaries predicted by different authors. Hence we conclude that the occurrence of high-pressure ice phases is very unlikely in Uranus and Neptune. For ice phases to occur, the planet must have had a cold start after formation, see also § 5.3.4. The occurrence of water plasma as in Jupiter and maybe in Saturn's deep interior is unlikely too, unless the temperature gradient is strongly super-adiabatic, see § 5.3.4.

Figure 4.14 (*left panel*) shows typical temperature profiles of Uranus and Neptune with respect to mass coordinate. Colors along the profiles indicate the phase of water, and numbers the electrical conductivity. The conductivity contains contributions by electrons, protons, and ions as far as these species occur at all. In the lower-density region of the superionic phase, protonic conductivity dominates over electric conductivity [FrenchEtAl09]. An ionic water fluid has been suggested to cause the magnetic fields of Uranus and Neptune [Stevenson82, StaBlo06]. Here we see that the conductivity in the superionic phase (indeed: the *protonic* conductivity at these planetary temperatures and pressures) surpasses that of the ionic phase, which also covers less planetary mass. We have to keep in mind that these findings may not reflect the real states of matter in the planets, but they are an unpreceded starting point to derive new implications thereof (dynamo generation, cooling behaviour) that can be checked against observation (magnetic field, heat flux).

[5]The superionic phase characterizes a bcc oxygen lattice and mobile protons. At Neptune interior conditions, the proton conductivity surpasses that of the electrons.

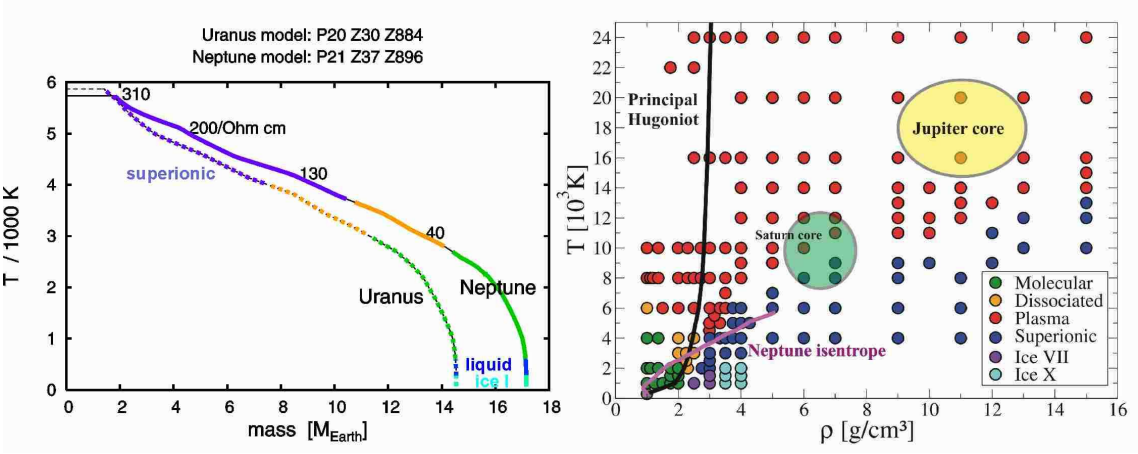

Figure 4.14:

Right panel: Phase diagram of water at high pressures > 1 GPa, $T \geq 1000$ K, and $\rho \geq 1$ g/ccm including a 300 K point at 1g/ccm. Filled circles are FT-DFT-MD calculations by French. The fill color encodes the thermodynamic phase of water. Part of this phase diagram is published in [FrenchEtAl09]. Ovals show Jupiter and Saturn core conditions as found by interior models both if pure water cores are assumed or an ice layer around a central rocky part. The violet line shows $\rho_{\mathrm{H_2O}}(T, P)$ along a typical Neptune isentrope in (T, P) space, where the water fraction of the underlying Neptune model is chosen to give an acceptable interior model among the ones presented in Fig. 4.13.

Left panel: Profiles $T(m)$ of Uranus and Neptune interior models that are quite similar with respect to transition pressure and metallicities. Colors along the profiles indicate the phase of water according to the phase diagram on the right hand side. Numbers along the profile are electrical conductivity in $1/(\Omega$ cm) calculated by Martin French in February 2009. Evidently, water ice I occurs in the very most outer region of the planets, but along the adiabatic gradient the temperature rises too much for the interior to cross a phase boundary to an ice phase (e.g. ice VII, ice X) deeper inside. If the real temperature gradient in Uranuns and Neptune does not strongly deviate from such an adiabatic gradient, a large part of the deep interior may contain water in the superionic phase.

Conclusions

1. By present constraints on the interior structure, a similar range of solutions for both planets is obtained. They have $T_{core} = 5200-6300$K, $M_{core} = 0-2.5(\mathrm{Nep}:4)\,M_\oplus$, $P_{1-2} = 10-35$GPa, $Z_1 = 0.04 - 0.40$, and $Z_2 = 0.8 - 0.95$.

2. From these models we cannot conclude which planet is warmer or more enriched in metals.

3. More accurate measurements of J_4 would be very helpful, but a small uncertainty in P_{1-2} greatly widens the range of possible solutions, so that further constraints are required in order to better understand these planets. The heat flux is a serious candidate. Calculating cooling curves matching the heat flux is indispensable.

4. To overcome the problem of Uranus' small heat flux, a warmer interior of Uranus is suggested in literature. Within the adiabatic three-layer approach, central temperatures of Uranus differ not more than 1000 K from that of Neptune.

5. Within the adiabatic three-layer approach, water at deep interior temperatures and pressures of Uranus and Neptune is in the superionic phase and not in an ice phase or the plasma phase. This may have severe consequences on the magnetic field and the cooling behaviour.

4.4 Standard Three-Layer Pie Charts

Here we illustrate three-layer models of the outer planets in form of *pie charts*. In Fig. 4.15, each pie chart shows the distribution of chemical species H_2, H, H^+, He, He^+, He^{++}, and components (H, He, Z) with radius. A full arc segment corresponds to 100% in mass, and the radius scales linearly from the center, where the core is located, to the surface. At the surface and the two internal layer boundaries, pressure and temperature are given.

In the upper row we see two models of Jupiter, J3 and J2; in the second row two models of Saturn, S1 and S2, and in the lower row we see Uranus model U1 and the Neptune model N4 (Tab. A.5). These models are typical, but not to be taken as the most preferred ones.

J3 is characterized by a small outer envelope metallicity, $P_{1-2} \gg 3$ Mbar, below 1% ionization of He even at deep interior conditions, and dissociation and metalization occuring at $\simeq 80\%$ of Jupiter's radius well in the outer envelope. Consequently, the layer boundary for metals at $\simeq 65\%$ is disconnected from hydrogen metalization. J2 is characterized by significant He ionization in the inner envelope, a sharp transition from a *molecular* outer envelope to a *metallic* inner envelope at the PPT at $\simeq 1.7$ Mbar, and occurrance of a small fraction of neutral atomic H everywhere which Saumon et al. (1995) judge a non-physical behaviour due to the neglection of a plasma microfield in the EOS. Jupiter models have $R_{core} \ll R_J$. S1 is an exemplary acceptable Saturn model with LM-REOS. It has $Y_1 = 10\%$ and hence a huge $Y_2 > 40\%$. Metalization occurs at about $0.5\,R_S$. With $P_{1-2} = 1.4$ Mbar and $Y_1 = 0.18$, SCvH-i EOS based Saturn model S2 has first-choice values. Compared to Jupiter, significant ionization occurs only within $0.4\,R_S$ predicting an essentially molecular Saturn. Future magnetic field models might help to constrain the onset of metalization in Saturn. U1 is chosen to display the possibility of $Z_1 \ll Z_2$ indicating a planet with an eroded ice-rock core overlayd by an H/He outer envelope. N4 is chosen to display a $Z_1 \gg 10\%$ model that in principle be validated by future entry-probe measurements. Just not shown although present in the deep envelope is metalic hydrogen in both U1 and N4. The focus of these Uranus and Neptune models is more to highlight phases of water than ionization of hydrogen. In particular, U1 and N4 show the confinement of ionically conduction water to a region at $\approx 0.5 - 0.75 R_p$ and the transition to the superionic phase. P_{core} and T_{core} are quite typical here with 5 (7) Mbar for Uranus (Neptune) at ≈ 6000 K.

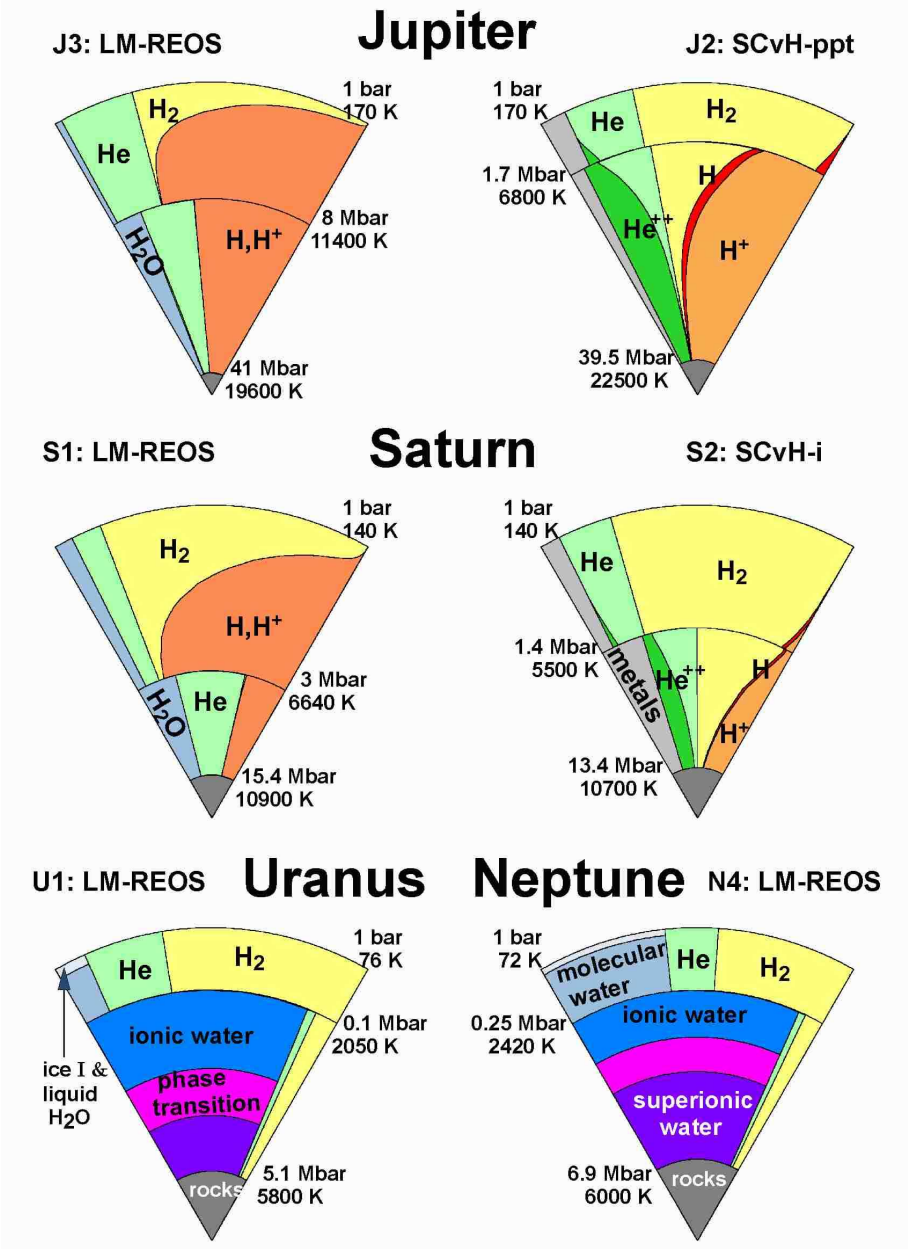

Figure 4.15: Pie chart illustrations of exemplary 3-layer models. See § 4.4 for explanation. These models are not meant to illustrate our current knowledge of the interior structure of the outer planets, but to illustrate properties of state-of-the-art three-layer models.

Chapter 5

Planetary Evolution

Planets are long-living objects. Planets are presumably not ever-lasting objects. Protons, whether bound or not, might decay with a half-life time of 10^{30} years or more as predicted by *Grand Unified Theories*. When radiating the energy from proton decay into space, planets will slowly dissolve (as will do all other objects) with an estimated lifetime of about 10^{40} years [WWW,§ 13.6].

Since planets are by definition not interstellar free-floating objects, but gravitationally bound to a parent star, their fate can be influenced on much shorter timescales by stellar evolution. After billions of years of relatively small changes, low-mass, sunlike stars will increase in luminosity by ~ 4 and in radius by ~ 1 order(s) of magnitude, when they leave the main sequence and start hydrogen shell burning. The extension of the Sun for instance in her *Red-Giant phase* before and during central He burning will reach beyond the orbit of Mercury, and water on Earth will evaporate in the next 1 to 3 billion years due to increasing solar luminosity.

Depending on star-planet distance, irradiation by the parent star can play a major role on planetary evolution already during the quiet main sequence phase of the star. This especially becomes important for planets at close orbits such as OGLE-Tr-132b ($a = 0.03$ AU) orbiting an F star and CoRot-7b ($a = 0.017$ AU) orbiting a solar-like star. In case of the gas giant HD209458b, the evolution is probably retarded by strong stellar irradiation [BaraffeEtAl03]; in case of the Super-Earth CoRoT-7b, a significant mass loss of several $M_\oplus$ may have occured due to strong XUV irradiation, whatever the composition of the planet [ValenciaEtAl09]. At larger distances around 1 AU the planets we know are Venus, Earth, and Mars. On Venus, solar irradiation causes a strong greenhouse effect without evaporating the atmosphere. On Earth, the atmosphere and the crust evolved dramatically during its lifetime, in particular with respect to habitability, and Mars lost its liquid water supposed to once have been floating through its great canyons.

These interesting aspects of planetary evolution are not the ones we are interested in here. We draw our attention on changes of internal properties of giant planets that are related to the matter under extreme conditions in the deep interior and give observable signatures. These are luminosity and radius.

The giant planets in the solar system are observed to radiate more energy than they receive from the Sun. The spectrum of this excess-luminosity is obtained by subtracting the solar spectrum from the observed spectrum at all wavelengths (or bands). The observed spectrum is characterized by two clearly separated frequency bands, one in the visible and one in the infrared [Hubbard84]. The visible band resembles that of the Sun and hence is attributed to reflected sunlight and to absorbed and re-emitted sunlight without spectral modification. The infrared band contains all other contributions. These are energy loss from the interior (intrinsic energy) and transmitted sunlight. Intrinsic energy is transported mostly by convection from the deep interior to the photosphere where it is radiated away from. For weakly irradiated planets, the photosphere is above the 1-bar

level. Transmitted energy is irradiation that was able to penetrate through the atmosphere down into the convective envelope, became absorbed, and then re-emitted from the photosphere with a spectral distribution according to the temperature there. Around its maximum, the observed luminosity L_{ir} in the infrared band resembles to good approximation that of a black body. The atmosphere is called *grey*. The Stefan-Boltzmann law

$$L_{ir} = 4\pi R^2 \, \sigma T_{\rm eff} \tag{5.1}$$

is reasonably applied to attribute an effective temperature $T_{\rm eff}$ to the planetary photosphere. Of course, real planetary infrared-spectra are non-grey due to molecular absorption lines. In particular, the blue-green color of Uranus und Neptune arises from red light absorption by methane in the atmosphere. Spectral-lines are highly important for instance for determination of the atmospheric composition by comparing with model atmospheric spectra. However, calculating non-grey atmospheres requires solving radiative transfer equations on the basis of spectral line tables and opacity tables [SchwHauBar00], which is very complicated. *Model atmospheres* are calculated [HellingEtAl08] using different levels of approximation regarding, e.g. dust settling and cloud formation. Beside element abundances, model atmospheres also yield a relation between the real temperature profile of the planetary atmosphere from the photophere down to the convective region and the infrared luminosity or, equivalently, the effective temperature. Before we address this topic further in § 5.1, we introduce the cooling equation. In the following, we omit the subscript *ir* and just write L while having in mind the infrared luminosity.

5.1 The cooling equation

An object which is not in thermal equilibrium with its surrounding but warmer, must radiate energy into the surrounding according to its surface temperature. In case of planets that are not in thermal equilibrium with the irradiation received from their parent star, this energy loss per time is called *intrinsic luminosity* L_{int}. For planets in thermal equilibrium with the star, $L_{int} = 0$. If this energy loss is not compensated for by internal heat sources such as nuclear fusion (as in stars), or radioactive decay (as in satellites), the planet must shrink and/or cool. If it shrinks or cools or does both depends on the compressibility of the equation of state. For an ideal gas of H_2 molecules –an example for a compressible material and a good approximation of the early stages of giant planet evolution– it can be shown ([KippWei94], [Guillot05]), that only 2/3 of the energy gained by contraction is radiated away, the other 1/3 goes into increasing its internal energy, in particular into increasing the energy of the ions. Very young ideal-gas planets and brown dwarfs are heating up while contracting. If, alternatively, the pressure-density profile becomes determined by degenerate electrons (or by a mono-atomic ideal gas) such as in old brown dwarfs and in white dwarfs (or in stars), it can be shown [Guillot05] that only 1/2 of the energy gained by contraction is radiated away, and the other half goes into increasing the internal energy. In case of stars, again the ions are heated; in case of degenerate electrons and non-degenerate ions however, the internal energy is mainly spent to enhance the Fermi energy of the electrons, while the energy of the ions decreases: the interior of white dwarfs cools [KippWei94]. Ions in the interior of brown dwarfs and giant planets of course are far from being ideal. But it is argued [Guillot05] that this limiting case applies to the late stages of giant planet and brown dwarf evolution when they become cold, degenerate matter. No analytic theory of the evolution of warm dense matter in giant planets is known to me. In § 5.2.3 we will see that indeed giant planets are cooling while contracting.

The *energy balance equation*

$$L = L_{\odot} + L_{int} \tag{5.2}$$

states that the observed energy loss L equals the stellar irradiation plus the intrinsic luminosity (remind: in the infrared!). In the following we will give expressions for L, $L_\odot$, and L_{int}. L is given by (5.1) and was already discussed there. $L_\odot$ is the stellar energy input per time. It is convenient to write $L_\odot$ in terms of an equilibrium temperature T_{eq} the planet would have in case of zero intrinsic luminosity, i.e. if it was in thermal equilibrium with the stellar energy input:

$$L_\odot = 4\pi\sigma R_{planet}^2 T_{eq}^4 \quad . \tag{5.3}$$

T_{eq} can be expressed by the effective temperature T_* of the star, the orbital distance a, the stellar radius R_*, and the albedo A of the planet as

$$T_{eq} = T_* \, (R_*/2a)^{1/2} \, (1-A)^{1/4} \tag{5.4}$$

Equilibrium temperatures for the outer planets are given in Tab. A.2.

In order to derive an expression for L_{int}, we need to know the contributions to the total energy of the planet. Kippenhahn & Weigert (1994) suggest for substellar objects the contributions gravitational energy E_g and internal energy E_i. For stars, there are additional contributions. For main sequence stars, the energy gain dE_n/dt due to nuclear reactions is most relevant; for young brown dwarfs, deuterium fusion is a small energy source (the amount of available D being very limited). For young and hot neutron stars (temperature $\gg 10^6$ K), production and emission of neutrinos plays the dominant role. Since the interaction of neutrinos, once produced in a neutron star, with matter below 10^9 K is neglegible, the neutrinos immediately leave the star and contribute without delay to its cooling ([KippWei94], Klähn (*pers. comm.*)). For stars, planets, and old neutron stars on the other hand, the energy is finally lost by photons radiated from the photosphere; it is the atmosphere which limits the energy that can be lost. Energy gained but not lost in stars or planets serves to heat the objects or to expand the radius. For metal-rich objects such as planets, radioactive decay may also contribute [GuiChaGauMor95]. If planets have become cold enough, first order phase transitions may occur such as the PPT in hydrogen, or in water the transition towards the superionic phase, releasing latent heat δq_L. An important effect of phase transitions on the cooling behaviour is for instance found for hydronic matter in neutron stars [BlaGriVos04]; δq_L is implicitly included in the internal energy. In accordance with the literature we assume the total energy E be composed of E_g and E_i and the intrinsic luminosity thus be

$$L_{int} = -\frac{dE}{dt} \qquad \text{with} \qquad E = E_g + E_i \quad . \tag{5.5}$$

In the following, we abbreviate the time derivative of a quantity A by $\dot{A} := dA/dt$.

Within a mass shell dm, the number of particles does not change with time and thus we can use the first law of thermodynamics to express the internal energy du per mass shell as

$$du \;=\; T\,ds - P\,dv \;=\; \delta q + \frac{P}{\rho^2}\,d\rho \quad , \tag{5.6}$$

where ds is the entropy and dv the volume per mass shell, and $\delta q = T\,ds$ is the thermal energy content (heat) of a mass shell. The gravitational potential of a spherical mass agglomeration is $\phi(r) = -Gm(r)/r$, and the gravitational energy of a planet can be defined [KippWei94] as

$$E_g := \int_0^M dm\;\phi(r) = -\int_0^M dm\;\frac{Gm}{r(m)} \quad . \tag{5.7}$$

Inserting (5.6) and (5.7) into (5.5) we have

$$L_{int} = -\int_0^M dm\;\frac{d}{dt}\left(T\,ds + \frac{P}{\rho^2}\,d\rho - \frac{Gm}{r}\right) \quad . \tag{5.8}$$

As shown in the appendix (D.4), the second and third term in (5.8) cancel each other and hence L_{int} simply is

$$L_{int} = -\int_0^M dm \frac{T\,ds}{dt} \quad . \tag{5.9}$$

Comparing (5.8) and (5.9), we just have to show

$$\dot{E}_g = -\int_0^M dm\, \frac{P}{\rho^2}\, \frac{d\rho}{dt} \quad . \tag{5.10}$$

The proof of (5.10) is given in § D.4 in the appendix. The gravitational energy gained by contraction is completely converted into work required to compress the material (5.10), and the internal energy increases. How this increment in internal energy is then distributed between ions and electrons depends on the equation of state. As stated above, in an ideal, classical gas, the ions are heated, whereas in an ideal Fermi gas of electrons and non-degenerate ions the internal energy is spent to enhance the Fermi energy of the electrons while the ions are even loosing kinetic energy which is then radiated away.

In any case, equation (5.9) is general and states that the intrinsic luminsity of a planet is due to the change of total heat content with time. The integral in (5.9) is a summation over all mass shells which may in principle differ in temperature $T(m)$ and specific entropy $s(m)$. $T(m)$ and $s(m)$ also change with time, so that we can write

$$L_{int} = -\int_0^M dm\, \frac{T(m,t)\, ds(m,t)}{dt} \quad . \tag{5.11}$$

With (5.1), (5.11), and (5.3) the cooling equation becomes

$$4\pi\sigma R_p^2 \left(T_{\rm eff}^4 - T_{eq}^4\right) = -\int_0^M dm\, \frac{T(m,t)\, ds(m,t)}{dt} \quad \textit{(cooling equation)} \quad . \tag{5.12}$$

It is also convenient to write cooling equations in terms of an emissivity ε with dimension energy per time and volume. Equation (5.11) would then read

$$L_{int} = -\int_{V_{planet}} d^3r\, \varepsilon(r) \quad \text{with} \quad \varepsilon(r) = \rho(r)\frac{T(r)\, ds(r)}{dt} \quad . \tag{5.13}$$

The cooling equation holds for any time t. Integrating it over time from the time the planet was formed to the present epoch $t_0 = 4.56$ Gyr, we would like to obtain the observed $T_{\rm eff}(t_0)$ and the radius $R(t_0)$. In this sense, evolution calculations are an important method to probe present-day structure models. In this form (5.12), the cooling equation is almost ready to be integrated over time. What we still need is a closure relation that connects $T_{\rm eff}$ with $T_{\rm 1bar}$, or with the physical temperature at some other pressure level.

$\mathbf{T_{eff}(T_{1bar})}$ and $\mathbf{T_{1bar}(T_{eff})}$

Few relations have been suggested in literature. Graboske et al. (1975) calculated model atmospheres on a grid of surface gravities g and effective temperatures $T_{\rm eff}$ typical for Jupiter's atmosphere. Such model atmospheres are $P-T$ relations in dependence on $(g, T_{\rm eff})$. They range from high altitudes where the temperature profile depends on radiative energy transport by line emissions of chemical species down to convective energy transport dominated levels. Model atmospheres for a large range in g and $T_{\rm eff}$ appropriate for stars, brown dwarfs and giant planets have been calculated by a few groups. The colder the atmosphere, the more molecules are formed and more spectral lines for the energy transfer equations have to be taken into account. State-of-the-art model

atmosphere codes for brown dwarfs and giant planets make use of huge opacity tables including millions of spectral lines [SchwHauBar00]. Model atmospheres are useful to derive the composition and are the only chance to obtain surface conditions of (irradiated) extrasolar giant planets. Most evolution investigations on Jupiter and Saturn in literature [SauHubbChaHor92, SauGui04] rely on model atmospheres by Graboske et al. (1975).

Jupiter's photosphere is at 0.1mbar; at higher pressures (lower altitudes) the adiabatic temperature profile is a valid assumption. Around $g \approx 10^3\,\mathrm{cm}/s^2$ and $T_{\rm eff} \approx 100\,\mathrm{K}$, the model atmospheres by Graboske et al. (1975) can be fitted by $P = 0.236 g^{0.5} T_{\rm eff} T^3$ [Hubbard 1977]. For the 1-bar pressure level this gives the relation

$$T_{\rm eff} = 0.700\, g^{0.134}\, T_{\rm 1bar}^{0.804} \quad . \tag{5.14}$$

Relation (5.14) was applied [Hubbard77, SauHubbChaHor92] on evolution investigations of Jupiter and Saturn. The inverse relation to (5.14) can be written as [GuiChaGauMor95]

$$T_{\rm 1bar} = K\, g^{-0.167}\, T_{\rm eff}^{1.244} \quad , \tag{5.15}$$

where constant K can be adjusted to give agreement with most recent observational $T_{\rm 1bar}$ and $T_{\rm eff}$ determinations. Using $K = (1/0.700)^{1/0.804}$ from the fit to the model atmospheres [GraboskeEtAl75] preceding the temperature determinations, we would have $K = 1.558$. Guillot et al. (1995) use $K_J = 1.519$ for Jupiter and $K_S = 1.511$ for Saturn. These values I also use. For Neptune I found $K_N = 1.454$. For Uranus I used by accident also K_N. It should have been $K_U = 1.485$. Higher K values tend to prolong the cooling time.

Although the model atmospheres were originally constructed for solar atmosphere composition (Y=0.24, Z=0.02), the $T_{\rm eff} - T_{\rm 1bar}$ relation was later on also applied to the thermal evolution of Uranus and Neptune [Hubbard78, PodRey81] in lack of any alternative. Furthermore, formulas (5.14, 5.15) are only valid for $T_{\rm eff} < 200$ K. Guillot et al. (2004) estimate the error induced by application of (5.15) on the cooling curve of Jupiter to 10%. Consequently, to the cooling curves of Uranus and Neptune the application of the $T_{\rm eff} - T_{\rm 1bar}$ relation once developed for Jupiter induces a badly quantified uncertainty.

5.2 Homogeneous evolution

5.2.1 Introduction

Unlike the label *homogeneous evolution* suggests, it does not necessarily mean a completely homogeneous interior evolving in time. Homogeneous evolution we define here as the evolution of a planet with mean molecular weight conservation per mass shell. Molecular weight gradients confined to *thin* layer boundaries in the interior are allowed, but they are not allowed to change with time. Homogeneous evolution thus precludes processes such as He sedimentation or core erosion. We thus have, for all $1 \le n \le N$ layers, Y_n *const*, Z_n *const*, and M_n *const* with time, where M_n is the mass of layer number n.

History: model assumptions and results

Hubbard (1970) was the first who calculated the evolution of 1-layer models of Jupiter. He assumed *'complete convective equilibrium'* and found an age of $4-8$ Gigayears (Gyr, 1 Gyr= 10^9 yr) depending on the consideration of electron screening in the H-He EOS of those days. With improved *'thermodynamics of liquid metallic hydrogen'*, Hubbard (1977) derived an age of 5.1 Gyr for Jupiter within an uncertainty of 10%. Similar calculations for Saturn yield an age of only 2 Gyr. With improved H-He EOS data and stricter observational constraints from *Voyager* and *Pioneer*

missions, structure models with at least one, better two density discontinuities were required in order to meet the constraints [ChaSauHubbLun92]. Guided by these models, Saumon et al. (1992) calculated the evolution of Jupiter and Saturn assuming 2- or 3-layer models with an IR-core and He abundances adjusted to give good match to the structure-related constraints (R_{eq}, J_2, J_4). For Jupiter, they found an age τ_J of $5.2 - 5.3$ Gyr depending on the EOS (SCvH-i or SCvH-ppt); for Saturn, they found an age $\tau_S = 2.6$ Gyr independent on the EOS and the underlying interior models (M_{core}, Z, 2 or 3 layers). Guillot et al. (1995) examined the effect of an intermediate radiative layer within a two-layer structure type (homogeneous envelope and core) and found the radiative layer to shorten the cooling time of Jupiter from 5.2 to 4.2 Gyr and from 2.6 to 2.4 Gyr for Saturn, using SCvH-ppt EOS. Fortney & Hubbard (2003) used impoved model atmospheres by Burrows et al. (1997), assumed homogeneous envelope+core structures and inferred the envelope water mass fraction and the core mass by requiring –as also Saumon et al. (1992)– to give the correct present-epoch mean radius and axial moment of inertia (J_0) of non-rotating Jupiter and Saturn models. For their 10 $M_\oplus$ core Jupiter model they found $\tau_J = 4.7$ Gyr and for their 21 $M_\oplus$ core Saturn model $\tau_S = 2.1$ Gyr. Saumon & Guillot (2004) assumed two-layer structure models using diverse EOS and found $\tau_J = 5.4$ Gyr (Sesame-p), $\tau_J = 4.8$ Gyr (LM-SOCP), $\tau = 4.7$ Gyr (SCvH-i), and $\tau_J = 4.0$ Gyr (LM-H4). A common feature of these homogeneous evolution calculations is an inferred age of $\approx 4 - 5$ Gyr for Jupiter and $\approx 2 - 3$ Gyr for Saturn.

Uranus and Neptune state-of the art evolution calculations were summarized by Stevenson (2008, *personal communication*), saying about *'structure models of type rock core, ice shell, and H-He-ice envelope give too long cooling times and thus cannot hold'*. This is consistent with conclusion 1) in § 4.3 and partially based on investigations by Podolak & Reynods (1981), who assumed Uranus and Neptune models with three layers (rock core, ice shell, H-He-ice envelope) and with two layers (rock core, H-He-ice envelope). They found the ice-shell models to be too warm after cooling by 4.6 Gyr corresponding to too long cooling times to attain the observed effective temperatures. Their no-ice-shell models are cooler from the very beginning (and also cooler than my models from § 4.3), and so they can attain a good agreement with the age of the solar system. Most recent studies are those by Hubbard, Podolak, and Stevenson (1995). They assumed two-layer models with a H-He-ice envelope and an ice core. In contrast to Podolak & Reynolds (1981), they could not find cooling times as short as 4.6 Gyr unless they either reduced the initial planetary heat content (cold start) or prohibited energy release from the deep interior to surface (inihibited convection). A common feature of these homogeneous evolution calculations for Uranus and Neptune is the tendency to infer cooling times larger than 4.6 Gyr, especially for Uranus.

This work: model assumptions

In this work, I use for Saturn a 10 $M_\oplus$ water core model with two layers (S3), where the envelope metallicity Z is adjusted to match R (this work was done by U. Kramm). As we have seen in § 4.3, a two-layer structure with one homogeneous envelope and a core certainly is a bad approximation for Uranus and Neptune, and as we will see in § 5.2.3, homogeneous evolution itself is a bad assumption for Saturn. Thus I updated my code (the last update before the submission of this Thesis) to set layer boundaries by the mass coordinate (transition mass, compare: transition pressure). This enables to calculate the evolution of a multi-layer structure with –as before– thin layer boundaries, i.e. without boundary layers. For Uranus, Neptune, and Jupiter I use three-layer models U3, N3, J3 among those presented in § 4 and as listed in Tab. A.5 in the appendix.

5.2.2 Performance

Solving the cooling equation together with some relation $T_{1\mathrm{bar}}(T_{\mathrm{eff}})$ is performed as follows. The cooling equation tells us that the planet's intrinsic luminosity is solely due to a decrease of its internal heat content with time. At each time step, the heat content is uniquely defined by the outer boundary condition $T_{1\mathrm{bar}}$. From $T_{1\mathrm{bar}}$ we can calculate the entropy and generate the adiabat in the outermost layer. We then can calculate the whole interior profile by requiring continuity in T and P at layer boundaries. Contrary to present day interior structure models, we do *not* know the radius in advance, but we know the core mass in advance as well as the transition masses $m_{n-(n+1)}$, the metallicities Z_n, and the He abundances Y_n in all layers, since we require the evolution to be homogeneous. So we have to find iteratively the radius R for given $T_{1\mathrm{bar}}$ that gives the desired core mass. When integrating the structure equations (3.33) and (3.31) we have to switch at given layer boundaries $m_{n,n+1}$ from the adiabat in layer number n to the adiabat in layer number $n+1$. Having thus calculated the interior profiles for two different 1-bar temperatures $T_1^{(k)}$ and $T_1^{(k+1)} > T_1^k$, we can calculate the heat difference $\delta Q^{(k)}$ using a mean temperature profile $T(m) = 0.5\,[T^{(k)}(m) + T^{(k+1)}(m)]$ as

$$\delta Q^{(k)}(T_1^{(k)}, T_1^{(k+1)}) = \int_0^M dm \left\{ 0.5 \left[T^{(k)}(m) + T^{(k+1)}(m) \right] \left[s^{(k)}(m) - s^{(k+1)}(m) \right] \right\} < 0 \quad .$$

By the cooling equation, the heat difference has to satisfy

$$L^{(k)}(T^{(k)}) = \frac{\delta Q^{(k)}}{dt} \quad ,$$

and determines the time span dt within δQ is lost as

$$dt = t^k - t^{(k+1)} = \delta Q^{(k)} / L^{(k)} < 0 \quad .$$

In practise, I first choose about 50 1-bar temperatures (in particular, 40 for Uranus and Neptune, 50 for Saturn, and 80 for Jupiter) and calculate the corresponding interior profiles. In a second step, I use these primary profiles to generate 150−200 interior profiles by interpolation. In a third step, the cooling equation together with (5.14) is solved using the interpolated profiles. As initial condition for the time integration I choose the present day values $L(t_0), T_1(t_0)$ and integrate backwards in time until the luminosity (or T_{eff}) rises steeply. Other authors prefer the opposite direction starting with arbitrarily high initial luminosity [SauHubbChaHor92] and proceeding until the present-day luminosity is reached. Furthermore, one usually keeps the angular velocity constant at the present day value. This possibly overestimates the angular momentum at the time the planet was young and more extended. It might be better to keep instead the angular momentum constant, but this would require an additional iteration loop. On the other hand, due to interaction with satellites (compare Earth-Moon system), a planet's angular velocity might once have been larger than today. Thus the convenient approximation $\omega = \omega(t_0)$ is reasonable. Hubbard (1970) arrives at the same conclusion based on more sophisticated considerations. Neglecting higher-order rotational terms and the corresponding flattening of the planet is estimated to add a further uncertainty of at most 0.2 Gyr to the inferred planetary age [GuiChaGauMor95].

5.2.3 Results for Jupiter, Saturn, Uranus, and Neptune

Homogeneous cooling curves for Jupiter, Saturn, Uranus, and Neptune are presented in figures 5.1 and 5.2. As described above, the calculations are performed by starting at present time $t = 4.56$ Gyr and integrating the cooling equation (5.11) together with (5.15) backwards in time. During the first ~ 500 million years of their lifetime, the giant planets were extended, warm, and luminous.

Because of their high luminosity $L \sim T_{\rm eff}^4$, they cooled fast. Looking backwards in time, their birth (with an uncertainty of 0.1 Gyrs), is indicated by the steep rise in $T_{\rm eff}$ and R. For Jupiter, this occured 4.48 Gyr ago, for Neptune 4.70 Gyr ago, for Saturn only 2.5 Gyr ago, and for Uranus as long as 6.8 Gyr ago.

Before evaluating these ages, we have a closer look at the cooling behaviour regarding the radius $R_{\rm 1bar}$, the isothermal rocky core temperature T_{core}, and the pressure P_{core} at the core mantle boundary as shown in Fig. 5.1.

Today the planets have reached a state where small changes of a few percent in these parameters will take place on timescales of billions of years. While cooling (both $T_{\rm eff}$ and T_{core} are decreasing with time), the pressure increases (P_{core} is just an example). Extrapolating these curves, Jupiter and Saturn are approaching a state of degenerate, cold matter. Possibly H and He will solidify. In contrast, Saumon et al. (1992) suggest an extension of the molecular, non-metallic H region with time at the expenses of the metallic region believing matter will cross the PPT boundary as predicted by SCvH-ppt EOS in the direction of latent heat release and not vice versa. In Uranus and Neptune, high-pressure water ice phases VII and X may occur in the future. Water on Earth, by then, will be evaporated. During the first 500 million years, water in Uranus and Neptune, also methane, must have been in a plasma state together with H and He. Latent heat release from the transition to the superionic phase or any other form of solidification of a water-methane-rock mixture, would slightly prolong the calculated cooling time.

Without taking into account possible phase transitions, the ages inferred from these homogeneous evolution calculations are, in Gyr, 4.48 for Jupiter, 2.5 for Saturn, 6.8 for Uranus, and 4.70 for Neptune. The age we would like to obtain is the age of the solar system, 4.56 Gyr.

In § 5.2.1 we have learned that the age of Jupiter and Saturn inferred is relatively independent on (*i*) the EOS used, (*ii*) the interior models, and (*iii*) the authors who performed the calculations. It varies within ± 0.5 Gyr. The age of Uranus and Neptune inferred can vary by several Gyr with the common tendency to too long cooling times.

For Jupiter and Neptune, the variety of structure models and authors is apparently enough to find interior models that are consistent with the age. For Saturn (this work: -2.1 Gyr) and Uranus (this work +2.2Gyr) this is not enough. Consequently, some contributions to the cooling behaviour of Saturn and Uranus must be missing. These contributions must not necessarily be unimportant for Jupiter and Neptune; the possibility of further effects in Jupiter and Neptune counter-acting the contributions we are looking for has to be taken into account.

What we are basically looking for can be read from Fig. 5.2, where we see the same cooling curves as in the two panels with arrows in Fig. 5.1, but here shifted in time so that the birth of the planets coincides with the birth of the solar system at $t = 0$, neglecting the duration of formation of ~ 0.01 billion years. *Dotted lines* indicate the observed effective temperatures. Imagine an extrapolation of Saturn's cooling curve until present time. Evidently, Saturn's observed $T_{\rm eff}$ is larger than predicted by homogeneous evolution. At present time, the planet radiates more energy into space than expected. This suggests an additional internal energy source in Saturn [SteSal77]. Uranus on the contrary, and to a lesser extend also Neptune, apparently radiate less energy ($L \sim T_{\rm eff}^4$ is smaller) than expected from homogeneous evolution. Consequently, processes may by present in Uranus (and Neptune) reducing the energy loss. We first discuss processes influencing the energy loss that are consistent with the assumption of homogeneous evolution in order to understand that Saturn and Uranus challenge this assumption.

Processes influencing the energy loss of homogeneous planets

In case of Saturn, possible additional energy sources are, beside minor ones such as radioactive decay, cooling of the isothermal core, and phase transitions.

Cooling of the isothermal core was for instance included by Guillot et al. (1995). The additional

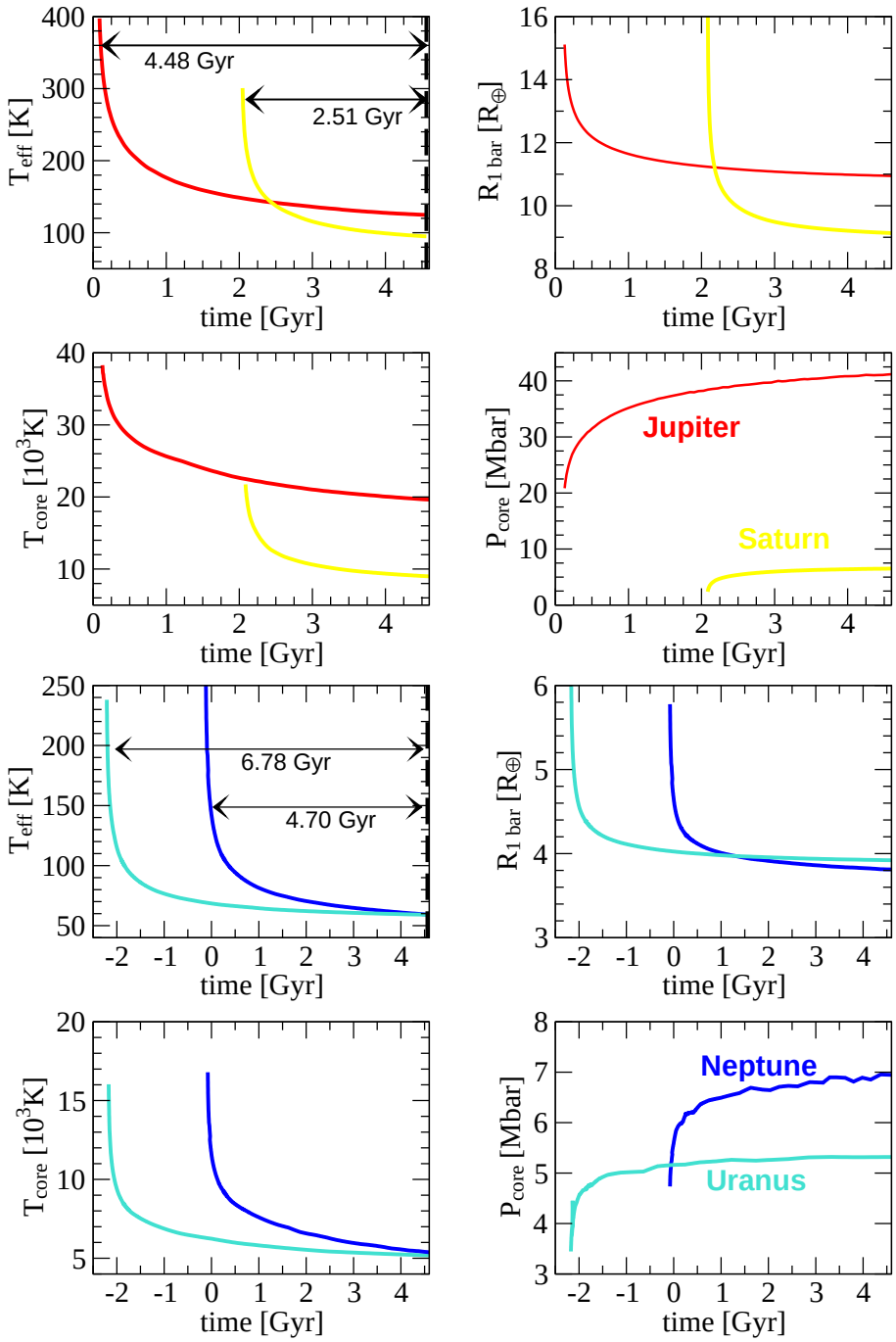

Figure 5.1: Cooling behaviour of Jupiter (*red*), Saturn (*yellow*), Uranus (*turquoise*) and Neptune (*blue*). For each planet, the time-evolution of effective temperature, 1-bar radius, isothermal rocky core temperature and pressure at core-mantle boundary are shown. The black arrows indicate the time span between present time t_0 (*thick dashed line*) and the time where $T_{\rm eff}$ and R rise to infinity which can be considered as the birth of the planet. The underlying structure models respectively are: J3, S3, U3, and N3. See Tab. A.5 for details.

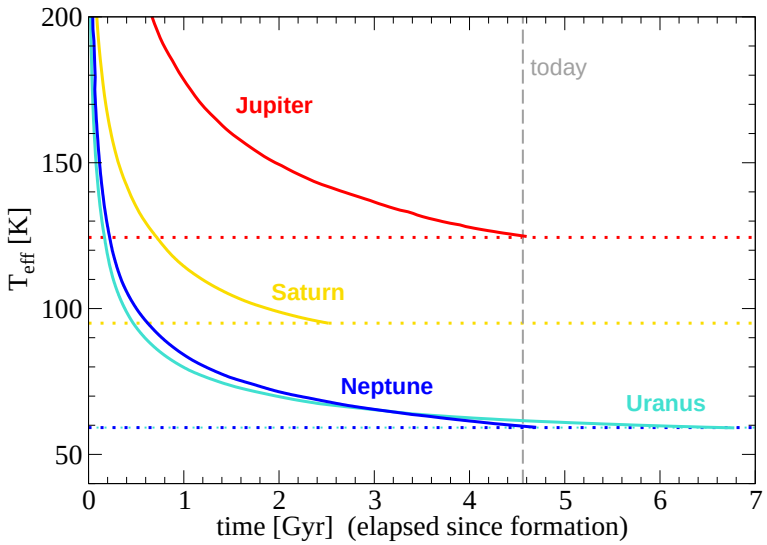

Figure 5.2: Cooling curves of the outer planets assuming homogeneous evolution. The time of formation has been placed at $t = 0$ and the calculated evolution proceeds until the observed effective temperatures (*dotted lines*) are reached. This figure is to show that for Saturn and Uranus the assumption of homogeneous evolution is not consistent with the known age of the planets of 4.56 Gyr.

energy release due to the specific heat c_V of the core material is

$$Q_{core} = M_{core}\, c_V \Delta T = 5.97\, 10^{30}\mathrm{J} \times \frac{M_{core}}{[M_\oplus]} \frac{c_V}{[\mathrm{J/g/K}]} \frac{\Delta T}{[1000\,\mathrm{K}]} \quad .$$

Using LM-REOS-H_2O for a water core, we find $c_V = 4 - 5$ J/gK relatively independent on temperature and pressure. For rocks, Podolak & Reynolds (1981) calculate c_V =0.8 J/gK. Applied to the evolution of a Saturn model with a 10 $M_\oplus$ water core, this contribution prolongs the cooling time by +0.1 Gyr.

Candidates for phase transitions in Saturn are the PPT of hydrogen and the transition from water plasma to superionic water of core material. For SCvH-ppt EOS, the entropy gap at the transition from metallic to molecular hydrogen is $0.5\,k_B$ per proton $\sim$ 4.1 J/gK. Saumon et al. (1992) found an influence on the age of Saturn of 1−2%. Note that this kind of phase transition would even shorten the cooling time if molecular mass shells transit into the metallic phase with time and not conversely.

Present-time structure models of Saturn predict core temperatures of 9000−12000 K and core-mantle pressures of 10 or more Mbar, see Fig. 4.10. If the core contains water, it will be close to the phase boundary between superionic and plasma phase, see Fig. 4.14. French et al. (2009) found an energy shift $du = 2.5$kJ/g at 4500 K and 3 g/cm^3 indicating a first-order phase transition with an entropy gap of 0.6 J/gK. Applied to a 10 $M_\oplus$ water core, I found a corresponding cooling time prolongation of 0.1 Gyr. Hence, latent heat release due to first order phase transitions is very small compared to the thermal cooling of the H-He envelope.

We conclude that the energy release of an IR core and latent heat from first-order phase transitions are too small to explain Saturn's luminosity within the assumption of homogeneous evolution.

In case of Uranus, possible sources affecting the present time energy loss are the $T_{\rm eff} - T_{\rm 1bar}$ relation and time-dependence of the cooling curve.

It is convenient to apply basically the same relation between $T_{1\mathrm{bar}}$ and T_{eff} to the evolution of Uranus and Neptune as for Jupiter and Saturn, even though this relation was developed for the metal-poor atmosphere of Jupiter and not for the metal-rich atmosphere of Uranus and Neptune. Unmodified, this relation does not give the proper $T_{\mathrm{eff}} - T_{1\mathrm{bar}}$ relations at present time. This is why I changed the factor 0.700 in equation (5.14) to 0.740. This slight change strongly reduced Neptune's age by about 2 Gyr. Remembering that the outer envelope metallicity can differ by as much as 35 percentage points between these two planets, also different $T_{\mathrm{eff}} - T_{1\mathrm{bar}}$ relations may apply. We conclude that the relation between T_{eff} and $T_{1\mathrm{bar}}$ imposes a large uncertainty on the cooling time of Uranus and Neptune. Methane-rich model atmospheres should be calculated.

The time-dependence of the cooling behaviour can become important if a process occurs at high internal temperatures and stops when the planet has cooled below a certain threshold. An inhibited energy loss at early times for instance suppresses cooling of the deep interior. Such a planet (P1) appears less luminous compared with a fully adiabatic, homogeneously evolving planet (P2) during the first epoch of evolution. After a sufficiently long time however, P2 has lost so much energy that its luminosity finally becomes smaller than that of P1 which still has stored a significant amount of its inital heat content. Then P1 would wrongly seem to have an internal energy source, while instead it just was delayed at early times. For comparison, crossing of cooling curves obtained for different assumptions about the emissivity is also known in case of neutron stars [BlaGriVos04]. Uranus can either be still in the phase of delayed cooling implying a hot interior, or it can have lost much energy during its youth implying a cold interior [HubbPodSte95]. Both scenarios are not consistent with permanent homogeneous evolution.

We conclude that the atmospheric boundary condition bears a large uncertainty on the evolution of metal-rich planets and that Uranus may evolve or have evolved inhomogeneously.

Results and conclusions obtained in this chapter agree with results and conclusions published in literature. Within the various uncertainties regarding homogeneous evolution, the age of Jupiter and Neptune can be reconciled with the age of the solar system, but the ages of Saturn of Uranus obtained point strongly to inhomogeneous evolution.

5.3 Inhomogeneous evolution

We call the evolution of a giant planet *inhomogeneous*, if (a) particle concentrations in two or more mass shells change with time, or if (b) there exists an extended inhomogeneous region in the planet, i.e. a region with a vertical gradient in particle concentrations. This definition is consistent with specific cases of non-homogeneous evolution studied in literature [SteSal77, ChaBar07].

Case (b) applies to extended layer boundaries (i.e. boundary layers) or to a large number (> 50) of layers effectively forming an inhomogeneous region. In this case, the usual construction of interior profiles that neglects temperature gradients at the transition between neighboured convective, homogeneous layers leads to wrong temperature profiles for a given surface temperature and consequently the cooling equation applied to these wrong profiles gives a wrong cooling time.

Case (a) applies to chemical separation of chemical species. This can happen in the course of the PPT in hydrogen, where equality of chemical potentials of He and minor species requires different concentrations in the molecular an the metallic phase of H [SteSal77]. With time the location of the PPT is shifting and so is the discontinuity in He and metals. Case (a) can also happen due to immiscibility of He or minor constituents. In this case, two phases will form with concentrations of He according to the phase diagram of the mixture, the phase of larger mean molecular weight being richer in He (H/He phase separation). We do not consider immiscibility of minor constituents here. Salpeter (1973) pointed out that He-rich droplets might be able to

sink downward and permanently enrich deeper shells with He (gravitational layering) despite the presence of convection. Central condensation of the planet would then increase and the loss of gravitational energy be seen as an additional luminosity. Conversely, a planet decreasing in central condensation, e.g. because of core erosion, would be less luminous. Furthermore, if core erosion proceeds in such a way that eroded material does not instantaneously gets mixed with the inner envelope material but forms a sequence of layers with subsequently decreasing metallicity with height, we again have case (a).

H/He phase separation is the most promising mechanism to explain Saturn's present luminosity. Its probable occurrance is further supported by the observed helium depletion in the atmosphere of Saturn (and also of Jupiter), see § 3.1.4. We will discuss H/He phase separation and its application to planets in § 5.3.1-5.3.3. The idea of an extended inhomogeneous boundary layer inhibiting convection seems promising for Uranus and will be discussed in § 5.3.4.

5.3.1 H/He phase separation: the phase diagram

The effect of H/He phase separation on the evolution of H-He rich giant planets was studied in great detail by Stevenson and Salpeter (1977). Since then, large disagreement of available H/He phase diagrams [Stevenson75, KlepeisEtAl91, PfaHohBal95] and their incompleteness at relevant pressures around 1 Mbar let scientists hesitate to calculate inhomogeneous evolution of Saturn based on H/He phase separation, while its potential and unique effect on the cooling time was often mentioned in the literature. Fortney & Hubbard (2003) performed the inverse procedure: they modified available H/He phase diagrams until they reproduced the correct age of Jupiter and Saturn in order to predict what the real phase diagram should look like. Finally, Lorenzen [LorHolRed09] calculated a H/He phase diagram based on ab initio simulations which –for the first time– seemed promising in its potential to explain Saturn's cooling behaviour. In the following we focus on that property of the H/He phase diagram that is relevant for the planets: the *miscibility gap*, also called *demixing region* or *region of phase separation*.

The distribution of helium in the planet and the corresponding gravitational energy release depends strongly on the miscibility gap in dependence on pressure and He concentration. It is convenient to display the miscibility gap as a function $T_{demix}(P, x_{\rm He})$, where $x_{\rm He} = N_{\rm He}/(N_H + N_{\rm He})$ is the helium number fraction and T_{demix} the largest temperature below which the hydrogen-helium system prefers to demix for given P and x_{He}. Results based on simulations by Lorenzen et al. (2009) and other groups are shown in Fig. 5.3.

The *left panel* shows $T_{demix}(P, x_{He})$ at constant pressures of 4, 10, and 24 Mbar. Solid lines are with FT-DFT-MD [LorHolRed09], dashed lines are former results with CP-MD [PfaHohBal95]. For example, assuming an initial He fraction $x = 0.4$ at $P = 4$ Mbar and a temperature below $10,000$ K, the FT-DFT-MD based demixing curve predicts demixing into two phases A and B with number fraction $x_A \approx 0.09$ (mass fraction Y_A) and $x_B \approx 0.75$ (mass fraction Y_B). In contrast, the CP-MD based demix curve (*green dashed*) predicts no demixing.

For large He fractions, the demixing curves by Lorenzen et al. (2009) approach levels labeled T_m. These are experimentally varified melting temperatures of pure helium. However, the behaviour at $x_{He} \to 1$ is still a matter of intense discussion, and the plateaus shown here may have to be modified when calculations with many more particles in a simulation cell are available. This region of the H/He phase diagram is related to solidification of both H and He and metalization of H. For $x_{He} \ll 1$ and $P \geq 1$ Mbar, the demixing behaviour is related to a region in the H/He phase diagram where H becomes metallic, but not He. At $P \ll 1$ Mbar, H forms a non-metallic, molecular fluid in which He is miscible. The transition between 1 and 4 Mbar is quite complicated and work in progress by Lorenzen. For sufficiently large temperatures, H and He are miscible since mixing enhances the ideal entropy of mixing which in turn helps to attain a deeper level of the Gibbs free

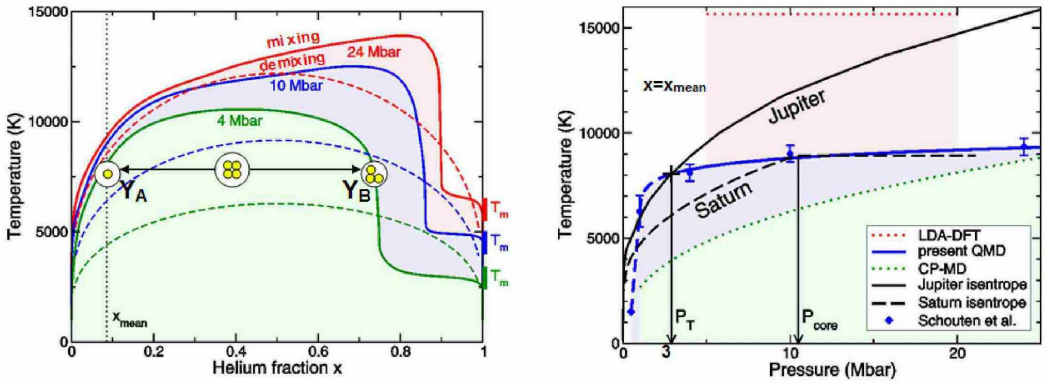

Figure 5.3: Demixing region $T_{demix}(x_{\rm He})$ and demixing curve $T_{demix}(P)$

Left panel: Demixing region $T_{demix}(P, x_{\rm He})$ at constant pressure $P = 4\,$Mbar *(green)*, 10 Mbar *(blue)*, and 24 Mbar *(red)*; *solid*: FT-DFT-MD calculations by Lorenzen, *dashed*: CP-MD [PfaHohBal95]. He mass concentrations Y_A and Y_B illustrate the preferred separation of a system with $P = 4\,$Mbar and $T = 7500\,$K. Vertical bars labeled T_m are experimental error bars of the He melting line.

Right panel: Demixing curve $T_{demix}(P, x_{\rm He})$ at constant composition $x_{\rm He} = 0.086$. *Blue solid:* FT-DFT-MD by Lorenzen, *green:* CP-MD [PfaHohBal95], *red:* DFT calculations using Local Density Approximation [KlepeisEtAl91]. Meanwhile, the interpolated *dashed blue* curve could be confirmed by FT-DFT-MD calculations [Lorenzen et al. *in preparation*]. *Black lines* are typical quasi-adiabats for Jupiter and Saturn, where '$\rm P_T$' denotes Jupiter's P_{1-2} and '$\rm P_{core}$' Saturn's core-mantle boundary pressure. This figure was essentially prepared by Lorenzen.

energy.

Keeping the He fraction constant at the mean value of the giant planets, T_{demix} can be mapped against pressure (Fig. 5.3, *right panel*). FT-DFT-MD based results are labeled '*present QMD*' (*blue curve*). We furthermore see results by Pfaffenzeller et al. (1995) (*green*) and results by Klepeis et al. (1991) (*red*), and typical quasi-adiabats of acceptable models of Jupiter and Saturn. The green demixing curve predicts no demixing in Jupiter and Saturn, the red curve predicts demixing in both planets but the onset of the immiscibility region remains undetermined, and the blue curve predicts demixing in a narrow region in Jupiter around 1-4 Mbar and in Saturn from 1 Mbar down to the core. Note that todays demixing regions in the planets can only be derived by self-consistent inhomogeneous evolution calculations.

We compare predictions based on inhomogeneous evolution calculations [ForHubb03] with results by Lorenzen et al. (2009). For Saturn, Fortney and Hubbard predict

(1) $Y_B = 1$;

(2) *if* demixing occurs for one pressure level, it also occurs for all higher pressure levels;

(3) because of 1) and 2) a pure Helium layer builds up around the core;

(4) T_{demix} rises with pressure;

(5) separation beginning at $T_{\rm eff} \approx 107 - 98\,$K gives the correct age and $Y_1 = 0.185 - 0.20$;

(6) if the demixing region extends down to the core, no intermediate inhomogeneous layer is formed,

(7) the distribution of metals is constant at all times;

(8) the proper cooling time for Saturn cannot be obtained unless He sinks down to the core or another species also suffers phase separation with hydrogen;

(9) instantaneous sedimentation: $Y_1 = Y_A$ (see below);

Based on FT-DFT-MD calculations, Lorenzen et al. (2009) predict

at (1) $Y_B = 0.6 - 0.9 < 1$ for $P = 1 - 24$ Mbar

at (2) and (3): because of the small rising of T_{demix} with pressure compared to an adiabatic gradient, crossing with an isentrope can occur; in particular: high-entropy adiabats touch the demixing curve $T_{demix}(P, x_{\rm He} = const)$ around 1 Mbar; lower entropy adiabats have more extended demixing regions around 1 Mbar, and sufficiently cold adiabats leave the demixing region not before very high pressures. Sufficiently cold present time Saturn adiabats (and thus He layer formation) are possible.

at (4) no critical temperature is found, instead $T(P, x_{\rm He} = const)$ continues rising up to at least 50 Mbar;

at (5) separation starts at $T_{\rm eff} \approx 117$ K.

Since young giant planets are luminous and warm (§ 5.2.3), their adiabats do not touch the H/He demixing curve of any phase diagram before they have cooled down for some long enough time. We call the time when H/He separations begins to operate t_{dmx}. Of course, t_{dmx} depends on the H/He phase diagram.

Degrees of freedom/different modes

Now that we have at hand an accurate, promising H/He phase diagram, we still have to face some uncertainties regarding the He distribution in a planet. Stevenson and Salpeter (1977) claimed *'the interior evolves along the phase boundary'* and Guillot (2008, pers.comm.) recommended in the same sense to force consistency between the internal He distribution and the H/He phase diagram. Consistency means an evolution along the phase boundary of the immiscibility region. At any time, no mass shell is in the demixing region. In general, this implys different He concentrations for neighbouring mass shells, and an intermediate inhomogeneous region occurs. It begins with the mass shell that crosses the phase boundary first, and it ends with the mass shell that leaves the phase boundary. These crossing points depend on the local He concentration and have to be calculated at any time in a selfconsistent manner.

However, we do not know to which size droplets can grow, how fast they can sink compared to vertical convection speed, and how fast they dissolve again if mixing is favoured again at deeper layers. Thus we should not exclude the possibility of a He-rich layer around the core even if demixing ends at $P < P_{core}$. In order to study the effect of a He-layer around the core as predicted, I implemented two types of sedimentation as illustrated in Fig. B.4 [1]. In the *right panel* of Fig. B.4 we see *type 2* sedimentation. For this type, metals are lifted because of a smaller mean molecular weight of the deep envelope material compared to pure He droplets. With *type 1* sedimentation in Fig. B.4, *left panel*, I illustrate the case where two envelopes are forming, one of them depleted in He, the other one enriched in He with a transition at a pressure level in agreement with the end of the demixing region. An intermediate inhomogeneous region is neglected. To be consistent with the phase diagram, this pressure level can only be found iteratively. For both type 1 and type 2 sedimentation, the underlying structure type has three layers.

Stevenson and Salpeter (1977) claim a strong response of the distribution of metals to the distribution of He. However, a quantitative estimate was not made, and for simplicity I assume

(i) the initial state at $t = 0$ is a two layer structure with one homogeneous envelope and a core (compare item (6) above);

(ii) sinking of helium leaves metals unaffected in type 1 sedimentation (compare item (7) above);

(iii) there is no permanent layer boundary due to a discontinuity in metals (apart from the core) in the presence of He sinking (compare item (7) above).

[1] Because of page formatting problems, this figure had to be put in the appendix (§ B)

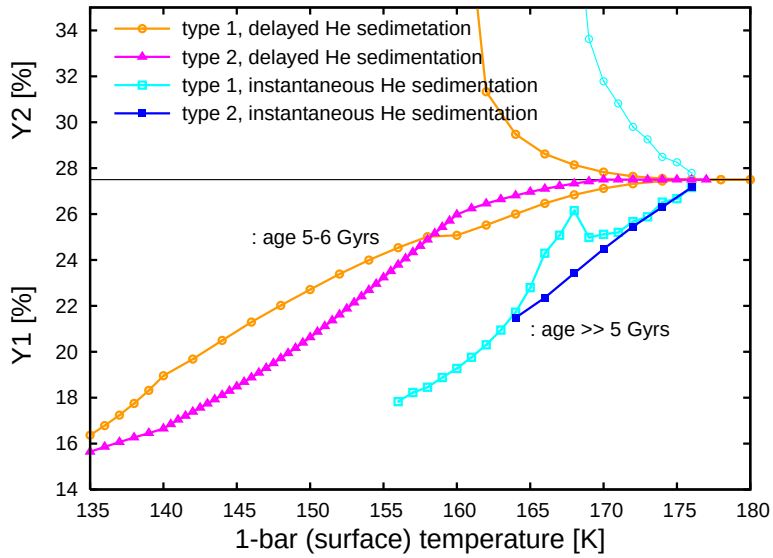

Figure 5.4: Evolution of the helium mass fraction Y_1 in the outer envelope and Y_2 in the inner envelope for the four cases of He sedimentation in Saturn based on the same (FT-DFT-MD) demixing diagram. The evolution is shown with respect to surface temperature. The *black* line separates Y_1 from Y_2. The *orange* curve and the *blue* curve have $Y_2 = 1$ (helium layer) by definition, and the *cyan* and the *blue* have $Y_1(t) = Y_A(t)$ by definition.

Assumption (iii) contradicts our conclusions from Saturn interior structure models (§ 4.2.2).

Another uncertainty regards the He abundance in the layer where the onset of phase separation takes place (the mass of helium in the other layer –pure He or He-enriched or both– being determined by the condition to conserve $\bar{Y}$). By assumptions (i)-(iii), it is the outer envelope where phase separation sets in. Evolution along the phase boundary [SteSal77] implies that at any time the He-abundance Y_A of the He-poor phase A is established in the whole outer envelope up to the demixing region. This case ($Y_1 = Y_A$) is called *instantaneous* sedimentation. It requires several convective cycles to transport all the envelope material with $Y_1(t_{i+1}) > Y_1(t_i) = Y_A(t_i)$ [2] into the region of demixing. We cannot be sure that instantaneous sedimentation is realized in the planets and therefore I also implemented another case, which I call *delayed* sedimentation. In this case, a weighted average abundance establishes in the outer envelope with $Y_1(t_{i+1}) > Y_1(t_i) > Y_A(t_i)$ according to the mass enclosed in the demixing region. First results for these 2×2 cases are shown in Fig. 5.4 and described in § 5.3.2.

5.3.2 H/He phase separation in Saturn: first results (work in progress)

Figure 5.4 shows preliminary results for the helium distribution in Saturn during cooling (decreasing surface temperature) assuming instantaneous He sedimentation (*blue and cyan curves*) or delayed He sedimentation (*orange and magenta curves*) and type 1 or type 2 He sedimentation. This is work in progress. Already some important features become evident.
For delayed He sinking, depletion in the outer envelope proceeds much more slowly. Derived Y_1 values of present time profiles ($T_1 = 135{-}140$ K) are just slightly smaller than the re-interpreted Voyager measurements ($Y^{\rm atm} = 0.18 - 0.25$). On the other hand, with instantaneous sedimenta-

[2] remember t_0 = today, so $t_{i+1} < t_i$.

tion, Y_1 is sinking so fast that it reaches 0.18 already at $T_1 \approx 155\,\mathrm{K}$. Consequently, this indicates a present Y^{atm} below 0.18 or, alternatively, an evolution not along the phase boundary. We conclude that accurate measurements of Saturn's helium abundance are urgently needed.

Considering the *orange* and the *cyan* curve, we observe a steep rising of the inner envelope abundance Y_2. Since $\bar{Y}$ is conserved, this rising must be accompanied by a fast reduction of the mass contained in the inner envelope. Indeed, the high-pressure end of the immiscibility region in Saturn extends rapidly toward deeper levels. Finally, when the inner envelope has become very small, it can happen that it is not capable anymore of comprising the whole amount of He lost from the outer layer. This is the onset of He layer formation around the core. In case of the *cyan* curve, P_{1-2} was kept fixed when He layer formation started, and the excess He amount was redistributed in the outer envelope (hence the local maximum at $T_1 \approx 165$); in case of the *orange* curve, Y_1 was kept fixed instead and P_{1-2} re-adjusted. When a He layer occurs in type 1 sedimentation, the procedure switches to type 2 sedimentation, in order not to change the number of layers.

An improved version has to allow for four layers from this point on: an outer envelope with proceeding depletion, an inner enriched envelope, and a He layer which grows in steps exactly when the He-rich layer above cannot comprise the He anymore. We conclude that Saturn probably contains a discontinously growing He layer around the core.

Blue and *cyan* curves: The derived cooling time up to $T_1 = 155\ K$ already is ≈ 5 Gyr (for some forgotten reason I did not calculate colder profiles). Adding the time span of $1-2$ Gyr needed to cool to $T_1 \leq 140\,\mathrm{K}$, the total age would amount to more than 6 Gyr. Hence, in case of instantaneous sedimentation, more gravitational energy is released than required to explain Saturn's excess luminosity. If we believe in an evolution along the phase boundary, an additional mechanism is required to reduce the total excess luminosity.

From this preliminary-work-in-progress we finally conclude that if the interior evolves consistently with the new H/He phase diagram, then in the present Saturn a He layer around the core exists, $Y_1 < 0.18$ and at least one mechanism affecting the cooling behaviour is still missing. This preliminary work suggests alternatively an evolution not along the phase boundary.

5.3.3 H/He phase separation in other planets than Saturn

With Saturn we might have found a planet whose luminosity is particularly strongly affected by H/He phase separation. Generally we can expect H/He phase separation to occur in other planets as well, if they contain metallic hydrogen at low enough temperatures where the electronic structure of He atoms is very different from that of H. Jupiter, Uranus, and Neptune are such candidates.

Jupiter's atmospheric He depletion points to the presence of H/He phase separation. On the other hand, homogeneous evolution using various EOS gives a correct age. Hence, if H/He phase separation occurs in Jupiter, it either has a small effect on Jupiter's heat loss, for instance because it has just begun, or it does have an effect, but there are other processes compensating for the additional energy gain.

In case the effect is small, the missing He cannot have been sinking a large radial distance downward, since otherwise the gravitational energy gain would be seen in the luminosity. For this scenario we would need a layer boundary close to the onset pressure of H/He phase separation, i.e. close to 3 Mbar. This scenario is in good agreement with the most recent phase diagram by Lorenzen. In case the effect is not small, the missing He has been sinking downward a large distance releasing gravitational energy. A compensating process might be an upward motion of

other particles. The most abundant species after He we expect to be H_2O. This scenario suggests a slowly eroding water core. According to the phase diagram of water, at Jupiter core conditions H_2O indeed is in the plasma phase which is miscible with H. Which of these scenarios applies to Jupiter and is consistent with present structure models, remains to be examined in detail in the future.

Uranus and Neptune's atmospheric He abundance is consistent with protosolar values and with the cosmic He abundance. Nevertheless, due to their relatively low temperatures, H/He phase separation probably occurs in the deep interior. That we do not see a depletion in the atmosphere could be explained by an ineffective exchange of particles between the outer envelope where H and He do not phase separate and the inner envelope where it occurs [HubbPodSte95]. A limited exchange between the envelopes is also supported by their cooling curves (§ 5.3.4).

H/He phase separation in extrasolar planets is discussed by Fortney and Hubbard (2004).

5.3.4 Inhibited convection in Uranus and Neptune

For Uranus, and to a lesser extent also for Neptune, inhibited convection in the deep interior has been proposed [HubbPodSte95] to explain the observed low intrinsic luminosity. The idea behind inhibited convection is a non-convecting thick boundary layer separating the deep interior from the convecting outer envelope, from which energy is lost by radiation from the planetary atmosphere. While the outer envelope once cooled efficiently as today observed by a small $L \sim T_{\rm eff}^4$, the interior below the non-convecting intermediate layer cannot loose its heat because of inefficient heat transport across the boundary layer.

We have learned in § 3.1.1 that convection requires a sufficiently large temperature gradient (Schwarzschildt criterion). The larger an eventual compositional gradient, the larger the temperature gradient required to maintain convection. Hence, inhibited convection indicates either a sub-adiabatic temperature gradient (e.g. due to a cold start) or a strong and extended compositional gradient.

The effect of (convection inhibiting) compositional gradients that cause a sequence of numerous thin layers on the evolution of exoplanet HD209458b was found [ChaBar07] to delay cooling of the deep interior by several Gyr and to delay shrinking of the planet. Transferred to Uranus, we would thus expect it not only to have an inhomogeneous deep region but also be warmer and larger than predicted by traditional homogeneous evolution. Both properties (T_{core} and R_p) act to require a larger deep envelope metallicity in order to yield a suffiently high mass density to satisfy the gravity field data. Model U1 (Fig. 4.15 and Tab. A.5) already has $Z_2 \simeq 90\%$ when using water for metals. Concluding, such a high metallicity may indeed be reasonable for Uranus even if using silicates and iron for metals.

With respect to the internal mass fraction prohibited of taking part in convection while demanding $L(t_0)$ to be satisfied, Hubbard et al. (1995) found for this mass fraction up to 70% for Uranus and up to 40% for Neptune depending on the initial central temperature. How can an inhomogeneous boundary layer be realized that shelters $\approx 50\%$ of the interior against energy loss? For exoplanet HD209458b, Chabrier and Baraffe (2007) proposed core erosion. Interpreting a deep envelope with 90% metals, preferably ices, as part of an eroding core (§ 6.2), this proposal may also apply to Uranus and Neptune.

Furthermore, pie chart illustrations (Fig. 4.15) reveal an extended region, where water transitions from an ionic fluid to the superionic phase along the oxygen subsystem melting line. By Fig. 4.14, an enhancement of T_{core} by $\leq 2000\,\mathrm{K}$ will not alter this result, since the phase boundary rises steeply with temperature at relevant densities. At earlier times when T_{core} was much larger, water and other ices prefered the plasma phase, driving erosion of the core's ice content into the

metallic H-rich outer envelope above. Whether this process has come to an end today or not, an eroded but incompletely redistributed water shell together with an extended phase transition region of water presumably gives rise to an inhomogeneous intermediate layer.

The planetary mass fraction excluded from efficient cooling as predicted [HubbPodSte95] agrees well with the extension of the superionic phase and the transition region. Furthermore, the properties of layers in Uranus and Neptune predicted by our structure models agree well with properties predicted by magnetic field models. Stanley & Bloxham (2006) for instance predict a non-convecting ([FrenchEtAl09]/this work: oxygen lattice), conducting ([FrenchEtAl09]/this work: proton conductivity), fluid ([FrenchEtAl09]/this work: proton mobility) interior. Whether the extension of a non-convecting layer needed for an acceptable cooling time can also be reconciled with the requirements by the gravity filed data remains to be examined in the future. Planetesimal infall during formation may also be responsible for building up an inhomogeneous layer.

A cold start has to be considered together with the process of formation which is beyond the scope of this work.

Concluding, the long cooling time of Uranus indicates inhibition of convection in the deep interior. Possible reasons are a cold start, a strong compositional gradient, or an extended phase transition region. Further work is required to decide whether Uranus and Neptune are adiabatic, subadiabatic, or superadiabatic.

Conclusions

In this chapter we have applied LM-REOS to calculate cooling curves of the outer planets assuming homogeneous evolution. The results obtained for the cooling time and luminosity qualitatively agree with previous work based on other equations of state and interior models. While the results for Jupiter and Neptune are surprisingly good, Saturn and Uranus are insufficiently described by homogeneous evolution. We therefore conclude that all four planets probably evolve inhomogeneously, and that in Jupiter and Neptune processes of opposite influence on the cooling time pretend validity of homogeneous evolution.

Important sources of inhomogeneity are sedimentation, core erosion, and phase transitions. However, even if accurate phase diagrams of H/He mixtures or other mixtures are available, there remain significant uncertainties regarding the process of He sedimentation itself. The theoretical description of the opposed process core erosion has just started to be developed and applied to planets. An accurate phase diagram of water is now available for planetary conditions; its modification due to impurities remains to be investigated and predictions for the evolution at this stage are speculative.

Acceptable interior structure models of these planets require –Uranus and Neptune in any case, Jupiter and Saturn depending on the EOS– an inhomogeneous distribution of metals in some range of transition pressures in order to satisfy the gravity field data. If we want to find realistic structure models that meet all observational constraints, we have to face the problem of simultaneously taking into account thin layer boundaries hindering particle transport but not heat transport, and eventually thick boundary layers hindering both particle and heat transport, He sedimentation, and core erosion. The presence of a layer boundary of metals in addition to that for He has not yet been investigated in literature. This will be addressed in future work.

Chapter 6

From the far past to the near future

Before we perspectively look into the near future (§ 6.4), we first have a look into the far past, when planets were young and bright (§ 6.1). We then rest at the present time and discuss more realistic structure models of Jupiter, Saturn, Uranus, and Neptune (§ 6.2 and § 6.3). Planetary science is currently progressing in vast steps thanks to modern observational techniques and generous funding for extrasolar planet hunters. In § 6.4 we exemplary consider GJ 436b and briefly discuss extrasolar planet modelling.

6.1 Giant Planet Formation

Research on the formation on giant planets has been persued with great intensity in the past years, partially spured by observations of circumstellar disks around young (proto-) stars, partially spured by nowadays sufficient computer power allowing to virtually observe the formation of astrophysical objects. Such objects range from galaxies and galaxy clusters to interstellar nebulae –the place of birth of young star clusters, down to the formation of single stars or brown dwarfs together with their surrounding disk and objects forming in the disk. These are the planets: giant planets as well as telluric planets.

Despite many open questions, some properties of giant planet formation are generally accepted. We list some of them:

- Giant planets form within a protoplanetary disk, not in isolation.
- Protoplanetary disks consist of gas and dust with an upper mass limit of about 5% that of the star. The gas disappears after ~ 10 Mio. or less years. This is the time span gas-rich giant planets have for growing to their final mass.
- The gas component is mainly made of H and He. The gas composition equals that of the star. This implies no alteration (diminishing) in metallicity by formation of metal-rich objects such as planetesimals or planets.
- Planetesimals contain mostly silicates, iron, and magnesium, and, depending on gas temperature, ices. The gas temperature decreases with orbital distance with a so-called snowline at about 300 K. Beyond the snowline, H_2O condenses enriching planetesimals with ice. Corresponding condensation regions for NH_3 and CH_4 are at larger distances than for H_2O.

- Planetesimals are dusty, extended objects with a broad range of masses. They can grow to several $M_\oplus$ by agglomeration of several other, smaller planetesimals or be destroyed by collision. If they grow or defractionate depends on relative velocities in the disk. Planetesimals can also trap some amount of gas.
- After the formation of massive planets, their gravity field competes with that of the parent star. The gravity field of the star decreases with $\sim 1/a^2$, where a is semi-major axes, and thus, depending on a, other objects of much lower mass (planetesimals, small rocky planets) can be strongly influenced in their orbital parameters by the gravity field of the more massive planets. At several AU from the parent star, even small eccentricities of low-mass objects can cause orbit-crossing with massive planets. The probability of being accelerated towards far outer regions of a stellar system by such events is much larger than the probability of being captured by a massive planet [LissauerEtAl95].

Several mechanisms have been proposed for the formation of giant planets. The most popular ones are formation by *core accretion* and formation by *disk-instability.*

Formation by core accretion

The core-accretion scenario was proposed by Mizuno (1980) and further developed by Pollack et al. (1996), and Alibert et al. (2005). It relies on fast formation of solid core embryos that themselves are able to accrete planetesimals, thereby growing to about $10M_\oplus$, such that surrounding gas is attracted. A gaseous envelope around the core forms, and the planet grows by accretion of both planetesimals and gas. Depending on migration velocity in the disk, i.e. the motion of the protoplanet perpendicular to its more or less circular orbit, this first phase of accretion may be fast (order of 10^6 years) [AlibertEtAl05] or slow (order of 10^7 years) [PollackEtAl96]. The short lifetime of protoplanetary disks thus gives strong support for the occurrence of planetary migration. Accreted planetesimals may either sink through a tenuous envelope down to the core enhancing its mass [PollackEtAl96] or dissolve in the envelope enriching it with heavy elements [AlibertEtAl05]. Which of these processes is favoured depends on the properties of both the planetesimals (size, density) and the envelope. Furthermore, since the planetesimal accretion rate is thought to decrease with time, and the gas accretion rate is thought to increase with time [AlibertEtAl05], compositional inhomogeneity with radius may occur. At the same time, the protoplanet is warming up by friction and compression of infalling material, its luminosity rises. When the energy loss due to radiation cannot be supplied anymore by gravitational energy gain from accreted material, the whole proto-planet starts to contract with an even enhanced gas accretion rate (runaway-growth). This is the phase where most of the mass of Jupiter-like planets is accreted, and where it heats up (warm start). Freshly accreted material will have the temperature of the surrounding disk, while central temperatures can attain several $10^4 - 10^5$ K. Hence, convection is general thought to take place in young planets homogenizing the envelope. Whether convection barriers due to initial compositional gradients can persist [ChaBar07], belongs to the unsolved questions regarding this scenario. The thermodynamic states during accretion of the envelope [PecWuch05] and the thermodynamic state of the final-mass planet [MarleyEtAl07] (the initial state for evolution calculations) are important and difficult-to-handle issues that will have to be investigated for future progress in understanding planet formation, and constraining their current state. Predictions of the core mass of Jupiter and Saturn range from $6M_\oplus$ to $15M_\oplus$, and envelope metallicities of $10-20\%$ are consistent with this scenario.

Formation by disk-instability

The gravitational disk-instability scenario [Boss97] suggests that giant planets form as a result of protoplanetary disk fragmentation in a similar way as stars form as a result of protostellar cloud

fragmentation. The driving mechanism for fragmentation are density fluctuations leading to gravitational instability of an extended, massive cloud. An important objection against the application of this scenario to planets is the unsolved question [HellSchu08] whether such gravitationally unstable planetary mass fragments can cool fast enough during contraction in order to remain bound objects and finally form proto-planets. Recently, Helled and Schubert (2008) applied this formation scenario to investigate the final core mass of Saturn- and Jupiter-sized planets. Without additional assumptions, gaseous giant planets formed by gravitational instability have no core and the mantle metallicity is that of the surrounding disk. However, depending on the initial state of the protoplanetary clumps, in particular the initial temperature, silicate grain settling can occur leading to the formation of small ($< 1\,M_\oplus$) rocky cores. Furthermore, as for the core accretion scenario, the accretion of planetesimals can strongly enhance the overall metallicity. Since it depends mostly on the size of the planetesimals accreted and the conditions in the protoplanetary disk, whether they dissolve within the envelope or sink down to the core, the resulting core mass is only roughly constrained to at most a few $M_\oplus$. Two interesting predictions [HellSchu08] of this scenario are (i) a core size decreasing with planetary mass due to larger interior temperatures acting against silicate or icy grain settling (in particular, water and methane are predicted not to occur in the core of Jupiter); and (ii) an envelope heavy element enrichment increasing with planetary mass including at least solar abundance in case of Jupiter and Saturn.

To complicate the situation further, observations indicate significant planet-disk, planet-planet, and planet-star interaction: close orbits $\ll 1$ AU indicate planet migration, far orbits > 100 AU indicate gravitational scattering, and super-Earths at very close orbits (CoRot-7b) indicate envelope evaporation. Fortunately, we are just at the beginning of an era of direct observations of young, forming planets. Two young giant planet candidates have already been detected. GQ Lupi [NeuhäuserEtAl05] and CT Cha [SchmidtEtAl08] with an age of respectively < 2 Myr and 2 ± 1 Myr have been directly imaged and their spectra analyzed in detail using various model atmospheres in order to derive information about $T_{\rm eff}$ and g (surface gravity). In contrast to all other (apart from microlensing) observational techniques of extrasolar planet detection, direct imaging requires a large planet-star separation in order to resolve the faint planet from the background of the luminous star. With for instance $a \approx 440$ AU in case of CT Cha, the usual mass determination by Keplerian motion can hardly be applied. Instead, theoretical evolution tracks are used to estimate the mass of the objects. However, the uncertainty in the initial conditions at a few Myr translates into a large uncertainty of the mass determination finding respectively $M_p = 1 - 42\,M_\oplus$ and $M_p \approx 17 \pm 6\,M_\oplus$ for the two giant planet candidates imaged so far.

Concluding, planet formation scenarios, theoretical initial states, observations of young, forming, and old, evolved planets, accurate model atmospheres, accurate EOS data, knowledge of time-dependent processes affecting the evolution are to be connected in order to achieve a major step forward in understanding planets. We choose a much simpler path and turn back to typified few-layer models of the outer planets.

6.2 Core erosion

In § 4 we investigated core mass and metallicity of Jupiter, Saturn, Uranus, and Neptune. Underlying interior models presented in this Thesis and in literature are based on the state-of-the-art assumptions of envelope metals being ices and rocks (this work: water) and a core of rocks, overlayed by an ice shell (this work: pure rocks or pure ices). A common feature of Uranus and Neptune models is a large inner envelope metallicity, in our case up to ∼95% in mass, bringing it close to an ice shell. The small rocky core of Uranus and Neptune models together with this almost-ice shell resembles a large core. With $0-2.5\ M_\oplus$ (Neptune: $4M_\oplus$) central rocks and $9-12\ M_\oplus$ of envelope H_2O in Uranus (Neptune: $12-14.5\ M_\oplus$), this gives a central mass of heavy elements of $\sim 11.5M_\oplus$ for Uranus and $\sim 14.5M_\oplus$ for Neptune. Let us call this mass $M_{Z,23}$, the mass of the Z-component

in layers 2 and 3. It is in good agreement with the core mass predicted by core accretion formation models by Pollack et al. (1996), and somewhat larger than the more recent ones by Alibert et al. (2005), see § 6.1. Uranus' and Neptune's $M_{Z,23}$ is larger than Jupiter's M_{core} (if we neglect the solitaire Militzer and Hubbard model). Hence, an obvious consequence is the following hypothesis:

Giant planets in the solar system formed by core accretion with an initial core mass of $5 - 15 M_\oplus$. *A deviation of their present core mass from this value indicates dissolving of initial core material within the deep interior, and* not *an inconsistency with core accretion formation.*

This dissolving of core material may have happened in the early hot stages of the evolution or within a continuous, slowly progressing process. To explain relatively small Jupiter core masses, Saumon & Guillot (2004) for instance suggest a larger mixing of core material in Jupiter than in Saturn due to a larger gas accretion rate during formation; in this sense, the high metallicity of Uranus' and Neptune's inner envelope would imply weak core erosion and thus a small gas accretion rate in agreement with their relatively small total H/He mass fraction of 10-20%.

A small Jupiter core today can also be explained by continuous, slow erosion. If the proto-core contained ice, this ice at present Jupiter core conditions of ~ 20000 K and > 40 Mbar would be in the plasma phase [FrenchEtAl09] which is soluble with hydrogen. However, we do not know how fast such an ice-enriched H/He/ice mixture can be redistributed by convection. Instead, a deep layer of H/He/ice can form which is stable against convection due to a compositional gradient. Note that an extended compositional gradient is not a preferred solution because of Jupiter's large heat flux strongly pointing to large-scale convection. Note furthermore that an upward transport of core material would shorten the cooling time because of gravitational energy gain. Thus by § 5.3, this mechanism is a candidate to counteract the prolongation of Jupiter's cooling time if calculated through inhomogeneous evolution.

We examine the probability that Jupiter once had a central agglomeration of $\sim 10 M_\oplus$ of heavy elements that has become eroded and at present time resides in a central region. For this we use a very simplified model and LM-REOS. We assume a central region containing H/He and H_2O in the same relative fraction as in the usual deep envelope and vary the fraction of rocks in the central region. The result is shown in Fig. 6.1, where the curve of interest is the *dashed line*.

It turns out that for rock mass fractions $X_{R,\,core}$ between 100 and 60% in the central region, the mass $M_{Z,\,core} := M_{R,\,core} + M_{H_2O,\,core}$ of heavy elements is essentially unaffected. In order to obtain $M_{Z,\,core} \geq 10 M_\oplus$, a reduction in $X_{\mathrm{R,\,core}}$ down to $< 20\%$ is required. These models have more than $30 M_\oplus$ H/He in the central region, the pressure at the core-mantle boundary decreases from 39 to 23 Mbar, and the core region grows from $\sim 1 R_\oplus$ to $> 3 R_\oplus$. We conclude that the presence of several $M_\oplus$ of residual core material in Jupiter's deep interior is highly unlikely. Eroded core material more probably has dissolved completetly in the inner envelope.

On the other hand, even a relatively small amount of eroded core material has a significant effect on Z_1 and Z_2. A larger core region tends to enhance J_2 which in turn forces the fitting procedure to smaller inner envelope metallicities Z_2. In order to keep also $|J_4|$ at constant value, which decreases with smaller Z_2, Z_1 must become larger by some ΔZ_1. For $X_{R,\,core} < 0.2$ we find $\Delta Z_1 > 50\%$. Hence, eroded core models offer an appealing possibility to bring Jupiter's Z_1 in better agreement with the observed atmospheric heavy element enrichment (§ 4.1.5).

Concluding, the core mass and inner envelope metallicity of the four outer planets is consistent with a similar initial core mass of $\approx 10\, M_\oplus$. Deviations by present structure models from this value can be explained by core erosion. Eroded core material in Jupiter either has completely dissolved within the inner envelope or does not exceed a few $M_\oplus$.

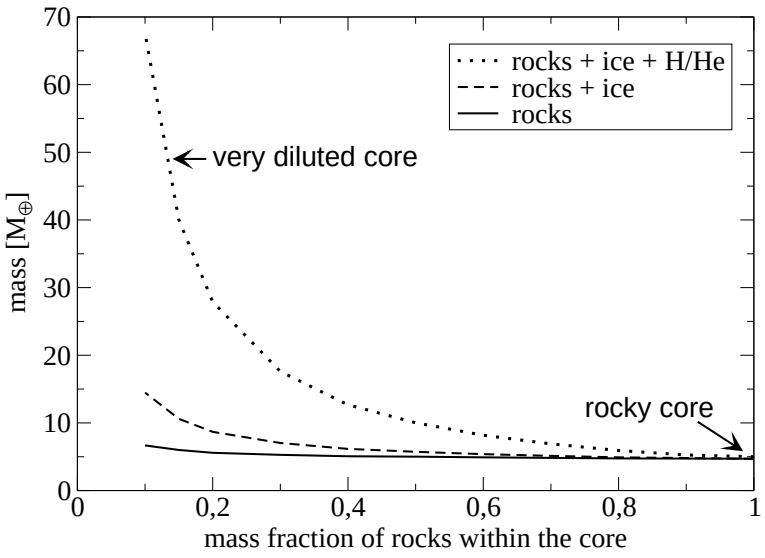

Figure 6.1: Core mass of Jupiter assuming an isothermal core of H/He, water, and rocks with varying rock mass fraction. For all underlying models, the water to H/He mass ratio in the core is the same as in the inner envelope. The rock mass fraction in the core is varied between 100% (usual rocky core) and 10% (very diluted core). *Solid line*: mass of rocks in the core, *dashed line*: mass of rocks and water in the core, *dotted line*: total core mass. This figure is published in [ForNett09].

6.3 Layer boundaries

We have seen that the position of a layer boundary can largely influence the resultant core mass and metallicity. Here we discuss the number of layers reasonably assumed.

Four-layer models of Saturn

As an example for next generation interior structure models we consider Saturn in detail. In § 5.3.2 we concluded that present Saturn probably has four layers: a He depleted outer envelope, a He enriched inner envelope, a He-layer surrounding the core, and a core of rocks and/or ices. Some mass shells close to the first layer boundary may be inhomogeneous due to He sedimentation with a molecular weight gradient shallow enough not to inhibit convection. This conclusion was derived from preliminary inhomogeneous evolution calculations based on new H/He phase separation curves obtained from FT-DFT-MD simulations. In § 4.2.2 we concluded that most probably there is a heavy element discontinuity between 1 and 4 Mbar.

Putting things together, the inevitable question arises about the total number of layers and the coincidence of layer boundaries regarding He and regarding metals. H/He phase separation certainly affects the distribution of metals [SteSal77], but if it can explain Z_2 up to $3 \times Z_1$ as obtained with LM-REOS (§ 4.2.2) has not been shown. Giant planet formation scenarios (§ 6.1) on the other hand can explain a strong heavy element enrichment in the deep interior due to a dust/planetesimal accretion rate decreasing with time in favour of the gas accretion rate (core accretion scenario) or due to silicate sedimentation in the early cold stages of planet formation (disk instability scenario). Hence, it seems reasonable to assume for present Saturn a permanent layer boundary regarding metals around 1−4 Mbar as a relict from formation, and a strongly time-dependent layer boundary between the deep H-He-metals envelope and the He-layer surrounding the core. Remember that the He-layer grows, when the immiscibility region extends deeply enough

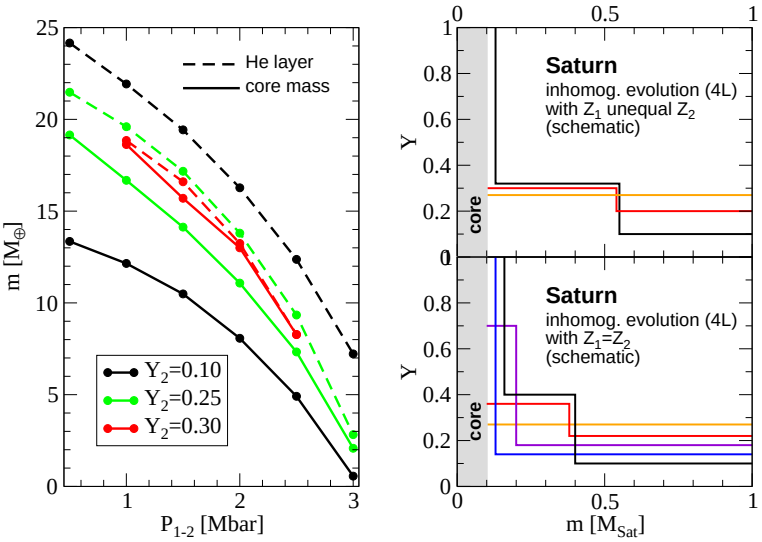

Figure 6.2: 4-layer models of Saturn with He layer.

Left panel: M_{core} (*solid lines*) and M_{core}+ mass of He layer (*dashed lines*) in $M_\oplus$ for various transition pressures P_{1-2} and three values of Y_2. For all models, $Y_1 = 0.18$ and calculations (July 2008) with the 2 bugs. Z_1 and Z_2 are chosen to match J_2 and J_4.

Right panels: Schematic He distribution of 4-layer Saturn models during inhomogeneous evolution matching present time constraints (*upper right panel*) or predicted by H/He separation curves neglecting a heavy element discontinuity (*lower right panel*). *Orange curves:* constant He abundance before onset of He sedimentation, *black:* possible present time distribution, *red, violet, blue*: intermediate curves in this time-order.

down, otherwise sinking He droplets just enrich the He-enriched layer above the He-layer.

Consequently we assume the following four-layer structure type. It has two convective H-He-metals envelopes. The masses of heavy elements $M_{1,Z} = Z_1 * M_1$ and $M_{2,Z} = Z_2 * M_2$ in the envelopes and M_{core} are relicts from formation. As usual, Z_1 and Z_2 are obtained by the condition to meet J_2 and J_4. In the outer two envelopes, H/He phase separation is happening leading to $Y_1 < \bar{Y}$ and $Y_2 > \bar{Y}$ at present time. The position of the layer boundary P_{1-2} is given by the condition to conserve $M_{1,Z}$ and $M_{2,Z}$, not by the H/He phase diagram. Within the convective envelopes, sinking He is redistributed and may be inhomogeneous in some region. Values Y_1 and Y_2 are thus meant as average values within the layers. The He layer is taken into account by setting $Y_3 = 1$ and $\bar{Y}$ conserved by the choice of P_{2-3}. This structure type has the potential to give interior models that are equally consistent with J_2, J_4 and the new H/He demixing curves. Whether this model is also able to reproduce Saturn's luminosity or not, remains a fascinating question.

Results for M_{core} and the mass of the He-layer are shown in Fig. 6.2 (*left panel*). Clearly, the more He we arbitrarily put into layer No. 2, e.g. 25%, the less He remains to form a He-layer around the core. The most interesting property of the 4-layer structure models is the impossibility of a He layer already for $Y_2 \simeq 30\%$. This is, because with $1-3$ Mbar, the first layer boundary is further out than the end of the demixing region (illustrated in the *upper right panel, black curve*), and thus M_2 and $Y_2 * M_2$ become relatively large, reducing the amount of He in the core region (Fig. 4.5). From these models we conclude a significantly smaller central condensation, and consequently a much smaller gravitational energy release as when we allow He to sink below the end of the demixing

region (*lower right panel*). This would greatly help to obtain a more moderate prolongation of Saturn's cooling time as in case of the preliminary inhomogeneous calculations of § 5.3.2.

Since the evolution of the He distribution is crucial for the cooling time, I give a schematic illustration in Fig. 6.2. In the upper right panel we see the predicted He distribution of 4-layer models before He sedimentation (*orange*), today (*black*), and in between (*red*), in each case with $Z_1 \neq Z_2$; in the lower right panel we see the He distribution as predicted by inhomogeneous evolution described in § 5.3, i.e. when the position of the layer boundary coincides with the end of the demixing region, and $Z_1 = Z_2$. The stronger central condensation enhancing the gravitational energy release is clearly seen.

Four-layer models for other planets

In Jupiter, a He-layer is not expected to exist. Jupiter's core region may be partially eroded and best described by a corresponding 4-layer structure type. However, partial core erosion can hardly be distinguished from core erosion as discussed in § 6.2, and hence a three-layer structure type with $Z < 1$ in the core region should be most reasonable. As for Saturn, the formation process itself offers an explanation for a discontinuity in metals.

In metal-rich giant planets, such as Uranus and Neptune, in addition to the formation process also phase transitions of ices or of rocks may cause layer boundaries. In case of Uranus and Neptune, magnetic field models and seismic data can help to constrain the models further in the next ten years (near future). Recent models of Uranus and Neptune's magnetic field [StaBlo06] predict four layers: a central core (layer 4), either a conducting, fluid, and non-convecting extended shell, or an isolating and solid extended shell (layer 3), a conducting and convecting thin shell (layer 2), and some isolating outer layer occupying 20-25% of the radius.

Concluding, if all constraints from observations, evolution theory, theoretical EOS data and H-He mixing behaviour, formation, and magnetic field theory are to be satisfied, the three-layer structure type has outgrown its use for the outer planets, apart maybe from Jupiter. As long as the assumption of four layers does not conflict with any constraints, it seems the most reasonable one, while we must have in mind to consider homogeneous abundances as average values within a layer.

6.4 Extrasolar Planets

Extrasolar planets have become a rapidly evolving research field, with many surprising findings in the past years and many more expected to be found in the near future.

If modelling detected extrasolar giant planets, special care has to be taken of several properties that are not important for solar giant planets, and other properties on the other hand are not (yet) available. Among the properties potentially relevant for this class of objects are, for instance, strong irradiation by the parent star, evaporation, tidal forces and tidal heat dissipation, and bound rotation[1].

Out of the observational constraints described in § 3.1 and § 5, we have M_p, R_p, T_{eq}, τ_p, and in rare cases also $T_{\rm eff}$. In this section I choose the Neptune-mass planet GJ436b ($M_p = 23\,M_\oplus, R_p = 4.2\,R_\oplus$) to show that modelling the atmosphere would extremely help constraining that planet's H-He content, and thus to decide about it being a Super-Earth or not. Series C and D in Fig. 6.3

[1] Bound rotation of planets has been suggested already in the 5th century BC by some greek man called Philolaos who developed the hypothesis of Earth rotating around a fire located at the center of the universe that illuminates the stars, the planets and the moon. But just because of bound rotation of the spherical Earth, we cannot directly see the fire [Kan91].

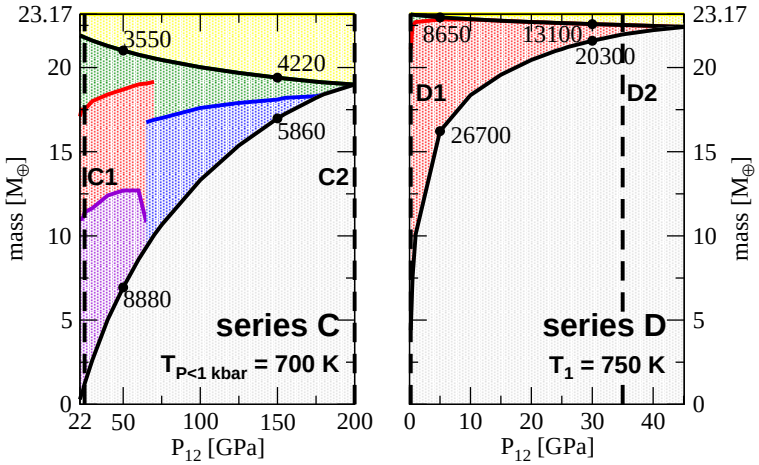

Figure 6.3: Mass distribution between the three layers under variation of the transition pressure P_{12}. Numbers close to filled black circles denote the temperature in K for two selected models per series.

are three-layer models assuming a rocky core overlayed by an adiabatic water shell, overlayed by an adiabatic H-He envelope. The surface temperature is taken to be 700 K, and the series just differ in the temperature profile below 1 kbar, where series C assumes an isothermal atmosphere due to irradiation. Obviously, this assumption leads to significantly colder internal temperatures with even the possibility of superionic water (*blue shaded*). In this figure, *green* indicates molecular water, *red* water plasma, *violet* a water phase transition region, *yellow* the H-He envelope, and *grey* core material. Super-Earth models are possible in case of an adiabatic profile throughout the thin H-He atmosphere. Heavily water rich solutions might be excluded by formation theory. This figure is taken from [NettKraRedNeu09].

These simple models of an extrasolar planet confirm my conclusion that progress in constraining the interior structure of giant planets needs to combine all available information with various calculations: the atmospheric boundary condition, gravity field data, structure type assumptions such as the number of layers, the cooling behaviour, formation theory, and equations of state. The additional method of statistics will be contributed by astrophysical observations in the near future.

Chapter 7

Summary

EOS During the course of my PhD time, several hydrogen equations of state in the chemical and in the physical picture have been developed and applied to Jupiter. Among them, H-REOS shows best consistency both with available laboratory data and astrophysical observational constraints. H-REOS, supplemented by He-REOS and H_2O-REOS, constitute the first ab initio data based equations of state extensively applied to giant planet interior models.

Methods Available observational quantities constraining interior model and evolution calculations were presented and discussed, and the theoretical background including the standard Theory of Figures explained in detail.

Transition pressure Assuming three-layer models, I demonstrated a great influence of the location of the layer boundary on resulting values of the envelope metallicities Z_1 and Z_2, the core mass M_{core}, and the range of possible solutions. Since M_{core} in turn responds to Z_1 and Z_2, and Z_2 to Z_1 when adjusting the observational constraints, the response of the core mass to the transition pressure P_{1-2} strongly depends on the EOS used. In particular, Jupiter models with LM-REOS are acceptable if $P_{1-2} \approx 8\,\mathrm{Mbar}$, Saturn models if $P_{1-2} \approx 1-3\,\mathrm{Mbar}$, and Uranus and Neptune models if $P_{1-2} \approx 0.1 - 0.3\,\mathrm{Mbar}$.

Jupiter Equations of state applied in this work yield $M_{core} = 0 - 10\,M_\oplus$ compared to $0 - 18\,M_\oplus$ in the literature. Preferred models with LM-REOS have $M_{core} = 0 - 3\,M_\oplus$. Small core masses together with the phase diagram of water suggest erosion of an initial ice shell around a rocky core. Diluted core models imply that an initial ices shell, if exceeding a few $M_\oplus$, has dissolved in the inner envelope. Preferred models have at most solar metallicity envelopes and motivate further studies on the effect of non-linear mixing between H and He and on the possibility of a superadiabatic temperature gradient.

Homogeneous evolution reproduces Jupiter's intrinsic luminosity L_{int}, but the measured atmospheric He abundance indicates active He sedimentation. In the near future, inhomogeneous evolution calculations will be performed taking this effect into account. To reduce the expected prolongation of cooling time, core erosion should be taken into account as well.

Saturn We investigated Saturn with respect to M_{core}, the atmospheric He abundance Y_1, and Z_1. We found M_{core} to range from $0 - 20\,M_\oplus$, and $Y_1 \approx 10\%$ in order to achieve $Z_1 \approx 3Z_\odot$. This is significantly less than the most recent measurement-based value of $Y_1 = 18\%$.

A more accurate determination of M_{core} is hampered by the uncertainty in the location of a layer boundary between outer and inner envelope. Gravity field data for Saturn require to place the layer boundary deep into the planet, thereby increasing the ambiguity between a mass-less (massive) core and high-metallicity (low-metallicity) deep envelope.

For progress on Saturn's internal structure, the strategy I suggest is to calculate inhomogeneous evolution in the framework of a four-layer structure type (i) in a consistent way with H/He phase separation curves based on ab initio data, (ii) including delayed sedimentation adjusted to reproduce the observed L_{int}, and (iii) by fixing the outermost layer boundary for metals not in accordance with the H/He diagram but in order to meet L_{int}. This strategy should help to estimate the presence of further effects (case i), the process of sedimentation (case ii), and the real position of a density discontinuity on metals (case iii).

Uranus and Neptune The standard three-layer structure type yields similar ranges of solutions for Uranus and Neptune. Heavy elements, most likely water, contribute to the inner envelope up to 95% in mass and up to 50% in particle number fraction. Especially for Uranus, the long cooling time derived from homogeneous evolution points to inhibited convection, possibly a result of a large density gradient or of a phase transition in water. Their internal temperatures may rise sub- or superadiabatically.

Future work on Uranus and Neptune should (i) tackle the implementation of heat transport through diffusive layers, and (ii) include a determination of the electric conductivity along the interior profiles as input into dynamo models.

Though in the near future space missions are not planned that could motivate further studies on Uranus and Neptune, progress in ab initio EOS data for ices, rocks and their mixtures needs application. Furthermore, the interior of illuminated Neptune-like extrasolar planets will stay in darkness as long as Uranus and Neptune do.

Formation Jupiter and Saturn interior models are consistent with recent updates of the core accretion scenario and the gravitational instability scenario of giant planet formation.

EGPs Extrasolar giant planets impose challenges beyond the focus of this work, such as radius anomalies and irradiated atmospheres. Simple three-layer models for metal-rich planets already reveal the importance of an accurate determination of the atmospheric temperature profile in order to discriminate between Super-Earths with thin H-He layer and water-rich giant planets with thick H-He atmosphere.

Bibliography

[AdaSeaElk08] Adams E.R., Seager S., and Elkins-Tanton L. (2008), ApJ. 673, 1160
Ocean planet or thick atmosphere: on the mass-radius relationship for solid exoplanets with massive atmospheres

[AlibertEtAl05] Alibert Y., Mordasini C., Benz W., and Winisdoerffer C. (2005), ApJ 434, 343
Models of Giant Planet formation with migration and disc evolution

[AnGrev89] Anders E. and Grevesse N. (1989), Geochim. Cosmochim. Acta 53, 197
Abundances of the elements: Meteoritic and solar

[AndSchu07] Anderson J.D. and Schubert G. (2007), Science 317, 1384
Saturn's gravitational field, internal rotation, and interior structure

[BahPin95] Bahcall J.N. and Pinsonneault M.H. (1995), Rev. Mod. Phys. 67, 781
Solar models with helium and heavy-element diffusion

[BaraffeEtAl03] Baraffe I., Chabrier G., Barman T.S., Allard F., and Hauschildt P. (2003), A&A 402, 701
Evolutionary models of cool brown dwarfs and extrasolar giant planets. The case of HD209458

[BarChaBar08] Baraffe I., Chabrier G., and Barman T.S. (2008), A&A 482, 315
Structure and Evolution of super-Earth to super-Jupiter exoplanets: heavy element enrichment in the interior

[BlaGriVos04] Blaschke D., Grigorian H., and Voskresensky D.N. (2004), A&A 242, 979
Cooling of Neutron stars. Hydronic model

[Boss97] Boss A.P. (1997), Science 276, 1836
Giant planet formation by gravitational disk instability

[BurrowsEtAl97] Burrows A., Marley M., Hubbard W.B., Lunine J.I., Guillot T., Saumon D., Freedman R., Sudarsky D., and Sharp C. (1997), ApJ 491, 856
A nongrey theory of extrasolar giant planets and brown dwarfs

[CamAnd89] Campbell J.K. and Anderson (1989), Astronom. J., 97, 1485
Gravity field of the Saturnian system from Pioneer and Voyager tracking data

[CamSyn85] Campbell J.K. and Synnott S.P. (1985), Astronom. J., 90, 364
Gravity field of the Jovian system from Pioneer and Voyager tracking data

[ChaSauHubbLun92] Chabrier G., Saumon D., Hubbard W.B., and Lunine J.I. (1992), ApJ 391, 826
The molecular-metallic transition of hydrogen and the structure of Jupiter and Saturn

[ChaBar07] Chabrier, Baraffe (2007), ApJ 661, L81
Heat transport in (exo)planets: a new perspective

[ConrathEtAl87] Conrath B.J., Gautier D., Hanel R., Lindal G., and Marten A. (1987), J. Geophys. Res. 92, 15003
The helium abundance of Uranus from Voyager measurements

[ConGau00] Conrath B.J. and Gautier D. (2000), Icarus 144, 124
Saturn Helium Abundance: A Reanalysis of Voyager Measurements

[DeMarcus58] DeMarcus W.C. (1958), Astronom. J 63, 2
The constitution of Jupiter and Saturn

[FeiWag06] Feistel R. and Wagner W., J. Phys. Chem. Ref. Data 35, 1021 (2006)
A new Equation of State for H_2O Ice Ih

[ForHubb03] Fortney J.J. and Hubbard W.B. (2003), Icarus 164, 228
Phase Separation in Giant Planets: Inhomogeneous evolution of Saturn

[ForHubb04] Fortney J.J. and Hubbard W.B. (2004), ApJ 608, 1039
Effects of helium phase separation on the evolution of extrasolar giant planets

[ForNett09] Fortney J.J. and Nettelmann N. (2009), Springer Space Science Review, workshop proceedings
The Interior Structure, Composition, and Evolution of Giant Planets

[FrenchEtAl09] French M., Mattsson T.M., Nettelmann N., and Redmer R. (2009), Phys. Rev. B 79, 054107
Equation of state and phase diagram of water at ultrahigh pressures as in planetary interiors

[FriedEtAl02] Fried L.E., Howard W.M., and Souers P.C. (2002) in 'Technical Papers of the 12th Int. Detonation Symposium' San Diego
Exp6: A new equation of state library for high pressure thermochemistry

[GautierEtAl95] Gautier D., Conrath B.J., Owen T., De Pater I., and Atreya S.K. (1995) in *Neptune and Triton*, 547, Cruishank D.P. (Eds.), University of Arizona, Tucson, *The Troposphere of Neptune*

[GraboskeEtAl75] Graboske H.C.Jr., Pollack J.B., Grossman A.S., and Olness R.J. (1975), ApJ 199, 265
The structure and evolution of Jupiter – the fluid contraction stage

[GudZha99] Gudkova T.V. and Zharkov V.N. (1999), Planet. Space Sci. 47, 1201
Models of Jupiter and Saturn after Galileo mission

[GuiChaMorGau94] Guillot T., Chabrier G., Morel P., Gautier D. (1994), Icarus 112, 354
Nonadiabatic models of Jupiter and Saturn

[GuiChaGauMor95] Guillot T., Chabrier G., Gautier D., and Morel P. (1995), ApJ 450, 463
Effect of radiative transport on the evolution of Jupiter and Saturn

[GuiGauHubb97] Guillot T., Gautier D., and Hubbard W.B. (1997), Icarus 130, 534
New Constraints on the Composition of Jupiter from Galileo Measurements and Interior Models

[Guillot99] Guillot T. (1999), Planet. Space Sci. 47, 1183
A comparison of the interiors of Jupiter and Saturn

[GuiSteHubbSau03] Guillot T., Stevenson D.J., Hubbard W.B., and Saumon D. (2004), In: Bagenal F., Dowling T.E., McKinnon W.B. (Eds.), Jupiter: The Planet, Satellites, and Magnetosphere, Cambridge University Press, Cambridge, UK, *The Interior of Jupiter.*

[Guillot05] Guillot T. (2005), Ann. Rev. Earth & Plan. Sciences 33, 493
The Interior of Giant Planets: Models and Outstanding Questions

[HellingEtAl08] Helling Ch., Dehn m., Woitke P., and Hauschildt P.H. (2008), ApJ 675, L105
Consistent Simulations of Substellar Atmospheres and Nonequilibrium dust cloud formation

[HellSchu08] Helled R. and Schubert G. (2008), Icarus 198, 156
Core formation in giant gaseous protoplanets

[HellSchu09] Helled R. and Schubert G. (2009), ApJ 697, 1256
Heavy-element enrichment of a Jupiter-mass protoplanet as a function of orbital location

[HolNettRed07] Holst B., Nettelmann N., and Redmer R. (2007), Contrib. Plasma Phys. 47, 368
Equation of state for dense hydrogen and plasma phase transition

[HolRedDes08] Holst B., Redmer R., and Desjarlais M.P. (2008), Phys. Rev. B 77, 184201
Thermophysical properties of warm dense hydrogen using quantum molecular dynamics simulations

[Hubbard68] Hubbard W.B. (1968), ApJ 152, 745
Thermal structure of Jupiter

[Hubbard69] Hubbard W.B. (1969), ApJ 155, 333
Thermal models of Jupiter and Saturn

[Hubbard70] Hubbard W.B. (1970), ApJ 162, 687
Structure of Jupiter: Chemical composition, contraction, and rotation

[Hubbard74] Hubbard W.B. (1974), Icarus 21, 157
Inversion of Gravity Data for Giant Planets

[Hubbard77] Hubbard W.B. (1977), Icarus 30, 305
The Jovian Surface Condition and Cooling Rate

[Hubbard78] Hubbard W.B. (1978), Icarus 35, 177
Comparative evolution of Uranus and Neptune

[Hubbard84] Hubbard W.B. (1984), *Planetary Interiors* (Van Nostrand Reinhold Company)

[HubbMar89] Hubbard W.B. and Marley, M.S. (1989), Icarus 78, 102
Optimized Jupiter, Saturn, and Uranus Interior Models

[HubbPodSte95] Hubbard W.B., Podolak M., and Stevenson D.J. (1995) in *Neptune and Triton*, 109, Cruishank D.P. (Eds.), University of Arizona, Tucson,
The Interior of Neptune

[Jacobson03] Jacobson R.A. (2003) JUP230 orbit solution, http://ssd.jpl.nasa.gov/?gravity_fields_op

[Juranek04] Juranek H. (2004), PhD Thesis, Universität Rostock
Zustandsgleichung von Wasserstoff bei hohen Drücken im Mbar-Bereich

[JuranekEtAl05] Juranek H., Nettelmann N., Kuhlbrodt S., Schwarz V., Holst B., and Redmer R. (2005), Contrib. Plasma Phys. 45, 432
Metal-Nonmetal Transition in Dense Plasmas

[Kan91] Kanitscheider B. (1991), Reclam Universalbibliothek Nr. 8025
Kosmologie. Geschichte und Systematik in philosophischer Perspektive

[Kerley03] Kerley G.I. (2003), Sandia National Laboratories Rep. SAND2003-3613 (Albuquerque: Sandia)
Equation of State for Hydrogen and Deuterium

[Kerley04a] Kerley G.I. (2004a), Kerley Tech. Services Research Rep. KTS04-1 (Appomattox: Kerley)
Structures of the planets Jupiter and Saturn

[Kerley04b] Kerley G.I. (2004b), Kerley Tech. Services Research Rep. KTS04-2 (Appomattox: Kerley)
An Equation of Sate for Helium

[KippWei94] Kippenhahn R. and Weigert A. (1994), A&A Library, Springer-Verlag Berlin Heidelberg
Stellar Structure and Evolution

[KietzmannEtAl07] Kietzmann A., Holst B., Redmer R., Desjarlais M.P., and Mattsson T.R. (2007), Phys. Rev. Lett. 98, 190602
Quantum molecular dynamics simulations for the nonmetal-to metal transition in fluid helium

[KlepeisEtAl91] Klepeis J.E., Schafer K.J., Barbee T.W., and Ross M. (1991), Science 254, 986
Hydrogen-helium mixtures at megabar pressures - Implications for Jupiter and Saturn

[Kramm08] Kramm U. *The Love numbers of Jupiter*, Studienarbeit (2008)

[Lindal85] Lindal G.F., Sweetnam D.N., and Eshleman V.R (1985), Astronom. J. 90, 1136
The atmosphere of Saturn - an analysis of the Voyager radio occultation measurements

[Lindal92] Lindal (1992), Astronom. J. 103, 967
The atmosphere of Neptune: An analysis of radio occultation data required with Voyager 2

[LissauerEtAl95] Lissauer J.J., Pollack J.B., Wetherhill G.W., and Stevenson D.J. (1995), in *Neptune and Triton*, 547, Cruishank D.P. (Eds.), University of Arizona, Tucson,
Formation of the Neptune System

[LiuGolSte08] Liu J., Goldreich P.M., and Stevenson D.J. (2008), Icarus 196, 653
Constraints on deep-seated zonal winds inside Jupiter and Saturn

[Lodders03] Lodders K. (2003), ApJ 591, 1220
Solar System Abundances and Condensation Temperatures of the Elements.

[LorHolRed09] Lorenzen W., Holst B., and Redmer R. (2009), Phys. Ref. Lett. 102, 5701
Demixing of Hydrogen and Helium at Megabar Pressures

[MarleyEtAl07] Marley M.S., Fortney J.J., Hubickyj O., Bodenheimer P., and Lissauer J.I. (2007), ApJ 655, 541
On the Luminosity of Young Jupiters

[MattDes06] Mattsson T.R. and Desjarlais M.P. (2006), Phys. Rev. Lett. 97, 017801
Phase diagram and electrical conductivity of high energy-density water from density functional theory

[MilitzerEtAl08] Militzer B., Hubbard W.B., Vorberger J., Tamblyn I., and Bonev S.B. (2004), ApJ 688, L54
A massive Core in Jupiter predicted by First-Principles Simulations

[MilHubb09] Militzer B. and Hubbard W.B. (2009), Astrophys. and Space Sci. 322, 129
Comparison of Jupiter Interior Models Derived from First-Priciples Simulations

[Mizuno80] Mizuno H. (1980), Prog. Theoret. Phys. 64, 544
Formation of the Giant planets

[MouAliBen06] Mousis O., Alibert Y., and Benz W. (2006), A&A 449, 411
Saturn's internal structure and carbon enrichment

[NASA/Caltech] source: NASA/Caltech (2004)
http://www.solarviews.com/cap/index/oortcloud1.html

[NellisEtAl83] Nellis W.J., Mitchell A.C., van Thiel M., Devine G.J., and Trainor R.J. (1983), J. Chem. Phys.79, 1480
Equation-of-state data for molecular hydrogen and deuterium at shock pressures in the range 2-76 GPa

[NettRedBla08] Nettelmann N., Redmer R., and Blaschke D. (2008), Phys. Particles Nuclei Lett. 39, 1122
Warm dense matter in planets and exoplanets

[NettelmannEtAl08] Nettelmann N., Holst B., Kietzmann A., French M., Redmer R., and Blaschke D. (2008), ApJ 683, 1217
Ab initio equation of state data for hydrogen, helium, and water and the internal structure of Jupiter

[NettKraRedNeu09] Nettelmann N., Kramm U., Redmer R., and Neuhäuser R., *submitted* to A&A (2009)
Interior structure models of GJ436b

[NeuhäuserEtAl05] Neuhäuser R., Guenther E.W, Wuchterl G., Mugrauer M., Bedalov A., and Hauschildt P. (2005), A&A 435, L13
Evidence for a co-moving sub-stellar companion of GQ Lup

[Nolting90] Nolting W., Grundkurs Theoretische Physik, Band 3, Verlag Zimmermann-Neufang, Ulmen (1990)
Elektrodynamik

[PecWuch05] Pecnik B. and Wuchterl G. (2005), A&A 440, 1183
Giant planet formation

[Peebles64] Peebles P.J.E. (1964), ApJ 140, 328
The structure and composition of Jupiter and Saturn

[PfaHohBal95] Pfaffenzeller O., Hohl D., and Ballone P. (1995), Phys. Rev. Lett. 74, 2599
Miscibility of Hydrogen and Helium under Astrophysical conditions

[PollackEtAl96] Pollack J.B., Hubickyj O., Bodenheimer P., Lissauer J.J., Podolak M., and Greenzweig Y. (1996), Icarus 124, 62
Formation of the Giant Planets by Concurrent Accretion of Solids and Gas

[PodRey81] Podolak M. and Reynolds T. (1981), Icarus 46, 40
On the Structure and Composition of Uranus and Neptune

[PodPodMar00] Podolak M., Podolak J.I., and Marley M.S. (2000), Planetary and Space Science 48, 143
Further investigation of random models of Uranus and Neptune

[RedmerEtAl06a] Redmer R., Holst B., Juranek H., Nettelmann N., and Schwarz V. (2006), J. Phys. A: Math. Gen. 39, 4479
Equation of state for dense hydrogen and helium: application to astrophysics

[RedmerEtAl06b] Redmer R., Juranek H., Nettelmann N., and Holst, B. (2006), in AIP Conf. proceedings, 845: 127,
Warm dense hydrogen in the chemical picture

[RedmerEtAl09] Redmer R., Nettelmann N., Kramm U., Holst B., Lorenzen W., and French M. (2009), Nashville Conf. proceed. *submitted*
Interior of solar and extrasolar giant planets

[Ree88] Ree F.H. (1988) in 'Shock Waves in Condensed Matter 1987' New York, Elsevier
Phase changes and chemistry at high pressures and temperatures

[Ross98] Ross M. (1998), Phys. Rev. B 58, 669
Linear-mixing model for shock-compressed liquid deuterium

[Salpeter73] Salpeter E.E. (1973), ApJ 181, L83
On convection and gravitational layering in Jupiter and in stars of low mass

[SalSte75] Salpeter E.E. and Stevenson D.J. (1975), The Physics of Fluids, 19, 502
Heat transport in a stratified two-phase fluid

[SauHubbChaHor92] Saumon D., Hubbard W.B., Chabrier G., and van Horn H.M. (1992), ApJ 391, 827
The role of the molecular-metallic transition of hydrogen in the evolution of Jupiter, Saturn, and brown dwarfs

[SauChaHor95] Saumon D., Chabrier G., and van Horn H.M. (1995), ApJ 99, 713
An equation of state for low-mass stars and giant planets

[SauGui04] Saumon D. and Guillot T. (2004), ApJ 609, 1170
Shock Compression of Deuterium and the Interiors of Jupiter and Saturn

[SchmidtEtAl08] Schmidt T., Neuhäuser R., Seifahrt A., Vogt N., Bedalov A., Helling Ch., Witte S., and Hauschildt P.H. (2008), A&A 491, 311
Direct evidence of a sub-stellar companion around CT Chamaeleontis

[SchwHauBar00] Schweitzer A., Hauschildt P.H., and Baron E. (2000), ApJ 541, 1004
Non-LTE treatment of molecules in the atmospheres of cool stars

[SESAME table (1992)] SESAME database: The Los Alamos National Laboratory Equation of State Database (1992), LANL report No. LA-UR-92-3407, Lyon S.P. and Johnson J.D. (eds.)

[StaBlo06] Stanley S. and Bloxham J. (2004), Nature 428, 151
Convective region geometry as the cause of Uranus' and Neptune's unusual magnetic field geometry

[Stevenson75] Stevenson D.J. (1975), Phys. Rev. B 12, 3999
Thermodynamics and phase separation of dense fully ionized hydrogen-helium fluid mixtures

[SteSal77] Stevenson D.J. and Salpeter E.E. (1977), ApJS 35, 239
The dynamics and helium distribution in hydrogen-helium fluid planets

[Stevenson82] Stevenson D.J. (1982), Ann. Rev. Earth Planet. Sci. 10, 257
Interiors of the giant planets

[ValSassConn07] Valencia D., Sasselov D.D., and O'Connell R.J. (2006), ApJ 665, 1413
Detailed models of Super-Earths: How well can we infer bulk properties?

[ValenciaEtAl09] Valencia D., Ikoma, M., Guillot T., and Nettelmann N. (2009) *submitted to A&A*
Composition and fate of short-period Super Earths: The case of CoRoT-7b

[VorTamMilBon06] Vorberger J., Tamblyn I., Militzer B., and Bonev S. (2006), Phys. Ref. B 75, 024206
Hydrogen-helium mixtures in the interiors of giant planets

[Wildt47] Wildt R. (1947), MNRAS 107, 84
Reports on the progress of astronomy: the constitution of the planets

[WagPru02] Wagner W. and Pruß A. (2002), J. Phys. Chem. Ref. Data 31, 387
Thermodynamic properties of ordinary water

[WWW05] Weigert A., Wendker H.J., and Wisotzki L. (2005)
Astronomie und Astrophysik, Ein Grundkurs, WILEY-VCH Verlag, Weinheim

[ZahHunLeh98] von Zahn U., Hunten D.M., and Lehmacher G. (1998), J. Geophys. Res. 103, 22815
Helium in Jupiter's atmosphere: Results from the Galileo probe helium interferometer experiment

[ZhaTru78] Zharkov V.N. and Trubitsyn V.P. (1978)
Physics of Planetary Interiors (Tucson:Parchart)

Appendix A

Long Tables

A.1 Table A.1: EOS applied to Jupiter

Table A.1: Overview of Jupiter model series.

Name (EOS)	H-EOS	He-EOS	Z-EOS	type	Ref. (J)
SCVH-I-99	H-SCVH-I	He-SCVH	He-SCvH	$Y_1 < Y_2$ $Z_1 \neq Z_2$	(1)
SCVH-I-04	H-SCVH-I	He-SCVH	Sesame 7154 (H_20), Sesame 7100 (sand)	$Y_1 < Y_2$ $Z_1 = Z_2$	(2)
LM-SOCP	LM-SOCP	”	”	”	”
LM-H4	LM-H4	”	”	”	”
Sesame-p	H-Sesame-p	”	”	”	”
Sesame-K04	Sesame-K03	Sesame-K04	linear mixture of H_2O, CH_4, NH_3, C, N, O, H_2S, S, SiO_2, Fe	$Y_1 < Y_2$ $Z_1 < Z_2$	(3)
LM-REOS	H-REOS	He-REOS	H_2O-REOS, He4-REOS	$Y_1 < Y_2$ $Z_1 < Z_2$	(4)
DFT-MD	DFT-MD	DFT-MD	CH_4, H_2O	$Y_1 = Y_2$ $Z_1 = Z_2$	(5)

References for Jupiter models: (1): [Guillot99], (2): [SauGui04], (3) [Kerley04a], (4) [NettelmannEtAl08], (5) [MilitzerEtAl08]. In all cases: $Y_1 = Y^{\rm atm} = 0.238$.

A.2 Table A.2: Observed parameters

	units		**Jupiter**	**Saturn**	**Uranus**	**Neptune**
L	$[10^{16}\mathrm{J/s}]$	$\star$	33.5[a]	8.6(6)[a]	0.035(35)[a]	0.33(4)[a]
F	$[\mathrm{J/m^2/s}]$		5.440(430)[a]	2.01(14)[a]	0.042(47)[a]	0.43(50)[a]
$T_{1\mathrm{bar}}$	[K]	$\star$	165-170	135	76	70
			165-170[a]	135(5)[a]	76(2)[a]	72(2)[a]
T_{eff}	[K]	$\star$	124(4)[a]	95(1)[a]	59.1(3)[a]	59.3(8)[a]
T_{eq}	[K]	$\star$	109.5	82.5	58.2	46.4
GM_P	$[10^{17}\mathrm{m^3s^{-2}}]$		1.26686533(100)[e]	0.37931272(200)[f]	0.5793947(23)[g]	0.6835096(21)[g]
				0.379312077(11)[b]		
G	$\left[10^{-11}\mathrm{m^3/kg/s^2}\right]$		6.67428(67)[c] – 6.673(1)[d]			
M_P	$[10^{27}\mathrm{kg}]$	$\star$	1.8986112(15)[a+d]	0.568319(560)[b+c]	0.08681(1)[g+c]	0.102435(1)[a+d]
				0.568464(3)[a+d]		0.10241(1)[g+c]
R_{eq}	$[10^7\mathrm{m}]$	$\star$	7.1492(4)[a]	6.0268(4)[a]	2.5559(4)[g]	2.4766(15)[g]
		$\star$		6.0356(3)[b]		
Y_1	[1]	$\star$	0.238(0.006)[l]	0.10-0.18	0.275	0.270
				0.06-0.25	0.262(48)[i]	$0.264^{+0.026\mathrm{j}}_{-0.035}$
$\bar{Y}$	[1]	$\star$	0.270 – 0.278[h]			
$2\pi/\omega$	[hr,min,sec]		9, 55, 30	10, 39, 17(5)[a]	17, 14, 20(40)[a]	16, 6(3), 40[a]
				10, 32, 35(13)[b]		
J_2	$[10^{-2}]$	$\star$	1.4697(1)[a]	1.6332(10)[a]	0.35160(32)[a]	0.3539(10)[a]
			1.4736(1)[e]	1.6298(10)[f]	0.33413(7)[k]	0.34084(45)[k]
		$\star$	1.4696(2)[k]	1.62907(3)[b]		
J_4	$[10^{-4}]$	$\star$	-5.84(5)[a]	-9.19(40)[a]	-0.354(41)[a]	-0.28(22)[a]
			-5.87(5)[e]	-9.15(40)[f]	-0.304(10)[k]	-0.334(29)[k]
		$\star$	-5.871(17)[k]	-9.355(3)[b]		
J_6	$[10^{-6}]$		31(20)[a,e]	103(50)[f]	–	–
			34.3(5.2)[k]	84.1(9.6)[b]		

Table A.2: Data constraining the interior models. Values marked by $\star$ are used for model calculations in this Thesis, if not stated otherwise.

[a] taken from Guillot (2005)
[b] Anderson & Schubert (2007)
[c] CODATA 2006
[d] CODATA 1998
[e] Campbell & Synott (1985) using *Pioneer 10,11*, *Voyager 1,2* data
[f] Campbell & Anderson (1989) using *Pioneer 11*, *Voyager 1,2* data
[g] Lindal (1992) using *Voyager 2* data (N) or taken from Lindal (1992)
[h] Bahcall & Pinsonneault (1995)
[i] Conrath et al. (1987)
[j] Burgdorf et al. (2003)
[k] htt://ssd.jpl.nasa.gov/?gravity_fields_op and references given there
[l] vonZahn et al.(1998)

A.3 Table A.3: Gravitational moments

Figure caption at table A.3

Values for $J_2 - J_8$ and R_{eq} listed in this table are results calculated by different authors for, as far as possible, the same interior model input parameters M, $\bar{R}$, ω, and the density distribution. Values published by Hubbard (1974) and by Zharkov & Trubitsyn (1978) are analytical results obtained for linear and polytropic density distributions of Jupiter and Saturn. In particular, the *polytropic model* by Hubbard (1974) has the density distribution $\rho(x) = 4.7 \sin \pi x/x$ where $x = l/\bar{R}$, the *polytropic models* by ZT78 have $\rho(x) = \bar{\rho} \sin \pi/3 \sin \pi x/x$, the *linear models* by ZT78 have $\rho(x) = 4\bar{\rho}(1-x)$. Models by ZT78 are uniquely defined by these density distributions and given $M, \bar{R}$, and m. From these parameters, $\bar{\rho} = 3M/4\pi\bar{R}^3$ and ω (3.62) are derived; R_{eq} and J_{2n} are output parameters. The model by Hubbard is defined by q (3.62) and R_{eq}. The total mass $M = m(x = 1)$ is derived by integrating dm/dr along the given density distribution. Using his result for R_{eq}, one can calculate $\omega(q, M, R_{eq})$, and then $m(\omega, M, R_{eq})$. With these values for ω and m listed here, Tristan Guillot (*personnal communication*) using the CEPAM code and I have independently from each other calculated the results for R_{eq} and J_{2n} listed here. Numbers appended to First Names indicate the order of approximation. Rows in brackets give my results from December 2008. Hubbard (1974) also offers a linear density model of Jupiter, but his value used for q is unclear so that comparative calculations would bear a large uncertainty regarding the input values of interior models.

Table A.3: Comparison of analytically and numerically determined gravitational moments $J_2 - J_8$

Author	q	m	ω	$R_{eq}\,[10^9\mathrm{cm}]$	$J_2/10^{-2}$	$J_4/10^{-04}$	$J_6/10^{-6}$	$J_8/10^{-6}$
**********	Jupiter Polytropic n=1 model from Hubbard 1974							
Hubbard 1974	0.0888	-	-	7.14000	1.39000	-5.20000	39.0000	
Tristan-3	–	0.082963	1.820e-04	7.13656	1.40774	-5.33538	32.4155	
Nadine-3	0.0848	0.082963	1.8203e-04	7.13635	1.40635	-5.32808	32.3605	
Tristan-4	-	0.082963	1.820e-04	7.13653	1.40760	-5.36349	28.4899	-2.20508
Nadine-4	0.0848	0.082963	1.8203e-04	7.13635	1.40635	-5.36279	30.1107	-2.35303
**********	Jupiter Linear model from Zharkov & Trubitsyn 1978, p.275							
Z&T-3		0.0830	–	7.140	1.47980	-5.877	35.28	
Tristan-3		0.0830	1.759e-04	7.13951	1.47993	-5.893	37.35	
Nadine-3		0.0830	1.759e-04	7.13914	1.47812	-5.882	37.26	
(Nadine-3		0.0830	1.759e-04	7.13943	1.47134	-5.847	49.17)	
Z&T-4		0.0830	–	7.140	1.47980	-5.929	34.57	-2.77
Tristan-4		0.0830	1.759e-04	7.13948	1.47976	-5.926	33.63	-2.62
Nadine-4		0.0830	1.759e-04	7.13914	1.47812	-5.923	34.59	-2.80
**********	Jupiter Polytropic n=1 model from Zharkov & Trubitsyn 1978, p.275							
Z&T-3		0.0830	–	7.138	1.40830	-5.327	30.70	
Tristan-3		0.0830	1.759e-04	7.13663	1.40836	-5.340	32.46	
Nadine-3		0.0830	1.759e-04	7.1363	1.40652	-5.329	32.37	
Z&T-4		0.0830	–	7.138	1.40820	-5.370	30.11	-2.33
Tristan-4		0.0830	1.759e-04	7.1366	1.40821	-5.368	28.53	-2.209
Nadine-4		0.0830	1.759e-04	7.1363	1.40652	-5.364	30.12	-2.354
**********	Saturn Linear model from Zharkov & Trubitsyn 1978, p.275							
Z&T-3		0.143	–	6.020	2.512	-16.65	17.26	
Tristan-3		0.143	1.67672e-04	6.02008	2.5116	-16.6865	19.132	
Nadine-3		0.143	1.676724-04	6.0199	2.5113	-16.780	19.114	
Z&T-4		0.143	–	6.020	2.510	-17.13	16.58	-24.3
Tristan-4		0.143	1.67672e-04	6.02008	2.5102	-17.0638	14.993	-21.2
Nadine-4		0.143	1.67672e-04	6.0205	2.51145	-17.1697	16.732	-25.05
(Nadine-4		0.143	1.67679e-04	6.0216	2.50328	-17.3305	22.693	-41.2)
**********	Saturn Polytropic model from Zharkov & Trubitsyn 1978, p.275							
Z&T-3		0.143	–	6.015	2.390	-15.10	15.02	
Nadine-3		0.143	1.67672e-04	6.0152	2.3893	-15.210	16.59	
Z&T-4		0.143	–	6.016	2.389	-15.55	14.46	-20.4
Nadine-4		0.143	1.67672e-04	6.0152	2.3893	-15.538	14.57	-21.02

A.4 Table A.4: Interior models with and without the 2 bugs

Table A.4: Influence of two bugs found in May 2009 on interior models of the outer planets.

T_{1-2} [K]	R_{1-2} [$R_\oplus$]	M_{core} [$M_\oplus$]	P_{core} [Mbar]	T_{core} [K]	Z_1 [%]	Z_2 [%]	J_4 [10^{-4}]	
*** **Jupiter**[a] **********								
7250	8.78	0.99	37.68	17890	10.009	11.673	-5.84	with bugs '.' , '-'
7150	8.78	0.95	37.61	17880	9.972	11.692	-5.84	with bug '.'
7060	8.85	1.31	40.11	18000	7.930	8.161	-5.84	with bug '-'
7060	8.85	1.26	40.06	18000	7.926	8.179	-5.84	June 2009
*** **Saturn**[b] **********								
5670	5.38	6.87	13.3	11030	11.37	29.22	-9.35	with bugs '.', '-'
5660	5.38	6.86	13.3	11020	11.34	29.22	-9.35	with bug '.'
5500	5.55	8.75	13.4	10670	6.205	21.82	-9.35	with bug '-'
5500	5.55	8.74	13.4	10670	6.204	21.84	-9.35	June 2009, (S2)
*** **Uranus**[c] **********								
2470	3.01	0.68	5.54	6190	0.25	0.919	-0.360	with bugs '.', '-'
2470	3.01	0.68	5.57	6040	0.25	0.918	-0.360	June 2009
*** **Neptun**[d] **********								
2360	3.08	1.09	7.4	6340	0.30	0.932	-0.345	with bugs '.' , '-'
2350	3.08	1.06	7.46	6210	0.30	0.932	-0.346	June 2009

[a]Jupiter models with SCvH-i EOS, $T_1 = 165$ K, $P_{1-2} = 2$ Mbar, $Y_1 = 0.238$, $\bar{Y} = 0.275$, $J_4 = -5.84/10^4$
[b]Saturn models with SCvH-i EOS, $T_1 = 140$ K, $P_{1-2} = 1.4$ Mbar, $Y_1 = 0.18$, $\bar{Y} = 0.275$, $J_4 = -9.35/10^4$
[c]Uranus models with LM-REOS, $T_1 = 76$ K, $P_{1-2} = 0.20$ Mbar, $Y_1 = Y_2 = 0.275$, $Z_1 = 0.25$
[d]Neptune models with LM-REOS, $T_1 = 72$ K, $P_{1-2} = 0.21$ Mbar, $Y_1 = Y_2 = 0.275$, $Z_1 = 0.30$

A.5 Table A.5: Selected interior models

name	P_{1-2} [Mbar]	Y_1 (H/He)	M_{core} [$M_\oplus$]	Z_1 [%]	Z_2 [%]	EOS	occurence
J1	8	0.238	0.53	1.79	15.68	LM-REOS	profile (Fig. 4.2)
J2	1.74	0.238	6.9	8.14	5.64	SCvH-ppt	profile (Fig. 4.2), pie chart (§ 4.4) [NettelmannEtAl08]
J3	8	0.238	1.83	2.099	14.55	LM-REOS	pie chart (§ 4.4), evolution (§ 5.2)
S1	3	0.10	5.41	5.71	26.17	LM-REOS	profile (Fig. 4.2) pie chart (§ 4.4)
S2	1.4	0.18	8.75	6.20	21.84	SCvH-i	profile (Fig. 4.2), pie chart (§ 4.4)
S3	2.32	0.275	10.0	8.74	8.74	LM-REOS	equivalent 2L-model for evolution (§ 5.2)
U1	0.10	0.275	1.28	10	87.6	LM-REOS	profile (Fig. 4.3), pie chart (§ 4.4
U2	0.25	0.275	0.61	30	92.9	LM-REOS	profile (Fig. 4.3)
U3	0.25	0.275	1.48	35	88.7	LM-REOS	evolution (§ 5.2)
N1	0.10	0.275	3.96	40	97.0	LM-REOS	profile (Fig. 4.3)
N2	0.21	0.275	1.09	30	93.2	LM-REOS	profile (Fig. 4.3)
N3	0.21	0.275	1.81	37	89.6	LM-REOS	evolution (§ 5.2)
N4	0.25	0.275	1.94	40	90	LM-REOS	pie chart (§ 4.4) [RedmerEtAl09]

Table A.5: Selected interior models.

Appendix B

Supplementary Figures

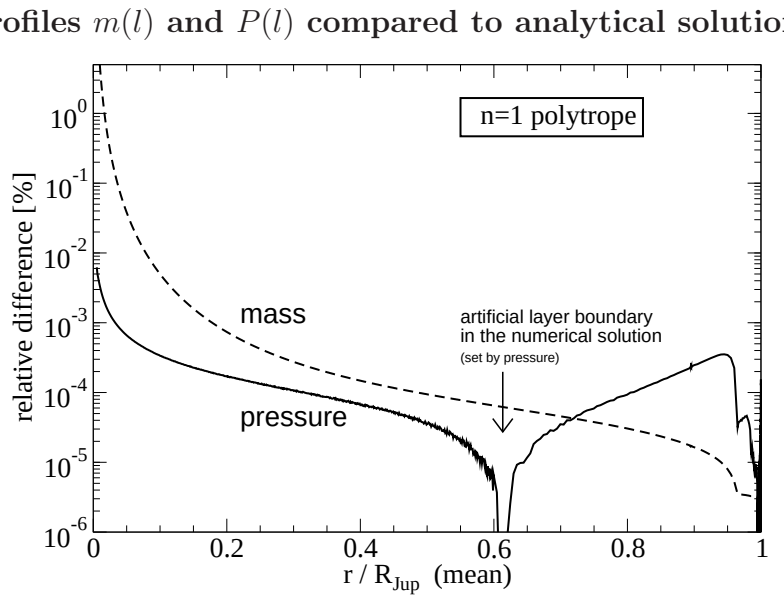

Figure B.1: Comparison of analytical and numerical solutions $m(r)$ and $P(r)$ for an $n = 1$ polytrope. Equations for the analytic solution for an (n=1) polytrope have been taken from [KippWei94]. See § 3.5 for details.

Functions $S_{2n}(l)$ and $J_{2n}(l)$

Figure B.2 also serves as a documentation of benchmarks of principal behaviour for comparison with somebody else's implementation.
We remember to have used the order relation $s_{2n} \sim m^n$ in the expansions above. For Jupiter, $m_J = 0.083$. Possible third order terms, for instance, are $m^3 \sim s_6 \sim s_2^3 \sim s_2 s_4$. As stated above, $s_2^{(1)}(l) = -m/3 < 0$ at iteration step 1. From A_2 in Tab. F.3 we have at iteration step 2 $s_2^{(2)} = -m/3 + S_2 + S_2' + [\frac{2}{7}(s_2^{(1)})^2 S_0 - \frac{6}{7} s_2^{(1)} S_2 + \frac{4}{7} s_2^{(1)} S_2' + \frac{10}{21} m s_2^{(1)}]$. From Tab. F.2 we also see $f_2 \sim s_2 + \mathcal{O}^4$, $f_2' \sim s_2 + \mathcal{O}^4$, $f_4 \sim s_4$, and thus $S_2 \sim S_2' \sim s_2$ to lowest order and $s_2 S_4 \sim m^{(1+2)}$ in A_2. The sign of s_2 is thus conserved at iteration step 2 and due to $S_2^{(1)} \sim s_2^{(1)} < 0$, $S_2^{'(1)} \sim s_2^{(1)} < 0$ its absolute value increases. This is clearly seen in Fig. 3.2. Addition of higher order terms cannot change this behaviour. For s_4, A_4 contains a sum of five positive and one negative fourth-order terms and s_4 will thus be positive as well as S_4 and S_4'. On the other hand, A_6, f_6, and f_6' are sums of six-order higher order terms of alternating signs. The sign of s_6, S_6, S_6' cannot as easily be predicted. In fact, S_6' (and S_4') turn out essentially zero. The integral functions S_2, S_2', S_4, S_4', and S_6 are shown in Fig. B.2a for a typical Jupiter model using SCvH-i EOS.
Fig. B.2b shows the behaviour of the gravitational moment functions $J_{2n}(l)$, calculated for the same Jupiter model as in Fig. B.2a. At the surface, the underlying Jupiter model reproduces the observed values $J_{2n}^{(\mathrm{obs})}$.

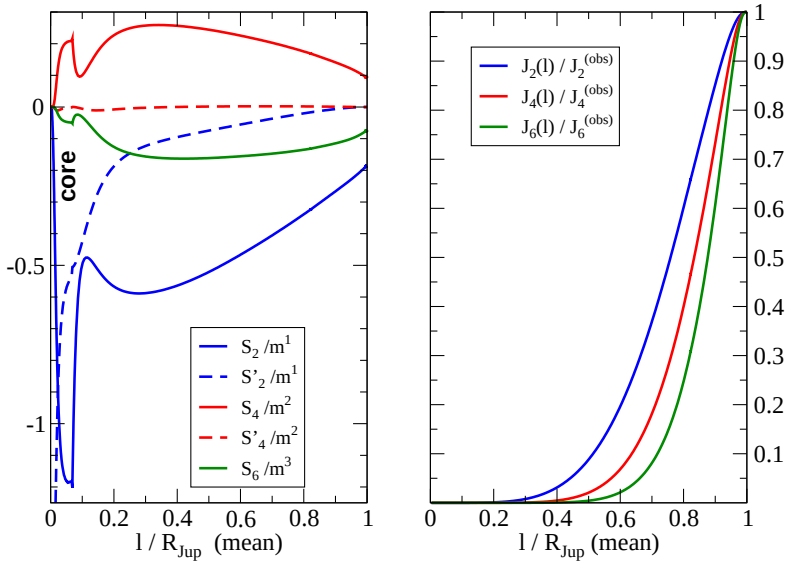

Figure B.2: a) (*left*): Integral functions S_{2n}, S_{2n}' scaled by m^n; b) (*right*): gravitational moments $J_{2n}(l)$, scaled by the observed values of Jupiter. The x-axis is $\beta = l/R_{\mathrm{Jup}}$. All these functions have been calculated from the final density profile of a three-layer Jupiter model using SCvH-i EOS.

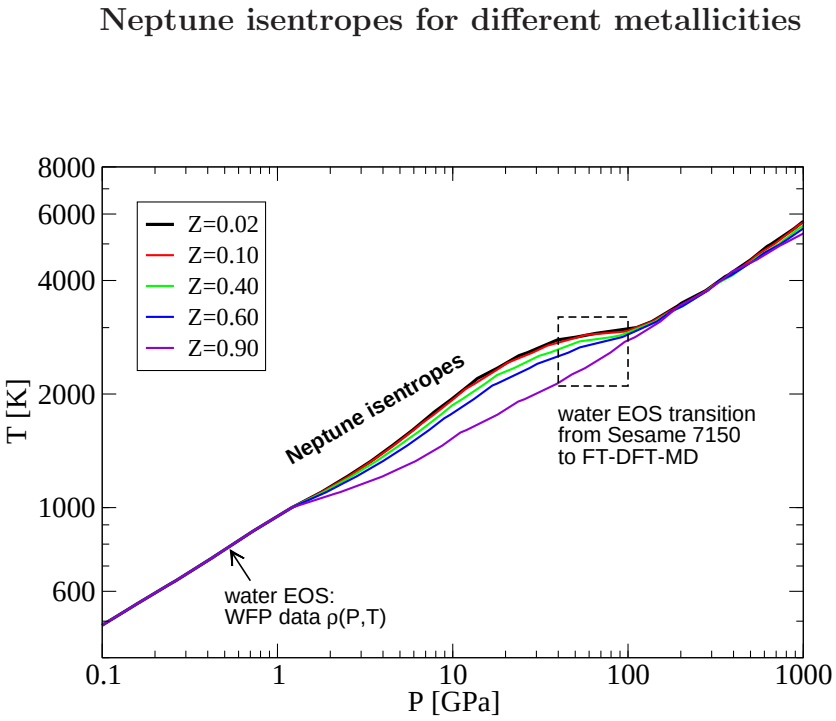

Figure B.3: Neptune isentropes ($T_1 = 72$ K) for different mass fractions of water, the rest being H-He. Below 1000 K all curves are identical in $T - P$ space, since the water data are not used to calculate the entropy there in order to avoid complications with water phase transitions, but only the mass density of the underlying H-He isentrope is modified according to Z and $\rho_{\mathrm{H_2O}}(T, P)$ using ice-I [FeiWag06] and liquid water [WagPru02] EOS data. Within the dashed box there is the region of interpolation between Sesame EOS 7150 and French's water EOS data (FT-DFT-MD). This figure is to show that the temperature along a planetary isentrope does not rise but fall with increasing metallicity.

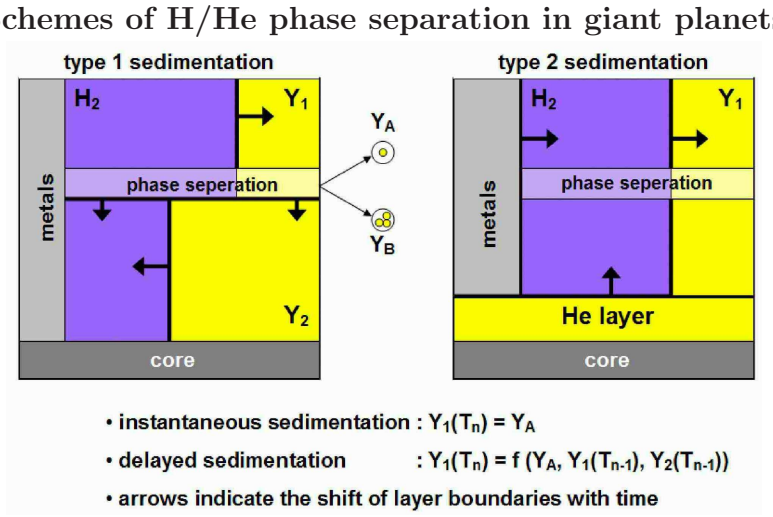

Figure B.4: Drawing to illustrate possible realizations of H/He phase separation and sedimentation in a planet. These drawings are to be read in a similar way as the pie charts in Fig. 4.15: with height above the central core region, radius and mass coordinate increase, while pressure and temperature decrease.

Left panel: Type 1 sedimentation: Formation of an outer, He depleted envelope and an inner, He enriched envelope. The layer boundary is given by the end of the demixing region. Metals are assumed not to be affected by the He rain. As indicated by the arrows, the layer boundary moves inward with time.

Right panel: Type 2 sedimentation: formation of a pure He layer around the core in case phase separation occurs somewhere in the interior. Due to the larger mean molecular weight of pure He compared to a mixture of H/He/metals, former deep envelope material is lifted. As indicated by the arrows, the envelope metallicity grows with time according to the loss of He towards the core.

Appendix C

Calculating the entropy

The entropy is a fundamental quantity in the calculation of the interior structure and cooling history of giant planets and brown dwarfs. Equation of state data tables generally/often/usually do not contain the entropy explicitly. This is partly due the method of EOS calculations (e.g. first-principles simulations using VASP or CP-MD), partly due to convention (e.g. chemical picture EOS such as Sesame or FVT$^+$). In this appendix I describe the method[1] applied in this work to derive the specific entropy $s(T,\rho)$ from given EOS data tables for the thermal EOS $p(T,\rho)$ and the caloric EOS $u(T,\rho)$ with respect to an offset σ, a reasonable value to be determined by other methods.

Since T and V are the *natural* variables of the free energy F, we start with the definition of F and transfer the problem of calculating s to the problem of calculating F/T:

$$F = U - TS \quad \Leftrightarrow \quad S = \frac{U}{T} - \frac{F}{T}$$

where $U = \mu u$ and $S = \mu s$ are the extensive internal energy and the extensive entropy, respectively, and $\mu = V\rho$ is the mass contained in volume V. If we set

$$\sigma := \frac{1}{\mu}\frac{F(T_0,V_0)}{T_0} \qquad \textit{(unknown entropy offset)}$$

with respect to a reference state (T_0, V_0), we can write

$$S(T,V) = \frac{U(T,V)}{T} - \left(\frac{F(T,V)}{T} - \frac{F(T_0,V_0)}{T_0}\right) + \sigma\mu\,.$$

The term in parenthesis is the solution of the line integral

$$\frac{F(T,V)}{T} - \frac{F(T_0,V_0)}{T_0} = \int_{T_0,V_0}^{T,V} d\frac{F(T,V)}{T} \quad .$$

For any scalar function $U(\vec{x})$, the total derivative dU and its line segment $\int dU$ are given by

$$dU(\vec{x}) = \mathrm{grad}U \cdot d\vec{x} \quad , \quad \int_{\vec{x}_1}^{\vec{x}_2} dU = \int_{\vec{x}_1}^{\vec{x}_2} \mathrm{grad}\,U(\vec{x}) \cdot d\vec{x} = \int_{w(\vec{x}_1)}^{w(\vec{x}_2)} \mathrm{grad}\,U(\vec{x}) \cdot \frac{d\vec{x}}{dw}\,dw$$

where $w \in \mathbb{R}$ is mapped to $\vec{x}(w) \in \dim(\vec{x})$ by some map $\mathcal{M}$. For our special case of the function $F(T,V)/T$ we define $\mathcal{M} : [0,1] \to \mathbb{R}^2$, $w \mapsto (T'(w), V'(w))$ with $(T'(0), V'(0)) = (T_0, V_0)$ and

[1] The main ideas have been developed by Juranek (*personal communication).*

$(T'(1), V'(1)) = (T, V)$ and thus have

$$\int_{T_0,V_0}^{T,V} d\tfrac{F(T',V')}{T'} = \int_{T_0,V_0}^{T,V} \left(\frac{\partial(F/T')}{\partial T'} \frac{dT'}{dw} + \frac{\partial(F/T')}{\partial V'} \frac{dV'}{dw} \right) dw \tag{C.1}$$

Using $F = U - TS$ and Gibbs' fundamental equation $dU = -pdV + TdS - \sum_i \mu_i dn_i$ with $\sum_i \mu_i dn_i = 0$ (canonical ensemble with chemical equilibrium) we find for the partial derivativs

$$\frac{\partial(\frac{U}{T'} - S)}{\partial T'} = -\frac{U}{T'^2} + \frac{1}{T'}\frac{\partial U}{\partial T'} - \frac{\partial S}{\partial T'} = -\frac{U}{T'^2} + \frac{1}{T'}\left(T'\frac{\partial S}{\partial T'}\right) - \frac{\partial S}{\partial T'} = -\frac{U}{T'^2}$$

$$\text{and} \quad \frac{\partial(\frac{U}{T'} - S)}{\partial V'} = \frac{1}{T'}\frac{\partial U}{\partial V'} - \frac{\partial S}{\partial V'} = \frac{1}{T'}\left(-p + T'\frac{\partial S}{\partial V'}\right) - \frac{\partial S}{\partial V'} = -\frac{p}{T'}\,.$$

Dividing the extensive quantities in (C.1) by μ and using $dV = -(\mu/\rho^2)d\rho$ we get

$$\frac{1}{\mu}\int_{T_0,\rho_0}^{T,\rho} d\tfrac{F(T',\rho')}{T'} = \int_{T_0,\rho_0}^{T,\rho} \left(\frac{1}{\rho^2}\frac{p(T',\rho')}{T'}\frac{d\rho'}{dw} + \frac{u(T',\rho')}{T'^2}\frac{dT'}{dw} \right) dw\,. \tag{C.2}$$

Still we have to specify the map $\mathcal{M}$. If the EOS data were consistent everywhere in the (T, ρ)-plane the choice of the map would not influence the integration. Yet there are equations of state that do not satisfy the condition of thermodynamic consistency, and LM-REOS belongs to them. For most EOS used in this work we first integrate along isochores and than along isothermes by choosing the map

$$\mathcal{M}_{TD}:\ w \in [0,1] \mapsto (T', \rho')$$

$$(T', \rho') = \begin{cases} (\rho_0 + (\rho - \rho_0))w, T_0 & : 0 \le w \le 0.5 \\ (\rho, T_0 + (T - T_0))w & : 0.5 \le w \le 1 \end{cases}$$

By switching the order of integration along isochores and isothermes we also define

$$\mathcal{M}_{DT}:\ w \in [0,1] \mapsto (T', \rho')$$

$$(T', \rho') = \begin{cases} (T_0 + (T - T_0))w, \rho_0 & : 0 \le w \le 0.5 \\ (T, \rho_0 + (\rho - \rho_0))w & : 0.5 \le w \le 1 \end{cases}$$

Applying $\mathcal{M}_{TD}$ onto Eq. C.2 gives

$$\frac{1}{\mu}\int_{T_0,\rho_0}^{T,\rho} d\tfrac{F(T',\rho')}{T'} = \int_{\rho_0}^{\rho} d\rho' \, \frac{1}{\rho'^2}\frac{p(T_0,\rho')}{T_0} + \int_{T_0}^{T} dT' \, \frac{u(T',\rho)}{T'^2}$$

and finally

$$s(T,\rho) = \frac{u(T,\rho)}{T} - \int_{\rho_0}^{\rho} d\rho' \, \frac{1}{\rho'^2}\frac{p(T_0,\rho')}{T_0} - \int_{T_0}^{T} dT' \, \frac{u(T',\rho)}{T'^2} + \sigma\,.$$

Emperically we find that a reference state (T_0 [K], ρ_0 [g/cm^3]) of (1000, 0.01) for hydrogen-rich mixtures and (1000, 0.1) for water-rich mixtures yields best-behaved isentropes. Best-behaved does not mean well-behaved. For a thermodynamically consistent EOS, neither the choice of the reference state nor of the map $\mathcal{M}$ should effect the resulting isentrope. However, diverse EOS used

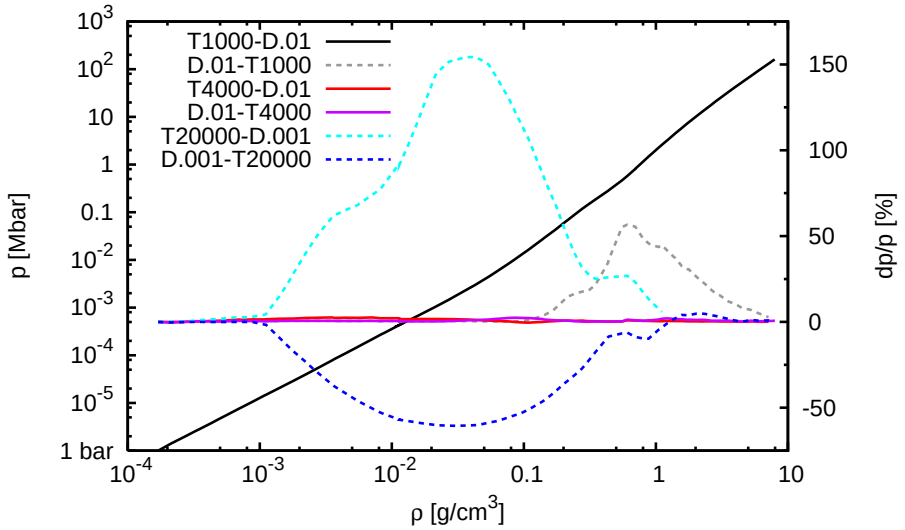

Figure C.1: Variability of a typical Jupiter isentrope ($T_1 = 170$ K, $Y = 0.20$, $Z = 0.06$) with respect to the choice of T_0 [K], ρ_0 [g/cm] and $\mathcal{M}$. *Solid black*: pressure-density relation along the reference isentrope defined by the choice $T_0 = 1000, \rho_0 = 10^{-2}, \mathcal{M} = \mathcal{M}_{TD}$; *color coded curves*: pressure difference relative to the reference isentrope; *grey dashed:* same as previous but $\mathcal{M} = \mathcal{M}_{DT}$; *red solid*: $T_0 = 4000, \rho_0 = 10^{-2}, \mathcal{M}_{TD}$; *violet solid*: same as previous but $\mathcal{M} = \mathcal{M}_{DT}$; *blue dashed*: $T_0 = 20,000, \rho_0 = 10^{-3}, \mathcal{M} = \mathcal{M}_{TD}$; *cyan dashed*: same as previous but $\mathcal{M} = \mathcal{M}_{DT}$. The underlying EOS is LM-REOS.

in this work appear not to satisfy these conditions. Figure C.1 shows the variability of a typical Jupiter isentrope ($T_1 = 170$ K, $Y = 0.20$, $Z = 0.06$) in case of LM-REOS using three settings of (T_0, ρ_0), each of them in combination with $\mathcal{M}_{TD}$ and $\mathcal{M}_{DT}$.

Placing the reference state at small densities and high temperatures, i.e. (20,000 K, 10^{-3} g/cm^{-3}) adds an uncertainty of 200% to the isentrope when integrating along different paths. The EOS appears too bad to calculate Jupiter models. On the other hand, placing the reference state close to the isentrope, i.e. $T_0 \sim 1000$ at $\rho_0 = 0.01$ gives isentropes with a deviation of only a few percent, in this case below 3%, for different paths of integration Eq. C.2. For paths crossing the region of high densities and small temperatures (e.g. *grey dashed curve*), where we know the EOS data are bad by construction, the deviation again rises.

Obviously, the entropy and consequently an isentrope derived from a thermodynamically inconsistent EOS has an error. This error can be minimized by chosing a path of integration where poor EOS regions do not contribute to. Emperically, I found paths with the property of being close to the final isentrope, avoiding high densities at low temperatures as well as small densities at high temperatures best suited. Resulting isentropes behave systematically under variation of Y, Z and $T_{1\mathrm{bar}}$. However, one should keep in mind that a special choice of $T_0, \rho, \mathcal{M}$ adds an arbitrariness to the isentrope. In the case of LM-REOS and a H-rich planet, this arbitrariness is of the order of the error of the QMD data. More systematic examinations should be performed to estimate the effect on resulting planetary models.

There are several possible reasons for thermodynamical inconsistency of an EOS. For instance, wide-range EOS for astrophysical applications are usually composed of different subsets calculated by different methods and connected to each other by interpolation. Hence, even if EOS data are very accurate in certain regimes of parameter space, on large scale they might not.

Appendix D

Derivations and Proofs

D.1 Derivation of equations 3.18 and 3.19

The following derivations are based on mixing length theory and are presented here, since they constitute the heart of the usual expression for the energy flux in a convective medium which itself is used to derive adiabaticity of planetary interiors.

Between the point where an element started from with $DT_0 = 0$ and the point where it mixes with the surroundings and looses its identity it has travelled in average the distance l_m, the *mixing length*. If encountered at a given level of pressure[1], some passing elements will have almost completed their motion, others just started, and in average moved a distance $dr = l_m/2$. Thus the average excess temperature DT at a temperature level T is

$$DT = \frac{dDT}{dr}\frac{l_m}{2} \quad . \tag{D.1}$$

With $DP = (dP_e/dr - dP/dr)dr = 0$ we find for the excess temperature gradient

$$\begin{aligned} \frac{1}{T}\frac{dDT}{dr} &= \frac{1}{T}\left(\frac{dT_e}{dr} - \frac{dT}{dr}\right) = \frac{1}{T}\left(\frac{dT_e}{dP_e}\frac{dP_e}{dr} - \frac{dT}{dP}\frac{dP}{dr}\right) \\ &= \frac{1}{P}\left(\nabla_{ad} - \nabla_T\right)\frac{dP}{dr} = \frac{1}{H_P}(\nabla_T - \nabla_{ad}) \quad , \end{aligned} \tag{D.2}$$

where $H_P := -P(dr/dP)$ is the pressure scale height. Hence, the expression for DT in (3.17) is

$$DT = \frac{T}{H_P}(\nabla_T - \nabla_{ad})\frac{l_m}{2} \quad . \tag{D.3}$$

Due to $DP = 0$, and since the equation of state $T(P, \rho)$ is the same for the element (index e) as for the environment (assuming homogeneity), and since both systems started from the same initial state before the element moved an average distance of $l_m/2$, we also have

$$\begin{aligned} \frac{DT}{T} &= \frac{l_m}{2}\frac{1}{T}\left(\frac{dT_e}{dr} - \frac{dT}{dr}\right) \\ &= \frac{l_m}{2}\frac{1}{T}\left[\left(\left(\frac{\partial T}{\partial P}\right)_{\rho_e}\frac{dP_e}{dr} + \left(\frac{\partial T}{\partial \rho}\right)_{P_e}\frac{d\rho_e}{dr}\right) - \left(\left(\frac{\partial T}{\partial P}\right)_{\rho}\frac{dP}{dr} + \left(\frac{\partial T}{\partial \rho}\right)_{P}\frac{d\rho}{dr}\right)\right] \end{aligned}$$

[1] Levels of constant pressure are equivalent to those of constant temperature or constant density, and in spherical objects, to those of constant radius.

$$= \frac{l_m}{2}\frac{1}{T}\left[\left(\frac{\partial T}{\partial \rho}\right)_P\left(\frac{d\rho_e}{dr}-\frac{d\rho}{dr}\right)\right] = \frac{l_m}{2}\frac{1}{T}\left[\left(\frac{-1}{\delta\rho}\right)\left(\frac{D\rho}{\rho}\right)\left(\frac{2\rho}{l_m}\right)\right]$$
$$= -\frac{1}{\delta}\frac{D\rho}{\rho} \tag{D.4}$$

with $\delta = -(T/\rho)(\partial\rho/\partial T)_P$. I leave it to the reader to find out if (D.4) also holds in the inhomogeneous case. The excess temperature (D.1) thus corresponds to an excess density $D\rho$. This causes a radial buoyancy force f_{buo} per unit mass given by

$$f_{buo} = -g\,\frac{D\rho}{\rho} = g\,\delta\,\frac{DT}{T}\,, \tag{D.5}$$

where g is gravity. This buoyancy force acts on the mass element at the end of its motion after travelling $l_m/2$. On average over its preceeding motion, the buoyancy force may have been half of this value, and the work w done thus $(1/2)f_{buo}(l_m/2)$. Some fraction of this work, say one half, may have transformed into kinetic energy $v_e^2/2$ of the unit mass element, the other half spent on pushing aside the surroundings. Under these assumptions, we have found an expression for v_e using (3.18):

$$v_e^2 \;\approx\; \frac{1}{2}f_{buo}\frac{l_m}{2} = \frac{g\delta}{2H_P}(\nabla_T - \nabla_{ad})\left(\frac{l_m}{2}\right)^2 \quad . \tag{D.6}$$

D.2 Derivation of equation 3.46

We aim to show the validity of the expansion

$$\frac{1}{|\vec{r}-\vec{r}\,'|} \;=\; \frac{1}{r}\times\begin{cases} \sum_{n=0}^{\infty}\left(\frac{r'}{r}\right)^n P_l(\cos\psi) & : \quad (r > r') \\ \sum_{n=0}^{\infty}\left(\frac{r'}{r}\right)^{-(n+1)} P_l(\cos\psi) & : \quad (r < r') \end{cases} \tag{D.7}$$

- We know, e.g. from electrodynamics (ED) or mechanics (M), that the Poisson equation

  $$\Delta\,\Phi(\vec{r}) = \alpha\,\rho(\vec{r}) \tag{D.8}$$

  for the potential Φ arised by a charge (ED) or mass distribution (M) $\rho(\vec{r})$, with and constant $\alpha = -1/\varepsilon_0$ (ED) or $\alpha = 4\pi G$ (M), has the solution

  $$\Phi(\vec{r}) = -\frac{\alpha}{4\pi}\int d^3r'\,\frac{\rho(\vec{r}\,')}{|\vec{r}-\vec{r}\,'|} \quad . \tag{D.9}$$

  This solution can be obtained from the method of Greens functions, where the source term in the differential equation of interest is replaced by a δ function and first this simplified problem is solved for the Greens function $\mathrm{G}(\vec{r}-\vec{r}\,')$. In case of the Poisson equation, the simplified diffential equation to be solved is

  $$\Delta\mathrm{G}(\vec{r},\vec{r}\,') = \delta(\vec{r}-\vec{r}\,') \quad ,$$

  with the solution known from (ED)

  $$\mathrm{G}(\vec{r},\vec{r}\,') = -\frac{1}{4\pi}\,\frac{1}{|\vec{r}-\vec{r}\,'|} \quad .$$

The solution (D.9) of the full problem (D.8) can be derived with help of $G(\vec{r},\vec{r}\,')$ in this way:

$$\int d^3r'\,(\alpha\rho(\vec{r}\,'))\quad \Delta_{\vec{r}}\,\mathrm{G}(\vec{r}-\vec{r}\,') \;=\; \int d^3r'\,(\alpha\rho(\vec{r}\,'))\quad \delta(\vec{r}-\vec{r}\,') \tag{D.10}$$

$$\Delta_{\vec{r}}\int d^3r'\,(\alpha\rho(\vec{r}\,'))\quad \mathrm{G}(\vec{r}-\vec{r}\,') \;=\; \alpha\rho(\vec{r}) \tag{D.11}$$

$$\Longrightarrow\quad \Phi(\vec{r}) \;=\; \int d^3r'\;(\alpha\rho(\vec{r}\,'))\quad \mathrm{G}(\vec{r}-\vec{r}\,') \tag{D.12}$$

$$\;=\; -\frac{\alpha}{4\pi}\int d^3r'\,\frac{\rho(\vec{r}\,')}{|\vec{r}-\vec{r}\,'|}\quad . \tag{D.13}$$

- In spherical coordinates, appropriate for spherical problems such as charged, empty, metallic spheres (ED), or planets (M), or an electron bound to an atom (QM), the Laplace-operator can be split into a radial part Δ_r and an angular part $\Delta_{\vartheta,\varphi}$ as

$$\left.\begin{aligned} \Delta &= \Delta_r + \tfrac{1}{r^2}\Delta_{\vartheta,\varphi} \\ \text{with}\quad \Delta_r &= \tfrac{1}{r^2}\tfrac{\partial}{\partial r}\left(r^2\tfrac{\partial}{\partial r}\right)\quad \text{and}\quad \Delta_{\vartheta,\varphi} = \tfrac{1}{\sin\vartheta}\tfrac{\partial}{\partial\vartheta}\sin\vartheta\tfrac{\partial}{\partial\vartheta} + \tfrac{1}{\sin\vartheta^2}\tfrac{\partial^2}{\partial\varphi^2}\quad . \end{aligned}\right\} \tag{D.14}$$

The eigenfunctions of $\Delta_{\vartheta,\varphi}$ are the so-called spherical harmonics

$$Y_{lm}(\vartheta,\varphi) \sim P_l^m(\cos\vartheta)\,\mathrm{e}^{im\varphi},\quad l=0,1,2,\ldots,\quad m=-l,-l+1,\ldots,l-1,1\quad .$$

They are defined by means of the *extended Legendre polynomials* P_l^m, see e.g. [Nolting90]. From ED or from QM we know that their eigenvalues

$$\Delta_{\vartheta,\varphi}\,Y_{lm} = -l(l+1)\,Y_{lm} \tag{D.15}$$

are degenerated with respect to m. The case of azimuthal symmetry (independence on φ) requires $m=0$, and the Y_{lm} reduce to the *Legendre polynomials* P_l:

$$Y_l(\vartheta) = \sqrt{\frac{2l+1}{4\pi}}\,P_l(\cos\vartheta)\quad .$$

The Y_{lm} offer a complete, orthonormal set of functions for spheres of unit length radius. Any function $f(r,\vartheta,\varphi)$ can be expressed by a series of spherical harmonics and appropriate expansion coefficients $R_{lm}(r)$ accounting for the radial dependence of f:

$$f(r,\vartheta,\varphi) = \sum_{l=0}^{\infty}\sum_{m=-l}^{+l} R_{lm}(r)Y_{lm}(\vartheta,\varphi)\quad . \tag{D.16}$$

- Next we consider the Laplace equation

$$\Delta\,\Phi_0 = 0\quad .$$

Using (D.14, D.15) and the expansion (D.16) for the solution Φ_0 of the Laplace equation, the radial part takes the convenient form

$$\frac{1}{r^2}\frac{d}{dr}\left(r^2\frac{dR}{dr}\right) - \frac{l(l+1)}{r^2}R(r) = 0\quad , \tag{D.17}$$

which is usually called the *radial equation*. Its general solution is

$$u_l(r) = A_l r^{l+1} + B_l r^{-l}\qquad ,\quad \text{where}\quad R_l(r) = \frac{u_l(r)}{r} \tag{D.18}$$

and the constants of integration A_l, B_l have to be determined by the boundary conditions.

- From (3.46) we see that $1/|\vec{r}-\vec{r}\,'|$ depends on the distance r $(0 < r < \infty)$ between the particles and the angle ψ $(0 \leq \psi \leq 2\pi)$ between their coordinate vectors $\vec{r}$ and $\vec{r}\,'$. An appropriate choice of coordinates for this problem therefore is spherical coordinates (r, θ, φ) with symmetry with respect to one of the angles. Since we are aiming towards an expansion into Legendre polynomials and not into trigonometric functions $(e^{im\varphi})$, we choose $\psi = \theta$.

From here on, the proof of (3.46) is almost straightforward. We first consider the differential equation

$$\Delta\, \mathrm{G}(\vec{r}, \vec{r}\,') = \delta(\vec{r}-\vec{r}\,') \tag{D.19}$$

with

$$\Delta = \Delta_r + \frac{1}{r^2}\Delta_\psi \tag{D.20}$$

$$\Delta_\psi = \frac{1}{\sin\psi}\frac{\partial}{\partial\psi}\sin\psi\frac{\partial}{\partial\psi} \tag{D.21}$$

$$\delta(\vec{r}-\vec{r}\,') = \frac{1}{r'^2\sin\psi\,'}\,\delta(r-r')\,\delta(\psi-\psi\,') \quad . \tag{D.22}$$

For $r \neq r'$, (D.19) reduces to the Laplace equation $\Delta\, \mathrm{G}(\vec{r}-\vec{r}\,') = 0$ which is solved by

$$\mathrm{G}(\vec{r}, \vec{r}\,') = \mathrm{G}(r, r', \psi) = \sum_{l=0}^{\infty}\left(A_l r^l + B_l r^{-(l+1)}\right) P_l(\cos\psi) \quad ,$$

where the constant coefficients A_l, B_l may depend on l and r'. Since $r \neq r'$ can occur for $r < r'$ and for $r > r'$, we split the solution into an internal part $\mathrm{G}^{(i)}$ and an external part $\mathrm{G}^{(e)}$ with

$$\mathrm{G}^{(i)}(r, r', \psi) = \sum_{l=0}^{\infty}\left(A_l^{(i)} r^l + B_l^{(i)} r^{-(l+1)}\right) P_l(\cos\psi) \qquad \text{for} \quad r < r' \tag{D.23}$$

$$\mathrm{G}^{(e)}(r, r', \psi) = \sum_{l=0}^{\infty}\left(A_l^{(e)} r^l + B_l^{(e)} r^{-(l+1)}\right) P_l(\cos\psi) \qquad \text{for} \quad r > r' \tag{D.24}$$

and determine the coefficients $A_l^{(i)}, B_l^{(i)}, A_l^{(e)}, B_l^{(e)}$ by boundary and continuity conditions.

For $r \to 0$ we like to have $\mathrm{G}(r, r', \psi)$ regular, and thus $B_l^{(i)} = 0$ for all l. For $r \to \infty$ we like to have $\Phi \to 0$ requiring $\mathrm{G} \to 0$ by (D.12), and thus $A_l^{(e)} = 0$ for all l. Because Φ shall be continuous everywhere, we must have $\mathrm{G}^{(i)}(r') = \mathrm{G}^{(e)}(r')$, and thus

$$A_l^{(i)}(r')^l = B_l^{(e)}(r')^{-(l+1)} \quad \Rightarrow \quad B_l^{(e)} = A_l^{(i)}(r')^{2l+1} \tag{D.25}$$

for all l. The only problem is to determine the $A_l^{(i)}$. In case of a one-dimensional δ-function $\delta(r-r')$, we could easily set up a condition for $(\partial\mathrm{G}/\partial\mathrm{r})_\psi$ at $r = r'$ by placing a Gaussian box at the layer boundary at r' letting go $dr \to 0$. This method is commonly used in (ED) to find the offset between the normal components of the electric field vectors $\vec{E}$ in front of and behind a layer boundary. With $\vec{E} = -grad\,\phi$ and the electric field potential ϕ also obeying the Poisson equation, we would be done. However, here we have a δ-function $\delta(\vec{r}-\vec{r}\,')$ with respect to all relevant coordinates, and a transfer of this method to our case I did not manage. On the other hand we are in the lucky situation to already know the final result (D.9) of (D.8) with $\alpha = 4\pi G$ and help of (D.12).

$$\Phi^{(e)} = -\frac{\alpha}{4\pi}\int d^3r'\,\frac{\rho(\vec{r}\,')}{|\vec{r}-\vec{r}\,'|} = -\frac{\alpha}{4\pi}\frac{1}{r}\int d^3r'\,\rho(\vec{r}\,')\left\{\frac{1}{\sqrt{1-2\frac{r'}{r}\cos\psi+\left(\frac{r'}{r}\right)^2}}\right\} \quad \text{(D.26)}$$

$$\overset{(D.12)}{=} -\frac{\alpha}{4\pi}\int d^3r'\rho(\vec{r}\,')\,\mathrm{G}^{(e)}(\vec{r},\vec{r}\,')$$

$$\overset{(D.25)}{=} -\frac{\alpha}{4\pi}\int d^3r'\left[\rho(\vec{r}\,')\sum_{l=0}^{\infty}A_l^{(i)}(r')^{2l+1}\,r^{-(l+1)}\,P_l(\cos\psi)\right]$$

$$= -\frac{\alpha}{4\pi}\frac{1}{r}\int d^3r'\,\rho(\vec{r}\,')\left\{\sum_{l=0}^{\infty}A_l^{(i)}(r')^{2l+1}\,r^{-l}P_l(\cos\psi)\right\} \quad , \quad \text{(D.27)}$$

$$\Phi^{(i)} = -\frac{\alpha}{4\pi}\frac{1}{r}\int d^3r'\,\rho(\vec{r}\,')\left\{\sum_{l=0}^{\infty}A_l^{(i)}\,r^{l+1}P_l(\cos\psi)\right\} \quad \text{(D.28)}$$

Since the curled braces in (D.27) and (D.26) must be identical for $r > r'$ (and in (D.28) and (D.26) for $r < r'$), we can use this condition to determine the $A_l^{(i)}$. For $r > r'$, the expansion of the square-root in (D.26) goes with powers of (r'/r) as

$$\begin{aligned}\frac{1}{\sqrt{1-2\frac{r'}{r}\cos\psi+\left(\frac{r'}{r}\right)^2}} &= 1+\frac{1}{2}\left[2\frac{r'}{r}\cos\psi-\left(\frac{r'}{r}\right)^2\right]+\frac{3}{8}\left[\left(2\frac{r'}{r}\right)^2\cos^2\psi+\left(\frac{r'}{r}\right)^4\right]+O\left(\frac{r'}{r}\right)^3\\ &= 1+\left(\frac{r'}{r}\right)\cos\psi+\left(\frac{r'}{r}\right)^2\left(\frac{3}{2}\cos^2\psi-\frac{1}{2}\right)+O\left(\frac{r'}{r}\right)^3\\ &= 1+\left(\frac{r'}{r}\right)^1P_1(\cos\psi)+\left(\frac{r'}{r}\right)^2P_2(\cos\psi)+O\left(\frac{r'}{r}\right)^3 \quad , \quad \text{(D.29)}\end{aligned}$$

and for $r < r'$ with powers of (r/r') as

$$\begin{aligned}\frac{1}{\sqrt{1-2\frac{r'}{r}\cos\psi+\left(\frac{r'}{r}\right)^2}} &= \frac{r/r'}{\sqrt{1-2\frac{r}{r'}\cos\psi+\left(\frac{r}{r'}\right)^2}}\\ &= \frac{r}{r'}\left(1+\left(\frac{r}{r'}\right)^1P_1(\cos\psi)+\left(\frac{r}{r'}\right)^2P_2(\cos\psi)+O\left(\frac{r}{r'}\right)^3\right)\\ &= \left(\frac{r'}{r}\right)^{-1}+\left(\frac{r'}{r}\right)^{-2}P_1(\cos\psi)+\left(\frac{r'}{r}\right)^{-3}P_2(\cos\psi)+O\left(\frac{r'}{r}\right)^3 \quad \text{(D.30)}\end{aligned}$$

From (D.29) and the comparison of the curled braces in (D.27) we find

$$A_l^{(i)} = \left(\frac{1}{r'}\right)^{l+1} \quad . \quad \text{(D.31)}$$

Expansion (D.30) serves as a check yielding of cause the same result (D.31). Inserting (D.31) into (D.27) and into (D.28) and comparing with (D.9) we have derived in this subsection the expansion (D.7).

While this derivation of $A_l^{(i)}$ is not a mathematical proof, it is sufficient for our purposes. Of interest in this work are coefficients up to order $l = 10$, which can be calculated directly by expanding the square-root as in (D.29) and (D.30). For a mathematical proof we would have to show that the scheme of these expansions holds for all $l \geq 0$, for instance by using the method of

induction and recursion formulas for the P_l. Alternatively, we could have derived (D.7) directly by expanding the square-root in (D.9). The way I chose, however, I consider much more instructive than just calculating the expansion coeffients, where the coincidence with the P_l turns out by chance. I am sure the square-root expansion in order to determine the $A_l^{(i)}$ can be replaced by a condition for $grad\,\Phi$ as in ED, but I did not find it.

D.3 Legendre polynomials: useful properties

$P_0 - P_6$ can easily be found in textbooks, but I regard it useful to repeat them here:

$$P_0(t) = 1 \tag{D.32}$$
$$P_1(t) = t \tag{D.33}$$
$$P_2(t) = \frac{3}{2}\,t^2 - \frac{1}{2} \tag{D.34}$$
$$P_4(t) = \frac{35}{8}\,t^4 - \frac{15}{4}\,t^2 + \frac{3}{8} \tag{D.35}$$
$$P_6(t) = \frac{231}{16}\,t^6 - \frac{315}{16}t^4 + \frac{105}{16} - \frac{5}{16} \tag{D.36}$$

D.3.1 Calculating products $P_m * P_n$

Here I give an example of expanding a product $P_m * P_n$ of Legendre polynomials into a new series of Legendre polymomials. Although this is straightforward, it illustrates the huge amount of primitive calculations to be done in order to derive the equations for the figure functions and the potential. And it illustrates the procedure I chose for my program package LegendreDevelop. We calculate $P_2 * P_2$ by first using (3.73a) and then (3.72b), and using expressions (D.32−D.35).

$$\begin{aligned}
P_2 * P_2 &= \left(\tfrac{3}{2}t^2 - \tfrac{1}{2}\right)^2 = \tfrac{9}{4}t^4 - \tfrac{3}{2}t^2 + \tfrac{1}{4} \\
&= \tfrac{9}{4}\tfrac{8}{35}\left(\tfrac{35}{8}t^4 - \tfrac{15}{4}t^2 + \tfrac{3}{8}\right) + \tfrac{9}{4}\tfrac{8}{35}\tfrac{15}{4}t^2 - \tfrac{9}{4}\tfrac{8}{35}\tfrac{3}{8} - \tfrac{3}{2}t^2 + \tfrac{1}{4} \\
&= \tfrac{18}{35}P_4 + \tfrac{3}{7}t^2 + \tfrac{2}{35} \\
&= \tfrac{18}{35}P_4 + \tfrac{3}{7}\tfrac{2}{3}\left(\tfrac{3}{2}t^2 - \tfrac{1}{2}\right) + \tfrac{3}{7}\tfrac{2}{3}\tfrac{1}{2} + \tfrac{2}{35} \\
&= \tfrac{18}{35}P_4 + \tfrac{2}{7}P_2 + \tfrac{1}{5}P_0 \qquad \textit{(exercise)}
\end{aligned}$$

D.3.2 Proofs and comments

Proof of $P_n = a_n t^n +$ lower order terms

We aim to show

$$P_n(t) = \sum_{j=0}^{n} a_j\,t^j \quad , \quad \forall j : a_j \quad \textit{rational number}$$

With $P_0 = 1t^0$ and $P_1 = 1t^1$, this statement is true up to $n = 1$. Let us assume this statement is true for any index n. For index $n+1$ we then have, using (3.71),

$$\begin{aligned}
P_{n+1}(t) &= \frac{1}{2(n+1)}\,\frac{d}{dt}\left[P_n(t)\,(t^2-1)\right] \\
&= \frac{1}{2(n+1)}\left[\Big(\sum_{j=0}^{n-1}(j+1)\,a_{j+1}\,t_j\Big)\Big(t^2-1\Big) + \Big(\sum_{j=0}^{n} a_j\,t^j\Big)\Big(2t\Big)\right]
\end{aligned}$$

$$= \frac{1}{2(n+1)} \left[\Big(\sum_{k=2}^{n+1} (k-1) a_{k-1} t^k \Big) - \Big(\sum_{k=2}^{n+1} (k-1) a_{k-1}\, t^{k-2} \Big) + \Big(\sum_{k=1}^{n+1} a_{k-1}\, t^k \Big) \right] \quad \text{(D.37)}$$

$$= \sum_{j=0}^{n+1} a'_j\, t^j \qquad \text{with} \quad a'_0 = -\frac{a_1}{2(n+1)} \quad \text{and} \quad a'_{n+1} = \frac{a_n}{2} \quad ,$$

the other coefficients a'_j also being rational numbers as easily seen from (D.37).

Properties (3.74 a,b)

We insert (3.70) into (3.74 a),

$$\int_{-1}^{1} dt\, P_n \;=\; \frac{1}{2^n n!} \int_{-1}^{1} dt\, \frac{d^n}{dt^n} (t^2-1)^n \;=\; \begin{cases} \displaystyle\int_{-1}^{1} dt\, 1 = 2 & (n=0) \\ \displaystyle \frac{1}{2^n n!} \left[\frac{d^{n-1}}{dt^{n-1}} (t^2-1)^n \right]_{-1}^{1} = 0 & (n>0) \end{cases} \quad \text{(D.38)}$$

and see that this intgral vanishes for $n > 0$, since every term of the chain of terms produced by $n-1$ derivatives of $(t^2-1)^n$ contains a factor (t^2-1) which becomes zero if taken at the integral boundaries ± 1. Property (3.74 b) is part of the orthogonality relation,

$$\int_{-1}^{1} dt\, P_n(t) P_m(t) = \begin{cases} \frac{2}{2n+1} & (n=m) \\ 0 & (n \neq m) \end{cases} \quad , \quad \text{(D.39)}$$

usually given in textbooks, e.g. [ZhaTru78], without proof. Using (3.73) and (D.38), we see that it is the zero-order cofficient d_0 of the product $P_n * P_m$ that contributes to the integral:

$$\int_{-1}^{1} dt\, P_n(t) P_m(t) \;=\; \sum_{j=0}^{n+m} \int_{-1}^{1} dt\, d_j\, P_j(t) \;=\; 2 d_0 \quad \text{(D.40)}$$

D.4 Proof of equation 5.10

The main ideas I took from Kippenhahn & Weigert (1994), § 3-4. We first show

$$E_g = -3 \int_0^M dm\, \frac{P}{\rho} \quad . \quad \text{(D.41)}$$

Partial integration of (5.7) using $dP/dr = -Gm/r^2$ (3.30) and $dm/dr = 4\pi r^2 \rho$ (3.33) gives

$$\begin{aligned} E_g = -\int_0^M dm\, \frac{Gm}{r} \;&=\; \int_0^M dm\, \frac{r}{\rho} \frac{dP}{dr} = 4\pi \int_0^M dm\, r^3 \frac{dP}{dm} \\ &=\; \big[4\pi r^3 P \big]_0^M - 4\pi \int_0^M dm\, 3r^2\, \frac{dr}{dm}\, P \\ &=\; -3 \int_0^M dm\, \frac{P}{\rho} \quad , \end{aligned} \quad \text{(D.42)}$$

since the term in brackets vanishes because of $r(0) = 0$ and $P(M) = 0$. Next we show

$$4\dot{E}_g = -3 \int_0^M dm\, \frac{\dot{P}}{\rho} \quad . \quad \text{(D.43)}$$

The time-derivative of $dP/dm = -Gm/4\pi r^3$ is

$$\frac{d\dot{P}}{dm} = -\frac{d}{dt}\frac{Gm}{4\pi r^4} = -\frac{G\dot{m}}{4\pi r^4} + 4\frac{Gm}{4\pi r^5}\,\dot{r} = 0 + \frac{Gm}{\pi r^5}\,\dot{r} \quad .$$

Multiplying both sides with $4\pi r^3$ and integrating over m gives

$$4\pi \int_0^M dm\, r^3 \frac{d\dot{P}}{dm} = 4\int_0^M dm\, \frac{Gm}{r^2}\,\dot{r} \tag{D.44}$$

The left-hand side of (D.44) gives

$$\begin{aligned} 4\pi \int_0^M dm\, r^3 \frac{d\dot{P}}{dm} &= \left[4\pi r^3 \dot{P}\right]_0^M - 4\pi \int_0^M dm\, 3r^2 \frac{dr}{dm}\dot{P} \\ &= -3\int_0^M dm\, \frac{\dot{P}}{\rho} \quad , \end{aligned} \tag{D.45}$$

since the term in brackets vanishes because of $r(0) = 0$ and, to good approximation, $\dot{P}(M) = 0$. The right-hand side of (D.44) gives

$$4\int_0^M dm\, \frac{Gm}{r^2}\,\dot{r} = 4\,\frac{d}{dt}\int_0^M dm\, \frac{Gm}{r} = 4\,\dot{E}_g \quad . \tag{D.46}$$

Equating the right hand sides of (D.45) and (D.46) gives (D.43) which we aimed to show. Inserting $4\dot{E}_g$ from (D.43) into the formal time derivative of E_g from (D.41),

$$\dot{E}_g = -3\int_0^M dm\, \frac{\dot{P}}{\rho} + 3\int_0^M dm\, \frac{P}{\rho^2}\dot{\rho} \quad ,$$

we obtain

$$(1-4)\dot{E}_g = 3\int_0^M dm\, \frac{P}{\rho^2}\dot{\rho}$$

and have finally proved (5.10) and (5.9).

Appendix E

The 2 Bugs

For J_2, J_4, and J_6 there exist analytic solutions by Hubbard (1974) and by Zharkov & Trubitsyn (1978) for linear and polytropic density profiles of Jupiter and Saturn. Analytic solutions by these authors are listed in Tab. A.3 in § A.3 (Appendix) together with results by Guillot and my results from May 2009. These analytically derived values can be considered the ultimative chance for modelers to estimate the quality of their numerical procedure of calculating gravitational moments. However, the degree of agreement by which the numerical procedure can be called sufficiently free of bugs (or sufficiently accurate), is not clear. A deviation of 10% and more from several analytical values and/or values calculated by at least two other groups using different codes certainly indicates an error like, probably, a wrong coefficient. Some coefficients do not affect the final solution significantly, while others of same order do. The overwhelming part of interior models presented in this work and in publications [NettelmannEtAl08, ForNett09] have Jupiter and Saturn J_6 values too large by $\sim$ 50% compared with the analytical results, indicating an error in the code, since all other calculations (e.g. Kerley (2004), Yasunori Hori (2008, pers. comm.)) did not yield such systematically high J_6 values.

Of the existence of analytical results I first became aware of in September 2008, when I was, due to a lucky sequence of former scientific contacts, given the opportunity to meet the famous planetary scientist David Stevenson from Caltech, Pasadena, and later on Tristan Guillot from the Observatoire de la Côte d'Azur, Nice. It is Tristan's re-calculations from December 2008 that are given in Tab. A.3. My calculations from Dec 2008 (indicated by brackets in this Table) show a systematic shift of Jupiter J_6 values by $\sim$ 50% (which did not affect the final interior solution much since J_6 is not fitted), too small J_2 values by 0.6%, and too large J_4 values by 0.7%. The underlying bug(s) caused the calculated Jupiter core mass to increase by 10% and Z_1 to decrease by 20%. These shifts do not invalidate the conclusions about Jupiter made in [NettelmannEtAl08]. For Saturn, the underlying bug(s) acted to shift J_2 and J_4 in the same direction and thus shifts in the calculated core mass and metallicities become too large to be ignored for publication. After removing two bugs in May 2009, referred to as 'the 2 bugs', the agreement with analytical and T. Guillot's results (Tab. A.3) is now acceptable. Many Jupiter and Saturn interior models I recalculated in June 2009.

Tab. A.3 also shows the effect of including fourth order terms in the calculation of J_2 to J_6: the influence on J_2 values is neglegible, $|J_4|$ increases by 0.5-1% and J_6 decreases by $\sim$ 5%. In principle, these fourth order effects can be used to constrain three-layer models further, in particular if the observational error bar of J_4 and J_6 can be decreased below the influence of fourth order terms by the upcoming *Juno mission*.

Comparing interior models with and without the 2 bugs

After having removed the 2 bugs, recalculating the whole bunch of interior models of the outer planets would have consumed several weeks of time. Hence I recalculated for each planet only one single model in four versions: with and without the 2 bugs, with bug '-', a displaced minus sign, and with bug '.', a displaced dot in a floating point number. The result is given in Tab. A.4 in § A.4 in the Appendix.

Revised Jupiter model's Z_2 decreases by 3.5 percentage points at $200-280\,M_\oplus$ inner material corresponding to $7-10\,M_\oplus$. Adding further $0.02*(30-120\,M_\oplus)$ from the outer envelope, Jupiter's heavy element content reduces by $7-13\,M_\oplus$ compared to published values. For Saturn, Z_1 and Z_2 decrease about twice as much so that previous models based on these bugs should not be used anymore. For Uranus and Neptune, the 2 bugs have a neglegible effect and previously calculated models as published in [ForNett09] remain valid.

Appendix F

Theory of Figures: coefficients

Table F.1: **Expansion $(\mathbf{1}+\mathbf{\Sigma})^{\mathbf{2}}-(\mathbf{1}+\mathbf{\Sigma})^{\mathbf{2}}*\mathbf{P_2}=\sum_{\mathbf{n=0}}^{\mathbf{5}}\mathbf{A_{2n}^{(Q)}P_{2n}}$ in 5^{th} order**

$$
\begin{aligned}
A_0^{(Q)} &= \Big(1-\tfrac{2}{5}s_2-\tfrac{9}{35}s_2^2+\tfrac{22}{525}s_2^3-\tfrac{4}{35}s_2s_4+\tfrac{1}{21}s_2^4-\tfrac{97}{693}s_4^2-\tfrac{4}{35}s_2^2s_4\Big)\\
A_2^{(Q)} &= \Big(-1+\tfrac{10}{7}s_2+\tfrac{9}{35}s_2^2-\tfrac{4}{7}s_4+\tfrac{20}{77}s_2s_4-\tfrac{26}{105}s_2^3+\tfrac{8}{35}s_2^2s_4+\tfrac{1513}{9009}s_4^2-\tfrac{247}{3675}s_2^4\\
&\quad -\tfrac{180}{1001}s_2s_6\Big)\\
A_4^{(Q)} &= \Big(-\tfrac{36}{35}s_2+\tfrac{114}{77}s_4+\tfrac{18}{77}s_2^2-\tfrac{978}{5005}s_2s_4+\tfrac{36}{175}s_2^3-\tfrac{90}{143}s_6+\tfrac{306}{1001}s_2s_6-\tfrac{18}{1001}s_4^2\\
&\quad +\tfrac{24}{1225}s_2^4-\tfrac{114}{385}s_2^2s_4\Big)\\
A_6^{(Q)} &= \Big(-\tfrac{10}{11}s_4-\tfrac{18}{77}s_2^2+\tfrac{82}{55}s_6+\tfrac{34}{77}s_2s_4-\tfrac{178}{935}s_2s_6-\tfrac{190}{3927}s_4^2+\tfrac{2}{11}s_2^2s_4-\tfrac{56}{85}s_8\Big)\\
A_8^{(Q)} &= \Big(-\tfrac{56}{65}s_6-\tfrac{56}{143}s_2s_4+\tfrac{142}{95}s_8+\tfrac{5768}{13585}s_2s_6+\tfrac{1610}{8151}s_4^2\Big)\\
A_{10}^{(Q)} &= \Big(-\tfrac{270}{323}s_8-\tfrac{1512}{4199}s_2s_6-\tfrac{7350}{46189}s_4^2\Big)
\end{aligned}
$$

Table F.2: **Functions f_{2n} and f'_{2n}, $n = 0, \ldots, 5$ in 5^{th} order**

$$
\begin{aligned}
f_0 &= 1 + \tfrac{4}{175}s_2^5 \\
f_2 &= \tfrac{3}{5}s_2 + \tfrac{12}{35}s_2^2 + \tfrac{24}{35}s_2s_4 + \tfrac{40}{231}s_4^2 + \tfrac{60}{143}s_4s_6 + \tfrac{6}{175}s_2^3 + \tfrac{1346}{3003}s_2s_4^2 \\
&\quad + \tfrac{216}{385}s_2^2s_4 + \tfrac{324}{1001}s_2^2s_6 - \tfrac{184}{1925}s_2^4 - \tfrac{1488}{25025}s_2^3s_4 - \tfrac{43389}{875875}s_2^5 \\
f_4 &= \tfrac{1}{3}s_4 + \tfrac{18}{35}s_2^2 + \tfrac{40}{77}s_2s_4 + \tfrac{36}{77}s_2^3 + \tfrac{90}{143}s_2s_6 + \tfrac{162}{1001}s_4^2 + \tfrac{40}{143}s_4s_6 \\
&\quad + \tfrac{6943}{5005}s_2^2s_4 + \tfrac{900}{1001}s_2s_4^2 + \tfrac{810}{1001}s_2^2s_6 + \tfrac{5436}{5005}s_2^3s_4 + \tfrac{486}{5005}s_2^4 - \tfrac{948}{7007}s_2^5 \\
f_6 &= \tfrac{3}{13}s_6 + \tfrac{120}{143}s_2s_4 + \tfrac{336}{715}s_2s_6 + \tfrac{72}{143}s_2^3 + \tfrac{672}{1105}s_2s_8 + \tfrac{80}{429}s_4^2 + \tfrac{672}{2431}s_4s_6 \\
&\quad + \tfrac{4596}{2431}s_2^2s_6 + \tfrac{216}{143}s_2^2s_4 + \tfrac{11800}{7293}s_2s_4^2 + \tfrac{6144}{2431}s_2^3s_4 + \tfrac{432}{715}s_2^4 + \tfrac{216}{1105}s_2^5 \\
f_8 &= \tfrac{3}{17}s_8 + \tfrac{168}{221}s_2s_6 + \tfrac{144}{323}s_2s_8 + \tfrac{2450}{7293}s_4^2 + \tfrac{15120}{46189}s_4s_6 + \tfrac{80136}{46189}s_2^2s_6 \\
&\quad + \tfrac{3780}{2431}s_2^2s_4 + \tfrac{67200}{46189}s_2s_4^2 + \tfrac{8640}{2717}s_2^3s_4 + \tfrac{1296}{2431}s_2^4 + \tfrac{36288}{46189}s_2^5 \\
f_{10} &= \tfrac{1}{7}s_{10}
\end{aligned}
$$

$$
\begin{aligned}
f'_0 &= \tfrac{3}{2} - \tfrac{3}{10}s_2^2 - \tfrac{1}{6}s_4^2 - \tfrac{2}{35}s_2^3 - \tfrac{6}{35}s_2^2s_4 + \tfrac{2}{175}s_2^5 - \tfrac{20}{231}s_2s_4^2 + \tfrac{3}{50}s_2^4 \\
f'_2 &= \tfrac{3}{5}s_2 - \tfrac{3}{35}s_2^2 - \tfrac{6}{35}s_2s_4 - \tfrac{10}{231}s_4^2 - \tfrac{15}{143}s_4s_6 + \tfrac{36}{175}s_2^3 - \tfrac{17}{275}s_2^4 \\
&\quad + \tfrac{186}{1001}s_2s_4^2 - \tfrac{3918}{25025}s_2^3s_4 + \tfrac{36}{385}s_2^2s_4 + \tfrac{54}{1001}s_2^2s_6 + \tfrac{91031}{875875}s_2^5 \\
f'_4 &= \tfrac{1}{3}s_4 - \tfrac{9}{35}s_2^2 - \tfrac{20}{77}s_2s_4 - \tfrac{45}{143}s_2s_6 - \tfrac{81}{1001}s_4^2 - \tfrac{20}{143}s_4s_6 + \tfrac{1}{5}s_2^2s_4 + \tfrac{2}{105}s_2^3s_4 \\
f'_6 &= \tfrac{3}{13}s_6 - \tfrac{75}{143}s_2s_4 - \tfrac{42}{143}s_2s_6 - \tfrac{84}{221}s_2s_8 - \tfrac{50}{429}s_4^2 - \tfrac{420}{2431}s_4s_6 + \tfrac{3504}{2431}s_2^2s_6 \\
&\quad + \tfrac{810}{1001}s_2^2s_4 + \tfrac{14750}{17017}s_2s_4^2 + \tfrac{270}{1001}s_2^3 - \tfrac{7155}{2431}s_2^3s_4 - \tfrac{54}{143}s_2^4 + \tfrac{54}{143}s_2^5 \\
f'_8 &= \tfrac{3}{17}s_8 - \tfrac{588}{1105}s_2s_6 - \tfrac{504}{1615}s_2s_8 - \tfrac{1715}{7293}s_4^2 - \tfrac{10584}{46189}s_4s_6 + \tfrac{249312}{230945}s_2^2s_6 \\
&\quad + \tfrac{2352}{2431}s_2^2s_4 + \tfrac{125440}{138567}s_2s_4^2 - \tfrac{6048}{2717}s_2^3s_4 - \tfrac{4536}{12155}s_2^4 + \tfrac{36288}{46189}s_2^5 \\
f'_{10} &= \tfrac{1}{7}s_10 - \tfrac{1215}{2261}s_2s_8 - \tfrac{1890}{4199}s_4s_6 + \tfrac{4860}{4199}s_2^2s_6 + \tfrac{47250}{46189}s_2s_4^2 - \tfrac{8100}{4199}s_2^3s_4 + \tfrac{17496}{29393}s_2^5
\end{aligned}
$$

Table F.3: **Expansion coefficients $\mathbf{A_{2n}}$ in third order**

$$
\begin{aligned}
A_2 &= \Big(-s_2+\tfrac{2}{7}s_2^2-\tfrac{29}{35}s_2^3+\tfrac{4}{7}s_2s_4\Big)\mathbf{S_0}+\Big(1-\tfrac{6}{7}s_2+\tfrac{111}{35}s_2^2-\tfrac{6}{7}s_4\Big)\mathbf{S_2}-\tfrac{10}{7}s_2\,\mathbf{S_4}\\
&\quad+\Big(1+\tfrac{4}{7}s_2+\tfrac{1}{35}s_2^2+\tfrac{4}{7}s_4\Big)\mathbf{S'_2}+\tfrac{8}{7}s_2\mathbf{S'_4}\\
&\quad-\tfrac{\mathbf{m}}{\mathbf{3}}\Big(1-\tfrac{10}{7}s_2-\tfrac{9}{35}s_2^2+\tfrac{4}{7}s_4\Big)\\
\\
A_4 &= \Big(-s_4+\tfrac{18}{35}s_2^2+\tfrac{40}{77}s_2s_4-\tfrac{108}{385}s_2^3\Big)\mathbf{S_0}+\Big(-\tfrac{54}{35}s_2+\tfrac{648}{385}s_2^2-\tfrac{60}{77}s_4\Big)\mathbf{S_2}\\
&\quad+\Big(1-\tfrac{100}{77}s_2\Big)\mathbf{S_4}+\Big(\tfrac{36}{35}s_2+\tfrac{108}{385}s_2^2+\tfrac{40}{77}s_4\Big)\mathbf{S'_2}+\Big(1+\tfrac{80}{77}s_2\Big)\mathbf{S'_4}\\
&\quad-\tfrac{\mathbf{m}}{\mathbf{3}}\Big(\tfrac{36}{35}s_2-\tfrac{18}{77}s_2^2-\tfrac{120}{77}s_4\Big)\\
\\
A_6 &= \Big(-s_6+\tfrac{10}{11}s_2s_4-\tfrac{18}{77}s_2^3\Big)\mathbf{S_0}+\Big(-\tfrac{15}{11}s_4+\tfrac{108}{77}\Big)\mathbf{S_2}-\tfrac{25}{11}\mathbf{S_4S_6}\\
&\quad+\Big(\tfrac{10}{11}s_4+\tfrac{18}{77}s_2^2\Big)\mathbf{S'_2}+\tfrac{20}{11}s_2\mathbf{S'_4}+\mathbf{S'_6}\\
&\quad-\tfrac{\mathbf{m}}{\mathbf{3}}\Big(\tfrac{10}{11}s_4-\tfrac{18}{77}s_2^2\Big)
\end{aligned}
$$

Table F.4: **Expansion $(\mathbf{1}+\mathbf{\Sigma})^{-(\mathbf{2n+1})} * \mathbf{P_{2k}} = \sum_{\mathbf{n=0}}^{\mathbf{5}} \mathbf{B_{2n}^{(2k,-2n-1)}} \mathbf{P_{2n}}$ in 5^{th} order**

$$
\begin{aligned}
n=0: \quad & \Big(1+\tfrac{2}{5}s_2^2-\tfrac{4}{105}s_2^3+\tfrac{2}{9}s_4^2+\tfrac{43}{175}s_2^4-\tfrac{4}{35}s_2^2s_4-\tfrac{388}{5775}s_2^5-\tfrac{40}{693}s_2s_4^2+\tfrac{48}{385}s_2^3s_4\Big)\mathbf{P_0}\\
+ \quad & \Big(-s_2+\tfrac{2}{7}s_2^2-\tfrac{29}{35}s_2^3+\tfrac{4}{7}s_2s_4+\tfrac{100}{693}s_4^2+\tfrac{454}{1155}s_2^4+\tfrac{50}{143}s_4s_6-\tfrac{7369}{9009}s_2s_4^2\\
& -\tfrac{36}{77}s_2^2s_4-\tfrac{270}{1001}s_2^2s_6+\tfrac{5224}{5005}s_2^3s_4-\tfrac{124596}{175175}s_2^5\Big)\mathbf{P_2}\\
+ \quad & \Big(-s_4+\tfrac{18}{35}s_2^2-\tfrac{108}{385}s_2^3+\tfrac{40}{77}s_2s_4-\tfrac{540}{1001}s_2s_4^2+\tfrac{90}{143}s_2s_6+\tfrac{162}{1001}s_4^2+\tfrac{16902}{25025}s_2^4\\
& -\tfrac{7369}{5005}s_2^2s_4+\tfrac{40}{143}s_4s_6+\tfrac{18916}{15015}s_2^3s_4-\tfrac{486}{1001}s_2^2s_6-\tfrac{84564}{175175}s_2^5\Big)\mathbf{P_4}\\
+ \quad & \Big(-s_6+\tfrac{10}{11}s_2s_4-\tfrac{18}{77}s_2^3+\tfrac{28}{55}s_2s_6+\tfrac{20}{99}s_4^2-\tfrac{54}{77}s_2^2s_4+\tfrac{72}{385}s_2^4+\tfrac{56}{85}s_2s_8\\
& +\tfrac{56}{187}s_4s_6-\tfrac{271}{187}s_2^2s_6-\tfrac{2950}{3927}s_2s_4^2+\tfrac{2214}{1309}s_2^3s_4-\tfrac{2844}{6545}s_2^5\Big)\mathbf{P_6}\\
+ \quad & \Big(-s_8+\tfrac{56}{65}s_2s_6+\tfrac{490}{1287}s_4^2-\tfrac{84}{143}s_2^2s_4+\tfrac{72}{715}s_2^4+\tfrac{48}{95}s_2s_8+\tfrac{1008}{2717}s_4s_6\\
& -\tfrac{8904}{13585}s_2^2s_6-\tfrac{4480}{8151}s_2s_4^2+\tfrac{1632}{2717}s_2^3s_4-\tfrac{288}{2717}s_2^5\Big)\mathbf{P_8}\\
+ \quad & \Big(-s_{10}+\tfrac{270}{323}s_2s_8+\tfrac{2940}{4199}s_4s_6-\tfrac{2268}{4199}s_2^2s_6-\tfrac{22050}{46189}s_2s_4^2+\tfrac{15120}{46189}s_2^3s_4-\tfrac{1944}{46189}s_2^5\Big)\mathbf{P_{10}}\\
n=1: \quad & \Big(-\tfrac{3}{5}s_2+\tfrac{12}{35}s_2^2+\tfrac{24}{35}s_2s_4-\tfrac{234}{175}s_2^3+\tfrac{40}{231}s_4^2-\tfrac{72}{77}s_2^2s_4+\tfrac{52}{175}s_2^4\Big)\mathbf{P_0}\\
+ \quad & \Big(1-\tfrac{6}{7}s_2+\tfrac{111}{35}s_2^2-\tfrac{6}{7}s_4-\tfrac{1242}{385}s_2^3+\tfrac{144}{77}s_2s_4+\tfrac{4579}{3003}s_4^2-\tfrac{33174}{5005}s_2^2s_4\\
& +\tfrac{3364}{1225}s_2^4+\tfrac{1080}{1001}s_2s_6\Big)\mathbf{P_2}\\
+ \quad & \Big(-\tfrac{54}{35}s_2+\tfrac{648}{385}s_2^2-\tfrac{60}{77}s_4+\tfrac{21468}{5005}s_2s_4-\tfrac{122688}{25025}s_2^3-\tfrac{135}{143}s_6-\tfrac{8028}{1001}s_2^2s_4\\
& +\tfrac{1080}{1001}s_4^2+\tfrac{21096}{13475}s_2^4+\tfrac{1944}{1001}s_2s_6\Big)\mathbf{P_4}\\
+ \quad & \Big(-\tfrac{15}{11}s_4+\tfrac{108}{77}s_2^2+\tfrac{216}{77}s_2s_4-\tfrac{144}{77}s_2^3-\tfrac{42}{55}s_6+\tfrac{3924}{935}s_2s_6+\tfrac{5900}{3927}s_4^2\\
& -\tfrac{12678}{1309}s_2^2s_4+\tfrac{108}{77}s_2^4-\tfrac{84}{85}s_8\Big)\mathbf{P_6}\\
+ \quad & \Big(-\tfrac{84}{65}s_6+\tfrac{336}{143}s_2s_4-\tfrac{144}{143}s_2^3+\tfrac{35616}{13585}s_2s_6+\tfrac{8960}{8151}s_4^2-\tfrac{12240}{2717}s_2^2s_4-\tfrac{72}{95}s_8\Big)\mathbf{P_8}\\
+ \quad & \Big(-\tfrac{405}{323}s_8+\tfrac{9072}{4199}s_2s_6+\tfrac{44100}{46189}s_4^2-\tfrac{113400}{46189}s_2^2s_4\Big)\mathbf{P_{10}}\\
n=2: \quad & \Big(-\tfrac{5}{9}s_4+\tfrac{6}{7}s_2^2+\tfrac{200}{231}s_2s_4-\tfrac{12}{11}s_2^3\Big)\mathbf{P_0}\\
+ \quad & \Big(-\tfrac{10}{7}s_2+\tfrac{180}{77}s_2^2-\tfrac{500}{693}s_4+\tfrac{17890}{3003}s_2s_4-\tfrac{8856}{1001}s_2^3-\tfrac{125}{143}s_6\Big)\mathbf{P_2}\\
+ \quad & \Big(1-\tfrac{100}{77}s_2+\tfrac{6368}{1001}s_2^2-\tfrac{810}{1001}s_4-\tfrac{30308}{3003}s_2^3+\tfrac{5400}{1001}s_2s_4-\tfrac{100}{143}s_6\Big)\mathbf{P_4}\\
+ \quad & \Big(-\tfrac{25}{11}s_2+\tfrac{270}{77}s_2^2-\tfrac{100}{99}s_4+\tfrac{29500}{3927}s_2s_4-\tfrac{2385}{187}s_2^3-\tfrac{140}{187}s_6\Big)\mathbf{P_6}\\
+ \quad & \Big(-\tfrac{2450}{1287}s_4+\tfrac{420}{143}s_2^2+\tfrac{44800}{8151}s_2s_4-\tfrac{14280}{2717}s_2^3-\tfrac{2520}{2717}s_6\Big)\mathbf{P_8}\\
+ \quad & \Big(-\tfrac{7350}{4199}s_6+\tfrac{220500}{46189}s_2s_4-\tfrac{132300}{46189}s_2^3\Big)\mathbf{P_{10}}\\
n=3: \quad & \Big(\tfrac{360}{143}s_2^2-\tfrac{175}{143}s_4\Big)\mathbf{P_2} \quad + \quad \Big(-\tfrac{315}{143}s_2+\tfrac{648}{143}s_2^2-\tfrac{140}{143}s_4\Big)\mathbf{P_4}\\
+ \quad & \Big(1-\tfrac{98}{55}s_2+\tfrac{2093}{187}s_2^2-\tfrac{196}{187}s_4\Big)\mathbf{P_6} \quad + \quad \Big(-\tfrac{196}{65}s_2+\tfrac{83104}{13585}s_2^2-\tfrac{3528}{2717}s_4\Big)\mathbf{P_8}\\
+ \quad & \Big(\tfrac{21168}{4199}s_2^2-\tfrac{10290}{4199}s_4\Big)\mathbf{P_{10}}\\
n=4: \quad & -\tfrac{252}{85}s_2\mathbf{P_6} \quad + \quad \Big(1-\tfrac{216}{95}s_2\Big)\mathbf{P_8} \quad - \quad \tfrac{1215}{323}s_2\mathbf{P_{10}}\\
n=5: \quad & 1\mathbf{P_{10}}
\end{aligned}
$$

Table F.5: Expansion $(\mathbf{1}+\mathbf{\Sigma})^{\mathbf{2n}} * \mathbf{P_{2k}} = \sum_{\mathbf{n=0}}^{\mathbf{5}} \mathbf{B}_{\mathbf{2n}}^{\mathbf{(2k,2n)}} \mathbf{P_{2n}}$ in 5^{th} order

$$
\begin{aligned}
n=0: \quad & 1\mathbf{P_0} \\
n=1: \quad & \left(\tfrac{2}{5}s_2+\tfrac{2}{35}s_2^2-\tfrac{2}{25}s_2^3+\tfrac{4}{35}s_2s_4+\tfrac{20}{693}s_4^2-\tfrac{4}{525}s_2^4\right)\mathbf{P_0} \\
+ \quad & \left(1+\tfrac{4}{7}s_2+\tfrac{1}{35}s_2^2+\tfrac{4}{7}s_4-\tfrac{16}{105}s_2^3+\tfrac{24}{77}s_2s_4-\tfrac{8}{35}s_2^2s_4+\tfrac{107}{3675}s_2^4+\tfrac{180}{1001}s_2s_6\right. \\
& \left.-\tfrac{71}{3003}s_4^2\right)\mathbf{P_2} \\
+ \quad & \left(\tfrac{36}{35}s_2+\tfrac{108}{385}s_2^2+\tfrac{40}{77}s_4+\tfrac{3578}{5005}s_2s_4-\tfrac{36}{175}s_2^3+\tfrac{180}{1001}s_4^2-\tfrac{24}{1225}s_2^4+\tfrac{324}{1001}s_2s_6\right. \\
& \left.-\tfrac{8}{77}s_2^2s_4+\tfrac{90}{143}s_6\right)\mathbf{P_4} \\
+ \quad & \left(\tfrac{10}{11}s_4+\tfrac{18}{77}s_2^2+\tfrac{36}{77}s_2s_4+\tfrac{28}{55}s_6+\tfrac{654}{935}s_2s_6+\tfrac{2950}{11781}s_4^2-\tfrac{2}{11}s_2^2s_4+\tfrac{56}{85}s_8\right)\mathbf{P_6} \\
+ \quad & \left(\tfrac{56}{65}s_6+\tfrac{56}{143}s_2s_4+\tfrac{5936}{13585}s_2s_6+\tfrac{4480}{24453}s_4^2+\tfrac{48}{95}s_8\right)\mathbf{P_8} \\
+ \quad & \left(\tfrac{270}{323}s_8+\tfrac{1512}{4199}s_2s_6+\tfrac{7350}{46189}s_4^2\right)\mathbf{P_{10}} \\
n=2: \quad & \left(\tfrac{4}{9}s_4+\tfrac{12}{35}s_2^2+\tfrac{80}{231}s_2s_4+\tfrac{48}{385}s_2^3\right)\mathbf{P_0} \\
+ \quad & \left(\tfrac{8}{7}s_2+\tfrac{72}{77}s_2^2+\tfrac{400}{693}s_4+\tfrac{7156}{3003}s_2s_4+\tfrac{648}{5005}s_2^3+\tfrac{100}{143}s_6\right)\mathbf{P_2} \\
+ \quad & \left(1+\tfrac{80}{77}s_2+\tfrac{1346}{1001}s_2^2+\tfrac{648}{1001}s_4+\tfrac{4304}{15015}s_2^3+\tfrac{2160}{1001}s_2s_4+\tfrac{80}{143}s_6\right)\mathbf{P_4} \\
+ \quad & \left(\tfrac{20}{11}s_2+\tfrac{108}{77}s_2^2+\tfrac{80}{99}s_4+\tfrac{11800}{3927}s_2s_4+\tfrac{72}{1309}s_2^3+\tfrac{112}{187}s_6\right)\mathbf{P_6} \\
+ \quad & \left(\tfrac{1960}{1287}s_4+\tfrac{168}{143}s_2^2+\tfrac{17920}{8151}s_2s_4+\tfrac{1632}{2717}s_2^3+\tfrac{2016}{2717}s_6\right)\mathbf{P_8} \\
+ \quad & \left(\tfrac{5880}{4199}s_6+\tfrac{88200}{46189}s_2s_4+\tfrac{15120}{46189}s_2^3\right)\mathbf{P_{10}} \\
n=3: \quad & \left(\tfrac{150}{143}s_4+\tfrac{1350}{1001}s_2^2\right)\mathbf{P_2} \quad + \quad \left(\tfrac{270}{143}s_2+\tfrac{2430}{1001}s_2^2+\tfrac{120}{143}s_4\right)\mathbf{P_4} \\
+ \quad & \left(1+\tfrac{3783}{935}s_2^2+\tfrac{84}{55}s_2+\tfrac{168}{187}s_4\right)\mathbf{P_6} \quad + \quad \left(\tfrac{168}{65}s_2+\tfrac{8904}{2717}s_2^2+\tfrac{3024}{2717}s_4\right)\mathbf{P_8} \\
+ \quad & \left(\tfrac{8820}{4199}s_4+\tfrac{11340}{4199}s_2^2\right)\mathbf{P_{10}} \\
n=4: \quad & \tfrac{224}{85}s_2\mathbf{P_6} \quad + \quad \left(1+\tfrac{192}{95}s_2\right)\mathbf{P_8} \quad + \quad \tfrac{1080}{323}s_2\mathbf{P_{10}} \\
n=5: \quad & 1\mathbf{P_{10}}
\end{aligned}
$$

THE END

Danksagung

An dieser Stelle möchte ich all denen danken, die zum Gelingen dieser Arbeit beigetragen haben. Der erste Platz gebührt meinem Betreuer **Ronald Redmer**, der mich mit treffsicherem Gespür für die Strömungen der Zeit zur Modellierung großer Planeten motiviert hat, durch sein stetes Vertrauen in meine Arbeit diese Motivation in hohem Maße aufrechtzuerhalten verstanden hat, und es mir schließlich durch seine Förderung ermöglicht hat, auf internationaler Ebene wahrgenommen zu werden. Jedoch, ohne das beherzte Einfädeln der Zusammenarbeit seinerzeit durch **David Blaschke** wäre es nicht zu diesem Lauf der Dinge gekommen.
In der ersten Phase meiner Promotionstätigkeit in Rostock haben besonders **Hauke Juranek, Angelika Kuligk** und **Volker Schwarz** zu einer wirklich angenehmen Arbeitsatmosphäre beigetragen. In der zweiten Phase habe ich in **Martin French** einen super Partner zur Leitung von Übungsgruppen gefunden, und **Bastian Holst** danke ich für seinen Sofortservice bei Computerproblemen. **Andre Kietzmann** hat durch schlagfertigen Humor, und **Jörg Köhn** durch freundschaftliche Worte und Taten das Physikerleben enorm bereichert, und **Winfried Lorenzen** danke ich für gelegentliche Übersetzungsarbeit vom Deutschen ins Deutsche. In einer dritten Phase, der Phase des Übergangs von warmer, dichter Materie zum kalten, netzwerkartigen Weltraum (oder auch der Phase des kalten Wassers), runden in wissenschaftlicher Hinsicht viele hilfreiche und inspirierende Gespräche mit **Ralf Neuhäuser**, **Peter Hauschildt**, **Tristan Guillot**, **Jonathan Fortney**, **David Stevenson** und die von ihm hervorgebrachte Love-number Expertin **Ulrike Kramm** das Bild ab. In Anbetracht vielfältiger kleiner Hilfestellungen möchte ich auch **Frau Dulinski**, **Wolf Kraeft**, **Thomas Bornath** und **Robert Thiele** nicht ungenannt lassen.
Ohne die seltene, dann aber essenzielle Notfallhilfe durch meinen Freund **Matthias Meyer** wäre der Weg bis hierher ein steinigerer gewesen, und ohne seine Ablenkungen ein weniger lebendiger. Meinen Großeltern danke ich für materielle Unterstützung, und meiner Mutter für verlässliche Inpflegenahme von **Kilian**. Im Scheiden scheint es, als ob Planeten auf das Schicksal der Menschen denn doch einen Einfluss haben.

Zusammenfassung der Arbeit

Diese Arbeit knüpft an die langjährige Tradition der Rostocker Physik an, Zustandsgleichungen für den sowohl theoretisch als auch experimentell schwer zugänglichen Bereich der stark gekoppelten Materie zu entwickeln und intensiv zu testen. Große Planeten sind solche Testobjekte.

In der hier vorliegenden Arbeit habe ich eine ausführliche Darstellung des gesamten formalen, auf rein klassischer Mechanik beruhenden Unterbaus gewählt, auf dem die Modellierung starr rotierender Planeten im *hydrostatischen* Gleichgewicht fußt. Sein Verständnis ist von grundlegender Bedeutung für die Akzeptanz und Bewertung der Ergebnisse.

Mehrere Zustandsgleichungen (EOS) von Wasserstoff (H-EOS) werden an Jupiter getestet. Mit einigen H-EOS können keine Modelle erstellt werden, die mit allen Beobachtungsdaten gut verträglich sind, jedoch im Rahmen von Laborexperimenten nicht auszuschließen sind. Daher wird in dieser Arbeit erstmals dargelegt, wie Planetenmodelle auf eine durch die Zustandsgleichung vorgegebene Druck-Dichte Relation reagieren. Die daraus ergangenen Hinweise für im Hause erstellte H-EOS haben dazu beigetragen, die derzeit mit allen Daten am besten verträgliche Wasserstoffzustandsgleichung zu Stande zu bringen. Eine Vorhersage aus den Jupitermodellen, die sich noch in der Umsetzung befindet, ist z.B. die Unterschätzung des Druckes der EOS im 0.5-1 Megabar Bereich infolge von linearem Mischen von H und He. Die anhand der Jupitermodelle und experimentellen Daten für am besten befundene EOS, LM-REOS, enthält im relevanten Bereich der starken Kopplung ab initio EOS Daten.

Angewendet auf Saturn finden wir eine deutlich subsolare Heliumhäufigkeit im äußeren Mantel, und in Übereinstimmung mit in der Literatur angegebenen Grenzwerten für die Masse des Kerns finden wir Werte zwischen 0 und 1/4 der Gesamtmasse, je nach Wahl einer Schichtengrenze. Damit tragen wir zur Klärung der vor vielen Jahren aufgeworfenen Frage nach Saturns Kernmasse insofern bei, als dass erst die Frage der Schichtengrenze geklärt werden muss, die ein unabdingbarer Bestandteil der auf LM-REOS basierenden Modelle ist. Dies kann, ein wichtiges Ergebnis dieser Arbeit, nur zusammen mit einer Berechnung der Evolution unter Berücksichtigung von H/He Phasentrennung und Sedimentation geschehen mit der Zwangsbedingung, Saturns Leuchtkraft und, falls in naher Zukunft bekannt, Heliumgehalt in der Atmosphäre zu reproduzieren.

Es konnte in dieser Arbeit erstmals eine qualitative Erklärung für Uranus' geringe Leuchtkraft im Zusammenhang mit seiner Zusammensetzung gefunden werden. Der Übergang von molekularem Wasser im äußeren Mantel zu ionisch dissoziierten Wasser im inneren Mantel fällt mit einem hohen Dichtegradienten zusammen. Unterhalb der leitenden Schicht, deren Ausdehnung gut mit Vorhersagen zur Magnetfeldgeneration übereinstimmt, erstreckt sich ein ausgedehnter Bereich, in dem Wasser die Bildung eines Sauerstoffgitters bevorzugt. Beide Eigenschaften können Konvektion und Wärmeaustausch behindern. Diese Arbeit motiviert die Berechnung des Phasendiagramms und der Wärmeleitfähigkeit von Mischungen aus Wasser, Methan und Wasserstoff.

Die gewonnenen Ergebnisse wären nicht möglich gewesen ohne auf Dichtefunktionaltheorie und Molekulardynamik beruhenden EOS Daten für H, He, und H_2O. Diese wurden von A. Kietzmann, M. French und B. Holst mit hohem Rechenaufwand erstellt, teilweise durch den SFB 654 finanziert und das RZ Rostock unterstützt.

Stellungnahme

Hiermit erkläre ich, dass ich die vorliegende Arbeit selbständig verfasst habe und nach bestem Wissen keine anderen Hilfsmittel und Quellen verwendet habe als angegeben.

Rostock, den 4. September 2009

Dieser zur Veröffentlichung bestimmte Ausdruck der Arbeit wurde gegenüber dem am 7. September 2009 eingereichten Ausdruck nachträglich im Jahre 2011 überarbeitet, indem einige Hundert Tippfehler beseitigt wurden, das Seitenformat von einseitig auf doppelseitig umgestellt wurde, das Literaturverzeichnis mit ins Inhaltsverzeichnis aufgenommen wurde, und die Verwendung schwarzer Hilfslinien (Textunterstriche, Formelumrahmungen, Absatztrennlinien) reduziert wurde.